Semiconductors, Vol. 36, No. 11, 2002, pp. 1199–1201. Translated from Fizika i Tekhnika Poluprovodnikov, Vol. 36, No. 11, 2002, pp. 1281–1283.

DEDICATED
TO THE MEMORY OF V. F. MASTEROV

Vadim Fedorovich Masterov, a Scientist and a Teacher

V. K. Ivanov and B. P. Popov

St. Petersburg State Technical University,
Politekhnicheskaya ul. 29, St. Petersburg, 195251 Russia

Vadim Fedorovich Masterov was a prominent scientist and organizer of science. He made an outstanding contribution to the development of various lines of investigation in the physics of condensed states at St. Petersburg State Technical University. Masterov was born on December 17, 1941, in Arkhangelsk. In 1959, after graduating from secondary school in Arkhangelsk, he entered the mechanical engineering faculty of the Leningrad Polytechnical Institute (now St. Petersburg State Technical University). Later, Masterov transferred to the physics–mechanics faculty after passing, with excellent marks, the examinations in mathematical and theoretical physics—without attending lectures. After graduating from the institute in 1964, Masterov joined the department of experimental physics as a research worker. Later on, all his scientific activities were related to this department. In 1971, Masterov defended his candidate thesis in physics and mathematics; in 1979, he became a doctor of physics and mathematics. At this department, Masterov worked his way from junior researcher (1965) to a professor (1982). For many years, Masterov was the scientific deputy head of this department; later on, Masterov became the head of the same department (in 1991) and was in charge of this department until his untimely death in 1999. The results of his scientific works were published in more than 10 monographs and textbooks and in more than 200 papers in scientific journals in this country and abroad.

The range of scientific interests of Masterov was fairly wide. Masterov started his scientific activity under the supervision of Professor D.N. Nasledov, who was at that time the head of both a department and a laboratory at the Ioffe Physicotechnical Institute. However, Nasledov was mostly a consultant rather than a supervisor of scientific studies; as a result, Masterov soon started to work without assistance. His first scientific investigations were related to progress in experimental methods. While still a student, Masterov took an interest in the problem of magnetism in semiconductors; in order to solve this problem, it was necessary to develop new methods for experimental studies of solids. In 1965, Masterov initiated a new line of studies at the department of experimental physics—the radio-frequency spectroscopy of the condensed state. From that time on, this line of research became a main specialization of this department. Under Masterov's guidance and with his direct participation, a number of spectrometers for nuclear-magnetic and electron-spin resonances were developed, designed, and built; one of these spectrometers included a new type of resonator, i.e., the so-called spin induction resonator. Later on, this resonator was patented; it is now widely used in the Bruker radio-frequency spectrometers.

From 1967 to 1975, Masterov conducted studies concerned with the magnetism of deep-level centers in semiconductors. He suggested that these centers are characterized by a short-range potential; this concept turned out to be very fruitful and is now widely accepted. At that time, semimagnetic semiconductors based on iron-doped III–V compounds were obtained and studied for the first time. The electronic structure of impurity centers introduced into semiconductors by the elements that belong to the iron transition Group in the periodic table were studied. The phenomenon of super-

1063-7826/02/3611-1199$22.00

paramagnetism was discovered, and the parameters of spin-vitreous clusters in Fe-doped GaAs were determined. The experimental and theoretical works of Masterov devoted to the physics of deep-level multielectron centers in semiconductors became classics and gained wide recognition. The results of his studies in this field have been repeatedly reported at international conferences and have been published in two monographs and five reviews in the journals *Fizika tverdogo Tela* ("Physics of the Solid State") and *Fizika i Tekhnika Poluprovodnikov* ("Semiconductors").

In 1980, Masterov and his colleagues were the first to observe the photoluminescence and later (in 1982) electroluminescence related to intracenter transitions in III–V semiconductors doped with rare-earth elements. In 1993, Masterov suggested and theoretically substantiated the use of low-dimensional semiconductor structures in order to increase the efficiency of *f–f* emission. It has been shown that it is possible to develop a laser that operates at a wavelength of 1.54 μm and is based on the InP/$In_xGa_{1-x}As_yP_{1-y}$/InP heterostructure doped with erbium. It was shown in the corresponding series of publications that semiconductors doped with rare-earth elements are promising materials for the development of coherent and noncoherent sources of infrared radiation.

Starting in 1987, Masterov became deeply involved in solving the problem of high-temperature superconductivity (HTSC). The phenomenon of nonresonance microwave absorption in HTSC materials was discovered in his laboratory independently of and simultaneously with other scientific teams. Masterov and his colleagues developed a new method for studying the spatial distribution of charge in complex copper metallooxides; this method is based on emission Mössbauer spectroscopy. The results of corresponding studies were cited in reviews written by authors in this country and abroad; these studies are being actively pursued at present.

In the early 1990s, studies of fullerenes and other allotropic forms of carbon were initiated in the laboratory headed by Masterov. The discovery of an HTSC phase in copper-containing fullerene was the most interesting result of studies in the field of fullerene physics; the aforementioned phase features an unprecedentedly high (for this type of compound) temperature of superconducting transition T_c = 120 K. In the mid-1990s, a review dedicated to the studies of HTSC in copper-containing fullerene was published. Masterov and his colleagues developed and patented the technology for the production of fullerene single crystals. Simultaneously, he initiated a new line in the studies of solids at the department of experimental physics, specifically, radiation-physics materials science. The aim of these studies consisted in developing the physical foundations for the modification of semiconducting materials under the effect of various types of radiation.

It must be emphasized that the scientific activity of Masterov was invariably closely related to the leading scientific centers both in Russia and in a number of foreign countries. In his scientific activity, Masterov collaborated with leading scientists from the Ioffe Physicotechnical Institute of the Russian Academy of Sciences (RAS), the Vavilov State Optical Institute, the Konstantinov Institute of Nuclear Physics of the RAS, the Grebenshchikov Institute of Silicate Chemistry of the RAS, and the Research Institute "Domen", as well as with scientists from the United States, Germany, the Netherlands, and Italy. From 1994, Masterov had been a consultant to the University of Arizona; he had also been involved in numerous international projects and received many foreign grants.

From the very beginning, the scientific activity of Masterov was invariably combined with his pedagogical activity. Masterov was an excellent teacher and paid much attention to the improvement of teaching physics in institutions of higher education. In the early 1970s, Masterov, in collaboration with Professors I.P. Ipatova and Yu.I. Ukhanov, initiated a regularly convening seminar dedicated to the reconsideration and improvement of lecture courses. Not only the leading lecturers of the department of experimental physics but also the leading professors from other academic institutes participated in these seminars. The concept of modern courses in physics for students of various departments was thought out. First of all, the content of physics courses and the teaching of physics were brought into correspondence with the requirements of that time and the contemporary state of physics, i.e., with the latest and most important scientific achievements in physics in the twentieth century. The results of these efforts are presented in a new handbook on physics, the first volume of which was published this year.

In the late 1970s, the student-practice physical laboratory at the department of experimental physics was radically revised. In essence, Masterov and his colleagues founded a new practice facility equipped with modern instruments. Starting from their first year of studies, students could become acquainted with the latest achievements in experimental physics of that time. The laboratory for training in physics at the Leningrad Polytechnical Institute became one of the best in the Soviet Union and was awarded a gold medal at the Exhibition of Economic Achievements of the USSR in 1979.

Masterov spared no effort to turn the department of experimental physics into a prominent scientific and methodological center. Under his supervision, 14 candidate and 4 doctoral theses were defended. Many of his students and colleagues continue to be engaged successfully in scientific and pedagogical activities. Masterov published more than 30 books devoted to educational methods, including six textbooks. From 1992 to 1997, he was a member of the Scientific–Methodological Council on Physics at the Ministry of Higher Edu-

cation of the Russian Federation and was a member of the Scientific–Methodological Council at the St. Petersburg State Technical University. In 1994, Masterov initiated the foundation of a system of Bachelors and Masters of Science (Physics) at the department of experimental physics, with a specialization in physics with Masters of Science having a specialization in the physics of the condensed state. The Vavilov State Optical Institute, Konstantinov Institute of Nuclear Physics, and the Ioffe Physicotechnical Institute were involved in training students in the atomic spectroscopy of the condensed state and in physicochemical biology within the general field of the physics of the condensed state.

The department of experimental physics (the physics laboratory), which was founded thanks to the great efforts of Professor V.V. Skobel'tsyn, who later became the first head of this department, celebrates its 100th anniversary this year. The fame of this department was achieved through the diverse activities of prominent Soviet scientists: Academician A.F. Ioffe, Professor D.N. Nasledov, and Professor Yu.I. Ukhanov, who were the heads of the department of experimental physics at different times. Masterov was the fifth head of this department and headed it during the 1990s, which were very difficult years for science and education. Masterov deserves much credit for the fact that he not only preserved the scientific and pedagogical personnel of the department but even enhanced its scientific potential. Due to the efforts of Masterov during those years, new lines in both experimental and theoretical investigations were developed; moreover, the department began to turn out specialists rather than being just a department of general physics; links with research institutes also became stronger. The number of doctors of science and full professors increased from ten in the 1980s to 22 at present; furthermore, more than ten professors are part-time lecturers at the department.

Masterov will remain in the memory of his friends, colleagues, and students and in the history of the development of the department of experimental physics at St. Petersburg State Technical University.

Translated by A. Spitsyn

Semiconductors, Vol. 36, No. 11, 2002, pp. 1202–1203. Translated from Fizika i Tekhnika Poluprovodnikov, Vol. 36, No. 11, 2002, pp. 1284–1285.

DEDICATED TO THE MEMORY OF V. F. MASTEROV

International Symposium on Photoluminescence and Electroluminescence of Rare-Earth Elements in Semiconductors and Insulators

E. I. Terukov (the Chairperson of Organizing Committee of the Symposium)

Ioffe Physicotechnical Institute, Russian Academy of Sciences, Politekhnicheskaya ul. 26, St. Petersburg, 194021 Russia

e-mail: eug.terukov@pop.ioffe.rssi.ru

The international symposium "Photoluminescence and Electroluminescence of Rare-Earth Elements in Semiconductors and Insulators" was held in St. Petersburg from October 23 to October 24, 2001. The Symposium was organized by the Russian Academy of Sciences, specifically, by the Ioffe Physicotechnical Institute and St. Petersburg State Technical University. The chairperson of the organizing committee was E.I. Terukov, the cochairperson was V.K. Ivanov, and the secretary of the organizing committee was I.N. Trapeznikova.

There were 50 papers presented at the symposium. The participants included scientists from Sweden, Canada, Russia, Belarus, Ukraine, and Kazakhstan.

The symposium was dedicated to the memory of Professor V.F. Masterov, who was one of the pioneers of investigations and applications of amorphous semiconductors doped with rare-earth elements (REEs). In the course of the plenary session devoted to the scientific activity of Professor V.F. Masterov, lectures were delivered by leading scientists in the field of REE effects in semiconductors, i.e., by Z.F. Krasil'nik, G.V. Hansson, P.G. Baranov, E.I. Terukov, V.G. Golubev, M.M. Mezdrogina, and others; these lectures included reviews of the latest achievements in the REE physics of semiconductors and elucidated the contribution of Masterov to this field of research (the lectures delivered by Professor V.K. Ivanov and Professor V.I. Ivanov-Omskiĭ).

The papers presented at the symposium covered the following three topics:

(1) The REEs in semiconducting crystals and insulators;

(2) The REEs in unordered media; and

(3) Technological applications of REEs.

In the papers devoted to REEs in semiconducting crystals and insulators, much attention was given to the development of various theoretical models for the formation of radiative-recombination centers in Si, special features of photoluminescence spectra in semiconductors and insulators doped with REEs, emission of ions of various REEs, and the energy-transfer phenomena in emission.

The attention of the symposium participants was drawn to the papers presented by V.V. Kozlovskiĭ, E.S. Demidov, A.O. Zakhar'in, and M.M. Mezdrogina.

The authors of the papers devoted to REEs in unordered media investigated REE photoluminescence (PL) in porous materials, amorphous binary alloys, and composites; various methods for the introduction of REEs in porous materials; and the effect of thermal annealing on the luminescence of REE ions. In this section of the symposium, the attention of the participants was drawn to the papers presented by N.V. Gaponenko, É.É. Kolesnik, D. Khoptyar, I. Molchan, and V.G. Golubev. The lectures delivered by V.P. Bondarenko *et al*. aroused particular interest; in these lectures, the discovery of a hyperfine structure in the PL spectra of porous Si doped with Er and Fe was reported. The authors of these papers attribute the hyperfine structure to the formation of highly ordered nanoclusters composed of Si, O, Er, and Fe atoms. The studies reported in the papers presented by V.G. Golubev *et al*. were ingenious in their concept and pioneering in their implementation; these studies were devoted to the luminescence of Er ions in the opal–Er_2O_3 composite. The introduction of materials containing Er and emitting in the visible and near-infrared regions of the spectrum into pores in opal opens up fresh opportunities for the development of a new class of components for telecommunication data-processing and data-transmission systems. The paper presented by D. Khoptyar *et al*. deserves attention; in this paper, the problem of quenching the erbium PL in optical quartz amplifiers due to migration of excitation over the Er subsystem is discussed.

Many papers in the symposium program were devoted to practical applications of materials doped with REEs. Thus, this subfield was represented by the studies of (i) the current flow in heterojunctions based on materials doped with REEs (I. Tyagul'skiĭ *et al.*); (ii) the capacitance–voltage and current–voltage characteristics of light-emitting structures doped with REEs (A. Yakimenko); (iii) the REE cathodoluminescence

1063-7826/02/3611-1202$22.00

with the aim of obtaining ceramics to be used for the immobilization of nuclear wastes (M. Zamoryanskaya *et al.*); and (iv) the feasibility of using insulating layers doped with REEs to develop electroluminescent displays (A. Andreev *et al.*).

In the discussion at the end of the symposium, the timeliness, topicality, and high scientific level of the symposium were noted. It was also noted that a large number of the studies were of a high scientific level that corresponded to the contemporary state of world science in this field. The reported results of many studies were pioneering, e.g., the discovery of stimulated emission in films of amorphous Si doped with Er (the so-called laser effect), the development of planar microcavities for a wavelength of 1.54 μm, the obtainment of three-dimensional arrays of Er_2O_3 nanoclusters in an opal host, the properties of porous silicon doped with REEs, and so on.

According to the data contained in the abstracts of the papers presented at the symposium, five studies were supported by the Russian Foundation for Basic Research and seven studies were supported by grants from the Ministry of Science of the Russian Federation and the federal program "Integration."

All papers presented at the symposium were published in the corresponding proceedings. The program committee of the symposium recommended that the most interesting papers be published in this issue of "Semiconductors."

The symposium was made possible thanks to the support of the Russian Foundation for Basic Research (project no. 01-02-26102) and the Ioffe Physicotechnical Institute of the Russian Academy of Sciences.

Translated by A. Spitsyn

Semiconductors, Vol. 36, No. 11, 2002, pp. 1204–1208. Translated from Fizika i Tekhnika Poluprovodnikov, Vol. 36, No. 11, 2002, pp. 1286–1290.

DEDICATED TO THE MEMORY OF V. F. MASTEROV

V. F. Masterov's School and Fullerene Research at the Department of Experimental Physics, St. Petersburg State Technical University

A. V. Prikhodko and O. I. Konkov

St. Petersburg State Technical University, Politekhnicheskaya ul. 29, St. Petersburg, 195251 Russia

Submitted April 2, 2002; accepted for publication April 11, 2002

Abstract—Experimental studies of fullerenes at the department of experimental physics, St. Petersburg State Technical University, are reviewed. These studies were performed under the guidance of Professor V.F. Masterov, doctor of mathematics and physics. Primary attention is paid to the studies of the weak-superconductivity effect detected in copper-containing fullerene structures. *© 2002 MAIK "Nauka/Interperiodica".*

INTRODUCTION

This review is based on the results of studies of fullerenes performed under the guidance of Professor and Doctor of Physics and Mathematics V.F. Masterov at the department of experimental physics at St. Petersburg State Technical University. Attention is primarily paid to the effect of weak superconductivity detected in copper-containing fullerene structures based on films, powders, and crystals. The development of superconductivity models and practical implementation of the fullerene studies are treated at some length.

I. WEAK SUPERCONDUCTIVITY OF COPPER–OXYGEN CLUSTER STRUCTURES BASED ON C_{60} (POWDERS AND FILMS)

In 1993, Masterov initiated intensive studies of fullerene structures. A series of microwave, magnetic, and electrical experiments with powders and thin films of Cu_nC_{60} was carried out within a comparatively short period of time [1–15]. The results indicated that there is high-temperature superconductivity in a Cu_nC_{60} system. The following facts were ascertained: (i) a transition of the samples to the diamagnetic state is accompanied by the appearance of a microwave-absorption line (the transition-onset temperature is 118 K); (ii) the parameters of the line (the shape and width) in weak magnetic fields are close to those of the microwave-absorption line observed in high-temperature superconductors (HTSCs) at temperatures T below the critical temperature T_c ($T < T_c$); and (iii) there is a hysteresis in the dependence of the derivative of the microwave-power absorption with respect to the magnetic field (dP/dH) on the magnetic field H. This hysteresis is characteristic of microwave absorption in superconductors that contain internal Josephson junctions [6]. In order to verify the superconducting properties of the Cu_nC_{60} samples, Masterov *et al*. studied the total magnetic moment using a magnetometer based on a superconducting quantum-interference device (SQUID) in the temperature range of 4.2–150 K in zero (ZFC) and nonzero (FC) magnetic fields [10]. The total magnetic moment was paramagnetic at 4.2 K. As the temperature was increased, the paramagnetism was drastically enhanced in the temperature range of 100–120 K in the ZFC mode at a magnetic field of 98 G. It is worth noting that the onset temperature of the phase transition (120 K) coincided with the temperature obtained from the measurements of microwave absorption and magnetic susceptibility at low frequencies. The fractional volume of the Meissner phase in the sample was estimated at about 10% from the measurements in the ZFC mode. The observed paramagnetic moment was explained in the context of a model of weakly coupled loops; according to this model, negative critical points may exist in the Josephson loops that contain paramagnetic impurities. The results of electrical studies of powdery and thin-film Cu_nC_{60} samples using the method of nanosecond current–voltage (I–V) characteristics also indicated that sample resistance drastically decreased as the temperature decreased below 90 K [11, 12]. In the context of magnetic experiments, it was reasonable to relate this circumstance to the phase transition to the superconducting state.

The first stage of the studies revealed the following:

(1) For Cu_nC_{60} powders, the microwave absorption related to the manifestation of the Meissner effect is observed at temperatures below 100–120 K. The hysteresis of the line with respect to the magnetic field corresponds to the internal Josephson junctions.

(2) In Cu_nC_{60} powders, the reverse Josephson effect and an analogue of the Shapiro steps in the dependence of current on the microwave-radiation power were observed; the aforementioned steps are characteristic of internal Josephson junctions in the HTSC structures.

1063-7826/02/3611-1204$22.00

(3) The SQUID measurements were used to detect a diamagnetic transition at a temperature of 120 K against a paramagnetic background in the Cu_nC_{60} powders.

(4) Studies of transport properties in the nanosecond range of the voltage duration confirm the existence of a phase transition in the bulk (at 90 K) and thin-film (at 83–103 K) Cu_nC_{60} samples.

II. WEAK SUPERCONDUCTIVITY IN THE COPPER–OXYGEN STRUCTURES BASED ON C_{60} POLYCRYSTALS

The next stage of fullerene studies was based on a new method of producing fullerene polycrystals [16]. The parameters of the samples were unique: the sample diameter was 2.8–8 mm, the thickness was 2 mm, some of the single crystals were 0.2 mm in diameter, and the largest length was about 2 mm. The results of structural studies of a bulk polycrystalline fullerene sample (henceforth, a membrane) made of a mixture of C_{60} and C_{70} indicated that the initial side of sample growth (from the substrate size) is a plane formed of C_{60}, whereas the final side is represented by a C_{70} hemisphere [17, 18]. In Fig. 1a, we show a separate crystallite; a photograph of the sample cut is shown in Fig. 1b.

Comparing the Raman spectroscopy data with the results of X-ray diffraction analysis, we may assume that the sample under investigation is a fullerite whose composition varies from C_{60} to C_{70}. A comparative analysis of initial C_{60}/C_{70} and (C_{60}/C_{70}):Cu fullerene samples showed that a splitting of the X-ray reflections was observed for (C_{60}/C_{70}):Cu; these reflections corresponded to a structure with lattice parameters $a = 14.42$ and 14.47 Å. Splitting of the reflections signifies the appearance of tetragonality, i.e., the onset of a transition from the fcc structure to a structure with a lower symmetry. Thus, it may be assumed that the C_{60} molecules form complexes with oxygen and copper; apparently, these complexes are similar to those existing in graphite.

Combined studies of microwave and magnetic properties of polycrystalline C_{60}/C_{70} samples doped with copper were carried out [19–21]. The diamagnetism of separate fullerite crystals manifests itself in the samples at $T < 150$ K in the form of a specific dip in the temperature dependence of static magnetic susceptibility. The range of existence of such an anomaly in the diamagnetic properties is 75–150 K for various fullerite crystals from the membrane composition. The field dependence of magnetic susceptibility can be used to estimate the value of the critical magnetic field; this value is found to be equal to about 8 kOe for the sample under consideration at 80 K. Nonuniformity in the distribution of diamagnetic properties both over the volume of the entire polycrystalline sample and the volume of a separate crystallite, which manifests itself in the instability of the range of the dip depending on a specific

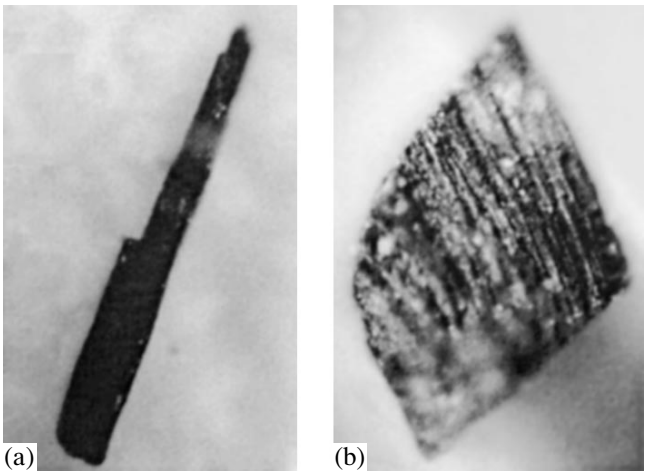

Fig. 1. Photographs of membrane's crystal structure: (a) a separate crystallite and (b) a section of the sample.

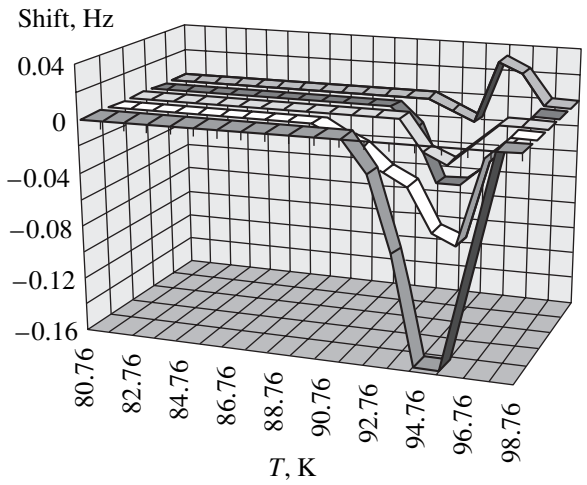

Fig. 2. Temperature dependences of the frequency shift for a thin (C_{60}/C_{70}):Cu membrane in the course of thermal cycling. The number of cycles increases from left to right and into the depth of the drawing.

crystal and its size, is obviously caused by the nonuniform distribution of copper in the samples.

According to the data of mass spectrometry analysis, the copper content in the C_{60} membrane did not exceed 10^{-2}%. It is ascertained that the fabrication of thinner membranes (with the thickness at the center no larger than 0.5 mm) is accompanied with corresponding changes in the sizes of separate crystallites; as a result, the diamagnetism of the crystallites is reduced drastically. In Fig. 2, we show experimental data on the magnetic permeability of the sample using the method of disbalance between the frequencies of quartz oscillators; the disbalance itself, *df* (shift), depends linearly on magnetic permeability. The existence of a well-defined diamagnetic dip (the existence of diamagnetic properties in a certain temperature range) is apparently related

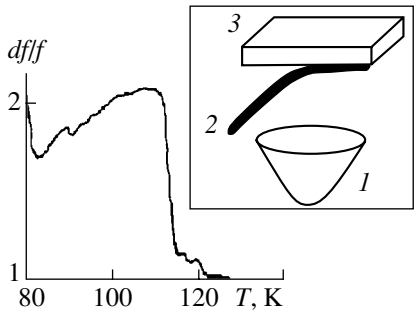

Fig. 3. Temperature dependence of the frequency disbalance df/f. In the inset, we illustrate the experiment aimed at direct detection of the effect of the magnetic-field expulsion from the sample bulk at 110 K: (*1*) the sample, (*2*) the ferromagnetic film, and (3) the quartz surface.

to the destruction of the diamagnetic state in highly inhomogeneous regions of the sample, similarly to the effects observed in HTSC structures under various conditions of their fabrication. In this stage of the studies, an experiment was conducted with the aim of directly observing the expulsion of a magnetic field from the sample bulk at 110 K [22]. A modified method based on a disbalance between the frequencies of quartz oscillators was used; in this case, the relative disbalance df/f (f is the oscillator frequency) depended linearly on the quartz mass. When a force related to the Meissner effect appears in sample *1* (Fig. 3), ferromagnetic film *2* comes in contact with the surface of quartz *3*; as a result, the quartz-oscillator frequency increases.

In the second stage of the studies, the following results were obtained:

(i) The effect of the phase-composition separation and modification of the initial C_{60}–C_{70} mixture in the course of membrane fabrication was observed; the resulting samples consisted of either a polycrystalline fullerene with its composition varying from C_{60} to C_{70} or highly homogeneous C_{60} (or C_{70}).

(ii) Fullerenes C_{60} form complexes with oxygen and copper; these complexes reduce the symmetry of the fullerene's crystal lattice.

(iii) A drastic change in microwave absorption was observed at 260 K in the C_{60} fullerite.

(iv) A diamagnetic effect was detected experimentally in the temperature range of 100–150 K; this effect correlated with special features of microwave conductivity. In addition, the Meissner effect was detected at 110 K.

(v) The emergence of a transition to the superconducting state can be related to clusterization of carbon atoms (a transition from the graphene plane to a fullerene molecule) with the simultaneous existence of a copper–oxygen substructure.

(vi) Special features of microwave emission in the temperature range of 90–100 K were elucidated.

III. NEW APPLICATIONS OF COPPER-CONTAINING FULLERENE MEMBRANES

Masterov paid much attention to the practical implementation of the results of fullerene studies [23–27]. The outcome of this activity became the screens for nanoelectronic devices, gas sensors, quarter-wave emitting dipoles, and random reflecting gratings based on the Costas arrays of such dipoles.

IV. A MODEL OF SUPERCONDUCTIVITY IN COPPER–OXYGEN STRUCTURES BASED ON UNORDERED SEMICONDUCTORS

Masterov was actively involved in solving the problem of HTSC in copper-containing fullerenes. In particular, he suggested that attention be given to the model of negative-U centers as an alternative to the Bardeen–Cooper–Schrieffer model for interpreting the HTSC in the aforementioned fullerenes. This line of research was further developed (and is being developed) at the department of experimental physics, St. Petersburg State Technical University. The approach based on the model of negative-U centers is validated by the following reasoning. It is ascertained that rotational disorder, which gives rise to the state of a "plastic crystal," is characteristic of the behavior of C_{60} molecules at room temperature. Spherical disorder is illustrated by the calculated [28] nonuniform distribution of the charge density for a C_{60} sphere at room temperature. Below a temperature of 261 K, four molecules of a crystal cell become orientationally equivalent and the system undergoes a phase transition of the first kind from the fcc to the simple cubic structure. Experimentally, such a transition was also observed in the fullerene samples under investigation. It was also ascertained that the orientational disorder persisted even at a temperature of 90 K. Thus, it is believed that C_{60} molecules are subject to orientational disorder in a wide temperature range of 260–90 K. It is also known that the attachment of a single oxygen atom (the chemical formula is $C_{60}O$) scarcely affects the molecular structure of C_{60}, with the orientational disorder at room temperature and the phase transition at 278 K being preserved. We now dwell on the role of another intercalant (copper) in the manifestation of orientational disorder. It is known [29] that the existence of an impurity copper atom above the graphene plane gives rise to nonuniformity in the effective-charge distribution; i.e., nonequivalent charge states in the graphene plane for neighboring atoms come into existence. This situation may bring about a change in the charge density at the C_{60} sphere and, consequently, an increase in orientational disorder. Thus, there is good reason to believe that C_{60} fullerene may be treated as an orientational glass. In this case, one may assume that the concept of the Anderson negative-U centers can also be used. In addition, the fairly high critical temperatures observed for the transition to the superconducting state are consistent with estimates of

these temperatures in terms of the model of negative-U centers [30, 31].

CONCLUSION

We will now list the main inferences from the fullerene studies.

(1) A new class of unordered structures based on polycrystalline fullerene-based solid solutions and copper-containing fullerene solutions was produced.

(2) On the basis of the observed Meissner effect and the results of electromagnetic and microwave studies, it was demonstrated that high-temperature superconductivity existed in the structures under investigation.

(3) It was suggested that the superconductivity model based on the synchronization of the negative-U centers be used to interpret the superconductivity of copper-containing fullerene structures.

In this article, we reviewed the results of studies conducted under the guidance of V.M. Masterov and supported by the programs "Fullerenes and Atomic Clusters" (grant no. 98063) and "Basic Research in Higher Education in the Fields of Science and the Arts. Universities of Russia" (grant no. 991144).

REFERENCES

1. V. L. Aver'yanov, N. E. Bazieva, V. F. Masterov, *et al.*, Pis'ma Zh. Tekh. Fiz. **19** (12), 77 (1993) [Tech. Phys. Lett. **19**, 388 (1993)].
2. S. G. Yastrebov, M. N. Kotov, A. V. Prichodko, *et al.*, in *Proceedings of the International Conference on Millimeter and Submillimeter Waves and Applications*, Ed. by Mohammed N. Afsar, Proc. SPIE **2250**, 322 (1994).
3. N. E. Bazieva, S. G. Yastrebov, V. F. Masterov, and A. V. Prichodko, Mol. Mater. **4** (1–3), 143 (1994).
4. V. F. Masterov, O. I. Kon'kov, A. V. Prikhod'ko, *et al.*, Pis'ma Zh. Tekh. Fiz. **20** (15), 17 (1994) [Tech. Phys. Lett. **20**, 614 (1994)].
5. V. F. Masterov, L. Z. Dapkus, and A. V. Prikhod'ko, Pis'ma Zh. Tekh. Fiz. **21** (20), 34 (1995) [Tech. Phys. Lett. **21**, 830 (1995)].
6. V. F. Masterov, A. V. Prikhod'ko, and B. P. Popov, Fiz. Tverd. Tela (St. Petersburg) **37** (8), 2503 (1995) [Phys. Solid State **37**, 1371 (1995)].
7. V. F. Masterov, A. V. Prichodko, O. I. Konkov, and E. I. Terukov, in *Abstracts of International Workshop on Fullerenes and Atomic Clusters, IWFAC-95, St. Petersburg, Russia, 1995*, p. 136.
8. V. F. Masterov, A. V. Prikhod'ko, O. I. Kon'kov, and E. I. Terukov, Pis'ma Zh. Tekh. Fiz. **21** (1), 66 (1995) [Tech. Phys. Lett. **21**, 30 (1995)].
9. V. F. Masterov, A. V. Prichodko, O. I. Konkov, and E. I. Terukov, Mol. Mater. **8**, 41 (1996).
10. V. F. Masterov, A. V. Prikhod'ko, O. I. Kon'kov, *et al.*, Fiz. Tverd. Tela (St. Petersburg) **38** (6), 1709 (1996) [Phys. Solid State **38**, 943 (1996)].
11. V. F. Masterov, A. V. Prikhod'ko, O. I. Kon'kov, and E. I. Terukov, Fiz. Tverd. Tela (St. Petersburg) **38** (6), 1687 (1996) [Phys. Solid State **38**, 931 (1996)].
12. V. F. Masterov, A. V. Prikhod'ko, O. I. Kon'kov, *et al.*, Fiz. Tverd. Tela (St. Petersburg) **38** (5), 1401 (1996) [Phys. Solid State **38**, 775 (1996)]; V. F. Masterov, A. V. Prikhodko, and O. I. Konkov, in *Proceedings of E-MRS Spring Meeting, 1998*, Symposium K, p. 12.
13. V. F. Masterov, A. V. Prikhod'ko, N. I. Nemchuk, *et al.*, Fiz. Tverd. Tela (St. Petersburg) **39** (9), 1703 (1997) [Phys. Solid State **39**, 1522 (1997)].
14. V. F. Masterov, A. V. Prikhod'ko, O. I. Kon'kov, and E. I. Terukov, Fiz. Tverd. Tela (St. Petersburg) **39** (5), 816 (1997) [Phys. Solid State **39**, 722 (1997)].
15. V. F. Masterov, A. V. Prichodko, and O. I. Konkov, Fullerene Sci. Technol. **6** (3), 481 (1998); V. F. Masterov, A. V. Prikhod'ko, and O. I. Kon'kov, in *Proceedings of the All-Russia Symposium with Participation of Scientists from Commonwealth of Independent States, St. Petersburg, 1998*, p. 81.
16. V. F. Masterov, A. V. Prikhod'ko, O. I. Kon'kov, and V. Yu. Davydov, RF Patent No. 2135648 (1997), Byull. Izobret., No. 24 (1999).
17. V. F. Masterov, A. V. Prikhod'ko, T. R. Stepanova, *et al.*, Fiz. Tverd. Tela (St. Petersburg) **40** (3), 580 (1998) [Phys. Solid State **40**, 535 (1998)]; V. F. Masterov, A. V. Prikhod'ko, T. R. Stepanova, *et al.*, in *Proceedings of the 2nd Russian Symposium "Heat-and-Mass Transfer Processes and Growth of Single Crystals and Thin-Film Structures", Obninsk, 1998*, p. 271; V. F. Masterov, A. V. Prichodko, and O. I. Konkov, in *Proceedings of E-MRS Spring Meeting, 1998*, Symposium K, p. 5.
18. V. F. Masterov, A. V. Prikhod'ko, O. I. Kon'kov, *et al.*, Fiz. Tverd. Tela (St. Petersburg) **40** (3), 577 (1998) [Phys. Solid State **40**, 532 (1998)]; V. F. Masterov, A. V. Prikhod'ko, O. I. Kon'kov, *et al.*, in *Proceedings of Scientific and Technical Conference "Basis Research in Technical University, St. Petersburg, 1997*, p. 243.
19. V. F. Masterov, A. V. Prikhod'ko, O. I. Kon'kov, *et al.*, Fiz. Tverd. Tela (St. Petersburg) **41** (4), 748 (1999) [Phys. Solid State **41**, 676 (1999)].
20. A. V. Prikhod'ko and O. I. Kon'kov, Pis'ma Zh. Tekh. Fiz. **25** (20), 44 (1999) [Tech. Phys. Lett. **25**, 820 (1999)].
21. V. F. Masterov, A. V. Prichodko, V. V. Romanov, *et al.*, in *Book of Abstracts of International Workshop on Fullerenes and Atomic Clusters, IWFAC99, 1999*, p. 204; V. F. Masterov, A. V. Prikhod'ko, and O. I. Kon'kov, Nauchno-Tekh. Vedomosti S-Peterb. Gos. Tekh. Univ., No. 3, 18 (2000).
22. A. V. Prikhod'ko and O. I. Kon'kov, Fiz. Tekh. Poluprovodn. (St. Petersburg) **35** (6), 687 (2001) [Semiconductors **35**, 659 (2001)].
23. V. F. Masterov, A. V. Prikhod'ko, and O. I. Kon'kov, in *Proceedings of the All-Russia Scientific and Technical Conference "Micro- and Nanoelectronics - 98", 1998*, Vol. 2, p. 15.
24. V. F. Masterov, A. V. Prikhod'ko, O. I. Kon'kov, *et al.*, Pis'ma Zh. Tekh. Fiz. **25** (8), 71 (1999) [Tech. Phys. Lett. **25**, 326 (1999)].
25. V. F. Masterov, A. V. Prikhod'ko, and O. I. Kon'kov, Nauchno-Tekh. Vedomosti S-Peterb. Gos. Tekh. Univ., No. 2, 38 (2000); V. F. Masterov, A. V. Prikhod'ko, and O. I. Kon'kov, in *Proceedings of the II International*

Conference "Amorphous and Microcrystalline Semiconductors", St. Petersburg, 2000, p. 140.

26. O. I. Kon'kov and A. V. Prikhod'ko, Pis'ma Zh. Tekh. Fiz. **26** (6), 27 (2000) [Tech. Phys. Lett. **26**, 236 (2000)].
27. V. F. Masterov, A. V. Prikhod'ko, and I. N. Kapitonov, in *Proceedings of the International Symposium "Carbonic Formations in Geological History - CFGH98", Petrozavodsk, 1998*, Part 3, p. 118.
28. J. E. Fischer and P. A. Heiney, J. Phys. Chem. Solids **12**, 1 (1993).
29. V. I. Ivanov-Omskiĭ and É. A. Smorgonskaya, Fiz. Tverd. Tela (St. Petersburg) **41** (5), 868 (1999) [Phys. Solid State **41**, 786 (1999)].
30. B. P. Popov and K. D. Tsendin, Pis'ma Zh. Tekh. Fiz. **24** (7), 45 (1998) [Tech. Phys. Lett. **24**, 265 (1998)].
31. K. D. Tsendin and B. P. Popov, Supercond. Sci. Technol. **12**, 255 (1999).

Translated by A. Spitsyn

Semiconductors, Vol. 36, No. 11, 2002, pp. 1209–1214. Translated from Fizika i Tekhnika Poluprovodnikov, Vol. 36, No. 11, 2002, pp. 1291–1296.

DEDICATED TO THE MEMORY OF V. F. MASTEROV

A Model for the Formation of Donor Centers in Silicon Layers Implanted with Erbium and Oxygen Ions

O. V. Aleksandrov and A. O. Zakhar'in

St. Petersburg State Electrotechnical University, St. Petersburg, 197376 Russia

e-mail: aleks_ov@mailbox.alkor.ru

Submitted April 2, 2002; accepted for publication April 11, 2002

Abstract—Formation of donor centers in the course of annealing of layers of single-crystal silicon FZ-Si (grown by the float-zone method) and Cz-Si (grown by the Czochralski method) implanted with Er^+ and O^+ ions was simulated. The diffusion–kinetics equations accounting for the formation of erbium-related donor centers of three types were solved numerically. These centers were formed with the involvement of oxygen in the substrate or implanted oxygen and also self-interstitials *I* produced during annealing of implantation-induced defects; i.e., the Er–*I*, Er–O, and Er–O–*I* centers were considered. The results of calculations satisfactorily describe the concentration profiles of donor centers and also the influence of oxygen in the substrate and implanted oxygen on the dependence of the donor-activation coefficient of erbium on the annealing temperature in the range of 600–1200°C. © *2002 MAIK "Nauka/Interperiodica".*

1. INTRODUCTION

Doping of silicon with rare-earth elements (REEs) and, particularly, with erbium is of considerable interest in the context of the development of optoelectronic structures integrated with silicon microcircuits (see reviews [1, 2]). Ion-implantation doping is one of the most efficient methods for introducing REE impurities, which have a low (no higher than 1×10^{18} cm^{-3}) equilibrium solubility in silicon. Annealing of single-crystal Si layers implanted with Er^+ ions gives rise to optically and electrically active (donor) centers. At present, there is no clear knowledge about the composition and structure of these optically and electrically active centers. An increase in the concentrations of optically active centers and donor-type electrically active centers in silicon grown by the Czochralski method (in which case there is a high concentration of grown-in oxygen) or coimplanted with O and Er is observed [1, 2]. It has been shown that the photoluminescing centers in crystalline silicon that contains oxygen and is doped with erbium are Er–O clusters [3]. The implantation of O ions in combination with Er ions brings about the formation of shallower donor levels [4, 5] related [5] to the Er–O complexes and oxygen associations. The formation of optically active centers and donor electrically active centers is affected by the atmosphere in which the postimplantation annealing is performed [6, 7]; this indicates that native point defects are involved in the formation of electrically and optically active centers. The formation of donor centers in silicon implanted with Er^+ ions has been simulated [8] on the assumption that these centers include silicon self-interstitials. The objective of this study is to simulate the donor-center formation as a result of combined implantation of Er^+ and O^+ ions into silicon on the assumption that oxygen atoms are incorporated into these centers.

2. EXPERIMENTAL

For substrates, we used polished wafers of single-crystal *p*-Si grown by the float-zone (FZ-Si) or Czochralski (Cz-Si) methods; the Si resistivity was equal to 20 Ω cm. Erbium ions with an energy of 1 MeV and at a dose of 1×10^{13} cm^{-2} were implanted using a High Voltage Engineering Europa 2-MV accelerator. Oxygen ions with an energy of 135 keV and at a dose of 1×10^{14} cm^{-2} were additionally implanted into a part of the wafers. In both cases, the implantation doses did not exceed the threshold doses for silicon amorphization. Isochronous annealings were performed for 30 min in a chlorine-containing atmosphere at T = 600–1200°C. The donor-activation coefficient k for erbium was determined from the sheet resistances R_s measured via the four-point probe method with allowance made for the concentration dependence of mobility; i.e.,

$$k = 1/e\mu R_s Q_{Er},$$

where Q_{Er} is the dose of implanted erbium, e is the elementary charge, and μ is the electron mobility. The charge-carrier concentration profiles were determined either from the capacitance–voltage characteristics of the Schottky barrier with a mercury contact or via the method of differential conductivity with the step-by-step removal of the layers using anodic oxidation.

3. MODEL EQUATIONS

We assume that annealing of oxygen-containing silicon layers implanted with Er^+ ions gives rise to

erbium-containing donor centers of three types. These are the centers W_1, a complex of Er with a self-interstitial (Er–*I*), W_2, a complex of Er with O (Er–O), and W_3, a complex of Er with oxygen and a self-interstitial (Er–O–*I*). Formation of these complexes is described by the following quasi-chemical reactions:

$$\mathrm{Er} + I \underset{k_2}{\overset{k_1}{\rightleftarrows}} W_1, \quad (1)$$

$$\mathrm{Er} + \mathrm{O} \underset{k_4}{\overset{k_3}{\rightleftarrows}} W_2, \quad (2)$$

$$W_1 + \mathrm{O} \underset{k_6}{\overset{k_5}{\rightleftarrows}} W_3. \quad (3)$$

Here, k_1, k_3, and k_5 are the rate constants for the direct reactions of complex formation; k_2, k_4, and k_6 are the rate constants for the reverse reactions of decomposition of the complexes; and $k_i = k_{i0}\exp(-E_{ki}/k_BT)$, where E_{ki} are the activation energies for formation or decomposition of the complexes (i = 1–6), and k_B is the Boltzmann constant. The kinetics of formation of the donor centers according to reactions (1)–(3) is described by the following system of diffusion–kinetics equations:

$$\frac{\partial[W_1]}{\partial t} = k_1[\mathrm{Er}][I] - k_2[W_1] - k_5[W_1][\mathrm{O}] + k_6[W_3], \quad (4)$$

$$\frac{\partial[W_2]}{\partial t} = k_3[\mathrm{Er}][\mathrm{O}] - k_4[W_2], \quad (5)$$

$$\frac{\partial[W_3]}{\partial t} = k_5[W_1][\mathrm{O}] - k_6[W_3], \quad (6)$$

$$\frac{\partial[I]}{\partial t} = D_I\frac{\partial^2[I]}{\partial x^2} - k_1[\mathrm{Er}][I] + k_2[W_1] + G - R, \quad (7)$$

$$\frac{\partial[\mathrm{O}]}{\partial t} = D_{\mathrm{Ox}}\frac{\partial^2[\mathrm{O}]}{\partial x^2} - k_3[\mathrm{Er}][\mathrm{O}] + k_4[W_2] - k_5[W_1][\mathrm{O}] + k_6[W_3]. \quad (8)$$

Here, x is the coordinate along the axis perpendicular to the surface and directed into the depth of the layer; t is time; D_I is the diffusion coefficient of self-interstitials, $D_I = 2.75\times10^{-4}\exp(-1.5/k_BT)$ cm^2/s [8]; D_{Ox} is the diffusion coefficient of oxygen atoms, $D_{\mathrm{Ox}} = 0.22\exp(-2.5/k_BT)$ cm^2/s [9]; G is the generation rate for self-interstitials in the course of annealing of defects produced by ion implantation; and R is the rate of recombination of self-interstitials at the centers in the bulk. In contrast to self-interstitials and oxygen atoms, the Er atoms and their complexes W_1, W_2, and W_3 were assumed to be immobile. Therefore, we have the following condition for the conservation of the total erbium concentration at each point of the initial erbium concentration after implantation:

$$[\mathrm{Er}](x,t) + [W_1](x,t) + [W_2](x,t) + [W_3](x,t) = [\mathrm{Er}](x,0). \quad (9)$$

Here, [Er](x, 0) is the initial distribution of implanted erbium (the experimental distribution was approximated by two Gaussian distributions and a function $\exp(-ax)$ for the tail of the distribution). The generation rate for self-interstitials is governed by the annealing rate of radiation defects produced by ion implantation; i.e.,

$$G(x,t) = \frac{\chi_{\mathrm{Er}}C_{\mathrm{Er}}(x) + \chi_{\mathrm{Ox}}C_{\mathrm{Ox}i}(x)}{\tau}\exp\left(-\frac{t}{\tau}\right). \quad (10)$$

Here, τ is the time constant for the annealing of radiation defects, $\tau = \tau_0\exp(E_\tau/k_BT)$, where E_τ is the activation energy for the annealing of radiation defects; the terms in the numerator represent the initial concentrations of self-interstitials after implantation of erbium and oxygen, respectively; $C_{\mathrm{Er}}(x)$ and $C_{\mathrm{Ox}i}(x)$ are the initial distributions of erbium and oxygen after implantation (these distributions are shifted by 10% away from the surface); and the quantities χ_{Er} and χ_{Ox} represent the number of self-interstitials formed per incident erbium and oxygen ion, respectively. The values of displacements (~10%), χ_{Er} and χ_{Ox}, were taken from [10] according to the expression $\chi = 1 + (0.42/R_p^{3/4})\sqrt{Em}$, where R_p, E, and m are the mean projected range, energy, and mass of incident ions, respectively. As a result, we have $\chi_{\mathrm{Er}} = 3.1$ and $\chi_{\mathrm{Ox}} = 1.25$. Some of the nonequilibrium self-interstitials produced as result of the annealing of implantation damage are involved in the formation of electrically active centers; other self-interstitials recombine in the bulk or drain to the surface. The rate of volume recombination of excess self-interstitials is controlled by the diffusion coefficient and the diffusion length of self-interstitials (L_I); i.e.,

$$R(x,t) = \frac{D_I([I](x,t) - I_{\mathrm{eq}})}{L_I^2}, \quad (11)$$

where I_{eq} is the equilibrium concentration of self-interstitials, and $I_{\mathrm{eq}} = 1.25\times10^{25}\exp(-3.66/k_BT)$ cm^{-3} [11]. The boundary conditions for self-interstitials and oxygen atoms at the surface (x = 0) and at the end of the solution region ($x = d$) are given by

$$[I](0,t) = I_{\mathrm{eq}}; \quad \frac{\partial[I](d,t)}{\partial x} = 0; \quad \frac{\partial[\mathrm{O}](0,t)}{\partial x} = \frac{\partial[\mathrm{O}](d,t)}{\partial x} = 0. \quad (12)$$

The initial conditions for silicon self-interstitials, oxygen atoms, and donor centers are written as

$$[I](x,0) = I_{\mathrm{eq}}; \quad [\mathrm{O}](x,0) = C_{\mathrm{Ox}} + C_{\mathrm{Ox}i}(x); \quad [W_1](x,0) = [W_2](x,0) = [W_3](x,0) = 0. \quad (13)$$

It was assumed in calculations that the initial concentration of oxygen was $C_{\mathrm{Ox}} \approx 10^{18}$ cm^{-3} in Cz-Si (silicon

grown by the Czochralski method) and $C_{Ox} \approx 10^{16}$ cm^{-3} in FZ-Si (silicon grown by the float-zone method).

Diffusion–kinetics Eqs. (4)–(8), written for the components which are involved in the formation of donor centers and supplemented with condition (9), boundary conditions (12), and initial conditions (13), were solved by the finite-difference method using an implicit difference scheme. It was assumed that, in addition to the W_1 donor centers, either the $W_2(k_5 = k_6 = 0)$ donor centers or the $W_3(k_3 = k_4 = 0)$ donor centers were formed. We calculated the concentration profiles for the components and the donor-activation coefficient for erbium; the latter coefficient was determined from the relation

$$k = \frac{1}{Q_{Er}} \int_0^{x_j} W(x)dx,$$

where Q_{Er} is the implantation dose of Er^+ ions; x_j is the *p–n*-junction depth for the substrate boron-doping level of $C_{sub} = 1.5 \times 10^{15}$ cm^{-3}; and $W(x)$ is the distribution of erbium-containing donor centers over the depth, $W(x) = W_1(x) + W_2(x)$ or $W(x) = W_1(x) + W_3(x)$.

4. INFLUENCE OF THE MODEL PARAMETERS ON THE ERBIUM DONOR-ACTIVATION COEFFICIENT

Experimental dependences of the donor-activation coefficient for erbium on the annealing temperature for both the separate erbium implantation (circles *1*, *2* in Fig. 1) and the coimplantation of erbium and oxygen (symbols *1*, *2* in Fig. 2) take the form of curves with peaks. This result can be interpreted in the following way in the context of the suggested model. As the annealing temperature increases, the activation coefficient first increases as a result of an increase in the generation rate for nonequilibrium self-interstitials in the course of annealing of radiation defects produced by ion implantation and as a result of the formation of the W_1 donor centers (the Er–*I* complexes). As the annealing temperature is increased further, oxygen atoms become mobile, diffuse to immobile Er atoms or their complexes with self-interstitials, and form, respectively, W_2 (the Er–O complexes) or W_3 (the Er–O–*I*) donor centers. At temperatures above 700°C, the activation coefficient decreases owing to completion of the implantation-damage annealing and, correspondingly, to the exhaustion of the source of excess self-interstitials as a result of diffusion of excess self-interstitials to the surface, which represents an efficient sink for the self-interstitials, and also as a result of decomposition of the Er–O and Er–O–*I* complexes.

The time constant τ for the decomposition of implantation-produced defects in expression (7) governs the generation rate of self-interstitials in the course of annealing of implantation damage. At low heat-treatment temperatures, the implantation-produced defects

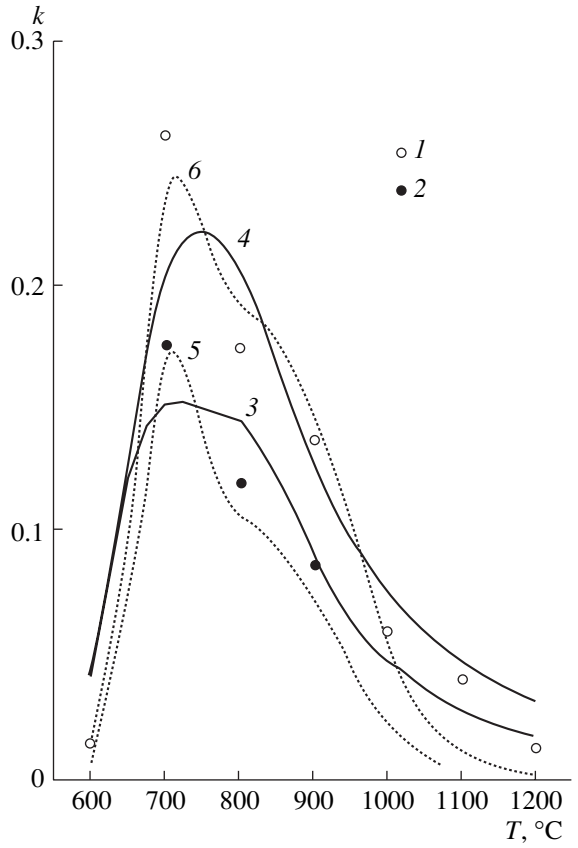

Fig. 1. Temperature dependences of the donor-activation coefficient for Er in the (*1*, *3*, *5*) FZ-Si and (*2*, *4*, *6*) Cz-Si samples. Circles (*1*, *2*) correspond to experimental data and curves (*3–6*) represent the results of calculations on the assumption that the donor centers (*3*, *4*) W_1 and W_2 or (*5*, *6*) W_1 and W_3 are formed.

are annealed out at a rather low rate, so that the concentrations of self-interstitials and donor centers W_1 are low. As the heat-treatment temperature increases, the decomposition rate for implantation-produced defects increases; as a result, the activation coefficient increases. An increase in the parameter τ_0 brings about a shift of the activation coefficient to higher temperatures and also a decrease in the peak height (see Fig. 3, curves *1*, *2*). The aforementioned shift is caused by a decrease in the generation rate for self-interstitials with increasing τ, whereas a decrease in the peak height is attributed to enhancement of the rate of diffusion of self-interstitials to the surface at higher annealing temperatures. The diffusion length L_I for self-interstitials governs the recombination rate of excess self-interstitials. An increase in L_I brings about an increase in the erbium donor-activation coefficient at temperatures higher than 800°C (Fig. 3, curves *2*, *3*). An increase in *k* is caused by an increase in the concentration of excess self-interstitials as a result of a decrease in the rate of recombination of interstitials at the volume traps. The parameters k_1–k_6 govern the concentrations of the W_1, W_2 and W_3 complexes and, consequently, their contributions to the total concentration of donor centers.

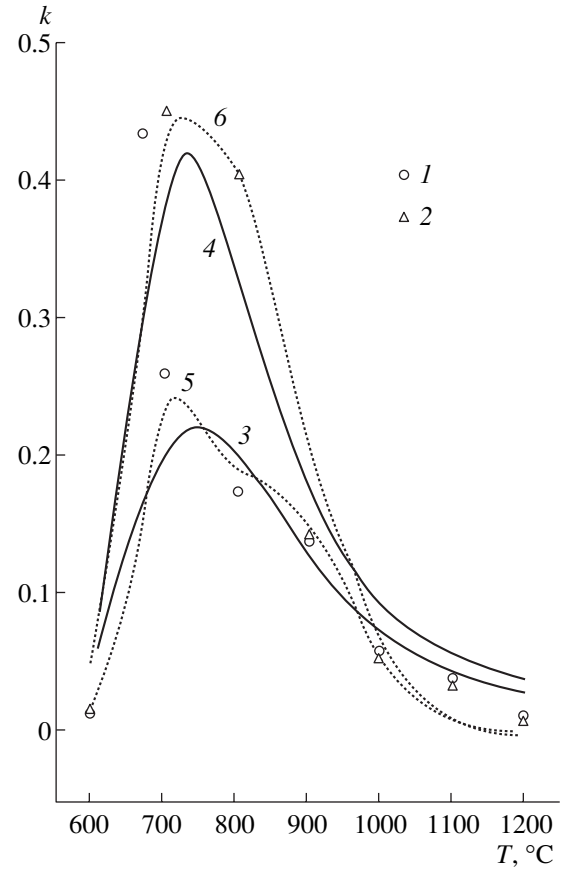

Fig. 2. Temperature dependences of the donor-activation coefficient for implanted Er in Cz-Si if O^+ ions (*1*, *3*, *5*) were not and (*2*, *4*, *6*) were additionally implanted. Circles and triangles (*1*, *2*) correspond to experimental data, and curves (*3*–*6*) represent the results of calculations on the assumption that the donor centers (*3*, *4*) W_1 and W_2 or (*5*, *6*) W_1 and W_3 are formed.

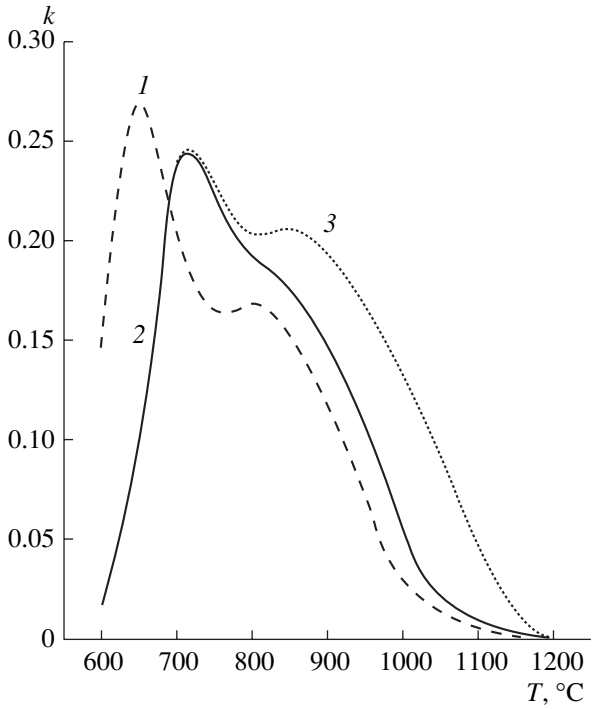

Fig. 3. Influence of (*1*, *2*) the time constant τ_0 of the implantation-damage annealing and (*2*, *3*) the diffusion length L_I of silicon self-interstitials on the donor-activation coefficient for Er in Cz-Si in the situation where the W_1 and W_3 donor centers are formed. τ_0 = (*1*) 5×10^{-8} and (*2*, *3*) 5×10^{-7} s; L_I = (*1*, *2*) 5×10^{-4} and (*3*) 8×10^{-4} cm (E_τ = 1.85 eV).

By comparing the calculated temperature dependences of the donor-activation coefficient for erbium with experimental data, we determined the following values of the parameters: $\tau_0 = 4.5 \times 10^{-7}$ s, $E_\tau = 1.61$ eV, $k_1/k_2 = 2.5 \times 10^{-11}\exp(1.3/k_BT)$, $k_3/k_4 = 3.2 \times 10^{-22}\exp(0.55/k_BT)$ in the case of formation of the W_1 and W_2 centers; and $\tau_0 = 5 \times 10^{-7}$ s, $E_\tau = 1.85$ eV, $k_1/k_2 = 1 \times 10^{-11}\exp(-1.2/k_BT)$, and $k_5/k_6 = 7 \times 10^{-18}\exp(-0.55/k_BT)$ if the W_1 and W_3 centers are formed. In both cases, $L_I = 5 \times 10^{-4}$ cm.

5. RESULTS OF CALCULATIONS

In Fig. 1, the results of calculating the activation coefficient in the FZ-Si and Cz-Si layers as a function of the annealing temperature are compared with corresponding experimental dependences. As can be seen from Fig. 1, the values of the activation coefficient in the Cz-Si samples with a higher oxygen concentration (curves *2*, *4*, *6*) are larger than those in the FZ-Si samples (curves *1*, *3*, *5*). The joint implantation of Er and O ions into Cz-Si results in a further increase in the activation coefficient (Fig. 2). It can be seen from Figs. 1 and 2 that, in the case of formation of oxygen-containing donor centers W_2 (Er–O)(curves *3*, *4*), the results of calculations more adequately describe the experimental dependences in the high-temperature heat-treatment range of 1100–1200°C; at the same time, the results of calculations (curves *5*, *6*) have a better fit with the experimental dependences for the annealing temperatures of 700–800°C (in the vicinity of the peak) if the donor centers W_3 (Er–O–*I*) (i.e., the centers containing oxygen and interstitial silicon atoms) are formed. In Fig. 4, we show the calculated concentration profiles for the components under consideration, namely, the donor centers W_1 and W_2 (Fig. 4a), the donor centers W_1 and W_3 (Fig. 4b), and also oxygen atoms and self-interstitials, after the implantation of Er^+ and O^+ ions into Cz-Si and subsequent annealing at 700°C. In both cases, the concentrations of oxygen-containing donor centers W_2 (curve *6* in Fig. 4a) and W_3 (curve *6* in Fig. 4b) exceed the concentrations of oxygen-free donor centers W_1 (curves *5* in Figs. 4a and 4b). It is noteworthy that the peaks in the distribution curves for the donor centers W_1 and W_3 containing self-interstitials are shifted deeper into the layer relative to the maximum in the Er distribution in accordance with the shift of initial distributions of self-interstitials as given by

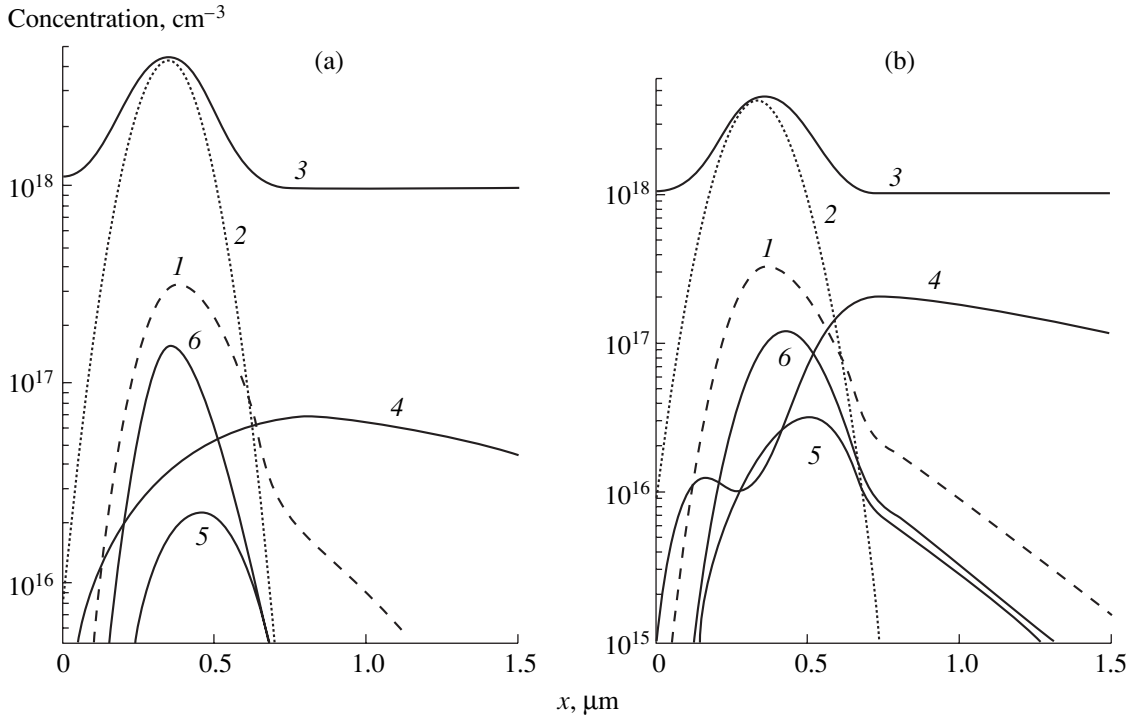

Fig. 4. Concentration profiles of components in Cz-Si after implantation of Er^+ and O^+ ions. (a) Calculations assuming that the W_1 and W_2 centers are formed and (b) the results of calculations on the assumption that the W_1 and W_3 centers are formed. (*1*) [Er](x, 0), (*2*) $C_{Oxi}(x)$, (*3*) [O](x, t), (*4*) [*I*](x, t), (*5*) [W_1](x, t), and (*6*) [W_2](x, t) (a) or [W_3](x, t) (b); T = 700°C, t = 30 min.

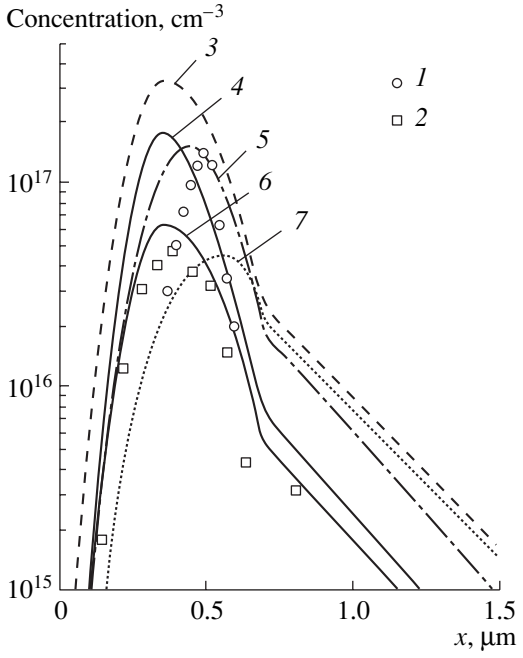

Fig. 5. The concentration profiles of donor centers in Cz-Si coimplanted with the Er^+ and O^+ ions: circles and squares *1* and *2* correspond to experimental data; curve *3* represents the initial Er distribution after implantation; curves *4* and *5* represent the results of calculations based on the assumption that the W_1 and W_2 donor centers are formed; and curves *6* and *7* were calculated on the assumption that the W_1 and W_3 donor centers are formed. The annealing temperature was equal to (*1*, *4*, *5*) 700 and (*2*, *6*, *7*) 900°C.

(10). In Fig. 5, the experimental charge-carrier concentration profiles (points *1*, *2*) are compared with calculated concentration profiles for the donor centers [W_1] + [W_2] (curves *4*, *5*) and [W_1] + [W_3] (curves *6*, *7*) in the case of annealing at 700 and 900°C. As can be seen from Fig. 5, the consideration of the donor centers W_1 and W_2 makes it possible to describe more adequately the charge-carrier concentration profile after annealing at 900°C; at the same time, if the donor centers W_1 and W_3 are taken into account, the charge-carrier concentration profiles after annealing at 700°C are described more adequately.

6. CONCLUSION

Thus, we simulated the formation of donor centers during the annealing of FZ- and Cz-Si layers implanted with Er^+ and O^+ ions. We set up and solved numerically a system of diffusion–kinetics equations in which we took into account the formation of donor centers in the form of complexes of three types; these include oxygen in the substrate, ion-implanted oxygen, and self-interstitials which formed in the course of the annealing of implantation-produced defects and are represented by the W_1 (Er–*I*), W_2 (Er–O), and W_3 (Er–O–*I*) centers. It is shown that a model involving the W_1 and W_2 donor centers, as well as a model involving the W_1 and W_3 donor centers, makes it possible to describe satisfactorily the experimental dependences of the donor-activa-

tion coefficient for Er in the case of implantation of Er^+ and O^+ ions into FZ- and Cz-Si on the annealing temperature in the range of 600–1200°C; the charge-carrier concentration profiles in the implanted and annealed layers can also be described adequately.

ACKNOWLEDGMENTS

We thank E.O. Parshina and E.I. Shek for preparation of the samples.

REFERENCES

1. N. A. Sobolev, Fiz. Tekh. Poluprovodn. (St. Petersburg) **29**, 1153 (1995) [Semiconductors **29**, 595 (1995)].
2. J. Michel, L. V. C. Assali, M. T. Morse, and L. C. Kimerling, Semicond. Semimet. **49**, 111 (1998).
3. V. F. Masterov, F. S. Nasredinov, P. P. Seregin, *et al.*, Fiz. Tekh. Poluprovodn. (St. Petersburg) **32**, 708 (1998) [Semiconductors **32**, 636 (1998)].
4. L. Palmetshofer, Yu. Suprun-Belevich, and M. Stepikhova, Nucl. Instrum. Methods Phys. Res. B **127/128**, 479 (1997).
5. V. V. Emtsev, V. V. Emtsev, Jr., D. S. Poloskin, *et al.*, Fiz. Tekh. Poluprovodn. (St. Petersburg) **33**, 649 (1999) [Semiconductors **33**, 603 (1999)]; V. V. Emtsev, Jr., C. A. J. Ammerlan, B. A. Andreev, *et al.*, Solid State Phenom. **82-84**, 93 (2002).
6. N. A. Sobolev, M. S. Bresler, O. B. Gusev, *et al.*, Fiz. Tekh. Poluprovodn. (St. Petersburg) **28**, 1995 (1994) [Semiconductors **28**, 1100 (1994)].
7. O. V. Aleksandrov, N. A. Sobolev, E. I. Shek, and A. V. Merkulov, Fiz. Tekh. Poluprovodn. (St. Petersburg) **30**, 876 (1996) [Semiconductors **30**, 468 (1996)].
8. N. A. Sobolev, O. V. Alexandrov, and E. I. Shek, Mater. Res. Soc. Symp. Proc. **442**, 237 (1997).
9. R. A. Devine, D. Mathiot, W. L. Warren, and B. Asper, J. Appl. Phys. **79**, 2302 (1996).
10. L. Pelaz, G. H. Gilmer, M. Jaraiz, *et al.*, Appl. Phys. Lett. **73**, 1421 (1998).
11. D. Maroudas and R. A. Brown, Appl. Phys. Lett. **62**, 172 (1993).

Translated by A. Spitsyn

Semiconductors, Vol. 36, No. 11, 2002, pp. 1215–1220. Translated from Fizika i Tekhnika Poluprovodnikov, Vol. 36, No. 11, 2002, pp. 1297–1302.

DEDICATED TO THE MEMORY OF V. F. MASTEROV

Emission from Rare-Earth Centers in (ZnTe:Yb):O/GaAs

V. M. Konnov, N. N. Loĭko, Yu. G. Sadof'ev, A. S. Trushin, and E. I. Makhov

Lebedev Physical Institute, Russian Academy of Sciences, Leninskiĭ pr. 53, Moscow, 117924 Russia

e-mail: mahov@ffke-campus.mipt.ru

Submitted April 2, 2002; accepted for publication April 11, 2002

Abstract—Layers of Yb-doped ZnTe were grown by molecular-beam epitaxy, and the photoluminescence of ZnTe:Yb structures was studied. It was found that additional doping with O should be performed to activate emission from Yb ions. The necessary conditions for intense emission from Yb^{3+} ions were determined. Stark splitting of levels of Yb^{3+} ions in the crystal field was measured experimentally. *© 2002 MAIK "Nauka/Interperiodica".*

1. INTRODUCTION

The aim of this study is to investigate rare-earth (RE) centers in semiconducting ZnTe films. Ytterbium was chosen as a model object to analyse specific features of formation of RE centers for the following reasons. To date, there is no complete understanding as to why a RE ion can be in one or another charge state in a crystalline matrix. In crystals doped with RE elements, RE ions can be in different charge states, which may significantly impede the interpretation of emission spectra. Ytterbium atoms, as well as Yb^{1+} and Yb^{2+} ions, have completed *f* shells. Therefore, only Yb^{3+} ions yield emission that is typical of RE centers. In addition to this, the optical-transition diagram for Yb^{3+} ions is one of the simplest. In the first approximation, it includes only two terms, specifically, the ground state $^2F_{7/2}$ and the only excited state $^2F_{5/2}$. All these factors simplify analysis of emission spectra.

The "4*f* compression" minimizes the size of Yb^{3+} ions to ~0.8 Å, which should facilitate their incorporation into the lattice. Another advantage of Yb, in comparison with other RE elements, is its low reactivity.

Various methods of forming Yb-doped GaAs and $Al_xGa_{1-x}As$ films via molecular-beam epitaxy (MBE) have already been discussed in [1–6]. In accordance with the reported results, in order to obtain stable and reproducible emission from RE centers in (III–V):RE semiconductors, at least three conditions should be fulfilled.

First, (III–V):RE layers should contain O impurity. This can be accomplished via the implantation of O ions. Second, in order to reduce the number of channels of nonradiative recombination, the layers of the RE-containing matrix should have a rather high crystalline quality. Therefore, additional thermal annealing should be performed after the O implantation. Third, Yb-containing crystals should contain at least some impurities that can react with Yb^0, Yb^{1+}, or Yb^{2+} ions under certain conditions. In our opinion, such impurities can convert the above-mentioned Yb ions to the "3+" charge state and keep them in this state.

In this study, we investigated the synthesis of ZnTe:Yb layers by MBE and the special features of initiating emission from RE centers in this system. More than 80 ZnTe:Yb samples were analyzed. One of our aims was to check whether the conclusions based on studies of (III–V):Yb systems are correct for wide-gap semiconductors, in particular, for ZnTe.

In Section 2, technical aspects of the fabrication of ZnTe films and doping these with Yb are described. Then, we report data on the optimization of annealing and doping, which is aimed at obtaining reproducible emission. The next section deals with the results of investigations of temperature features of photoluminescence. After that, our interpretation of some of the results obtained is reported.

2. EXPERIMENTAL

When MBE is used, a doubtless advantage of II–VI compounds is the relatively low temperature of their synthesis, due to which the rate of desorption of RE atoms from the surface of a substrate is rather low during the epitaxial growth. This makes it possible to obtain layers doped with a RE element in contents that are limited only by the allowable distortion of the matrix lattice.

In the first stage, a series of growth processes was carried out, due to which a technique for the growth of high-quality single-crystal ZnTe films on GaAs substrates was elaborated. In the next stage, the optimum conditions for doping films with Yb directly during

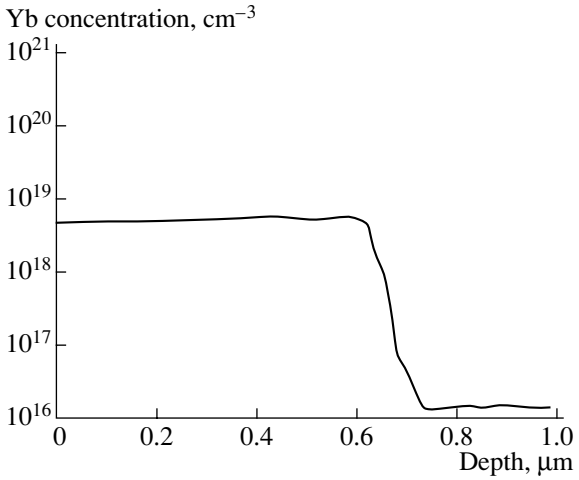

Fig. 1. Concentration profile of Yb in ZnTe:Yb according to the SIMS data.

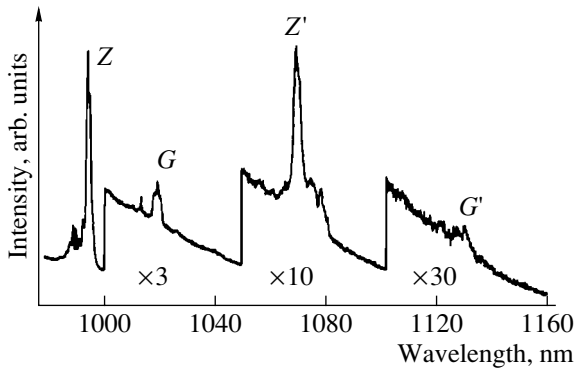

Fig. 2. Full-range photoluminescence spectrum of the (ZnTe:Yb):O system at 77 K.

their growth were found. Semi-insulating or n^+ (100) GaAs substrates were used. In our experiments, we obtained structures with concentrations of Yb ions in the range of 10^{18}–2×10^{20} cm^{-3}. When the doping level of $\sim 5 \times 10^{19}$ cm^{-3} was exceeded, we observed a clear transformation of RHEED patterns, which is indicative of the coexistence of lattices typical of sphalerite and rock salt. This was one of the reasons for the deliberate limitation of the Yb concentration in the ZnTe layers by the value of 5×10^{19} cm^{-3}.

Measurements using secondary-ion mass spectroscopy (SIMS) showed that the distribution of Yb is uniform in the entire range of the doping levels we used (Fig. 1).

For comparison, we also used another method for doping ZnTe crystals with Yb. Layers of ZnTe were grown on GaAs substrates by MBE without Yb doping. Then, the grown layers were implanted successively with several doses of Yb ions with different energies to obtain the calculated concentration of $\sim 10^{19}$ cm^{-3}. We should mention at once that the implanted layers contained much more radiation defects in comparison with the layers grown and doped by MBE. Thus, the implanted layers had to be annealed at higher temperatures in order to obtain an acceptable level of emission, while the emission of the implanted layers was weaker compared with that of the MBE-grown layers. However, on the whole, the emission spectra of both groups of samples changed similarly.

In the next stage, ZnTe:Yb samples were implanted with O ions of such energies and at such doses so as to obtain a uniform concentration of O atoms in a ~0.5-μm-thick layer. In order to reduce the number of radiation defects introduced into the samples during the O implantation and activate implanted impurities, we carried out photostimulated postimplantation annealing in a hydrogen atmosphere in the temperature range of 70–600°C. In each annealing stage, the sample temperature was maintained fixed for 5 min.

3. RESULTS

3.1. General Characteristic of Emission

Figure 2 shows a full-range PL spectrum. It can be seen that emission is concentrated in two spectral regions. One of them ranges from 980 to 1030 nm and the other is above 1030 nm. The bands in the lower wavelength region are denoted as *Z* and *G*, and the bands in the higher wavelength region are denoted as *Z*' and *G*'. The emission from the *Z* band was found to be the most stable and intense in the temperature range up to the sample temperatures of about 370 K, i. e., appreciably higher than room temperature. In what follows, when the emission intensity is concerned, we mean, first of all, emission in the vicinity of the *Z* band. The *G*' band was the weakest, and it was observed only in the spectra of the samples of highest quality.

3.2. Effect of Oxygen on Photoluminescence of ZnTe:Yb Layers

We should mention first of all that, as with III–V semiconductors, emission from Yb^{3+} ions was detected neither in ZnTe:Yb layers, doped during MBE growth, nor in Yb-implanted layers in spite of the fact that X-ray spectral analysis and SIMS measurements were indicative of large amounts of Yb in ZnTe.

The implantation of O up to concentrations of $\sim 10^{17}$ cm^{-3} makes it possible to activate Yb^{3+} ions. A further increase in the concentration (up to a certain limit) results in an increase in the RE-emission intensity. The fine structure of the spectra does not depend on the O concentration.

A series of samples with a Yb concentration of $\sim 5 \times 10^{18}$ cm^{-3} was chosen to determine the optimal ratio between O and Yb concentrations (see Fig. 3). It can be seen from Fig. 3 that the luminescence of a sample doped with O to a concentration of $\sim 3 \times 10^{19}$ cm^{-3} is the most intense. An increase in the O concentration to

10^{20} cm^{-3} results in a significant decrease in the emission intensity. When the Yb concentration is equal to 1.5×10^{19} cm^{-3}, the optimal O concentration is equal to 5×10^{19} cm^{-3}.

3.3. Effect of Thermal Annealing on Photoluminescence of ZnTe:Yb Layers

The emission intensity and location of spectral lines depended on the annealing temperature. In the absence of annealing, or after annealing at low temperatures (T_a = 75–150°C), the emission was relatively weak if it was detected at all. A large scatter in results obtained not only for the samples cut from the same wafer, but also within the same sample, was also observed. As the annealing temperature increased, the situation became more stable; the background luminescence, caused by implantation-induced lattice defects, was suppressed, while the intensity of emission from RE centers increased. With a further increase in the annealing temperature, the emission intensity attained some steady-state value and virtually did not change for samples annealed in a certain temperature range.

The basic tendency was as follows: the higher the Yb and O concentrations, the higher the annealing temperatures that were required to obtain maximum emission. For example, for O concentrations of 10^{18}, 10^{19}, and 10^{20} cm^{-3}, annealing had to be carried out in the temperature ranges of 140–200, 200–250, and 450–500°C, respectively. With a further increase in the annealing temperature, the emission intensity decreased. The films annealed at T_a > 600°C degraded, and no emission from them was observed at all. In the samples with the optimal ratio between Yb and O concentrations, the highest emission intensity of the most prominent *Z* band was observed after annealing at T_a = 400–450°C.

When the annealing temperature changed, the intensity of the *Z*' band changed proportionally to that of the *Z* band. A similar effect was observed for the *G* and *G*' bands. Although the intensity of the *Z* and *Z*' bands was highest after annealing in the temperature range of 400–450°C, the intensity of the *G* and *G*' bands was highest for films annealed at 460°C. Furthermore, the *Z* and *Z*' bands had similar fine structures. As for the *G* and *G*' bands, it was difficult to find such correlation, because we failed to resolve the fine structure of these bands.

3.4. Temperature Measurements of Photoluminescence

A detailed study of the PL spectra was carried out in the temperature range of 4.2–350 K. It can be seen from Fig. 4 that the strongest band in the spectrum recorded at *T* = 77 K, with a peak at 995.2 nm and a half-height width of 1.6 nm, splits at the liquid-helium temperature into five narrow lines with a spectral width of less than 0.1 nm. Four of these lines correspond to wavelengths of 995.1, 995.8, 996.4, and 996.8 nm. The fifth line is peaked at 997.4 nm and does not correlate with the four lines at shorter wavelengths: its spectral position and intensity vary from sample to sample. Thus, we may assume that this line is related to another type of Yb-based centers.

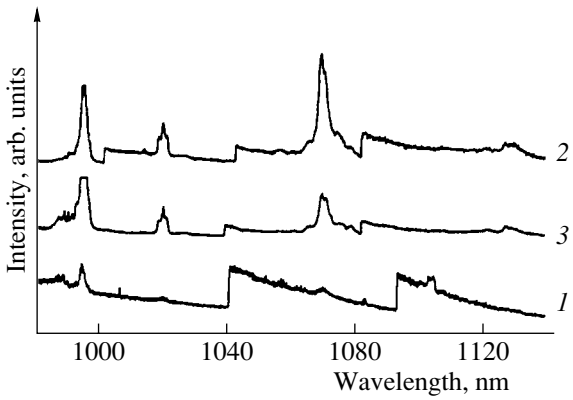

Fig. 3. Photoluminescence spectra of samples implanted with O to concentrations of (*1*) 10^{20}, (*2*) 10^{19}, and (*3*) 10^{18} cm^{-3}.

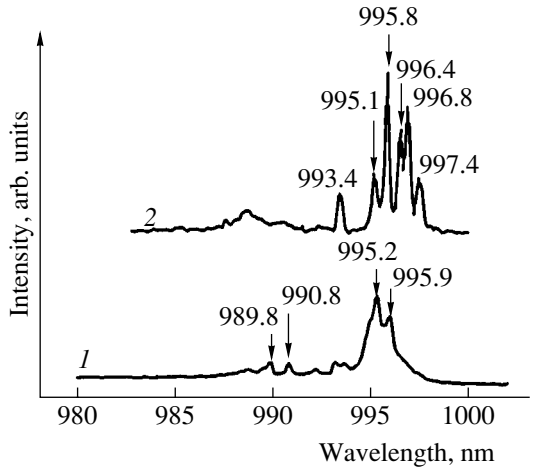

Fig. 4. Change in the shape of the Z_A band under transition from (*1*) liquid-helium to (*2*) liquid-nitrogen temperatures.

An increase in temperature from 4.2 to 350 K resulted in a steady decrease in the intensity of all four emission lines. Spectral broadening of these lines also occurred, due to which they merged to form the Z_A band with one distinct peak at 996 nm in the temperature range of 140–160 K. Further heating at higher temperatures caused a gradual shift of this peak to longer wavelengths (996.4 nm at 250 K). The PL intensity decreased with temperature approximately linearly. When the temperature became as high as 300 K, the Z_A band completely disappeared.

The most interesting evolution of the spectrum occurred when the temperature exceeded 150 K. Against the background of a gradual decrease in the

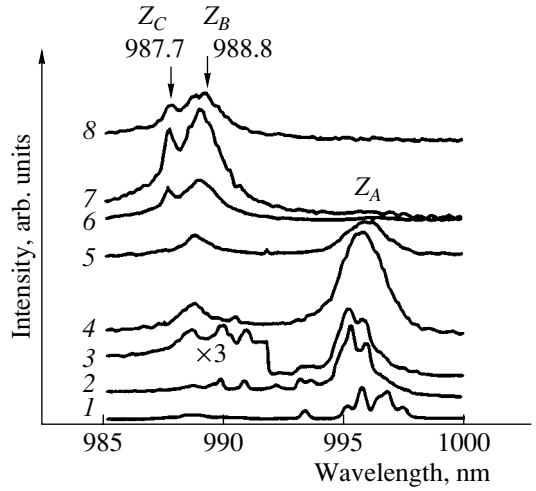

Fig. 5. Photoluminescence spectra recorded at sample temperatures T = (*1*) 4.2, (*2*) 80, (*3*) 100, (*4*) 160, (*5*) 200, (*6*) 273, (*7*) 300, and (*8*) 330 K. The left portion of spectrum *3* and spectra *4–8* are shown with intensities increased by a factor of 3 relative to the others.

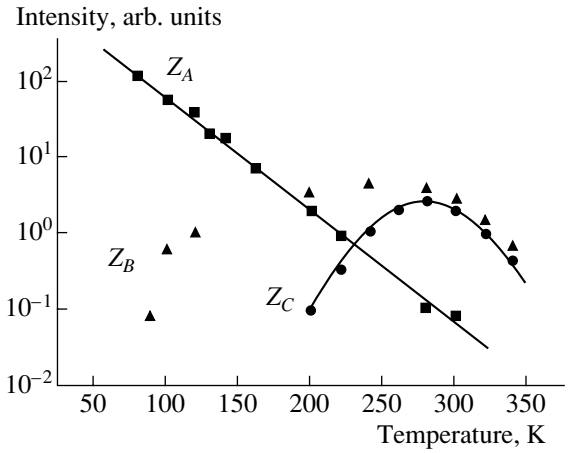

Fig. 6. Intensities of the Z_A, Z_B, and Z_C bands in relation to the sample temperature.

intensity of the 996-nm band, another band (previously absent) arose at 988.8 nm, and its intensity grew with temperature. When the temperature became as high as 250 K, one more band arose at 987.7 nm. We denote these bands as Z_B and Z_C, respectively. The intensities of both these bands attained maximum values at 300 K and then began to decrease, but still remained noticeable even at 370 K. We should also mention that virtually no background emission caused by impurity-atom–defect complexes was observed at $T > 250$ K. Thus, the Z_B and Z_C bands were found to have the highest thermal stability. Figure 5 illustrates the temperature dependences of the shapes and positions of the Z_A, Z_B, and Z_C bands; Fig. 6 shows the temperature dependences of the band intensities.

4. DISCUSSION

The absence of emission, which is typical of RE centers in ZnTe:Yb structures, can be explained by two basic causes: (i) Yb ions do not have the "3+" charge state, and (ii) there are no internal conditions which would make it possible to realize any mechanism of excitation of RE ions.

Our investigations of (III–V):Yb layers showed that, in order to activate emission from Yb^{3+} ions, impurities of two types should be present in the lattice which would react with Yb^{3+} ions to form Yb^{3+}-based complexes. The results obtained by triple implantation of Yb, O, and an impurity of another type (such as Te, Se, and S) into GaAs show that implantation of O ions gives rise to emission from RE centers. However, in our opinion, atoms of background impurities, specifically, S, Se, and Te, are also involved in the formation of RE centers. At the same time, deliberate introduction of these impurities in large amounts changes the fine structure of the emission spectra within a few tens of meV. An impurity of each type gives rise to a relevant band in the PL spectrum. A change in the O concentration neither shifts these bands nor generates new ones. However, an increase in the O concentration enhances the bands that already exist. When the O concentration is below 10^{17} cm^{-3}, no emission is observed, regardless of the amount of background impurities (Te, Se, and S).

As we can see, a similar situation occurs in crystalline ZnTe films. In order to make a definitive comparison, implantation of background impurities should be carried out. Nevertheless, similarly to GaAs films, there is good reason to believe that the appearance of the Z band is caused by a large amount of C.

We may assume that, during annealing, atoms of various impurities, such as S, C, and N, diffuse through the crystal and react with Yb ions, transforming the latter into the 3+ charge state. This transformation is accompanied by a significant decrease in the size of Yb ions, which facilitates their incorporation into the lattice by replacing Zn atoms.

However, apparently, the presence of such impurities in a crystalline matrix is not sufficient to initiate emission from RE ions. Some energy should still be supplied to a RE ion for its excitation. It is known that O atoms in ZnTe crystals behave as isoelectronic traps [7]. When an O atom located at the periphery of a RE center captures an electron and the captured electron recombines with a free hole, the energy of this pair passes (for example, via the Auger process) to the 4*f* shell of the Yb^{3+} ion, thus exciting the latter. A weak influence of O on the fine structure of the spectrum indicates that O atoms are located rather far from Yb^{3+} ions.

The quality of a crystalline matrix is important for the activation of emission from RE ions, because the activation processes are directly related to the diffusion

of background impurities. Both radiation defects and extended growth defects (low-angle boundaries, twins, dislocation loops, etc.) play an important role in the diffusion mechanisms. During annealing, when the damaged layer becomes recrystallized, the whole volume of the sample is subjected to heating. In addition to the annihilation of point defects, a number of extended defects (for example, low-angle boundaries) also disappear. It is quite plausible that, due to this effect, a large number of point defects are produced (or become released). When the annealing temperature exceeds 600°C, Zn atoms start leaving the film volume and the crystalline properties of the film begin to degrade. This results in a radical decrease in the ratio between the rates of recombination via radiative and nonradiative mechanisms and, eventually, in the total disappearance of PL. A relatively low concentration of point defects, for example, Zn vacancies, (no higher than 10^{18} cm^{-3}) is, most likely, quite favorable for the incorporation of Yb^{3+} ions into the lattice, but an excess of defects, as was already mentioned, can result in the total disappearance of emission from RE ions. Most likely, the low intensity of emission from RE centers in samples implanted with O to concentrations of ~10^{20} cm^{-3} is caused by a high concentration of defects.

As was mentioned above, a Yb^{3+} ion has one term that splits into two terms ($F_{5/2}$ and $F_{7/2}$) due to spin–orbit interaction. In a crystal field with a symmetry lower than cubic, the excited state is split into three Stark components with an interval of ~10 meV between neighboring components. The ground state is split into four components with an interval of ~2 meV between neighboring components. If one of the crystal atoms in the vicinity of a RE center is replaced by an impurity atom, the center symmetry is lowered to C_{3v}, which results in the above-described level diagram. We assume that the results of measurements at various temperatures can be interpreted from this point of view. At temperatures below 100 K, only the lowest Stark component of the $F_{5/2}$ state is occupied. The four lines of the Z_A band correspond to electronic transitions from this component to the four components of the ground state $F_{7/2}$. An increase in temperature results in line broadening due to electron-vibrational interaction, and, at temperatures above 100 K, thermal occupation of the next component of the $F_{5/2}$ state sets in, due to which the Z_B band arises. When occupation of the upper component of the $F_{5/2}$ state sets in, the Z_C band arises.

The first studies aimed at obtaining emission from Yb ions located in a wide-gap-semiconductor matrix date back to the beginning of the 1980s [8]. The general structure of the obtained spectra is similar to what we observed in our experiments. Thus, the strongest band is at 995.2 nm, and weaker bands at 1024, 1070, and 1075 nm are also present. However, there are a number of essential differences in the technique of sample fabrication and in the interpretation of results. First of all, the emission was observed without additional introduction of O into crystalline films. This can be attributed to the fact that ZnTe single crystals grown by the Bridgman–Stockbarger method contained larger amounts (by several orders of magnitude) of background impurities (including O) and defects in comparison with the MBE-grown films. In the latter case, the background O concentration appears to be insufficient for the activation of emission from RE ions. Due to high concentrations of nonstoichiometric defects in the grown crystals, the optimum annealing temperatures used in [8] were, on the average, 100°C higher than for MBE-grown films.

Having observed a dependence of the emission intensity of different bands on the annealing temperature, Bryant [8] showed that a portion of the emission lines had the highest intensity after annealing at T_a = 250°C (with a further increase in temperature, these lines were extinguished); the other group of lines attained highest intensities at a higher temperature (550°C). On the basis of these results, Bryant [8] assumed that there existed two types of emission centers, specifically, those with a Yb ion either at a lattice site or in an interstice. Thus, all emission was assumed to be caused by pure electronic transitions. As for us, we came to the conclusion that the lines correlating with each other when there is a change in the annealing temperature are related to an electronic transition and its recurrence with the participation of a local phonon. In their turn, the groups of emission lines that have maximum intensities after annealing at different temperatures are related to RE centers with a different impurity composition.

5. CONCLUSION

Reproducible emission from RE centers was obtained, and optimal annealing conditions and impurity concentrations were determined.

It was shown that one of the necessary conditions for the optical activation of emission from Yb^{3+} ions in ZnTe:Yb layers is the presence of O impurity that participates in the transfer of energy from the crystal matrix to RE centers, as well as in the compensation of excess charges of Yb^{3+} ions.

A hypothesis is suggested that some impurities participate in the activation of emission from Yb ions. These impurities react with Yb ions, transforming the latter into the 3+ charge state.

Measurements of the temperature dependence of the luminescence spectra were carried out. The Stark splitting of the levels of a Yb^{3+} ion in the crystal field was determined experimentally.

ACKNOWLEDGMENTS

This study was supported by the Russian Foundation for Basic Research, project no. 00-02-17521.

REFERENCES

1. V. M. Konnov, N. N. Loĭko, and A. A. Gippius, Kratk. Soobshch. Fiz., Nos. 9–10, 18 (1995).
2. V. M. Konnov, N. N. Loĭko, and T. V. Larikova, Kratk. Soobshch. Fiz., No. 3–4, 67 (1996).
3. V. M. Konnov and N. N. Loĭko, Kratk. Soobshch. Fiz., No. 9–10, 41 (1997).
4. V. M. Konnov and N. N. Loĭko, Kratk. Soobshch. Fiz., No. 9–10, 59 (1997).
5. V. M. Konnov, N. N. Loĭko, S. G. Chernook, and O. M. Borodina, Kratk. Soobshch. Fiz., No. 3, 3 (1999).
6. V. M. Konnov, N. N. Loĭko, A. M. Gilinskiĭ, *et al.*, Kratk. Soobshch. Fiz., No. 8, 17 (1999).
7. M. J. Seong, I. Miotkowski, and A. K. Ramdas, Phys. Rev. B **58** (12), 7734 (1998).
8. F. J. Bryant, Radiat. Eff. **65** (1–4), 81 (1982).

Translated by Yu. Sin'kov

Semiconductors, Vol. 36, No. 11, 2002, pp. 1221–1224. Translated from Fizika i Tekhnika Poluprovodnikov, Vol. 36, No. 11, 2002, pp. 1303–1306.

DEDICATED TO THE MEMORY OF V. F. MASTEROV

Temperature Dependences of Photoluminescence Spectra of Single-Crystal $Ca_2GeO_4:Cr^{4+}$ Films

O. N. Gorshkov*, E. S. Demidov*, E. M. Dianov, A. P. Kasatkin*, V. F. Lebedev**, G. A. Maksimov*, S. A. Tyurin*, A. B. Chigineva*, Yu. I. Chigirinskiĭ*, and A. N. Shushunov***

** Research Physicotechnical Institute, Nizni Novgorod State University, pr. Gagarina 23/5, Nizhni Novgorod, 603600 Russia*

e-mail: lab10@phys.unn.runnet.ru

*** Research Center of Fiber Optics, Institute of General Physics, Russian Academy of Sciences, ul. Vavilova 38, Moscow, 117942 Russia*

Submitted April 2, 2002; accepted for publication April 11, 2002

Abstract—The temperature dependence of photoluminescence spectra in the wavelength range of 1.1–1.4 μm was measured at temperatures of 77–573 K in single-crystal $Ca_2GeO_4:Cr^+$ films deposited onto the (110) surface of Ca_2GeO_4 single crystal and studied. The analysis of the spectra was based on the concept of interaction of emitting-center electrons with vibrations excited in the film. The results suggested that interaction of electrons with vibrations of the crystal lattice was suppressed and interaction with vibrations of the emitting center were dominant. The experimentally observed shift of the zero-phonon line in the spectra of the film in reference to that in the spectra of bulk single crystals is attributed to an increase in the symmetry of the oxygen tetrahedron in the olivine crystal structure; this increase is believed to be caused by the presence of defects in the films. © *2002 MAIK "Nauka/Interperiodica".*

1. Optical materials doped with chromium in the Cr^{4+} charge state are of interest in connection with the possibility of lasing at wavelengths of 1.2–1.5 μm, which are used in fiber-optics communication systems. It has been shown previously [1, 2] that bulk $Ca_2GeO_4:Cr^{4+}$ single crystals with an olivine structure are promising in this respect. It is important to obtain films of this material on various substrates in order to develop the technology of fabricating the components of integrated and fiber optics. We previously reported on photoluminescence (PL) studies of amorphous (according to the X-ray diffraction analysis) [3] and single-crystal [4] $Ca_2GeO_4:Cr^{4+}$ films formed by HF magnetron sputtering on fused-quartz substrates and on bulk Ca_2GeO_4 single crystals, respectively. The PL spectra of amorphous films were measured at room temperature; they included a broad band located in the wavelength range of 1150–1500 nm and almost coincided with the corresponding spectra of bulk single crystals. The PL spectra of single-crystal films were also measured at room temperature and featured a specific fine structure, which was explained [4] in terms of a model [5, 6] of interaction between electrons of a Cr^{4+} center and vibrations excited in the film.

In this study, we measured and analyzed the temperature dependence of PL spectra of single-crystal $Ca_2GeO_4:Cr^{4+}$ films in the temperature range T = 77–573 K. We discuss special features of these spectra (a shift of the zero-phonon line in reference to the position of this line in the PL spectra of bulk single crystals) and the origin of vibrational satellites corresponding to the excitation of vibrations in the films. The results indicate that the interaction of electrons with crystal-lattice vibrations in the films is suppressed to a great extent; as a result, electrons interact with higher energy vibrations of the emitting center. We show that the shift of the zero-phonon line in the PL spectra is related to the presence of defects, which cause the symmetry of the oxygen tetrahedron to increase.

2. Single-crystal $Ca_2GeO_4:Cr^{4+}$ films were formed on single-crystal (110)-oriented calcium germanate (Ca_2GeO_4) substrate undoped with Cr. The conditions of the film formation have been described elsewhere [3, 4]. PL was excited using diode-laser radiation with a power of ~1 W at a wavelength λ = 980 nm. The PL spectra were measured using a setup based on an MDR-23 monochromator and equipped with a DILAS InGaAs photodiode. In order to analyze the special features of electron-vibration spectra, we used the dependences of PL intensity I divided by the photon energy E in the third power (E^3) on E (see Fig. 1); these dependences characterize the so-called spectrum-shape function [6].

3. It was previously assumed [4] that the PL spectra of films measured at T = 77 and 300 K correspond to an electron transition from the $^3A_1$ state of a Cr^{4+} center in the crystal field of distorted oxygen tetrahedron to the ground $^3A_2$ state. When analyzing the spectra, we used [4] the model [5, 6] that accounted for the interaction of electrons in the aforementioned center with vibrations

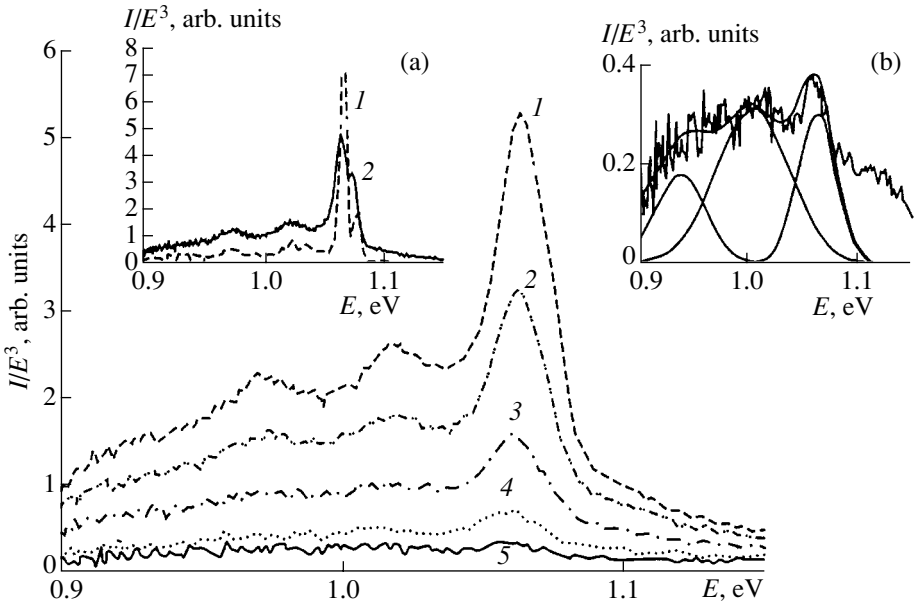

Fig. 1. The photoluminescence spectra of $Ca_2GeO_4:Cr^{4+}$ films deposited on the (110) surface of a Ca_2GeO_4 single crystal; the spectra were measured at temperatures of (*1*) 100, (*2*) 150, (*3*) 200, (*4*) 250, and (*5*) 300°C. The insets show (a) the photoluminescence spectra of the films at the (*1*) liquid-nitrogen temperature and (*2*) room temperature and (b) a part of the spectrum measured at T = 300°C and approximated by Gaussian functions.

excited in the film and made it possible to interpret the main features of the spectra. In what follows, we use the same concepts and do not consider the influence of nonradiative processes on the PL spectra of the films.

Measurements showed that the peak of the zero-phonon line in the spectrum measured at T = 77 K was located at $E_0 \approx 1.066$ eV. The full width at half-maximum (FWHM) of this line is equal to W = 59 cm^{-1}, which almost coincides with the FWHM of the zero-phonon line in the spectra of bulk single crystals at T = 15 K [2]. This means that the 0–0 transitions make a major contribution to the zero-phonon line in the spectra of the films at T = 77 K. The origination of a peak at $E_{01} \approx 1.078$ eV may be related to the factors that cause the vibrational levels to be nonequidistant and nonequivalent in the ground and excited electron states (these factors may include the frequency effect, anharmonicity, and variations in the vibration frequencies under electron excitation [5, 6]). This is confirmed by the measured energies of the first (E_1) and second (E_2) peaks of vibrational satellites that satisfy the condition $\Delta E_1 = E_0 - E_1 > \Delta E_2 = E_1 - E_2$, which is valid at all temperatures (see Fig. 2). As is well known [5, 6], the aforementioned factors may cause the zero-phonon line to shift and broaden with increasing temperature. It is noteworthy that these factors do not yet exert a pronounced effect on the FWHM and position of the zero-phonon line at T = 77 K (see Fig. 1, inset a).

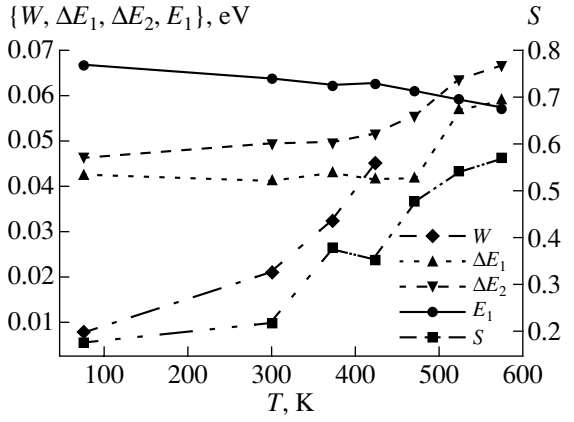

Fig. 2. Temperature dependences of the full width of the zero-phonon line at half-maximum (W); energy separation of the peaks corresponding to the zero-phonon line and to the first vibrational satellite (ΔE_1); similar separation of the first and second satellites (ΔE_2); the Huang–Rhys factor (S); and the quantity $E_1 = E_0 - 1$ eV, which characterizes the position of the peak of the zero-phonon line E_0.

At T = 300 K, the FWHM of the zero-phonon line is governed almost completely by the bands peaked at E_0 and E_{01}. Approximation of the spectra using Gaussian functions showed that contributions of the bands peaked at E_0 and E_{01} to the FWHM of the zero-phonon line are almost the same. However, the position of the peak of the zero-phonon line still coincides with that of the E_0 peak. At this temperature (see Fig. 1, inset a), broadening of the contour of the zero-phonon line at the high-energy wing becomes evident (the corresponding broadening at the low-energy wing sets in even at 77 K), which may be caused by the effect of anharmonicity [5]. At still higher energies, the anti-Stokes vibrational

satellites may contribute to the zero-phonon line and the high-energy wing of the PL spectrum.

At $T = 573$ K, the amplitude of the first vibrational satellite is nearly as large as that of the zero-phonon line and even slightly exceeds it (see Fig. 1, inset b). However, as the temperature increases, the width of vibrational satellites increases much more rapidly than that of the zero-phonon line. At high temperatures, the contribution of the zero-phonon line is added to that of the high-energy part of the first satellite. This leads to the broadening and shift of the spectral band under consideration.

Let us compare the positions of vibrational satellites in reference to the zero-phonon line in the spectra of the films with those of phonon satellites and satellites caused by vibrations of the Cr^{4+} center in the spectra of bulk single crystals [1, 2]. It can be seen from Fig. 2 that, even at the liquid-nitrogen temperature, the energy of observed vibrations in the films (340 cm^{-1}) is much higher than the energy of phonons in the bulk single crystals (~200 cm^{-1}) [1, 2]. As the temperature increases, the energy of vibrations in the films increases and approaches that of the emitting center in a bulk single crystal (740 cm^{-1}) [2]). This indicates that the occurrence of vibrational satellites in the PL spectra of the films is most probably related to vibrations of the emitting center rather than to the lattice vibrations. In Fig. 2, we show the temperature dependence of the Huang–Rhys factor S for vibrations of the Cr^{4+} center [7, 5]: $S = A_1/2A_0 \coth(\nu/2kT)$, where A_0 and A_1 are the areas under the zero-phonon line and the first vibrational satellite, respectively; $\nu = (\Delta E_1 + \Delta E_2)/2$ is the energy of vibrations excited by the center; and k is the Boltzmann constant. The value of S varies from 0.2 to 0.6 in the temperature range under consideration. It is worth noting that this factor is equal to 0.3 and 0.2 for vibrations of the Cr^{4+} center at 15 K in the Ca_2GeO_4:Cr^{4+} and Mg_2SiO_4:Cr^{4+} single crystals, respectively [2]. Using the values of S obtained for the films, we can determine the parameter $a = S\coth(\nu/2kT)$, which characterizes the transition from a spectrum with a fine structure (at $a \ll 1$) to a structureless broad band (at $a \gg 1$) [5]. At $T = 77$ K, we have $a = 0.1$, which corresponds to the fine structure of the spectra of the films. As the temperature increases to 573 K, the value of a increases to 1.0 and the fine structure is preserved. In this case, the amplitude of the first vibrational satellite approximately coincides with the amplitude of the zero-phonon line.

Thus, the PL spectra of the films involve only the satellites caused by vibrations of the Cr^{4+} center and do not include the satellites related to the lattice vibrations; this indicates that the phonon spectrum in the films differs from the corresponding spectrum in single crystals. This circumstance may be related to the fact that the films were formed by RF magnetron sputtering at temperatures which were much lower than those characteristic for the synthesis of bulk single crystals. A high concentration of defects should be expected in such films.

We note that the presence of defects may also be responsible for a shift of the zero-phonon line to higher energies (by approximately 260 cm^{-1}) in the spectra of the films in reference to the position of this line in the spectra of bulk single crystals [2]. There may be two factors that give rise to the shift under consideration: a decrease in the size of the oxygen tetrahedron, which contains the Cr^{4+} ion, and an increase in the symmetry of this tetrahedron. We should note here that the difference between the positions of zero-phonon lines in the Mg_2SiO_4:Cr^{4+} and Ca_2GeO_4:Cr^{4+} spectra for the electron transition under consideration is related to the difference in the Cr–O bond lengths in these materials [2], which is caused by different lattice constants [1, 8]. If we rely on these data and the values of Cr–O bond lengths for forsterite (see, for example, [9]), the shift of the zero-phonon line observed in the spectra of the films should correspond to the decrease in the bond length by ~0.06 Å. At the same time, it is known that distortion of the oxygen-tetrahedron symmetry in an olivine crystal structure gives rise to a shift of the low-energy level under consideration [8]; the difference between the largest and smallest bond lengths can be used to estimate the degree of this distortion. Estimations show that the observed shift can be caused by variation in this difference by a mere ~0.01 Å. Hence, it follows that the shift of the zero-phonon line in the spectra of the films in reference to that which is observed in the spectra of bulk single crystals is most probably caused by the processes which raise the symmetry of the oxygen tetrahedron rather than by the symmetric compression of this tetrahedron.

As is well known (see, for example, [9]), the difference between the bond lengths of an oxygen tetrahedron is caused by the fact that the Coulomb repulsion between the Cr^{4+} ion and the sets of three metallic ions located at the vertex and base of the tetrahedron is uncompensated. Therefore, the shift of the zero-phonon line under discussion could be ensured by the compensation of repulsion of metallic ions. Thus, for example, if there is an excess of Ca in the films, the aforementioned ions can occupy the octahedral voids that are located on the opposite side relative to the three Ca ions closest to Cr^{4+} (the excess positive charge should be wholly compensated by the corresponding negative charge, for example, by the charge of excess oxygen ions).

4. Thus, the results show that the interaction of emitting electrons of the Cr^{4+} center with crystal-lattice vibrations is suppressed in single-crystal Ca_2GeO_4:Cr^{4+} films; as a result, electrons interact with higher energy vibrations of the emitting center. The Huang–Rhys factor for the films is smaller compared with that reported for bulk single crystals; this fact manifests itself in the retention of a fine structure in the PL spectra up to $T = 573$ K. As the temperature increases in the range of

77–573 K, the spectral peak is governed by the position of the zero-phonon line, which shifts slightly to lower energies and broadens due to the factors that cause the vibrational levels to be nonequidistant and nonequivalent in the ground and excited electron states. The shift of the zero-phonon line to shorter wavelengths is most probably caused by an increase in the symmetry of the oxygen tetrahedron due to the presence of defects in the films.

ACKNOWLEDGMENTS

This study was supported by the Russian Foundation for Basic Research, project no. 01-02-16570.

REFERENCES

1. V. Petricevic, A. B. Bykov, J. M. Evans, and R. R. Alfano, Opt. Lett. **21**, 1750 (1996).
2. M. F. Hazenkamp, H. U. Gudel, M. Atanasov, *et al.*, Phys. Rev. B **53** (5), 2367 (1996).
3. O. N. Gorshkov, E. M. Dianov, N. B. Zvonkov, *et al.*, Kvantovaya Élektron. (Moscow) **30** (3), 261 (2000).
4. O. N. Gorshkov, E. M. Dianov, N. B. Zvonkov, *et al.*, Pis'ma Zh. Tekh. Fiz. **27** (17), 1 (2001) [Tech. Phys. Lett. **27**, 709 (2001)].
5. Yu. E. Perlin and B. S. Tsukerblat, *The Effects of Electron–Vibration Interaction in Optical Spectra of Paramagnetic Impurity Ions* (Shtiintsa, Kishinev, 1974).
6. N. N. Kristofel', *Theory of Impurity Centers of Small Radii in Ionic Crystals* (Nauka, Moscow, 1974).
7. K. Huang and A. Rhys, Proc. R. Soc. London, Ser. A **204** (1076), 406 (1950).
8. W. Jia, H. Liu, S. Jaffe, and W. M. Yen, Phys. Rev. B **43** (7), 5234 (1991).
9. T. F. Veremeĭchik, A. V. Gaĭster, E. V. Zharikov, *et al.*, Kvantovaya Élektron. (Moscow) **30** (5), 449 (2000).

Translated by A. Spitsyn

Semiconductors, Vol. 36, No. 11, 2002, pp. 1225–1226. Translated from Fizika i Tekhnika Poluprovodnikov, Vol. 36, No. 11, 2002, pp. 1307–1309.

DEDICATED TO THE MEMORY OF V. F. MASTEROV

Effect of Surface State Density on Room Temperature Photoluminescence from Si–SiO_2 Structures in the Range of Band-to-Band Recombination in Silicon

A. M. Emel'yanov*, N. A. Sobolev*, and S. Pizzini**

** Ioffe Physicotechnical Institute, Russian Academy of Sciences, Politekhnicheskaya ul. 26, St. Petersburg, 194021 Russia*

*** INFM and Department of Materials Science, I-20126 Milan, Italy*

Submitted April 2, 2002; accepted for publication April 11, 2002

Abstract—The relation between the intensity of band-to-band photoluminescence in single-crystal silicon and the surface state density at the interface between silicon and silicon dioxide in Si–SiO_2 structures fabricated by the technology used to manufacture charge-coupled devices was studied. The surface state density was measured by subjecting the Si–SiO_2 structures to annealing in hydrogen and to gamma irradiation. © *2002 MAIK "Nauka/Interperiodica".*

1. INTRODUCTION

The current keen interest in investigations of the band-to-band photoluminescence (PL) and electroluminescence (EL) in nondirect-gap single-crystal semiconductors is due to recent reports [1, 2]. These communications described the achievement in some silicon diodes of a quantum efficiency (η) of band-to-band EL that was nearly as high as the quantum efficiency in light-emitting diodes based on direct-gap semiconductors. According to [1], $\eta \approx 1\%$ can be obtained upon thorough minimization of the intensity of recombination in the bulk and at the surface of a semiconductor. In [3], the influence exerted by the technology of surface treatment of a number of nondirect-gap semiconductors on the band-to-band PL was investigated. In this study, the highest PL intensity in single-crystal silicon was achieved after thermal oxidation of Si. However, no data on the surface state density N_{ss} were reported in [1–3] for the samples studied. The aim of the present study is to compare changes in the surface state density and in the intensity of band-to-band PL in single-crystal silicon that are caused by gamma irradiation and annealing in hydrogen.

2. EXPERIMENTAL PROCEDURE

A Si–SiO_2 structure was fabricated on a (100) single-crystal KEF-15 (*n*-Si:P with resistivity of 15 Ω cm) wafer. A SiO_2 layer was obtained via the thermal oxidation of Si in moist oxygen at 900°C. The thickness of the silicon dioxide layer was 100 nm. To reduce the surface state density to $N_{ss} < 10^{10}$ cm^{-2} eV^{-1}, the Si–SiO_2 structure was annealed in hydrogen at 900°C for 30 min [4]. An Al layer was deposited onto the SiO_2 surface via thermal evaporation of the metal in a vacuum, and 1×1-mm^2 field electrodes were formed on a part of the surface by means of photolithography. Aluminum was also deposited onto the backside of the wafer to fabricate a rear contact to Si. This technique was chosen among other industrial procedures employed to manufacture charge-coupled devices because the stringent requirements for minimization of the intensity of generation-recombination processes on defects in Si are imposed upon procedures of this kind. In making this choice, various Si wafers oxidized in dry or moist oxygen and various kinds of annealing in hydrogen or inert gases were used. The technology employed in the present study ensured a maximum PL intensity with its sufficiently uniform distribution over the surface of the oxidized wafer. The surface state density was raised by the gamma irradiation of the structures with a ^{60}Co source at a dose rate of ~10^6 rad(SiO_2)/h. To determine N_{ss}, the small-signal capacitance and active conductance of an Al–SiO_2–Si structure were measured as functions of voltage applied to the structure [4]. The probing voltage frequency was 60 and 6 kHz. The PL was excited with visible light from a xenon lamp that passed through an SZS-24 optical glass filter and modulated with a chopper. The incident power was ~10 mW/mm^2. The PL signal was recorded with a Ge photodiode connected to a selective nanovoltmeter. The spectral characteristics were measured using a wide-aperture grating monochromator. The study was carried out at room temperature.

3. EXPERIMENTAL RESULTS AND DISCUSSION

The PL spectrum is peak-shaped with a maximum at $\lambda \approx 1.15$ μm and a half-width of 90 nm. The spectral characteristics of the peak indicate that it is due to nondirect (phonon-assisted) radiative transitions in single-crystal silicon [1–3]. The surface state density in the

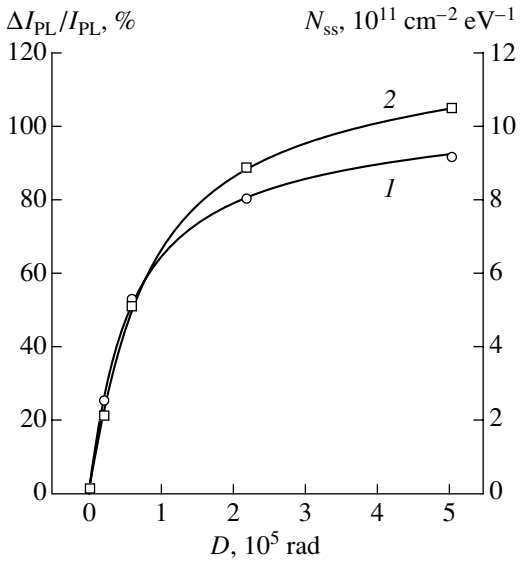

Fig. 1. Relative decrease in the PL intensity in the peak of the spectral distribution, $\Delta I_{PL}/I_{PL}$, and surface state density N_{ss} vs. the dose D of gamma irradiation for a sample preannealed in hydrogen.

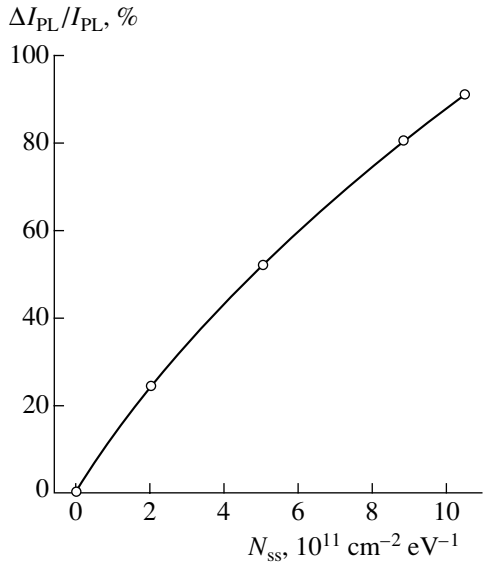

Fig. 2. Relative decrease in the peak PL intensity, $\Delta I_{PL}/I_{PL}$, vs. the gamma-stimulated surface state density for a sample preannealed in hydrogen.

initial Si–SiO_2 structures (prior to their annealing in hydrogen) was ~1×10^{11} cm^{-2} eV^{-1}. Annealing in hydrogen reduced the surface state density to ~4×10^9 cm^{-2} eV^{-1}. As a result of such an annealing, the PL intensity increased by ~10%. Figure 1 shows (curve *1*) how the relative decrease in PL intensity I_{PL} at the peak of the spectral distribution, $\Delta I_{PL}/I_{PL} = [I_{PL}(D = 0) - I_{PL}(D)]/I_{PL}(D = 0)$, depends on the dose D of gamma irradiation of a sample preannealed in hydrogen. The same figure presents the dependence of the surface state density on the dose of gamma irradiation (curve *2*). A comparison of curves *1* and *2* in Fig. 1 shows that gamma-stimulated changes in PL correlate with the generation of surface states at the Si–SiO_2 interface (the shapes of curves *1* and *2* are virtually the same). The quantitative relation between the relative changes in PL and in the surface state density is illustrated in Fig. 2. It is known that gamma irradiation may generate not only recombination centers associated with surface states, but also other kinds of recombination centers, in particular, bulk recombination centers in Si. It is difficult to distinguish the contribution of the latter to changes in PL. Therefore, the dependence in Fig. 2 should be regarded as one describing the maximum possible changes in PL, occurring as a result of gamma-stimulated generation of surface states. It is noteworthy that it follows from experimental data reported in, e.g., [5] that the effect of changes in the carrier lifetime in the bulk of Si on recombination processes can frequently be neglected when compared with the influence exerted by changes in the rate of surface recombination.

4. CONCLUSION

A quantitative relation between the surface state density generated by gamma irradiation and the maximum relative changes in the intensity of band-to-band PL in single-crystal silicon was obtained for Si–SiO_2 structures fabricated by the technology used to manufacture charge-coupled devices. The effect of annealing in hydrogen, which lowers the surface state density, on the PL intensity was studied.

ACKNOWLEDGMENTS

We thank S.P. Patrakeev for assistance in sample fabrication.

This study was supported in part by INTAS (grant no. 2001-0194); the Russian Foundation for Basic Research (project no. 02-02-16374); and the Russian Foundation for Basic Research together with the Bureau for International Research and Technology Cooperation of Austria (grant no. 01-01-02000 BNTS_a).

REFERENCES

1. M. A. Green, J. Zhao, A. Wang, *et al.*, Nature **412**, 805 (2001).
2. Wai Lek Ng, M. A. Lourenco, R. M. Gwilliam, *et al.*, Nature **410**, 192 (2001).
3. V. Yu. Timoshenko, J. Rappich, and Th. Dittrich, Appl. Surf. Sci. **123/124**, 111 (1998).
4. A. M. Emel'yanov and V. V. Golubev, Fiz. Tekh. Poluprovodn. (St. Petersburg) **28**, 2086 (1994) [Semiconductors **28**, 1148 (1994)].
5. V. S. Pershenkov, V. D. Popov, and A. V. Shal'nov, *Surface Radiation Effects in Elements of Integrated Circuits* (Énergoatomizdat, Moscow, 1988), p. 85.

Translated by M. Tagirdzhanov

Semiconductors, Vol. 36, No. 11, 2002, pp. 1227–1234. Translated from Fizika i Tekhnika Poluprovodnikov, Vol. 36, No. 11, 2002, pp. 1310–1317.

DEDICATED TO THE MEMORY OF V. F. MASTEROV

Buried Nanoscale Damaged Layers Formed in Si and SiC Crystals as a Result of High-Dose Proton Implantation

V. A. Kozlov*, V. V. Kozlovskiĭ, A. N. Titkov*, M. S. Dunaevskiĭ*, and A. K. Kryzhanovskiĭ***

** Ioffe Physicotechnical Institute, Russian Academy of Sciences, Politekhnicheskaya ul. 26, St. Petersburg, 194021 Russia*

*** St. Petersburg State Technical University, Politekhnicheskaya ul. 29, St. Petersburg, 195251 Russia*

e-mail: kozlovski@tuexph.stu.neva.ru

Submitted April 11, 2002; accepted for publication April 15, 2002

Abstract—Buried nanoscale damaged layers formed in Si and SiC crystals via 50- and 100-keV proton implantation were studied. It is shown that the sensitivity of atomic-force microscopy is sufficiently high to detect the initial stages of the development of hydrogen-containing voids and microcracks in subsurface layers of irradiated crystals and to study exfoliation of the crystals in the plane of microcracks. As a result, quantitative criteria for the formation of buried damaged layers in the studied crystals were derived; also, the conditions for blistering and for implementation of the "Smart-Cut" technology were determined. *© 2002 MAIK "Nauka/Interperiodica".*

1. INTRODUCTION

At present, buried nanoscale damaged layers that form in semiconductor crystals as a result of proton implantation are being actively studied. Interest in these layers is caused by the possibility of using them in a wide range of practical applications in the production technology of semiconductor materials and devices. In particular, the phenomenon of precision exfoliation in the plane of buried nanoscale damaged layers in the course of annealing irradiated crystals is used at present with good results in the new technology for the production of silicon-on-insulator structures; this technology, called "Smart-Cut" [1], can also be applied to other materials (Ge, GaAs, SiC, and so on) [2]. So far, the main methods for studying buried nanoscale damaged layers have been transmission and scanning electron microscopies and also scanning tunneling microscopy. In this paper, we report the results of using atomic-force microscopy (AFM) to study buried nanoscale damaged layers in Si and SiC crystals.

2. EXPERIMENTAL

In our experiments, we used KDB-40 (*p*-Si:B, ρ = 40 Ω cm) and KÉF-4.5 (*n*-Si:P, ρ = 4.5 Ω] cm) (100) silicon wafers, whose surfaces were subjected to chemical–mechanical polishing; we also used 6*H*-SiC *n*-type wafers, whose surfaces were polished mechanically using a diamond paste with granule sizes of 0.1 and 2 μm. Hydrogen ions with energies E of either 50 or 100 keV and doses in the range from 10^{15} to 6×10^{17} cm^{-2} were implanted into the samples at room temperature. The postimplantation annealing of irradiated samples was performed in an inert atmosphere in the temperature range of 300–900°C.

The surface morphology was studied via atomic-force microscopy using an HT-MDT P4SPM microscope. In the course of this study, we tested a new method for monitoring the parameters of the buried nanoscale damaged layers formed in silicon and silicon carbide from proton implantation. The method is based on scanning atomic-force microscopy of the initial and cleaved surfaces of irradiated crystals with subsequent statistical processing of the results of measurements. This method makes it possible to determine the depth and thickness of buried nanoscale damaged layers and also the sizes of pores and microcracks, reveal amorphized layers in SiC crystals, and determine the thickness of SiO_2 layers at the surface of the samples.

3. RESULTS

Studies of the surface morphology in irradiated samples showed that, in the entire range of the doses employed, proton implantation into silicon carbide did not bring about a change in the surface shape or in the level of microroughness and macroroughness of the SiC wafers. The SiC wafers polished with diamond paste having a granule size of 0.1 μm had an rms level of surface roughness $R_a \approx 0.5$–0.8 nm, which makes it possible to use these wafers for the process of solid-phase bonding in the Smart-Cut technology. Similar results were also obtained for Si wafers: the rms level of roughness R_a and the wafer-surface shape did not change after implantation with doses as high as $\approx 1.0 \times$

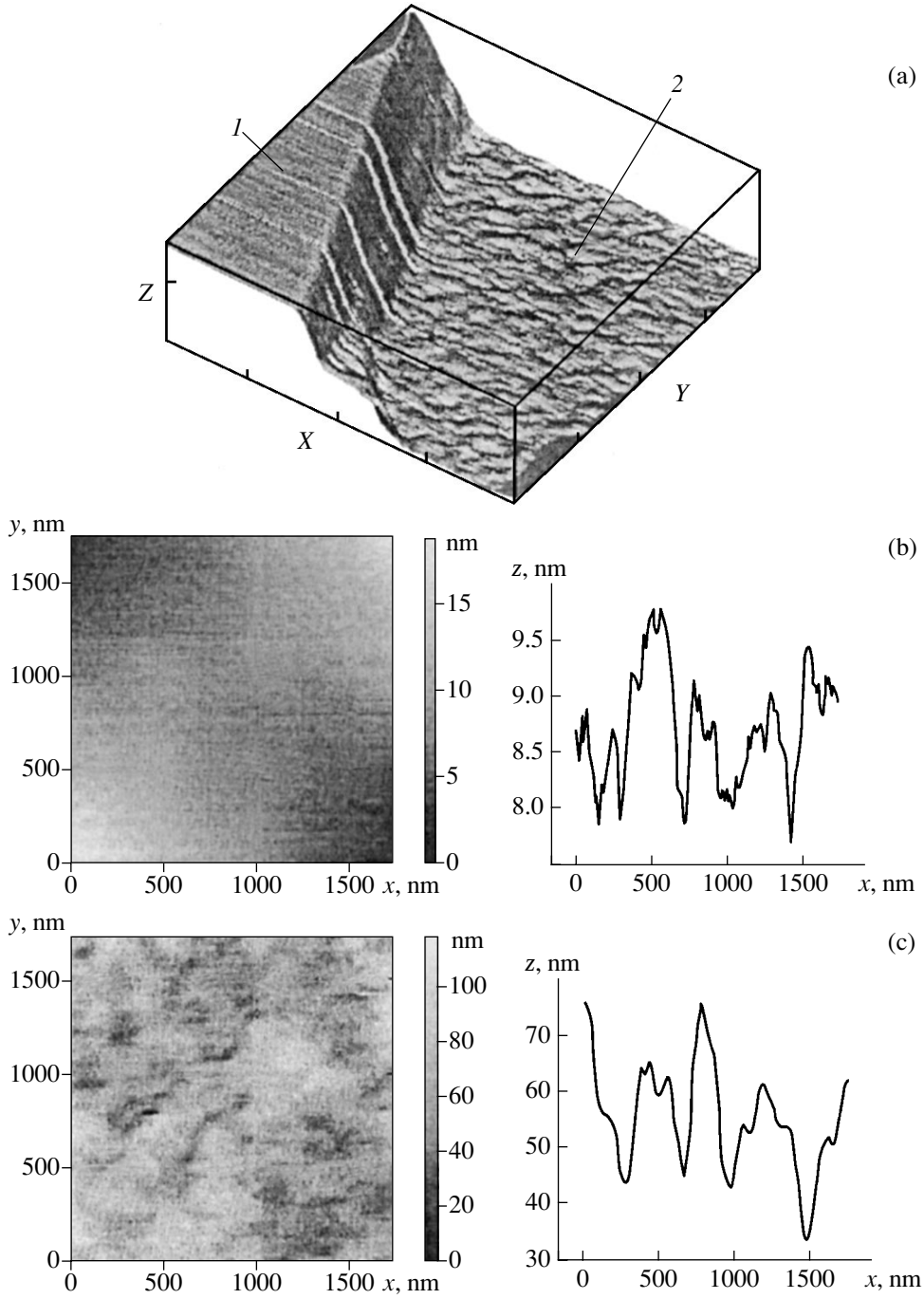

Fig. 1. An atomic-force microscopy (AFM) image of the *p*-Si surface irradiated with 100-keV hydrogen ions at a dose of 2×10^{17} cm^{-2}. (a) the AFM image of the crystal surface (*1*) with the area (*2*) where exfoliation of the surface layer in the plane of the buried nanoscale damaged layer took place; (b) the AFM image and profile of an area of the irradiated surface; and (c) the AFM image and the profile of the area with an exfoliated silicon surface layer.

10^{17} cm^{-2}, with the value of R_a being approximately equal to 0.1–0.2 nm.

For implantation doses higher than 2×10^{17} cm^{-2}, blistering was observed at the surface of *p*-Si samples: blistering and the separation of a material's flakes in the plane of the buried damaged layer were distinct after implantation even without using additional postimplantation annealing (Fig. 1). For the *n*-Si and *n*-SiC samples, blistering was not observed immediately after implantation; this phenomenon took place in these samples only after postimplantation annealing.

In Fig. 2a, we show the AFM image of the cleaved surface of the SiC sample subjected to implantation of hydrogen ions with an energy $E = 100$ keV and at a dose

$\Phi = 3 \times 10^{17}$ cm^{-2}. A layer of the material amorphized by irradiation is observed at the depth (≈650 nm) corresponding to the range of hydrogen ions. This layer has a thickness of ≈300 nm; in this region, the cleaved surface of the SiC sample is comparatively smooth, undulatory, and does not exhibit regular steps, which are characteristic of the regions of crystalline material. The undulatory surface profile in this layer indicates that there are fields of elastic stresses in this region of the crystal. A similar pattern of a buried damaged layer is shown in Fig. 2b for a 6*H*-SiC sample, which has an oxide layer on the irradiated surface. It can be seen from Fig. 2a that the SiO_2 layer also has a smooth (without steps) surface with a clearly defined Si–SiO_2 interface. For the Si samples implanted with hydrogen ions, the layer of amorphized material in the region of the proton range is not revealed by AFM even at high doses of implantation (6×10^{17} cm^{-2}).

However, if the proton-implantation dose is $\approx 1 \times 10^{17}$ cm^{-2} or higher, a layer with nanopores and a network of microcracks is clearly observed in *p*-Si samples (Fig. 3); these nanopores and microcracks develop in the plane of buried nanoscale damaged layers and ultimately bring about the separation of micrometer-size Si flakes in the plane of buried nanoscale damaged layers with the network of microcracks. In the plane where flake separation occurred, the crystal surface exhibits a typical magnitude of microroughness, $R_a \approx$ 3 nm, whereas the thickness of the separated flake is equal to (0.8–0.9)R_p, where R_p is the projected range of protons in the material. The thickness of the "cut-off" semiconductor layer can be determined with high accuracy using scanning of the crystal surface after blistering from the depth of dips both at the sites of separation of a material's flakes and at the cleaved surface of the sample from the depth of the layer with microcracks.

The defect concentration in the exfoliated semiconductor layer and the possibility of amorphizing this layer under the effect of irradiation with hydrogen ions still remains the subject of lively discussions. It is believed that a critical concentration of multivacancy complexes ($\approx 2 \times 10^{20}$ cm^{-3}) should be attained in order to induce a phase transition from single-crystal to amorphous states [3]. In the case of irradiation with heavy- and medium-mass ions, such a concentration is attained owing to the spatial separation of vacancies and interstitial atoms either within the disordered region formed by an ion or in the zones where these regions overlap. The mechanisms for the spatial separation of components of the Frenkel pairs turn out to be different for quasi-primary, coagulative, and heterogeneous processes [4]. Therefore, the threshold dose and accumulated concentration of primary defects for the establishment of quasi-equilibrium between the effective production and annihilation rates of defects should also be different. Conceivably, this quasi-equilibrium can set in in circumstances where the total number of defects and their assortment do not yet attain the level required for the transition of the semiconductor to the amorphous state. Experimentally, this inference is confirmed by the fact that attempts to detect multivacancy complexes in semiconductors, e.g., in silicon, failed in the case of room-temperature irradiation with light ions (hydrogen, helium) for doses as high as $\approx 10^{17}$ cm^{-2} [5]. Conceptually, there are conditions under which deviations from the general rule are possible. For example, if there are regions where the vacancy-type defects are predominantly gettered owing to the fields of elastic stresses (for example, at the Si–SiO_2 interface), a critical concentration of multivacancy complexes can be attained due to the buildup phenomenon; as a result, an amorphous layer is formed. Another possibility con-

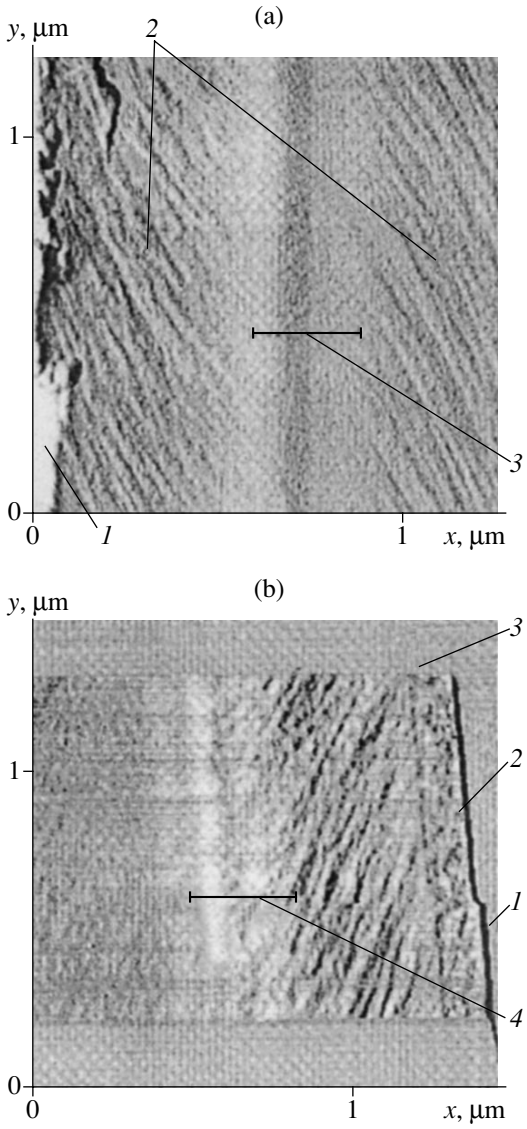

Fig. 2. An AFM image of the cleaved surface of a SiC wafer subjected to (a) a high-dose proton implantation (*1* indicates the surface; *2*, crystalline SiC; and *3*, the amorphized region) and (b) oxidation and subsequent high-dose implantation of hydrogen ions (*1* indicates the surface; *2*, the oxide layer; *3*, the oxide boundary; and *4*, the amorphized region).

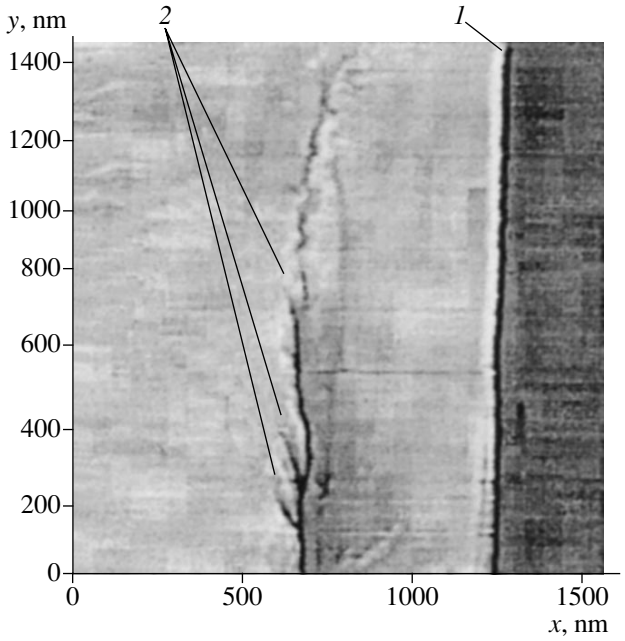

Fig. 3. An AFM image illustrating the origination of microcracks (*2*) in the plane of a buried nanoscale damaged layer at the cleaved surface of a *p*-Si wafer after irradiation of the wafer surface (*1*) with protons.

sists in using high-power pulsed proton beams, in which case the mechanisms for the spatial separation of components of the Frenkel pairs change drastically. Apparently, it is this circumstance that accounts for the amorphization of silicon [6] irradiated with protons at a very high pulse-current density (40 mA cm^{-2}) and integrated fluxes of about 2×10^{17} cm^{-2}. At the same time, according to our data and [7], irradiation of silicon with low-intensity (<10 μA cm^{-2}) steady beams with doses as high as $(6–8) \times 10^{17}$ cm^{-2} does not give rise to the amorphization of silicon. Apparently, the amorphization of another semiconductor (silicon carbide), observed in this study at comparatively low proton-beam current densities (<5 μA cm^{-2}), indicates that specific features of separation of primary radiation defects in silicon carbide bring about a buildup in the concentration of multivacancy complexes; ultimately, this concentration becomes sufficient for amorphization.

We studied the effect of heat-treatment conditions on the characteristics of buried nanoscale damaged layers. Figure 4 illustrates the dynamics of growth of blisters in irradiated *n*-Si in the course of low-temperature (500°C) annealing. After annealing for 30 min, the blisters have average heights of up to 100 nm and diameters of ≈10 μm; as the duration of annealing increases to 60 min, the blisters swell, so that their average height increases to 1 μm and their diameter, to ≈20 μm; and, as the duration of annealing is increased further, exfoliation of material and the formation of dips are observed. Figure 5 illustrates representative results. Figure 5a shows an image of the Si surface with blisters and the height distribution for blisters. Figure 5b represents a dip formed on the Si surface after separation of a flake from the upper silicon layer and the profile of this dip. Figure 5c shows the image of a separated flake and its profile.

We attempted to determine the optimal conditions (doses) of irradiation required for the successful implementation of the Smart-Cut technology in different semiconductors. The results of studies show that, in the case of implantation of 50- to 100-keV protons with subsequent annealing, these doses are equal to $(5–8) \times 10^{16}$ cm^{-2} for *p*-Si, $(0.8–1.5) \times 10^{17}$ cm^{-2} for *n*-Si, and $(0.5–1.0) \times 10^{17}$ cm^{-2} for *n*-6*H*-SiC.

We carried out a comparative analysis of the effect of the conductivity type on the special features of blistering and exfoliation of silicon crystals with different types of conductivity and of silicon carbide crystals subjected to proton implantation and postimplantation annealing. It is shown that blistering and exfoliation are observed when the dose of implanted protons exceeds a certain minimal threshold level Φ_{min}. This threshold dose depends on the conductivity type of the crystal and on the energy of implanted hydrogen ions. In the case of irradiation with 50- to 100-keV protons, we have $\Phi_{min} \approx 4 \times 10^{16}$ cm^{-2} for *p*-Si crystals, whereas $\Phi_{min} \approx 7 \times 10^{16}$ cm^{-2} for *n*-Si. In addition, the dynamics of the development of blistering and exfoliation in the plane of a buried nanoscale damaged layer in the course of postimplantation annealing is different for *n*- and *p*-Si samples. With identical conditions and doses of proton implantation into Si, the development of blisters and the exfoliation of the Si film proceeds much more slowly (by a factor of 5–10) in *n*-Si crystals than in *p*-Si at the same heat-treatment temperature (in the range of 400–600°C). In order to equate the rates of these processes, *n*-Si should be annealed at higher temperatures. Since the determining role in the development of defoliation of crystals in the plane of a buried nanoscale damaged layer is played by the migration (diffusion) of hydrogen and the formation of vacancy–hydrogen complexes [8, 9], it should be assumed that the special features of blistering reported here in *p*- and *n*-Si are related either to differences in the kinetics of atomic-hydrogen migration or to differences between the activation energies of formation of vacancy–hydrogen complexes in *n*- and *p*-Si. Differences in the migration kinetics may be caused by differences in the charge state of hydrogen in relation to the position of the Fermi level in a material, i.e., to the conductivity type and doping level of a crystal. Differences in the activation energies of formation of hydrogen-containing complexes are caused to a great extent by the types of doping and background impurities in the crystal and, in particular, by doping of *p*-Si with boron [9].

Compared to the blistering of Si crystals at relatively low temperatures, the blistering of SiC was observed only after the postimplantation annealing of irradiated samples at temperatures of 800–900°C. The

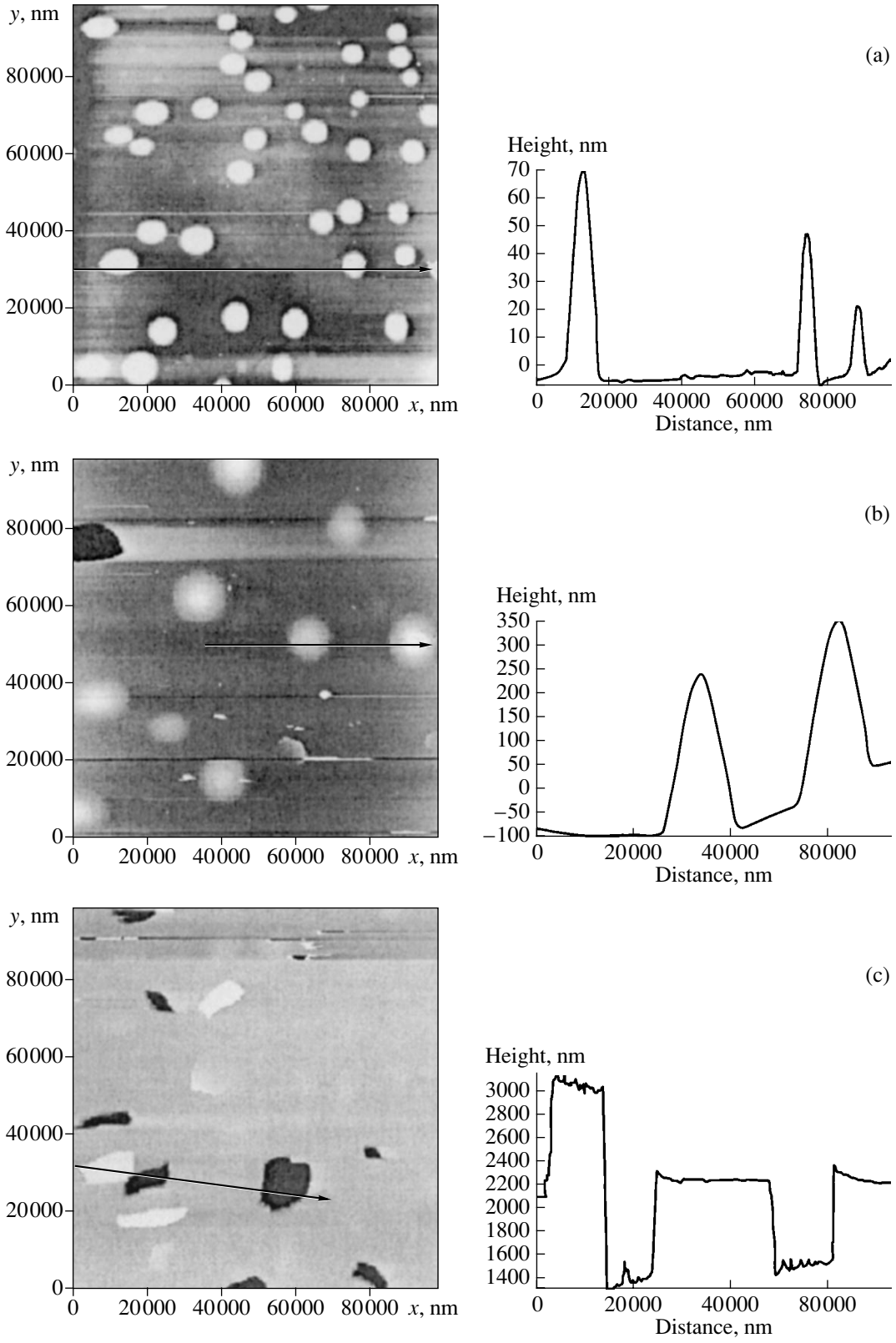

Fig. 4. Dynamics of the growth of blisters in irradiated *n*-Si as a result of postimplantation annealing for (a) 30, (b) 60, and (c) 540 min at 500°C. The profiles drawn through characteristic topographic features of the surface are represented to the right of the AFM images. The lines along which the profiles were obtained are indicated by arrows in the AFM images.

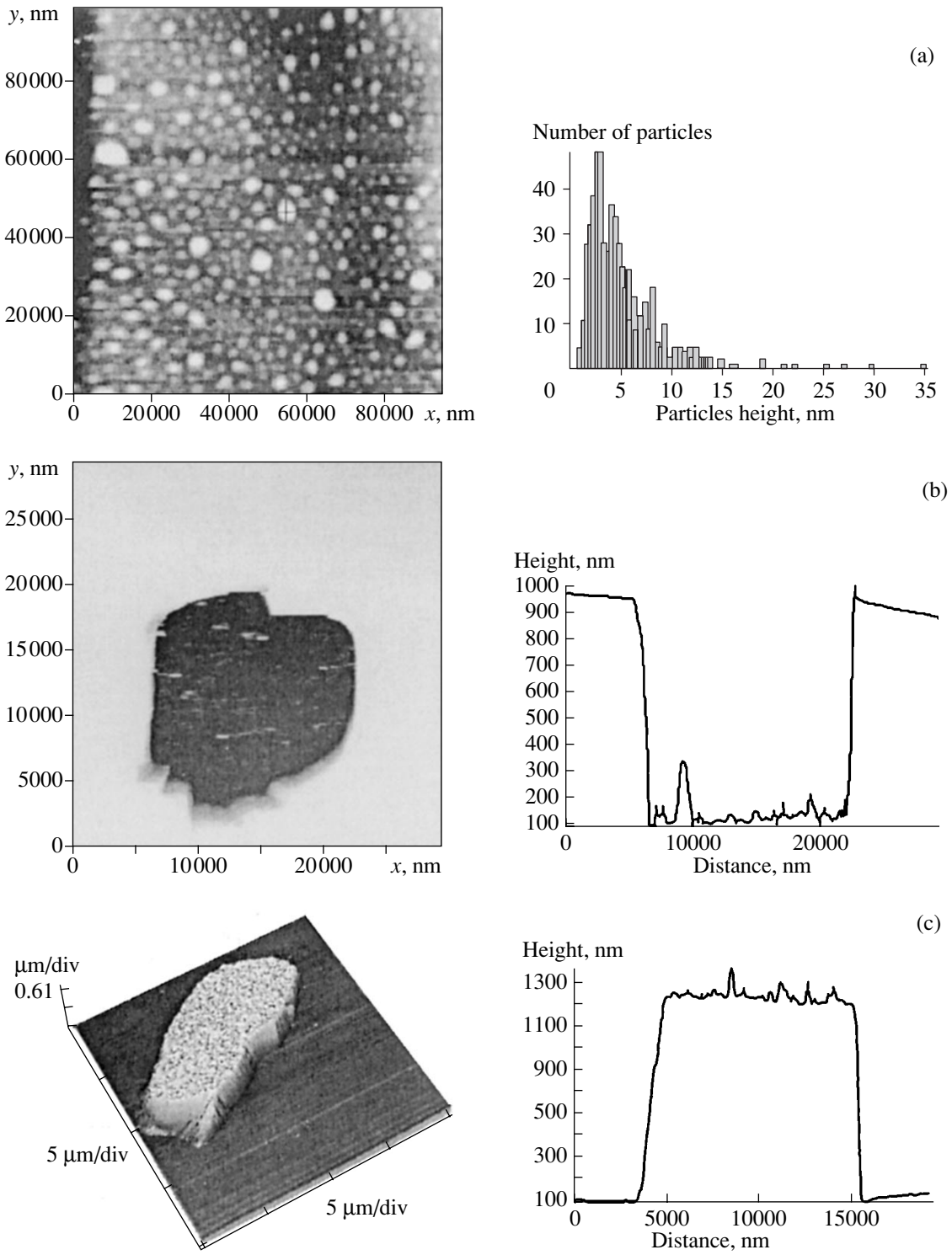

Fig. 5. (a) An AFM image of the Si surface and the blister height distribution after a high-dose implantation of hydrogen ions and subsequent annealing for 30 min at 475°C; (b) an image of a dip formed after separation of a flake from the upper layer of silicon and the profile of this dip; and (c) an image of one of the separated flakes and its profile.

higher temperature of annealing required for the development of exfoliation processes in SiC crystals in the plane of a buried nanoscale damaged layer is caused by the higher activation energy for this process (>3 eV) in SiC and also by the much lower diffusivity of atomic hydrogen in this material [10]. Another special feature of the exfoliation process of SiC crystals, which differentiates this process from that in Si, is the observed sup-

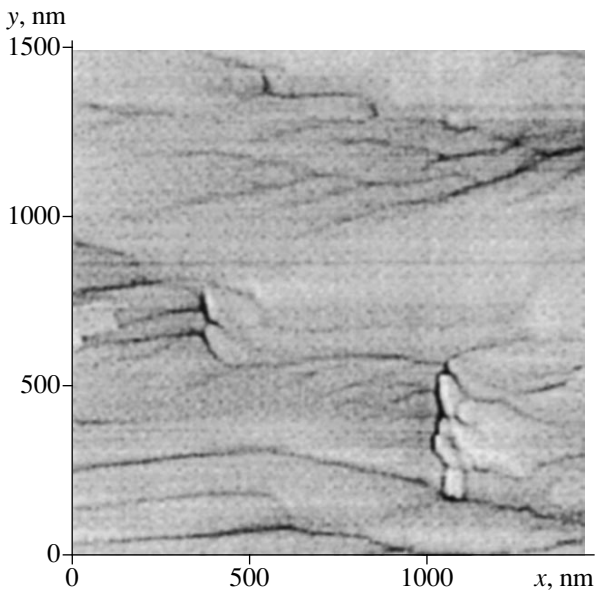

Fig. 6. An AFM image of the cleaved surface of SiC crystal implanted with hydrogen ions; a network of microcracks can be seen in the surface region. The microcracks develop as a result of postimplantation annealing of the crystal and grow toward the irradiated surface rather than in the plane of the buried nanoscale damaged layer.

pression of blistering in the SiC samples subjected to proton implantation at doses higher than 3×10^{17} cm^{-2}. In our opinion, this phenomenon is caused by the effect of the amorphization of silicon carbide in the region of the buried nanoscale damaged layer; this effect hinders the formation of planar two-dimensional vacancy–hydrogen defects, which are observed only in crystalline material and are involved primarily at the initial stage of the development of microcracks in the plane of a buried nanoscale damaged layer. Thus, the existence of both lower and upper limits of the hydrogen-implantation dose required for blistering and implementation of the Smart-Cut technology is characteristic of silicon carbide.

We were the first to study the effect of the degree of mechanical damage of the SiC wafer surface on the dynamics of development of microcracks and on blistering. We showed that it was impossible to attain blistering and exfoliation of SiC wafers whose surface had been polished mechanically using diamond pastes with granules 2 μm in diameter. This fact is caused by mechanical damage introduced into the surface layer of the crystals as a result of mechanical polishing. In this case, the thickness of the subsurface damaged layer is equal to the size of the polishing-paste granules by an order of magnitude; thus, hydrogen ions are implanted into the mechanically damaged layer (the projected range of 100-keV hydrogen ions in silicon carbide is equal to 0.65 μm). In the course of postimplantation annealing, microcracks in the layer grow preferentially towards the crystal surface (Fig. 6) through mechanical damage introduced by polishing. Thus, the initial mechanical damage in the crystal also suppresses the development of microcracks in the plane of the buried nanoscale damaged layer.

For SiC samples polished with diamond pastes with granule sizes ≤0.1 μm, the layer with mechanical damage produced by polishing had a thickness of ~0.1 μm. In this situation, the implantation of 100-keV hydrogen ions resulted in the formation of a buried nanoscale damaged layer at a depth greatly in excess of the mechanical-damage depth. In this situation, the surface layer damaged by polishing affected neither the development of microcracks in the plane of the buried nanoscale damaged layer nor the blistering and exfoliation of the wafers. Thus, in order to successfully implement the Smart-Cut technology in the course of fabricating semiconductor-on-insulator structures, one should form the buried nanoporous layers at a depth that far exceeds the depth of mechanical damage to the surface region of semiconductor wafers.

4. CONCLUSION

As a result of AFM studies of buried nanoscale damaged layers formed in Si and SiC crystals by the implantation of hydrogen ions with energies of 50 and 100 keV, we showed that the sensitivity of AFM is sufficiently high to detect the initial stages of development of hydrogen-containing pores in the aforementioned layers. The AFM studies of irradiated surfaces and cleavage planes intersecting these surfaces made it possible to directly observe and study the growth of pores and the development of microcracks initiated by these pores in the buried nanoscale damaged layers. The AFM studies of cleaved surfaces also made it possible to reveal the existing structure of the surface regions: the layer of surface oxide, the buried nanoscale damaged layer itself at a depth corresponding to the projected range of hydrogen ions, and the amorphized region surrounding this layer in SiC. As a result, we derived exact quantitative criteria for the formation of buried nanoscale damaged layers in the crystals under investigation.

We discovered that the processes of blistering and exfoliation in silicon depend on the type of conductivity. We suggested that special features of blistering in *p*- and *n*-Si are related to differences in the kinetics of migration of atomic hydrogen and in the activation energies of formation of vacancy–hydrogen complexes in silicon with different types of conductivity. It is characteristic of silicon carbide that there are both lower and upper limits for the proton-implantation dose required for blistering and implementation of the Smart-Cut technology.

REFERENCES

1. M. Bruel, Electron. Lett. **31**, 1201 (1995).
2. V. V. Kozlovskiĭ, V. A. Kozlov, and V. N. Lomasov, Fiz. Tekh. Poluprovodn. (St. Petersburg) **34**, 129 (2000) [Semiconductors **34**, 123 (2000)].
3. N. N. Gerasimenko, in *Proceedings of the First Moscow International Physical School of the Institute of Theoretical and Experimental Physics, Zvenigorod, 1998*, p. 173.
4. A. I. Baranov, in *Radiation Effects in Semiconductors*, Ed. by L. S. Smirnov (Nauka, Novosibirsk, 1979), p. 28.
5. *Physical Processes in Irradiated Semiconductors*, Ed. by L. S. Smirnov (Nauka, Novosibirsk, 1977).
6. V. R. Galakhov, I. V. Antonova, S. N. Shamin, *et al.*, Fiz. Tekh. Poluprovodn. (St. Petersburg) **36**, 598 (2002) [Semiconductors **36**, 568 (2002)].
7. P. A. Aleksandrov, E. K. Baranova, I. V. Baranova, *et al.*, in *Proceedings of the XI International Conference on Radiation Physics of Solids, Sevastopol, 2001*, p. 351.
8. Q.-Y. Tong and R. B. Bower, MRS Bull., No. 12, 40 (1998).
9. F. A. Reboredo and S. T. Pantefides, Solid State Phenom. **69–70**, 83 (1999).
10. V. V. Kozlovskiĭ and V. A. Kozlov, Fiz. Tekh. Poluprovodn. (St. Petersburg) **33**, 1409 (1999) [Semiconductors **33**, 1265 (1999)].

Translated by A. Spitsyn

Semiconductors, Vol. 36, No. 11, 2002, pp. 1235–1239. Translated from Fizika i Tekhnika Poluprovodnikov, Vol. 36, No. 11, 2002, pp. 1318–1322.

DEDICATED TO THE MEMORY OF V.F. MASTEROV

The Formation of β-$FeSi_2$ Precipitates in Microcrystalline Si

E. I. Terukov, O. I. Kon'kov, V. Kh. Kudoyarova, O. B. Gusev, V. Yu. Davydov, and G. N. Mosina

Ioffe Physicotechnical Institute, Russian Academy of Sciences, Politekhnicheskaya ul. 26, St. Petersburg, 194021 Russia

e-mail: kudoyarova@mail.ioffe.ru

Submitted April 2, 2002; accepted for publication April 11, 2002

Abstract—The formation of β-$FeSi_2$ precipitates was observed for the first time in microcrystalline Si films. The Fe-doped amorphous Si films (*a*-Si:Fe) were obtained using magnetron sputtering. Subsequent short-time thermal treatment led to the transition of amorphous Si to microcrystalline Si and to the formation of β-$FeSi_2$ precipitates. The samples synthesized emitted at the wavelength $\lambda \approx 1.54$ μm at 100 K.

1. INTRODUCTION

One of the lines of Si optoelectronics is the fabrication of thin-film structures emitting in the region close to 1.5 μm, which corresponds to the transparency window for Si and SiO_2. A new approach for solving this problem is associated with the synthesis of a number of compounds and their clusters in Si. The semiconductor iron disilicide β-$FeSi_2$ should be assigned to such compounds. Iron disilicide possesses some attractive optical properties, such as a direct optical gap of about 0.85 eV (1.46 μm), which corresponds to a wavelength close to 1.5 μm, and an optical absorption coefficient as large as 10^5 cm^{-1}. These properties make this material promising for fabricating new optoelectronic devices which are sensitive in the near-infrared region and can be integrated into Si microelectronic technology [1].

Studies on the synthesis of such Si films have been carried out intensively in recent years. Introducing β-$FeSi_2$ inclusions into Si has mainly been done using high-dose implantation of Fe^+ ions ($D > 1 \times 10^{17}$ cm^{-2}) and molecular-beam epitaxy with subsequent high-temperature (as high as 900°C) prolonged (to 20 h) thermal treatment [2, 3]. Such thermal treatments are undesirable in microelectronics during the fabrication of integrated microcircuits. The reason is that these treatments lead to significant Fe diffusion into the depth of the Si host due to the large Fe diffusivity at high temperatures ($D \approx 5 \times 10^{-6}$ cm^2/s at $T \approx 1000$°C). This causes the degradation of the main parameters of Si devices [4]. It is possible to overcome these difficulties by using pulsed-beam (laser, ion, electron) treatments, which affect only the surface layers of the material (~1 μm) for a short time (< 1 μs) and which exclude the undesirable diffusion of the Fe impurity into the host material [5, 6]. It is known that magnetron sputtering permits the obtainment of films of amorphous Si doped with various metals. In this case, similarly to the use of implantation, the dopant concentration may exceed the limiting solubility. Specifically, the limiting solubility of Fe in crystalline Si is 10^{13}–10^{15} cm^{-3} (at 900–1300°C) [7]. Owing to this, the purpose of this study was to develop the technology of light-emitting structures based on β-$FeSi_2$ in Si without using expensive implantation and prolonged thermal treatments.

In this study, the formation of β-$FeSi_2$ precipitates in microcrystalline Si films obtained via magnetron cosputtering of Si and Fe targets in an Ar atmosphere was observed for the first time. The samples synthesized emitted at a wavelength $\lambda \approx 1.54$ μm at 100 K.

2. TECHNOLOGY OF FABRICATION AND METHODS FOR INVESTIGATION

The Fe-doped amorphous Si films (*a*-Si:Fe) were fabricated using magnetron sputtering of Fe and Si targets in an Ar atmosphere. The subsequent thermal treatment in the Ar atmosphere at $T = 800$°C for 30 min transformed the films from the amorphous state (*a*-Si:Fe) to the microcrystalline state (μ*c*-Si:Fe). In these films, we observed the formation of iron disilicide β-$FeSi_2$.

The investigation of the Fe concentration profile over the depth and the determination of the film composition and thickness were carried out using Rutherford backscattering (RBS). The samples were irradiated with 0.9-MeV deuterons ($^2D^+$); the scattering angle was 135°. The concentration of Fe introduced ranged from 1.5×10^{20} cm^{-3} to 2.4×10^{21} cm^{-3}. The film thickness was 0.4–0.5 μm.

The sample structure was investigated using Raman spectroscopy. The Raman spectra were obtained with an automated setup based on a DFS-24 spectrometer.

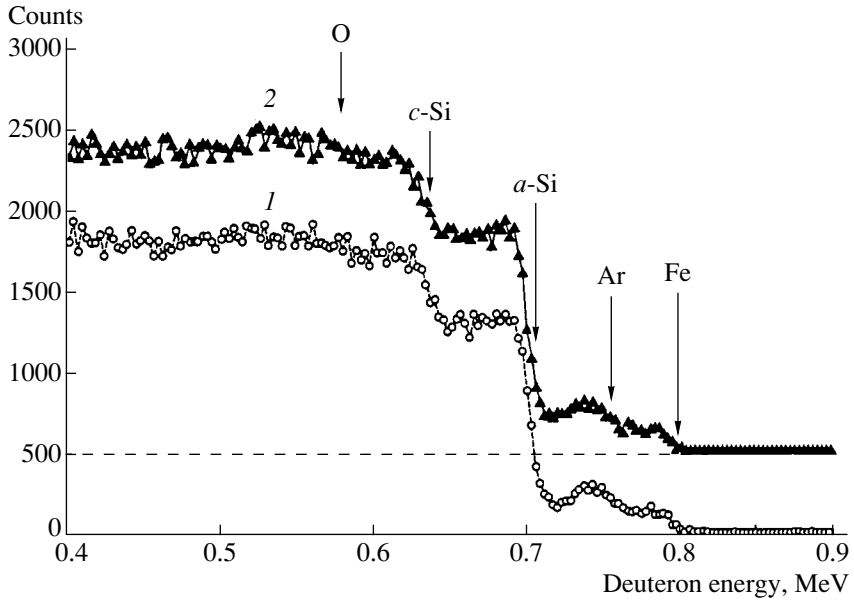

Fig. 1. Typical Rutherford backscattering spectra for the *a*-Si:Fe films: (*1*) prior to thermal treatment and (*2*) after thermal treatment (800°C, 30 min). The Fe concentration $N_{Fe} = 10^{21}$ cm^{-3}.

All spectra were recorded at 300 K in the range of 0–600 cm^{-1} with a resolution of 3 cm^{-1}. As the excitation source, an argon laser was used (λ = 514.5 nm).

The finer structure of the μ*c*-Si:Fe films was investigated using a transmission electron microscope. To determine the microstructure of the layers, transmission electron microscopy (TEM) in the bright-field mode and electron microdiffraction were used. Planar samples with a diameter of 3 mm were prepared for investigations. The photoluminescence (PL) signal was excited by a He–Ne laser (λ = 630 nm) with a power of 50 mW, and the PL was detected using a North Coast cooled Ge detector.

3. RESULTS

The RBS spectrum for the *a*-Si:Fe samples (*1*) prior to and (*2*) subsequent to thermal treatment (T = 800°C, 30 min) is shown in Fig. 1. As can be seen from Fig. 1, Ar (4 at. %) and O (5 at. %) are present in the films in addition to Fe. The presence of Ar in the films is associated with the magnetron cosputtering of the target in the Ar atmosphere. The emergence of O in the films is apparently associated with the presence of O in the *c*-Si target. The RBS data permit us to make two very important conclusions. First, Fe is found only in the film and is distributed uniformly. Second, short-term thermal treatment does not lead to the redistribution of Fe in *c*-Si.

The Raman spectra of the annealed samples (T = 800°C, 30 min) are shown in Fig. 2. We observed four strong spectral lines peaked at the wavelengths of 195, 247, and 480–520 cm^{-1}. The lines at 480–520 cm^{-1} are attributed to the amorphous and microcrystalline Si phases and correspond to the TO phonon mode. It can be seen from Fig. 2 that the spectrum in the range of 400–600 cm^{-1} consists of two lines with substantially different widths. The broad line with a center at about 480 cm^{-1} is attributed to the amorphous phase (the amorphous connecting texture, the network, and (or) the amorphous surface between microcrystalline grains). The narrow line with a center at ~520 cm^{-1} is indicative of the presence of the microcrystalline Si phase.

As for the lines located at 196 and 247 cm^{-1}, they are conditioned by the presence of β-$FeSi_2$. The β-$FeSi_2$ phase is crystallized in the orthorhombic space group D_{2h}^{18}. For Raman spectroscopy, the group-factor analysis predicts 12 active intrinsic modes, which are probably responsible for many of the 14 Raman lines [8]. In addition, the Raman susceptibility of three modes A_g should not vary with the rotation of the polarization of the excitation field relative to the polarization of the scattered light. This occurs in the case of the three most intense lines of the transversely polarized spectrum at 197, 253, and 346 cm^{-1} observed in the β-$FeSi_2$ film with a thickness of 1 μm on the FeSi substrate. The lines at 178, 201, and 252 cm^{-1} were measured for bulk polycrystalline β-$FeSi_2$. For the β-$FeSi_2$ film 200 nm thick, which was grown on the Si substrate, the fundamental lines were observed at 176, 195/200, and 247 cm^{-1} [8, 9]. It should be noted that in all cases the peak at 247 cm^{-1} (A_g mode) was most intense. Because of this, many authors focus their attention on this peak only. As can be seen from Fig. 2, the intensity of the peak at 247 cm^{-1} increases with an increase in the Fe concentration. This can be attributed to an increase in

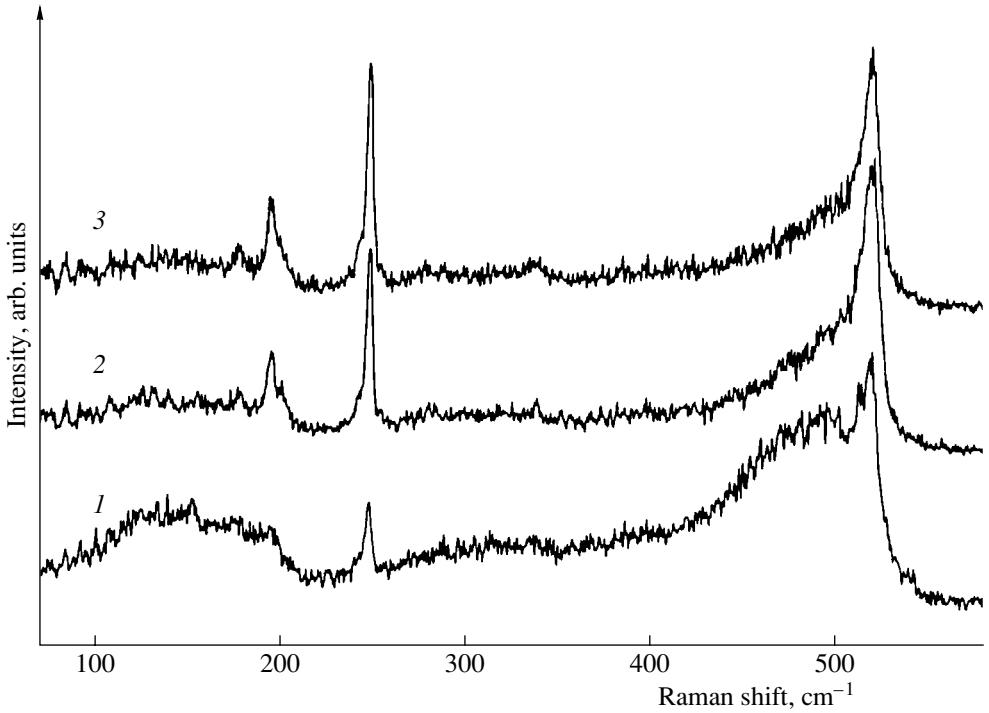

Fig. 2. Raman spectra of the films with Fe concentrations N_{Fe} = (*1*) 1.1×10^{21}, (*2*) 2.1×10^{21}, and (*3*) 2.4×10^{21} cm^{-3}.

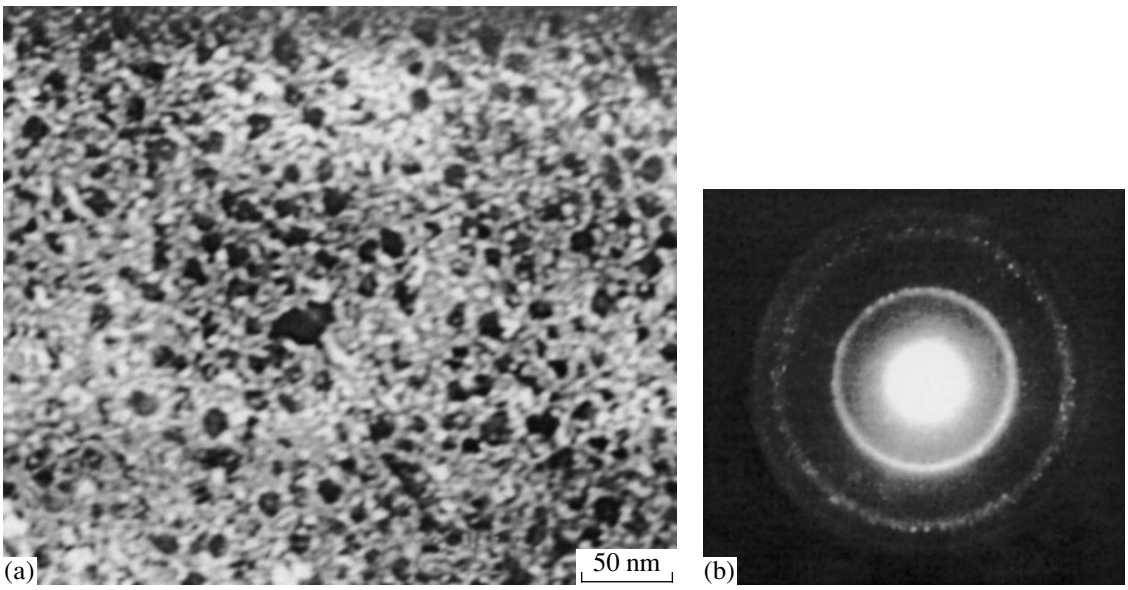

Fig. 3. (a) Bright-field electron microscopy image of the film, $N_{Fe} = 2.4 \times 10^{21}$ cm^{-3}; (b) corresponding microdiffraction pattern.

the amount of the β-$FeSi_2$ phase synthesized. It should also be noted that an increase in the Fe concentration leads to a decrease in the intensity of the broad line at about 480 cm^{-1}, which is attributed to the TO-phonon mode of amorphous Si.

The structural investigations, which were carried out using a transmission electron microscope, demonstrated (Figs. 3a, 3b) that the μ*c*-Si:Fe films consist of nanometer-size (2–4 nm) spheres, which partially coagulate to form plates as large as 25 nm in size (Fig. 3a). The spheres are incorporated into the amorphous Si matrix. The diffraction pattern from the part of the layers shown in Fig. 3a is shown in Fig. 3b. It includes three diffuse rings, the analysis of which demonstrated that the layer consists of particles of the crystalline

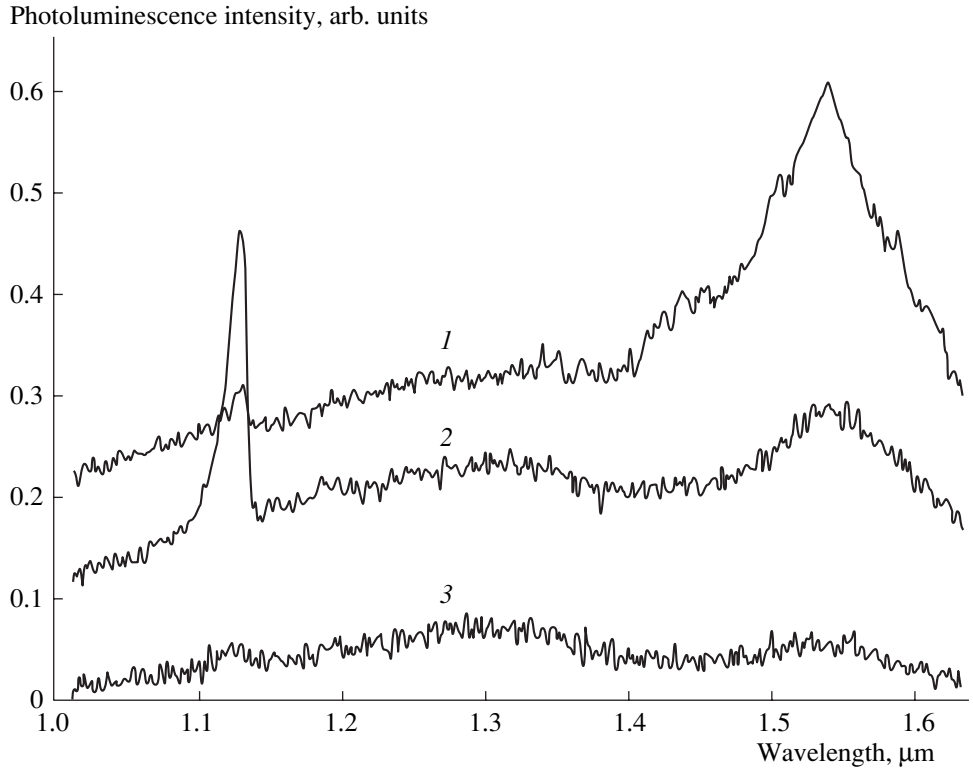

Fig. 4. Photoluminescence spectra of the films with Fe concentrations N_{Fe} = (*1*) 1.1×10^{21}, (*2*) 2.1×10^{21}, and (*3*) 2.4×10^{21} cm^{-3}. T = 100 K.

phase. The interplanar spacings for the film, which were calculated from the observed microdiffraction pattern, are given in the table in comparison with corresponding tabulated values for β-$FeSi_2$and *c*-Si [10]. The comparison carried out allowed us to conclude that the microcrystalline inclusions are the precipitates of the β-$FeSi_2$ phase. The largest precipitate size is 20–25 nm. It varies insignificantly as the Fe concentration increases. However, an increase in the Fe content by approximately a factor of 2 from 1.1×10^{21} to 2.4×10^{21} cm^{-3} leads to an increase in the density of β-$FeSi_2$ precipitates from 6.7×10^{10} to 2.1×10^{11} cm^{-2}.

Interatomic spacings *d* for the film with an Fe concentration of 2.4×10^{21} cm^{-3} calculated from the microdiffraction pattern in comparison with the tabulated values for β-$FeSi_2$ and *c*-Si [10]

Experimental values	Tabulated values for β-$FeSi_2$		Tabulated values for *c*-Si	
d, Å	*d*, Å	*hkl*	*d*, Å	*hkl*
3.157			3.13	111
3.08	3.07	202		
2.826	2.851	221		
2.476	2.412	222		
1.988	1.98	313		
1.94	1.95	040	1.92	220
1.83	1.822	204		
1.87	1.867	114		
1.73	1.746	042		
1.629	1.65	224	1.63	311
1.521	1.53	440		
1.358			1.357	400

The photoluminescence (PL) spectra observed at T = 100 K for the samples with various Fe concentrations are shown in Fig. 4. Two PL peaks are observed. These peaks correspond to the PL from the Si substrate ($E \approx 1.1$ eV, $\lambda \approx 1.12$ μm) and β-$FeSi_2$ ($E \approx 0.805$ eV, $\lambda \approx 1.54$ μm). It is evident that the first peak ($E \approx 1.1$ eV, $\lambda \approx 1.12$ μm) is associated with indirect transitions in the Si band gap. The second peak ($E \approx 0.805$ eV, $\lambda \approx 1.54$ μm) is related to direct band-to-band transitions within the limits of the β-$FeSi_2$ band gap.

One of the problems associated with the emission in the region $\lambda \approx 1.54$ μm in the crystalline Si (*c*-Si) is the origin of the PL signal. It is known that the dislocations existing in the crystal are capable of luminescing at a wavelength $\lambda \approx 1.5$ μm [11]. In this case, there arises the necessity of separating the contributions from dislocations and silicide to the emission of light. Because of this, for *c*-Si:Fe it is necessary to furnish proof showing that the origin of the PL signal at $\lambda \approx 1.54$ μm is not associated with the emission caused by dislocations,

but emerges due to direct band-to-band transitions through the optical gap of β-$FeSi_2$. Usually, such proof is the distinction between the obtained value of the thermal quenching energy for the PL signal and the data on the thermal quenching for the *D*1 dislocation center (E_a = 7–12 meV). The energy-level position of this center ($E \approx 0.81$ eV) [11] is closest to the PL peak ($E \approx 0.805$ eV).

In this study, β-$FeSi_2$ was obtained in microcrystalline Si films. Microcrystalline Si contains no dislocations. Because of this, we may ignore the contribution of dislocations to PL and attribute the PL observed in the region $\lambda \approx 1.54$ μm to β-$FeSi_2$. The PL peak from β-$FeSi_2$ ($E \approx 0.805$ eV, $\lambda \approx 1.54$ μm) comprises the broad band. The broadening of the PL line may be associated with the spread in the sizes of β-$FeSi_2$ precipitates. In addition, it was found that the PL intensity depends on the Fe concentration. Microstructural investigations demonstrated that the formation of the β-$FeSi_2$ phase is observed at Fe concentrations from 1.5×10^{20} to 2.5×10^{21} cm^{-3}. An increase in the Fe concentration led to an insignificant variation in the largest precipitate size (from 20 to 25 μm). A more considerable variation was observed in the density (amount) of the β-$FeSi_2$ phase. However, the highest PL intensity at $\lambda \approx 1.54$ μm is observed for the Fe concentration $\approx 1.1 \times 10^{21}$ cm^{-3}. For the Fe concentration of $\approx 2.4 \times 10^{21}$ cm^{-3}, the PL signal almost vanishes. For these Fe concentrations, the line at 480 cm^{-1}, which is assigned to the TO-phonon mode of amorphous Si, is not observed in the Raman spectra. It seems likely that the PL intensity at $\lambda \approx 1.54$ μm depends both on the size of β-$FeSi_2$ precipitates and on the ratio of the volumes occupied by the β-$FeSi_2$ phase and the amorphous Si phase.

It should be noted that, in this paper, we are reporting results obtained for the first time. In order to make a more definite conclusion on the PL mechanism at $\lambda \approx 1.54$ μm in microcrystalline Si, additional investigations are required.

4. CONCLUSION

In this study, the formation of iron disilicide β-$FeSi_2$ was observed for the first time in microcrystalline Fe-doped Si films. The amorphous Fe-doped Si films were obtained by magnetron sputtering of Si and Fe targets in an Ar atmosphere. The subsequent thermal treatment at T = 800°C for 20 min led to the formation of microcrystalline Si and iron disilicide β-$FeSi_2$. In such films, PL at a wavelength $\lambda \approx 1.54$ μm at 100 K was observed. The dependence of the PL intensity on the Fe concentration was found. This allowed us to attribute the PL observed to the precipitates of the β-$FeSi_2$ phase.

ACKNOWLEDGMENTS

This study was supported by the fundamental research program "Low-Dimensional Quantum Structures", grant no. 6.15, 4B19.

We thank V.M. Lebedev for measurements of Rutherford backscattering.

REFERENCES

1. M. C. Bost and J. E. Mahan, J. Appl. Phys. **58**, 2696 (1985).
2. D. Leong, M. Harry, K. J. Reeson, and K. P. Homewood, Nature **387**, 686 (1997).
3. K. Lefki, P. Muret, N. Cherief, and R. S. Cinti, J. Appl. Phys. **69**, 352 (1991).
4. B. O. Kolbesen and H. Cerva, Phys. Status Solidi B **222**, 303 (2000).
5. R. I. Batalov, R. M. Bayazitov, E. I. Terukov, *et al.*, Fiz. Tekh. Poluprovodn. (St. Petersburg) **35** (11), 1320 (2001) [Semiconductors **35**, 1263 (2001)].
6. R. I. Batalov, R. M. Bayazitov, I. B. Khaibullin, *et al.*, Nanotechnology **12**, 409 (2001).
7. B. L. Sharma, *Diffusion in Semiconductors* (Trans Tech Publications, Clausthal-Zellerfeld, 1970), p. 87.
8. K. Lefki, P. Muret, E. Bustarret, *et al.*, Solid State Commun. **80**, 791 (1991).
9. A. G. Birdwell, R. Glosser, D. N. Leong, and K. P. Homewood, J. Appl. Phys. **89**, 965 (2001).
10. *JCPDS Powder Diffraction File* (International Center for Diffraction Data, Swarthmore, 1989).
11. N. A. Drozdov and A. A. Patrin, Pis'ma Zh. Éksp. Teor. Fiz. **23**, 800 (1976) [JETP Lett. **23**, 597 (1976)].

Translated by N. Korovin

Semiconductors, Vol. 36, No. 11, 2002, pp. 1240–1243. Translated from Fizika i Tekhnika Poluprovodnikov, Vol. 36, No. 11, 2002, pp. 1323–1326.

DEDICATED TO THE MEMORY OF V. F. MASTEROV

Erbium Electroluminescence in *p–i–n* Amorphous Hydrogenated Silicon Structures

E. I. Terukov*, O. B. Gusev*, O. I. Kon'kov*, Yu. K. Undalov*, M. Stutzmann, A. Janotta**, H. Mell***, and J. P. Kleider******

** Ioffe Physicotechnical Institute, Russian Academy of Sciences, St. Petersburg, 194021 Russia*
*** Walter Schottky Institut, Technische Universität, München, Deutschland*
**** Phillips-Universität, Marburg, Deutschland*
***** Laboratoire de Genie Electrique de Paris, École Superieure d'Électricité, Université de Paris, Paris, France*

Submitted April 2, 2002; accepted for publication April 11, 2002

Abstract—A comparative analysis of $\lambda = 1.54$ μm electroluminescent structures based on amorphous hydrogenated silicon is made. The possibility of obtaining room-temperature electroluminescence from forward-biased conventional *p–i–n* structures based on this material is demonstrated for the first time, which is of interest for the development of effective emitting structures with current pumping. *© 2002 MAIK "Nauka/Interperiodica".*

1. INTRODUCTION

Promising results have been obtained lately in studies of the luminescence of Er-doped amorphous hydrogenated silicon *a*-Si:H(Er).

In particular, effective photoluminescence (PL) [1, 2] and electroluminescence (EL) are observed in Me/*a*-Si(Er)/*c*-*n*-Si/Me (Me is a metal) structures at room temperature [3, 4]. In these structures, an Er-containing active layer was produced by modified magnetron sputtering and effective EL was observed in reverse-biased diodes.

The goal of the present study is to reveal the possibility of obtaining erbium EL (1.54 μm) in *p–i–n* structures, which are the basic structures in *a*-Si:H(Er) devices.

2. FABRICATION TECHNOLOGY OF THE STRUCTURE AND EXPERIMENTAL METHODS

The three general concepts for the fabrication of *p–i–n a*-Si:H structures with an Er-doped active layer are as follows:

(i) the implantation of Er into an *i*-type layer with the further deposition of an n^+-type layer;

(ii) the deposition of an intermediate Er-doped active layer between the *i*- and n^+-type layers of a *p–i–n* structure;

(iii) the fabrication of a conventional *p–i–n* structure with an intrinsic Er-doped layer.

The first variant was immediately discarded. An implanted layer contained a large number of defects even after post-implantation annealing, and the structures did not sustain voltage. In the other two cases, we have succeeded in obtaining positive results. A structure with an embedded *p–i–n* layer was fabricated using a combination of glow discharge and magnetron sputtering techniques, the latter method was applied to deposit an Er-containing active layer. The structure of this element was a sequence of ITO/p^+-*a*-Si:H/*i*-*a*-Si:H/*a*-Si:H(Er)/n^+-*a*-Si:H/Me layers. Further, we denote this structure as a type-I structure.

The sequence of layers in a conventional type-II *p–i–n* structure are as follows: ITO/p^+-*a*-Si:H/p^--*a*-Si:H(Er)/n^--*a*-Si:H(Er)/n^+-*a*-Si:H/Me. All the layers, including *n*- and *p*-doped and Er-containing, were produced by RF glow discharge using a metal-organic compound of the *tris* type [2.4-pentanedionate-Er (III)] as the Er source. It is worth noting that, as shown in [5], this method, in contrast to magnetron sputtering, allows the fabrication of high-quality intrinsic and doped *a*-Si:H layers containing Er ions.

As shown earlier [2], the introduction of Er ions into *a*-Si:H results in weak doping with the formation of an *n*-type material. At the working concentrations of Er, the doping level corresponds to approximately 10 ppm of phosphine in the vapor phase. Therefore, in our case, the working type-II structure represents a p^+/p^-(Er)/n^-(Er)/n^+ combination of *a*-Si:H layers, where the "intrinsic" n^-(Er) layer is doped with diborane to a level of 100 ppm to provide compensation.

The current–voltage (*I–V*) characteristics of the structures were measured in the dc mode. The EL was studied with a stabilized voltage at a frequency of 100 Hz. The emitted radiation was analyzed using a double-grating

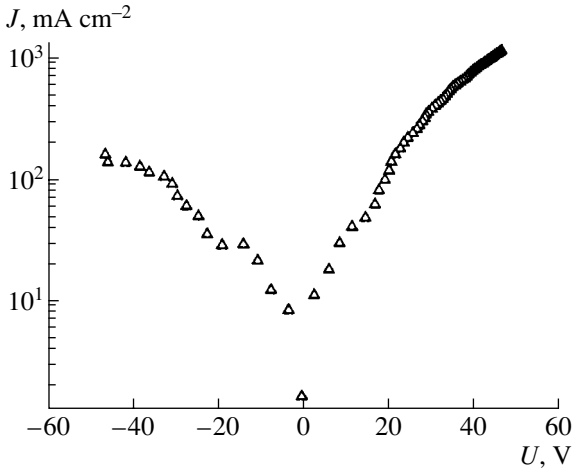

Fig. 1. *I–V* characteristic of a type-I *a*-Si:H(Er) *p–i–n* structure.

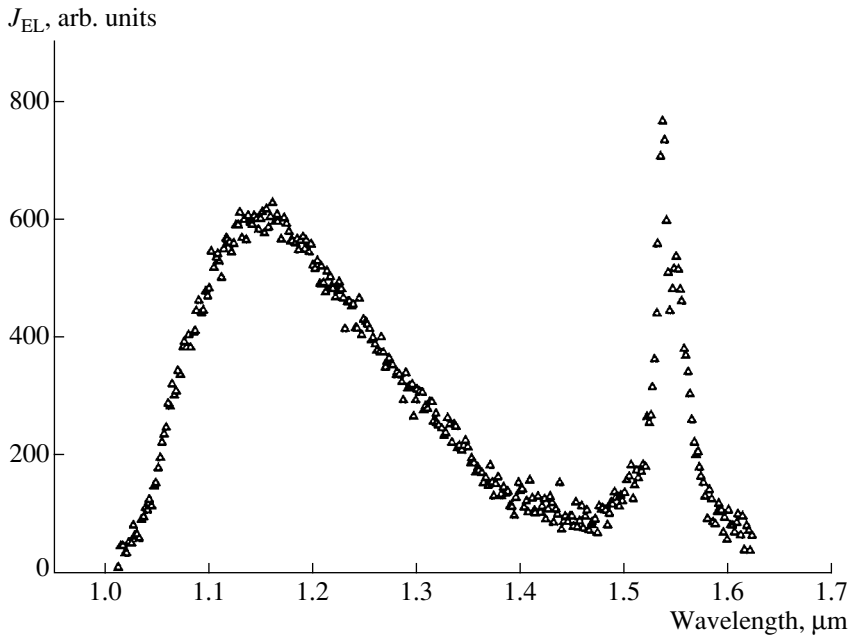

Fig. 2. EL spectrum of a type-I *a*-Si:H(Er) *p–i–n* structure.

spectrophotometer with a cooled Ge photodetector. All the measurements were done at room temperature.

3. EXPERIMENTAL RESULTS AND DISCUSSION

Figure 1 presents a typical *I–V* characteristic of a type-I structure. With forward bias applied to the substrate, the erbium EL at $\lambda = 1.54$ μm and the $\lambda = 1.15$ μm EL from defects of an amorphous matrix were observed (Fig. 2). We obtained similar results earlier for a *p–n* heterojunction, Al/*n*-*a*-Si:H(Er)/*p*-*c*-Si/Al [6]. The dependence of the Er EL intensity on the driving current exhibits a certain threshold current (about 2.5 mA) after which the dependence of the EL intensity on current is virtually linear.

Figure 3 shows the *I–V* characteristic of a type-II *p–i–n* structure. It is typical of standard Er-free *a*-Si:H *p–i–n* structures. When forward bias is applied to the structure, the current increases exponentially and levels off at a voltage of about 1.5 V. An EL signal was observed under forward bias. Figure 4 shows the EL spectrum of such a structure in the current saturation mode (about 100 mA cm^{-2}), with a voltage across the structure of about 3.5 V. For comparison, the EL spectrum of an Al/*a*-Si:H(Er)/*n*-*c*-Si/Al heterostructure is

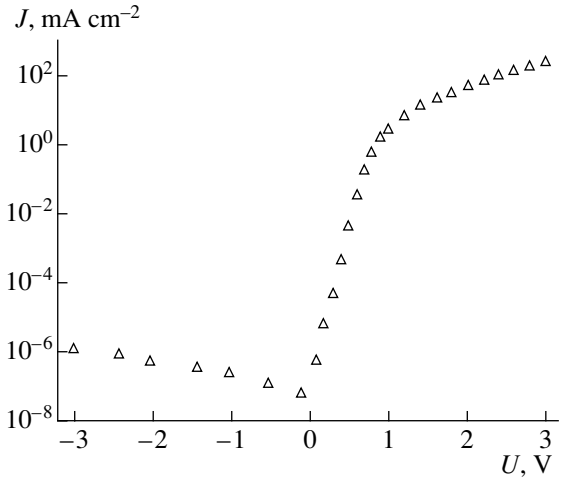

Fig. 3. *I–V* characteristic of a type-II *a*-Si:H(Er) *p–i–n* structure.

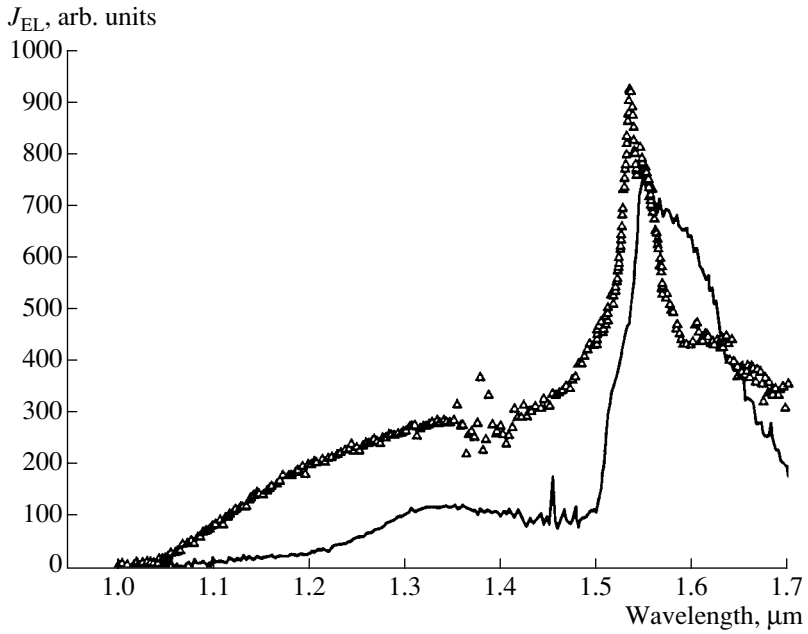

Fig. 4. EL spectra of (solid line) a type-II *a*-Si:H(Er) *p–i–n* structure and (triangles) an Al/*a*-Si:H(Er)/*n*-*c*-Si/Al heterostructure [4].

presented; we have already reported on the EL in these structures [3, 4]. It was observed only under reverse bias; a similar EL intensity was attained at a voltage of about 40 V and a current of 6 A cm^{-2}. Our studies have shown that the optimization of structures of this kind with respect to such parameters as carrier mobility and density of doping defects and dangling bonds is a complicated, and in some respects controversial, task. Another drawback of these structures is the high control voltage, which is hardly compatible with the demands of semiconductor microelectronics. The type-II $p^+/p^-/n^-/n^+$ structures offered in the present study are free of these drawbacks, and their optimization will be the subject of further investigations.

4. CONCLUSION

On the basis of investigations carried out, along with comparative analysis, we demonstrated the possibility of obtaining Er (1.54 μm) electroluminescence in *p–i–n* structures: ITO/p^+-*a*-Si:H/*i*-*a*-Si:H/*a*-Si:H(Er)/n^+-*a*-Si:H/Me under forward bias, and ITO/p^+-*a*-Si:H/p^--*a*-Si:H(Er)/n^--*a*-Si:H(Er)/n^+-*a*-Si:H/Me at a voltage of about 3.5 V across the structure. The EL in these structures is attractive owing to the small voltage

required for the onset of EL and the fact that these are the basic structures in devices based on amorphous hydrogenated silicon.

ACKNOWLEDGMENT

This study was supported financially by the Russian Foundation for Basic Research (project nos. 01-02-17825 and 02-02-17631).

REFERENCES

1. W. Fuhs, I. Ulber, G. Weiser, *et al.*, Phys. Rev. B **56**, 9545 (1997).
2. E. I. Terukov, O. I. Kon'kov, V. Kh. Kudoyarova, *et al.*, J. Non-Cryst. Solids **266–269**, 614 (2000).
3. O. B. Gusev, M. S. Bresler, E. I. Terukov, *et al.*, in *Proceedings of the 24th International Conference on Physics of Semiconductors* (World Scientific, Singapore, 1998), on CD-ROM.
4. O. B. Gusev, M. S. Bresler, E. I. Terukov, *et al.*, J. Lumin. **80**, 335 (1999).
5. A. G. Kazanskii, H. Mell, G. Weiser, and E. I. Terukov, J. Non-Cryst. Solids (2002) (in press).
6. I. O. Kon'kov, A. N. Kuznetsov, P. E. Pak, *et al.*, Pis'ma Zh. Tekh. Fiz. **27** (13), 30 (2001) [Tech. Phys. Lett. **27**, 542 (2001)].

Translated by D. Mashovets

Semiconductors, Vol. 36, No. 11, 2002, pp. 1244–1247. Translated from Fizika i Tekhnika Poluprovodnikov, Vol. 36, No. 11, 2002, pp. 1327–1331.

DEDICATED TO THE MEMORY OF V. F. MASTEROV

Photoluminescence and Excitation Features of Nd^{3+} Ions in $(La_{0.97}Nd_{0.03})_2S_3 \cdot 2Ga_2O_3$ Glasses

A. A. Babaev, E. M. Zobov, V. V. Sokolov, and A. Kh. Sharapudinova

Institute of Physics, Dagestan Scientific Center, Russian Academy of Sciences, Makhachkala, 367003 Russia

e-mail: kamilov@datacom.ru

Submitted April 2, 2002; accepted for publication April 11, 2002

Abstract—A combined study of the spectral photoluminescence distribution and excitation spectra of photoluminescence in $La_2S_3 \cdot 2Ga_2O_3$ and $(La_{0.97}Nd_{0.03})_2S_3 \cdot 2Ga_2O_3$ glasses, along with the study of the transmission spectra of these glasses, was carried out. The radiative channel was ascertained to be the main channel for the energy transfer from the host matrix to the Nd^{3+} ions upon excitation of the glasses with light at a wavelength of the fundamental absorption band. Oxygen centers with the level $E_c - 2.0$ eV act as sensitizing agents. The structural disordering of the glass host increases the variance in the magnitude of splitting of the multiplet levels from the 4*f* electronic states of the Nd^{3+} ion. This promotes nonradiative relaxation of the electrons from excited states to the laser $^4F_{3/2}$ level. The $(La_{0.97}Nd_{0.03})_2S_3 \cdot 2Ga_2O_3$ glasses can be considered as promising laser materials for obtaining the stimulated emission of radiation of Nd^{3+} ions under an optical pump in the range of the fundamental absorption band of the glass. *© 2002 MAIK "Nauka/Interperiodica".*

1. INTRODUCTION

Studies on the synthesis and growth of highly efficient phosphors on the basis of sesquisulfides and oxysulfides of rare-earth elements have as their objective the creation of a new class of active laser media with various pumping methods [1–5]. Studies based on the relation between the composition of a material, quantum yield of luminescence, and the nature of centers responsible for radiative recombination help towards the attainment of this objective.

Nd^{3+}-doped γ-La_2S_3 crystals have attracted interest as promising active laser components [2, 6–8]. This is due to the fact that, for the lasers, there exists the unconventional possibility of the optical excitation of a semiconductor matrix with light corresponding to the fundamental absorption, with a subsequent transfer of energy to the active impurity. These studies demonstrated the following:

1. The optical excitation of Nd^{3+} ions (the main laser transitions $^4F_{3/2} \longrightarrow {}^4I_{9/2}$, $I_{11/2}$) in the γ-La_2S_3 fundamental absorption band is inefficient. The quantum yield with a concentration of Nd^{3+} ions $C_A \approx 1\%$ amounts to $5 \pm 3\%$. Attempts to find a sensitizing ion which could efficiently transfer the excitation energy to the Nd^{3+} ions showed that the transfer coefficient of energy emitted by the Ce^{3+} ions may attain a value of 0.7 in crystals [2]. However, this process takes place only at low temperatures.

2. The times of energy relaxation from upper excited states to the laser $^4F_{3/2}$ level of the Nd^{3+} ion are anomalously long; this results in emission from the upper states, which is undesirable for the laser materials.

These experimental data reduced, to some extent, the interest in the γ-La_2S_3 single crystals and turned the direction of searching for promising laser materials toward oxysulfide compounds of lanthanum (La_2O_2S) [3, 6]. At the same time, the study of $La_2S_3 \cdot 2Ga_2O_3$ glasses activated with neodymium [9–12] showed that these compounds are free from the above drawbacks and may be considered as promising laser materials for obtaining stimulated radiation from Nd^{3+} ions subjected to an optical pump in the fundamental absorption band of the glass. The mechanism of energy transfer from the matrix to the Nd^{3+} ion is still unknown.

In order to clarify the mechanism of energy transfer to the Nd^{3+} ions in the Nd-doped $La_2S_3 \cdot 2Ga_2O_3$ glasses and to ascertain the causes of nonradiative relaxation of excited 4*f* electrons from upper states to the laser $^4F_{3/2}$ level, we conducted a combined study of the spectral distribution of photoluminescence (PL), excitation spectra of PL, and transmission spectra of these glasses.

2. RESULTS

The PL, excitation, and transmission spectra were measured with an automated and modified SDL setup. It includes two monochromators, MDR-12 (to study the excitation spectra) and MDR-23 (to study the emission spectra). A DKSL-120 lamp and an ILGI-503 laser were used as excitation sources. An FÉU-62 photomultiplier was used as a radiation detector. The output signal from the photomultiplier was recorded and processed with an IBM PC.

The PL spectra of the $La_2S_3 \cdot 2Ga_2O_3$ glasses (upon excitation in the range of the fundamental absorption

1063-7826/02/3611-1244$22.00

band) span the range of $\lambda \cong 0.5$–1.1 μm. They consist of three overlapping bands, of which the most intense band is peaked at $\lambda_m \cong 0.6$ μm (Fig. 1, curve *a*). Although the PL spectrum of the glass activated with neodymium, $(La_{0.97}Nd_{0.03})_2S_3 \cdot 2Ga_2O_3$, lies in the same spectral range, its structure is more complex in that it additionally exhibits two well-known emission bands of the Nd^{3+} ions; these bands are peaked at $\lambda_{m1} \cong 0.91$ μm and $\lambda_{m2} \cong 1.07$ μm (Fig. 1, curve *b*).

Unlike the $La_2S_3 \cdot 2Ga_2O_3$ glasses, the transmission spectra of the neodymium-doped samples are more complex (compare curves *b*, *c*, and *d* in Fig. 2), readily exhibiting known absorption bands of the Nd^{3+} ions [1, 7, 11].

Upon the excitation of the $(La_{0.97}Nd_{0.03})_2S_3 \cdot 2Ga_2O_3$ glass with monochromatic light from the spectral range corresponding to the absorption bands of the Nd^{3+} ions (compare spectra *a*, *d*, and *c* in Fig. 2), the PL spectrum contains only two emission bands, λ_{m1} and λ_{m2} (Fig. 1, inset *c*).

A comparison of these excitation, PL, and transmission spectra makes it possible to infer that (i) the mechanism of excitation and emission of the λ_{m1} and λ_{m2} bands due to the Nd^{3+} ions is of the intracenter type and (ii) the PL spectrum of the $(La_{0.97}Nd_{0.03})_2S_3 \cdot 2Ga_2O_3$ glass excited with light within the band of fundamental absorption is modulated by the absorption bands of the Nd^{3+} ions. However, in contrast to the single-crystal host [1, 7], the transmission, excitation, and emission bands of the Nd^{3+} ions in this glass are somewhat diffuse and do not exhibit a fine structure. We also note here that, on going from $T = 77$ K to $T = 295$ K, a partial quenching of the matrix PL is observed along with a corresponding decrease in the intensity of the emission bands of neodymium at $\lambda_{m1} \cong 0.91$ and $\lambda_{m2} \cong 1.07$ μm; this is accompanied by an increase in the half width of the PL bands and further broadening of the absorption bands.

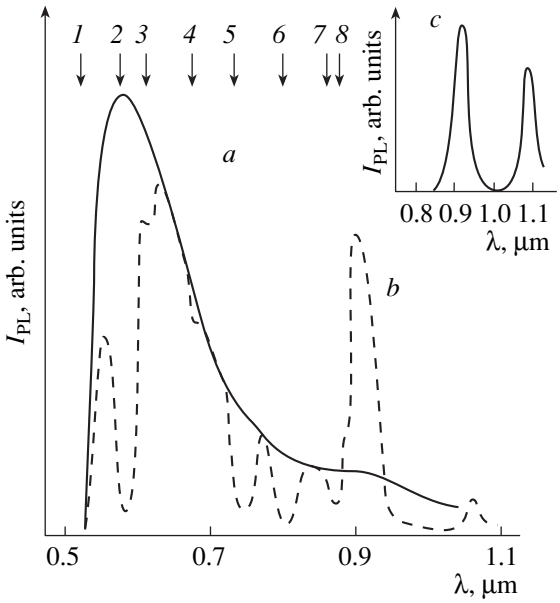

Fig. 1. (*1*) Luminescence spectra of glasses at $T = 77$ K upon band-to-band excitation: (*a*) $La_2S_3 \cdot 2Ga_2O_3$ and (*b*) $(La_{0.97}Nd_{0.03})_2S_3 \cdot 2Ga_2O_3$. The arrows and numbers *1–8* show the positions of the intracenter absorption bands of the Nd^{3+} ions. (*c*) Luminescence spectrum of the $(La_{0.97}Nd_{0.03})_2S_3 \cdot 2Ga_2O_3$ glass at $T = 295$ K and $\lambda_{ex} \cong 0.59$ μm.

3. DISCUSSION

Published data [8] show that there are three channels in γ-La_2S_3 single crystals for energy transfer from the host to the Nd^{3+} ions. The first of these is the radiative channel resulting from a partial overlap of the γ-La_2S_3 luminescence bands, which are associated with the interimpurity channel of carrier recombination, and the absorption bands of the Nd^{3+} ions. The second, nonradiative channel arises from the transfer of energy of the electrons captured by the trapping centers to the neodymium ions. The third channel is related to the recombination due to the capture of free electrons by the Nd^{3+} ions. It is believed that a very low quantum yield of the radiation of the Nd^{3+} ions in the single crystals results from the inefficient radiative-energy transfer to these ions.

Our data, along with the results obtained in [8], for the γ-La_2S_3:Nd^{3+} single crystals show that some of the most intense absorption bands of the neodymium ions (the transitions $^4I_{3/2} \longrightarrow {}^4G_{5/2}$, $^4H_{11/2}$, and $^4F_{9/2}$) overlap only with the edge of the PL band from the host crystal. The luminescence intensity of the crystal in this spectral range ($\lambda \cong 0.59$–0.69 μm) is minimal. At the same time, the PL peak of the host on the basis of the $La_2S_3 \cdot 2Ga_2O_3$ glass lies in this spectral range (Fig. 1, curve *a*), and, as the calculations show, the relative value of energy reabsorbed by the Nd^{3+} ions may amount to 60–70% of the total energy emitted by the host regardless of the measurement temperature of PL. We believe that it is the difference between the PL spectra of the single-crystal and glass hosts that leads to more efficient radiative-energy transfer in the $(La_{0.97}Nd_{0.03})_2S_3 \cdot 2Ga_2O_3$ glass. Moreover, we may state that, among three possible channels, the radiative-energy transfer from the glass host to the neodymium ions is the main channel, since at room temperature the capture of free carriers by trapping centers virtually does not take place and the energy transfer via the trapping centers can thus be ruled out. The recombination mechanism of energy transfer is also unlikely by virtue of the electronic structure of the Nd^{3+} ions.

As was shown in [13], the "orange" band of PL ($\lambda_m \cong 0.6$ μm) in the $La_2S_3 \cdot 2Ga_2O_3$ glass occurs due to oxygen that gives rise to centers with a level at $E_c - 2.0$ eV. Most likely, these centers act as efficient sensitizers for the Nd^{3+} ion in the $(La_{0.97}Nd_{0.03})_2S_3 \cdot 2Ga_2O_3$ glass. Therefore, in order to increase the coefficient of radiative energy transfer in the single-crystal host

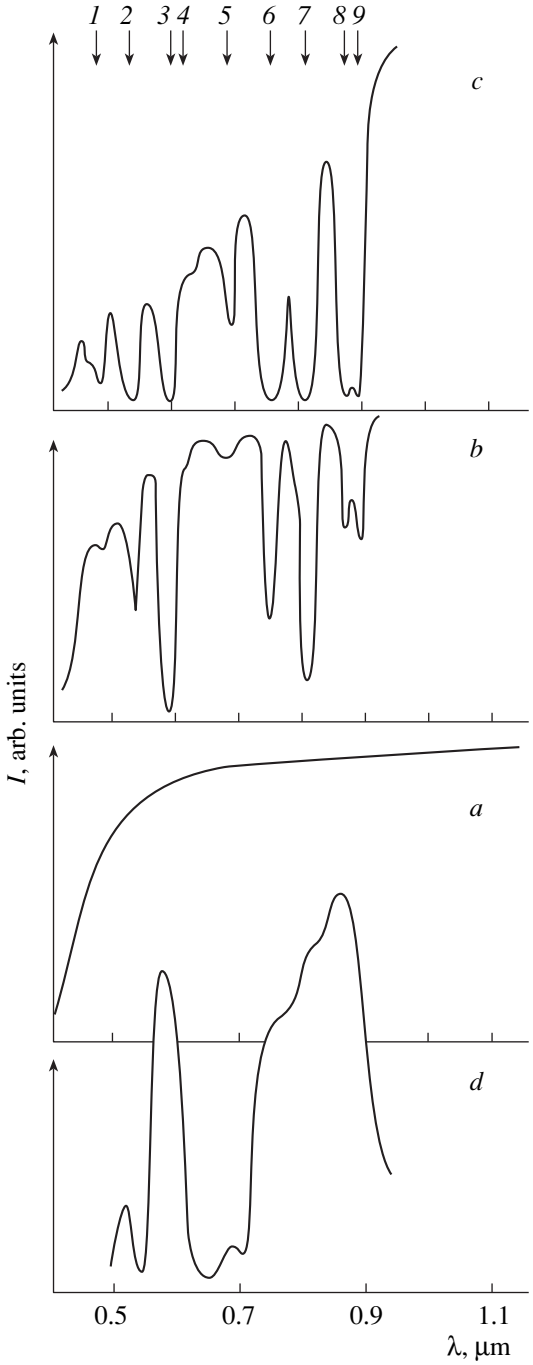

Fig. 2. Transmission spectra of glasses: (*a*) $La_2S_3 \cdot 2Ga_2O_3$, (*b*) $(La_{0.97}Nd_{0.03})_2S_3 \cdot 2Ga_2O_3$, and (*c*) $Nd_2S_3 \cdot 2Ga_2O_3$; (*d*) excitation spectrum of photoluminescence with $\lambda_{m1} \cong 0.91$ μm.

γ-La_2S_3, it is sufficient to dope this matrix with oxygen. This conclusion is supported by experimental data on La_2O_2S and $La_2O_{2-x}S_{1+x}$ single crystals [2, 3], which also exhibit an orange luminescence band with the coefficient of the radiative energy transfer from the host to the Nd^{3+} ions being larger than that in the γ-La_2S_3 single crystals.

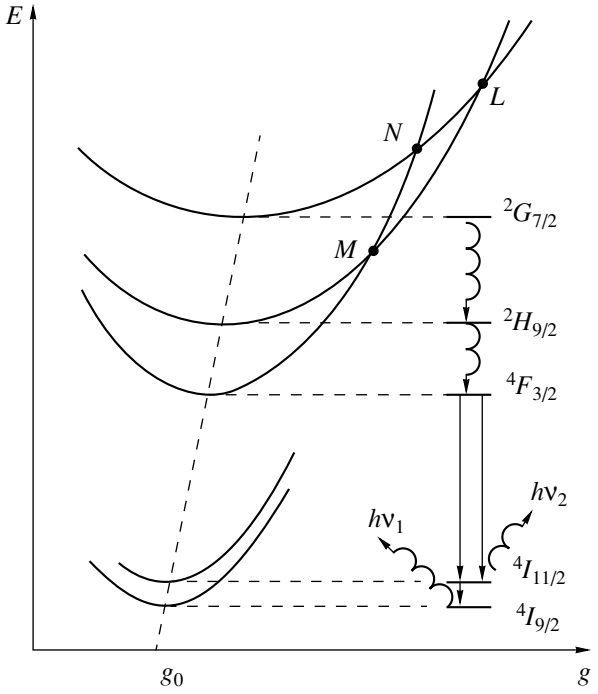

Fig. 3. Model of potential-energy curves for the 4*f*-electronic states of the Nd^{3+} ions in the $La_2S_3 \cdot 2Ga_2O_3$ host.

However, doping the γ-La_2S_3 crystals with oxygen as the sensitizing agent cannot eliminate such a drawback of this host (in comparison with other laser materials) as the low rate of intracenter relaxation of electrons to the laser $^4F_{3/2}$ level of the Nd^{3+} ion. According to the data [8], this can be related to the short range of the phonon spectrum of the γ-La_2S_3 crystals. At the same time, the PL spectra of the Nd-doped glasses exhibit only two emission bands of neodymium (transitions $^4F_{3/2} \longrightarrow {}^4I_{9/2}$ and $^4F_{3/2} \longrightarrow {}^4I_{11/2}$) regardless of whether the Nd^{3+} ions were excited with light in the range of the fundamental absorption band of the host matrix or in the range of the absorption band of the activator itself (Fig. 1, curves *b*, *c*). Therefore, the rate of the intracenter relaxation of the 4*f* electrons in the glass host exceeds that in the crystal host by two to three orders of magnitude. This is most likely related to the fact that, in the $La_2S_3 \cdot 2Ga_2O_3$ glasses, the Nd^{3+} ions reside in nonuniform local fields that differ in both their symmetry and strength due to the structural disorder of the matrix. The anisotropy of the internal crystal field in the glasses should increase the variance in the magnitude of splitting of the multiplet levels from the 4*f*-electronic states in comparison with that in the single crystals. This, in turn, makes it impossible to resolve the fine structure in the absorption spectra. The results of our study of the spectra of transmission, PL excitation, and PL for the Nd^{3+} emission bands $\lambda_{m1} \cong 0.91$ μm and $\lambda_{m2} \cong 1.07$ μm (Figs. 1, 2) confirm these assumptions.

In the context of the model of potential-energy curves [14], the potential energy curves of upper excited 4*f*-electron states of Nd^{3+} ions become progressively flatter and their minima shift due to the low symmetry of the crystal fields around these ions in the $(La_{0.97}Nd_{0.03})_2S_3 \cdot 2Ga_2O_3$ glass. As a result, the potential energy curves intersect each other (Fig. 3) and the electrons occupying the upper excited levels can have the same amount of energy as at the $^4F_{3/2}$ level. Such a situation is one in which the electrons may undergo a rapid nonradiative transition from the upper excited states to the lasing $^4F_{3/2}$ level and then radiatively to the $^4I_{9/2}$ and $^4I_{11/2}$ levels.

This model has made it possible to explain why, on increasing the glass temperature (from 295 to 600 K [10]), the emission bands of the Nd^{3+} ions are observed for the transitions not only from the $^4F_{3/2}$ level but also from neighboring excited states. The energy pattern considered (Fig. 3) provides both the rapid nonradiative relaxation of the electrons to the laser level and the much easier repopulation of the upper levels with increasing temperature.

4. CONCLUSION

We studied the spectra of PL, excitation of luminescence, and the optical transmission of the $La_2S_3 \cdot 2Ga_2O_3$ and $(La_{0.97}Nd_{0.03})_2S_3 \cdot 2Ga_2O_3$ glasses and ascertained that the transfer of radiative energy from the glass host to the Nd^{3+} ions is the main energy-transfer channel in these compounds. We showed that oxygen, with an energy level $E_c - 2.0$ eV, acts as a sensitizing agent.

The structural disordering of the glass matrix increases the variance in the magnitude of splitting of the multiplet levels from the 4*f* electronic states of the Nd^{3+} ion. This is conducive to the acceleration of nonradiative relaxation of the electrons from excited states to the lasing $^4F_{3/2}$ level.

The $(La_{0.97}Nd_{0.03})_2S_3 \cdot 2Ga_2O_3$ glass can be considered as a promising laser material for obtaining the stimulated emission of radiation of Nd^{3+} ions under an optical pump in the range of the fundamental absorption band of the glass.

Based on the results of studying the PL in $La_2(S_{0.5}Se_{0.5})_3 \cdot 2Ga_2O_3$ and $La_2(S_{0.7}Se_{0.3})_3 \cdot 2Ga_2O_3$ glasses [15], we may assume that, when doped with Nd^{3+} ions, these glasses can also be considered as promising laser materials. This assumption is based on the following:

(1) The highest intensity of the PL of glasses with a varying chalcogen composition lies in the range of $\lambda \cong 0.7$–0.9 μm (red and IR emission bands).

(2) The Nd^{3+} ions have a number of intracenter absorption bands in this range (transitions $^4I_{9/2} \longrightarrow {}^4F_{9/2}$, $^4F_{7/2}$, $^4F_{5/2}$; $^4I_{11/2} \longrightarrow {}^4F_{5/2}$) and, thus, can reabsorb the energy of photons emitted by the glass host upon its excitation by quanta with energies $h\nu \geq E_g$.

ACKNOWLEDGMENTS

This study was supported by the Russian Foundation for Basic Research (project no. 00-05-72031) and by the special Federal Program "Integration", subprogram 3.2 (project no. 96 (2001)).

REFERENCES

1. G. B. Pukinskas and G. A. Babonas, Litov. Fiz. Sb. **25** (4), 75 (1985).
2. A. N. Georgobiani, V. I. Demin, and E. S. Logozinskaya, Tr. Fiz. Inst. Akad. Nauk SSSR **182**, 69 (1987).
3. N. M. Ponomarev and Zh. A. Pukhliĭ, in *Physics and Chemistry of Rare-Earth Semiconductors* (Nauka, Novosibirsk, 1990).
4. D. G. Gzirishvili, L. N. Glurzhidze, T. N. Imuridze, and G. V. Kasradze, in *Proceedings of the V All-Union Conference on the Physics and Chemistry of Rare-Earth Semiconductors, Saratov, 1990*, Part 1.
5. M. V. Glushkov, A. A. Mamedov, A. M. Prokhorov, *et al.*, Pis'ma Zh. Éksp. Teor. Fiz. **31** (2), 114 (1980) [JETP Lett. **31**, 104 (1980)].
6. V. P. Zhuze and A. I. Shchelykh, Fiz. Tekh. Poluprovodn. (Leningrad) **23** (3), 393 (1989) [Sov. Phys. Semicond. **23**, 245 (1989)].
7. A. A. Kaminskiĭ, S. É. Sarkisov, Chan Ngok, *et al.*, Izv. Akad. Nauk SSSR, Neorg. Mater. **16** (8), 1333 (1980).
8. A. A. Kamarzin, A. A. Mamedov, V. A. Smirnov, *et al.*, Kvantovaya Élektron. (Moscow) **10** (3), 569 (1983).
9. A. A. Kamarzin, A. A. Mamedov, V. A. Smirnov, *et al.*, Fiz. Tverd. Tela (Leningrad) **25** (6), 1664 (1983) [Sov. Phys. Solid State **25**, 959 (1983)].
10. A. A. Kamarzin, A. A. Mamedov, V. A. Smirnov, *et al.*, Kvantovaya Élektron. (Moscow) **10** (8), 1560 (1983).
11. K. R. Allakhverdiev, A. A. Kamarzin, A. A. Mamedov, *et al.*, in *Proceedings of the IV All-Union Conference on the Physics and Chemistry of Rare-Earth Semiconductors, Novosibirsk, 1987*.
12. U. F. Kustov, G. A. Bondurkin, É. R. Murav'ev, and V. P. Orlovskiĭ, *Electron Spectra of Compounds of Rare-Earth Elements* (Nauka, Moscow, 1981).
13. E. M. Zobov, V. V. Sokolov, A. Kh. Sharapudinova, and S. M. Luguev, Fiz. Tverd. Tela (St. Petersburg) **35** (3), 636 (1993) [Phys. Solid State **35**, 325 (1993)].
14. A. M. Gurvich, *Introduction to the Physical Chemistry of Phosphor Crystals* (Vysshaya Shkola, Moscow, 1971).
15. E. M. Zobov, A. A. Babaev, A. Kh. Sharapudinova, and V. V. Sokolov, Izv. Akad. Nauk, Neorg. Mater. **34** (5), 632 (1998).

Translated by V. Rogovoĭ

Semiconductors, Vol. 36, No. 11, 2002, pp. 1248–1251. Translated from Fizika i Tekhnika Poluprovodnikov, Vol. 36, No. 11, 2002, pp. 1332–1336.

DEDICATED TO THE MEMORY OF V. F. MASTEROV

Conductivity and Structure of Er-Doped Amorphous Hydrogenated Silicon Films

O. I. Kon'kov, E. I. Terukov, and L. S. Granitsina

Ioffe Physicotechnical Institute, Russian Academy of Sciences, Politekhnicheskaya ul. 26, St. Petersburg, 194021 Russia

Submitted April 2, 2002; accepted for publication April 25, 2002

Abstract—A columnar structure of *a*-Si:H(Er) film serving as a working layer in electroluminescent structures has been demonstrated. The diameter of columns is in the range of 60–100 Å. In a structure of this kind, the conductivity depends on the direction of current. In the planar configuration, room-temperature transport occurs through hopping via localized states near the conduction band edge, within the band tail. In the sandwich configuration, the conduction occurs along the column boundaries, where the conductivity is higher, via hopping conduction at the Fermi level. © *2002 MAIK "Nauka/Interperiodica".*

1. INTRODUCTION

In recent years, considerable efforts have been concentrated on the obtaining and study of Er-doped amorphous hydrogenated silicon, *a*-Si:H(Er). This attention is due to the prospect of applying this material in waveguide optics and telecommunications. In this context, prime attention is given to studies of the luminescent properties of amorphous silicon at the wavelength of 1.54 μm. Nevertheless, while research and publications devoted to the photoluminescent properties of *a*-Si:H(Er) are considerable (see, e.g., [1–4]), the same cannot be said of electroluminescence (EL) in *a*-Si:H(Er) structures. Though EL has been observed [5, 6], its efficiency is absolutely insufficient for practical applications. Progress in this field is hindered by the fact that the electrical properties have been poorly investigated. The problems of the EL mechanism in this system, current transport, and contact effects have not been satisfactorily resolved; moreover, band diagrams have not been constructed, and so on.

The goal of the present study is the resolution of one of these problems. We report the results of investigating the electrical characteristics of magnetron *a*-Si:H(Er) films; i.e., the conductivity and its temperature dependence, including those for the EL structure configuration.

2. EXPERIMENTAL

a-Si:H(Er) films were produced via magnetron sputtering of metallic Er in a silane-containing atmosphere (MASD) [7]. In the present study, the technological parameters were the following: an initial gas mixture of 12.5% SiH_4 + 37.5% H_2 + 50% Ar, a magnetic field strength of 80 mT, an anode voltage of 600 V, a discharge power density of 0.2 W cm^{-2}, and a total pressure of the gas mixture of 4×10^{-3} Torr. Doping with erbium was done using a metallic Er foil of 99.99 purity. Films of 0.3–0.6 μm thickness were deposited onto crystalline *n*-Si substrates for the fabrication of Al/n^+-*a*-Si:H/*a*-Si:H(Er)/n^+-*a*-Si:H/Al structures for studying the sandwich configuration, and onto polished quartz for conductivity studies on the planar Al/*a*-Si:H(Er)/Al configuration. A heavily doped n^+-*a*-Si:H layer was produced via magnetron decomposition of a silane–phosphine mixture. Aluminum contacts were fabricated using thermal evaporation. In the sandwich configuration, the conductivity was measured in the ohmic portion of the current–voltage characteristic, with an applied voltage of 100 mV. In the planar configuration, the conductivity was measured with a fixed voltage of 10 V. The erbium content in the films was determined from Rutherford backscattering spectra to be 6×10^{20}–1.3×10^{21} cm^{-3}. The erbium concentration profile across the film thickness was nearly uniform within these limits. The band gap defined by optical methods was 1.7–1.8 eV.

3. RESULTS AND DISCUSSION

3.1. Planar Configuration

Figure 1 presents the temperature dependence of the dark conductivity typical of the samples under study. At temperatures above T_c = 85°C, the activation energy of conductivity is 0.66 eV, for lower temperatures it is ≈0.48 eV, with the scatter of values for different samples being no more than 0.04 eV. The conductivity at T_c is $\approx 8 \times 10^{-6}$ Ω^{-1} cm^{-1}.

This variation of the activation energy allows us to suggest that, in this configuration, at temperatures above T_c, carrier transport occurs via extended states above the mobility edge. Since *a*-Si:H(Er) is an *n*-type semiconductor [8], the conduction is defined by electron transport involving energy levels in the upper part

of the band gap, and in this case we can take the conduction band edge E_c as the mobility edge.

At temperatures below T_c, the transport occurs via hopping over localized states near the conduction band edge, within the band tail. So, the conduction mechanism changes at $T = T_c$.

Quite similar behavior of conductivity was described in [9] for Er-free low-quality amorphous silicon with a high density of localized states in the mobility gap produced by RF silane decomposition. Owing to the high level of Er doping, our material also contains a high density of these states, on the order of 10^{21} cm^{-3}. The density of localized states estimated by photothermal deflection [10] was on the order of 10^{19}–10^{20} eV^{-1} cm^{-3}.

In this case, the conductivity can be represented as

$$\sigma = \sigma_1 \exp[-(E_c - E_f)/kT] + \sigma_2 \exp[-(E_a - E_f + W)/kT],$$

where the first and second terms describe the conductivity via the extended states and within the conduction band tail, respectively; E_a is the characteristic energy corresponding to the end of the localized-state density tail of the conduction band; and W is the hopping energy. In this situation, the theory is insensitive to whether there exists a density-of-states tail ending at the energy E_a or a $2W$-wide peak of the density of localized states at the same energy [11]. Assuming W = 0.08 eV, which corresponds to the electron hopping energy in amorphous silicon with the density of localized states on the order of 10^{19} eV^{-1} cm^{-3} [12–14], and using the observed difference between the slopes before and after T_c, we obtain $E_c - E_a - W = 0.18$ eV and $E_c - E_a = 0.26$ eV. The latter value is the width of the localized-state region (tail) near the conduction band edge, or the distance between the conduction band edge and the peak of the density of localized states.

3.2. Sandwich Configuration

In this configuration, the conductivity differs drastically from the planar case. This is manifested by the conductivity temperature dependence with an activation energy of 0.06 eV (Fig. 1), with a scatter of about 0.01 eV for different samples. This energy is nearly independent of the direction of current through the structure. The most intriguing fact is that this energy is constant over the entire temperature range studied and does not change on passing through T_c. The room-temperature conductivity is $\approx 2 \times 10^{-5}$ Ω^{-1} cm^{-3}.

Since the activation energy is low and a bend of the characteristic, absent, we believe that, in this configuration, the conduction occurs via hopping near the Fermi level and that the activation energy for conductivity corresponds to the hopping energy. We have observed a similar value of the activation energy in the hopping conduction in amorphous silicon with the density of localized states at the Fermi level on the order of 10^{20} eV^{-1} cm^{-3} [14]. In the present study, no transition to variable-range hopping or $\sigma \propto T^{-1/4}$ behavior is observed.

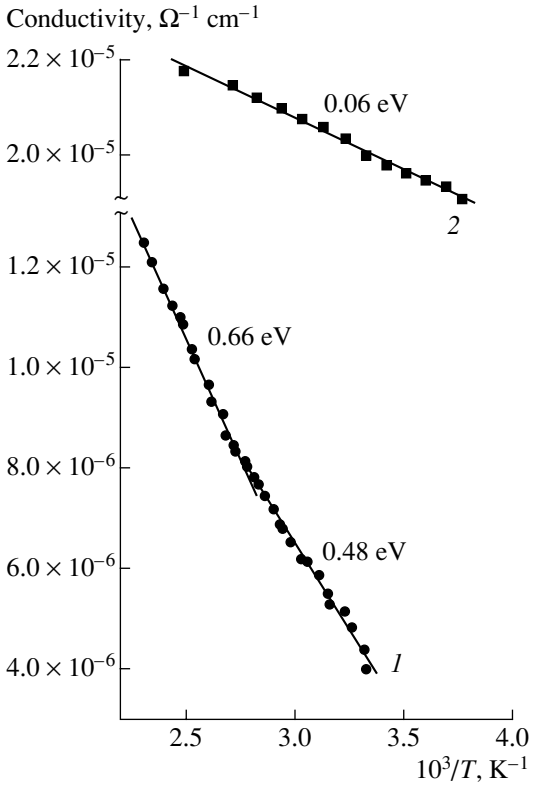

Fig. 1. Dark conductivity of *a*-Si:H(Er) films vs. the reciprocal temperature for (*1*) planar and (*2*) sandwich structures. Experimental points, approximating curves, and the activation energies are depicted.

3.3. Transmission Electron Microscopy

Figure 2 shows a TEM image of the *a*-Si:H(Er) film under study. Along with the general heterogeneity, a distinct structure is observed, which can be described as mosaic-like with the characteristic size of a mosaic element about 60–100 Å. A similar structure has been observed in *a*-Si:H produced through sputtering in hydrogen [15]. In particular, a relation has been revealed between the TEM-discernible microstructure with a characteristic size of 100 Å and the existence of structural heterogeneities in the form of columns visible in cross-sectional SEM images of the film. Moreover, the density fluctuations revealed by TEM are always associated with the columnar structure of a film [16, 17].

The fabrication technology and the TEM data of our study are similar to those in the above-cited reports, so we believe that our *a*-Si:H(Er) films have a columnar structure, with columns of 60–100 Å in diameter.

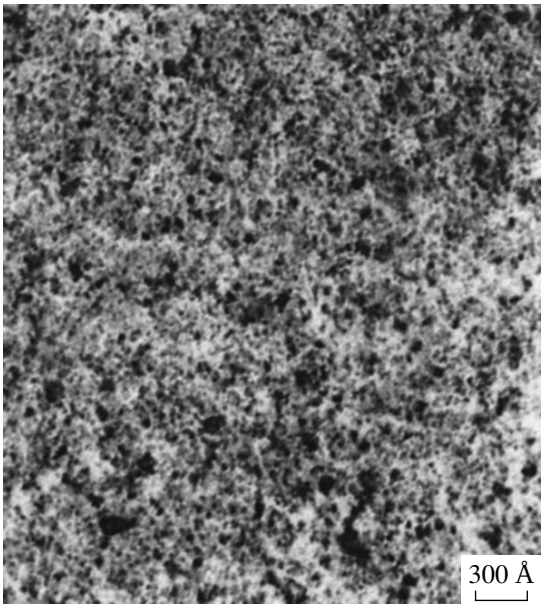

Fig. 2. TEM image of an *a*-Si:H(Er) film.

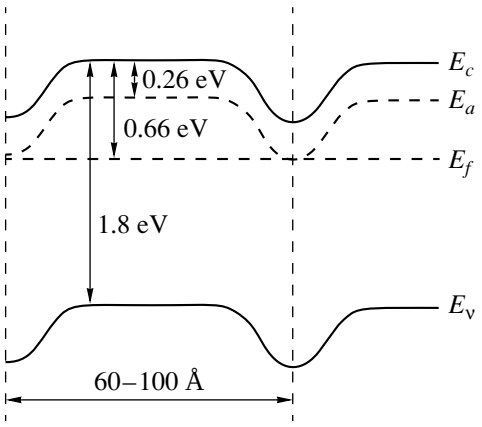

Fig. 3. Band diagram. A column core and an interface between the neighboring columns are shown.

3.4. Discussion

The difference between the conduction mechanisms along and across the film indicates structural heterogeneity. The heterogeneity can be parallel to the substrate, which gives a layered structure, or perpendicular, with a columnar structure. More complex combinations of these heterogeneities, such as, e.g., the interruption of columns, will not be discussed here. The combination of two established factors—(i) the ohmic conductivity indicating the absence of potential barriers and (ii) the higher conductivity in sandwich structures (2×10^{-5} Ω^{-1} cm^{-1} instead of $(4–5) \times 10^{-6}$ Ω^{-1} cm^{-1})—allows us to decide in favor of the columnar structure.

The TEM data allow us to reject the assumption that the film structure is a uniform matrix of a material with the same composition and properties with columnar insertions of a material with different composition and properties. This model might also explain the conductivity behavior. Nevertheless, TEM reveals only a structure of closely neighboring columns. No matrix is observed.

Therefore, we believe that the structure of the film under study is an array of closely neighboring columns, the characteristic diameter of which is in the range of 60–100 Å.

Figure 3 presents the relevant band diagram. One column and an interface between the neighboring columns are shown.

In planar configuration, the conductivity is defined by the depth of the Fermi level E_f at the center of a column, equal to 0.66 eV, and by the density-of-states peak at a distance of E_a 0.26 eV from the conduction-band edge. Both energies can be correlated with Er-associated levels since, first, the activation energy for conductivity is 0.8 eV in Er-free *a*-Si:H films produced by the same technique [18] and, second, Er-related centers with energies of 0.2–0.36 and 0.55–0.6 eV have been discovered both in crystalline [19, 20] and amorphous [21] silicon. This conduction mode is insensitive to column boundaries.

In the sandwich configuration, conduction occurs along the column boundaries, which have higher conductivity.

The increase in conductivity and the band bending shown in Fig. 3 can be explained as follows. During the growth of an *a*-Si:H(Er) film, Er segregates at the column boundaries. Though this effect has not yet been observed directly in amorphous silicon, it has been found in a heterogeneous *c*-Si/*a*-Si structure with Er [22]. The peak of the Er density is located in the bulk of amorphous silicon, at a distance of several nanometers from the *c*-Si/*a*-Si interface, with an abrupt drop deep in the *a*-Si bulk. Correspondingly, the region with a high Er density, which should be associated with the column boundary, is also on the order of several nanometers in size. A higher Er concentration produces an enhanced density of localized states, including those with an energy of 0.26 eV. This effect will be especially prominent near the column boundaries and can result in the pinning of the Fermi level at this energy at the column boundary.

Comparing the conductivity values for the column core and boundary, obtained from the relations for band-tail and hopping conductivity, respectively [23], we find that the conductivity at the column boundary exceeds the core conductivity at temperatures up to about 500 K. In the calculations, we assumed a wave function localization radius of 3 Å, hopping activation energies of 0.08 and 0.06 eV, and density of states of 10^{19} and 10^{20} eV^{-1} cm^{-3} for the column and column boundary, respectively. Thus, since the conductivity along column boundaries is higher and the dimensions of boundary regions are comparable with the remaining portion, the hopping conduction at column boundaries

dominates in sandwich samples in the studied temperature range.

To confirm this conclusion, we present conductivity data for real electroluminescent Al/*a*-Si:H(Er)/*c*-Si/Al structures with KÉF-5 (*n*-type, P-doped, 5 Ω cm resistivity), KDB-7.5 (*p*-type, B-doped, 7.5 Ω cm) or ÉKÉS-0.01 (epitaxial, *n*-type, Sb-doped, 0.01 Ω cm) wafers used as *c*-Si substrates. The measurements were done in the ohmic mode, with the voltage across the structure no more than 0.2 V. The measured activation energies for conductivity were 0.22, 0.24, and 0.09 eV, respectively. In these structures, current flows successively through the *a*-Si film and crystal substrate. In this situation, the activation energy must correspond to the higher of these energies for the film and substrate. Indeed, the obtained activation energies can be correlated with the values of 0.18, 0.22, and 0.01 eV for the above-listed crystal substrates, respectively; i.e., for high-resistivity substrate, it is the substrate that determines the conductivity and, for low-resistivity substrates, it is the *a*-Si film. Thus, the activation energy of conductivity in *a*-Si:H(Er) film is no more than 0.09 eV, which correlates with the value measured in Al/n^+-*a*-Si:H/*a*-Si:H(Er)/n^+-*a*-Si:H/Al and confirms our conclusions.

4. CONCLUSION

Our study has demonstrated that *a*-Si:H(Er) films produced by MASD and used as a working layer in EL structures have a columnar structure. The columns are 60–100 Å in diameter. The conductivity of this system depends on the direction of current. In planar configuration, the conductivity is defined by the Fermi level position in the core of a column, 0.66 eV deep, and by the density-of-states peak, 0.26 eV below the conduction-band edge. At temperatures above 85°C, carrier transport occurs via extended states above the mobility edge. At lower temperatures, transport is governed by hopping via localized states at the conduction band edge within the band tail, with capture at the level of 0.26 eV. In the sandwich configuration, the hopping conduction at the Fermi level occurs along column boundaries, where the conductivity is higher.

Conventional *a*-Si:H(Er) EL structures are fabricated in the sandwich configuration. Therefore, the analysis of mechanisms and methods of EL excitation should consider our data on the band structure, conduction mechanisms, and conductivities.

ACKNOWLEDGMENTS

We are grateful to A.A. Sitnikova, who performed the microscopic studies.

This study was supported by the Russian Foundation for Basic Research (project no. 01-02-17825); the technological part was supported by a private contributor.

REFERENCES

1. M. S. Bresler, O. B. Gusev, and V. Kh. Kudoyarova, Appl. Phys. Lett. **67**, 3599 (1995).
2. J. H. Shin, R. Serna, and G. N. van den Hoven, Appl. Phys. Lett. **68**, 997 (1996).
3. A. R. Zanatta, Z. A. Nunes, and L. R. Tessler, Appl. Phys. Lett. **70**, 511 (1997).
4. *Rare Earth Doped Semiconductors: Proceedings of E-MRC Spring Conference, Strasbourg, France, 2000.*
5. O. B. Gusev, A. N. Kuznetsov, E. I. Terukov, and M. S. Bresler, Appl. Phys. Lett. **70**, 240 (1997).
6. O. I. Kon'kov, A. N. Kuznetsov, P. E. Pak, *et al.*, Pis'ma Zh. Tekh. Fiz. **27** (13), 30 (2001) [Tech. Phys. Lett. **27**, 542 (2001)].
7. M. S. Bresler, O. B. Gusev, B. P. Zakharchenya, *et al.*, Fiz. Tverd. Tela (St. Petersburg) **38** (4), 1189 (1996) [Phys. Solid State **38**, 658 (1996)].
8. E. I. Terukov, O. I. Konkov, V. Kh. Kudoyarova, *et al.*, J. Non-Cryst. Solids **266–269**, 614 (2000).
9. P. G. Le Comber and W. E. Spear, Phys. Rev. Lett. **25**, 509 (1970).
10. V. Kh. Kudoyarova, A. N. Kuznetsov, E. I. Terukov, *et al.*, Fiz. Tekh. Poluprovodn. (St. Petersburg) **32** (11), 1384 (1998) [Semiconductors **32**, 1234 (1998)].
11. N. F. Mott and E. A. Davis, *Electronic Processes in Non-Crystalline Materials* (Clarendon, Oxford, 1971; Mir, Moscow, 1974).
12. P. G. Le Comber, A. Madan, and W. E. Spear, J. Non-Cryst. Solids **20**, 239 (1972).
13. A. A. Andreev, O. A. Golikova, M. M. Kazanin, *et al.*, Fiz. Tekh. Poluprovodn. (Leningrad) **15** (6), 1210 (1981) [Sov. Phys. Semicond. **15**, 697 (1981)].
14. A. A. Andreev, O. I. Kon'kov, N. A. Feoktistov, and T. Turgunov, Izv. Akad. Nauk UzSSR, Ser. Fiz.-Mat. Nauk **2**, 87 (1985).
15. R. Messier and R. C. Ross, J. Appl. Phys. **53**, 6220 (1982).
16. J. C. Knight and R. A. Lujan, Appl. Phys. Lett. **35**, 244 (1979).
17. R. C. Ross and R. Messier, J. Appl. Phys. **52**, 5329 (1981).
18. O. I. Kon'kov, E. I. Terukov, and L. S. Granitsina, Fiz. Tekh. Poluprovodn. (St. Petersburg) **35** (10), 1250 (2001) [Semiconductors **35**, 1197 (2001)].
19. R. A. Gresswell and M. M. Perlmann, J. Appl. Phys. **41**, 2365 (1970).
20. S. Libertino, S. Coffa, G. Franzo, and F. Priolo, J. Appl. Phys. **78**, 3867 (1995).
21. V. S. Lysenko, I. P. Tyagul'skiĭ, I. N. Osiyuk, *et al.*, Fiz. Tekh. Poluprovodn. (St. Petersburg) **35** (6), 649 (2001) [Semiconductors **35**, 621 (2001)].
22. J. S. Custer, A. Polman, and H. M. van Pinxteren, J. Appl. Phys. **75**, 2809 (1994).
23. A. Madan and M. Shaw, *The Physics and Applications of Amorphous Semiconductors* (Academic, Boston, 1988; Mir, Moscow, 1991).

Translated by D. Mashovets

Semiconductors, Vol. 36, No. 11, 2002, pp. 1252–1259. Translated from Fizika i Tekhnika Poluprovodnikov, Vol. 36, No. 11, 2002, pp. 1337–1344.

DEDICATED TO THE MEMORY OF V. F. MASTEROV

Nature of Impurity Centers of Rare-Earth Metals and Self-Organization Processes in *a*-Si:H Films

M. M. Mezdrogina*, I. N. Trapeznikova*, E. I. Terukov*, F. S. Nasredinov, N. P. Seregin**, and P. P. Seregin****

** Ioffe Physicotechnical Institute, Russian Academy of Sciences, Politekhnicheskaya ul. 26, St.Petersburg, 194021 Russia*

e-mail: trapez@mail.ioffe.ru

*** St.Petersburg State Technical University, Politekhnicheskaya ul. 29, St.Petersburg, 195251 Russia*

Submitted April 2, 2002; accepted for publication April 11, 2002

Abstract—The existence of self-organization processes in *a*-Si:H:Er films and the appearance of an ordered structure of [Er–O] crystallites in the unordered structural network of *a*-Si:H:Er were ascertained. The principal parameter of the self-organization process was shown to be the control parameter, which is the [Er–O]-complex content in the *a*-Si:H:Er films. A decrease in the sizes of crystallites and an increase in the particle density leads to an increase in the photoluminescence intensity for $\lambda = 1.54$ μm, i.e., to an increase in the optical activation of Er ions in the *a*-Si:H:Er films. *© 2002 MAIK "Nauka/Interperiodica".*

1. INTRODUCTION

The problem of electric inactivity of impurity atoms in amorphous hydrogenated silicon *a*-Si:H can be solved only under the condition of combined investigations of the state of impurity atoms when the methods [1] enabling one to identify the charge state of impurity atoms and the nature of their local surrounding are used in addition to conventional methods of the physics of semiconductors. In particular, such a method is Mössbauer spectroscopy, and the most promising object for Mössbauer investigations are rare-earth metals (REM), many of which have Mössbauer isotopes.

However, in spite of the evident importance and necessity of such investigations, they are virtually lacking in the literature. This fact is explained by experimental difficulties: as a rule, *a*-Si:H is doped from the gaseous phase, whereas REMs have virtually no gaseous compounds, and this impedes the preparation of the material required for investigations.

From the aforesaid, we developed and implemented a technology for depositing *a*-Si:H (nominally undoped and REM-doped) using high-frequency sputtering of a single-crystal silicon target and a target from the corresponding metal in a gaseous mixture of hydrogen, argon, and silane [2]. In this study, we report our results from investigating the influence of REM impurities on the properties of *a*-Si:H obtained by these methods.

2. EXPERIMENTAL

The doping of *a*-Si:H films with rare-earth metals is possible only through high-frequency sputtering of a mosaic target (silicon and REMs) in an argon–hydrogen atmosphere. However, the films obtained by this method do not have the parameters necessary for producing electron devices. In this study, REM-doped *a*-Si:H films were deposited using high-frequency sputtering of a mosaic target in a gaseous mixture containing argon, hydrogen, and silane. The substrate temperature T_s was equal to either 280 or 380°C. The chosen temperature range is due to the fact that the *a*-Si:H films fail to satisfy the requirements for device-grade films at a substrate temperature lower than 280°C, while, above 380°C, partial crystallization of the films sets in.

As dopants, we used the following REMs: Nd, Sm, Gd, Tb, Ho, Er, Dy, and Yb. The purity of dopants amounted to 99.999%. The impurity content was determined with allowance made for the sputtering yield and REM area on the mosaic target.

We measured the following parameters of the obtained films: the temperature dependence of dark conductivity, the photoconductivity for illumination with a flux of 3×10^{13} photon/(cm^2 s), the spectral dependence of photoconductivity, the optical energy gap, and the thermoelectric power at various temperatures. The charge state of impurities was determined from Mössbauer spectroscopy using ^{149}Sm, ^{151}Eu, and ^{161}Dy isotopes. In order to estimate the hydrogen concentration in the *a*-Si:H films and identify the type of hydrogen–silicon bonds, we used infrared spectroscopy.

3. RESULTS

In all the investigated films, the metal-impurity content amounted to (0.10 ± 0.01) at. %. The total hydro-

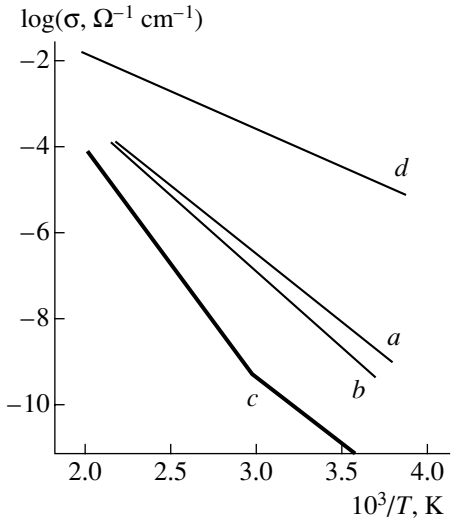

Fig. 1. Temperature dependences of conductivity σ for the films: (*a*) *a*-Si:H, (*b*) *a*-Si:H:Dy, (*c*) *a*-Si:H:Ho, and (*d*) *a*-Si:H:Eu. All the films were deposited at T_s = 380°C.

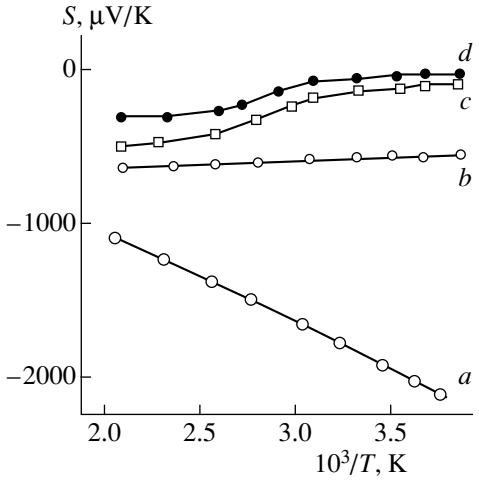

Fig. 2. Temperature dependences of thermoelectric power *S* for the films of (*a*) *a*-Si:H, (*b*) *a*-Si:H:Tb, (*c*) *a*-Si:H:Er, and (*d*) *a*-Si:H:Ho. All the films were deposited at T_s = 380°C.

gen content is unaffected by introducing an REM impurity; in all the films, it amounted to (15 ± 2) at. %. However, in this case, the ratio SiH_2/SiH between the components somewhat changes because the introduction of an REM impurity leads to an insignificant decrease in the SiH content in the films.

3.1. Optical Gap

The optical gap for a nominally undoped *a*-Si:H (substrate temperatures were T_s = 380 and 280°C) at 295 K amounted to E_g = (1.70 ± 0.02) eV. The rare-earth-metal doping of *a*-Si:H films (T_s = 380 and 280°C) was not accompanied by varying E_g; however, additional absorption was observed for the doped films in the long-wavelength region. This phenomenon is not anomalous and, as a rule, inherent for doped *a*-Si:H. It is assumed to be associated with the appearance of additional defects in the *a*-Si:H structure.

3.2. Temperature Dependence of Dark Conductivity

For a nominally undoped *a*-Si:H (T_s = 380°C), the dependence $\ln\sigma = f(1/T)$ is linear in the temperature range of 250–500 K (Fig. 1) with an activation energy E_0 = (0.58 ± 0.02) eV. The rare-earth-metal (except for europium) doping of *a*-Si:H films maintains the linear character of the dependence $\ln\sigma = f(1/T)$; however, the activation energy increases, while the electrical conductivity decreases at room temperature (Fig. 1 and Table 1). For the Nd and Ho impurities, we observed a kink in the dependence $\ln\sigma = f(1/T)$ in the low-temperature region and a transition to the conductivity with a lower activation energy (Fig. 1 and Table 1). Contrary to other REMs, the europium impurity (at T_s = 380°C) leads to an abrupt increase in conductivity and a decrease in E_0 (Fig. 1 and Table 1).

The conductivity of *a*-Si:H films obtained at T_s = 280°C proves to be virtually insensitive to doping (Table 1); i.e., all the REM impurities appear to be electrically inactive.

3.3. Temperature Dependence of Thermoelectric Power

The nominally undoped *a*-Si:H films (T_s = 380°C) have electron conductivity—the thermoelectric power *S* is negative in the temperature range of 250–560 K. The temperature dependence $S = f(1/T)$ is linear (Fig. 2) with an activation energy E_S = (0.58 ± 0.02) eV. The REM-impurity doping of the *a*-Si:H films (T_s = 380°C) is accompanied by a drop in the magnitude of *S* (Table 1); all the REMs can be divided into four groups according to their influence on the thermoelectric power.

(i) Tb, Dy, and Yb leave the sign of *S* unchanged in the temperature range of 250–560 K, and the magnitude of *S* decreases with increasing temperature, with the dependence $S = f(1/T)$ remaining linear (Fig. 2).

(ii) Sm, Er, and Gd decrease the magnitude of *S* to such an extent that we failed to determine its sign at room temperature, but this sign becomes negative at $T > 350$ K (Table 1) and the dependence $S = (1/T)$ ceases to be linear (Fig. 2).

(iii) Nd and Ho lead to the positive sign of *S* at room temperature, but the sign of *S* is inverted at higher temperatures (Table 1), while the dependence $S = f(1/T)$ is nonlinear (Fig. 2).

(iv) Eu reduces the magnitude of *S*, although its sign remains negative. The magnitude of *S* increases with

Table 1. Parameters of electrical conductivity of *a*-Si:H films

Impurity	T_s, °C	E_0, eV	σ_0, Ω^{-1} cm^{-1}	S (295 K) μV/K	S (500 K) μV/K	σ_{ph} (295 K) Ω^{-1} cm^{-1} μW
***	380	0.58	5.3×10^2	–1950	–1100	2×10^{-8}
Nd	380	1.02	2.5×10^6	+50	–300	4×10^{-10}
	380	0.7*	–	–	–	–
Sm	380	0.97	2.8×10^6	0	–500	4×10^{-9}
Eu	380	0.25	22	–400	–750	10^{-6}
Gd	380	0.89	46	0	–480	5×10^{-9}
Tb	380	0.80	3.4×10^5	–350	–600	2×10^{-9}
Dy	380	0.73	2.4×10^4	–400	–600	7×10^{-7}
Ho	380	1.01	10^6	+50	–300	7×10^{-10}
	380	0.7*	–	–	–	–
Er	380	0.91	1.6×10^6	0	–520	5×10^{-9}
Yb	380	0.70	6.5×10^4	–375	–580	2×10^{-7}
***	280	0.70	2×10^{-10}**	–	–	–
Sm	280	0.69	1.8×10^{-10}**	–	–	–
Eu	280	0.70	1.8×10^{-10}**	–	–	–
Dy	280	0.71	1.9×10^{-10}**	–	–	–
Errors	–	±0.02	–	10	10	–

* Temperature region below 300 K. ** Conductivity at 295 K. *** *a*-Si:H.

temperature (Table 1), with the dependence $S = f(1/T)$ being linear with an activation energy E_S = (0.23 ± 0.02) eV.

3.4. Spectral Dependence of Photoconductivity

The spectral dependences of photoconductivity σ_{ph} are shown in Fig. 3a for nominally undoped *a*-Si:H (T_s = 380°C) at 220, 295, and 325 K. At room temperature, the photoconductivity peak corresponds to a wavelength λ_{max} = 0.59 μm of the incident light. With decreasing temperature, the photoconductivity peak shifts to the shorter wavelengths (at 220 K, λ_{max} = 0.56 μm).

The REM-impurity atoms can be divided into two groups according to their influence on the photoconductivity of *a*-Si:H obtained at T_s = 380°C (Table 1).

(i) The Eu, Dy, and Yb impurities stimulate photoconductivity, the effect of europium being the most profound; as can be seen from Fig. 3, the photoconductivity of such films increases by more than two orders of magnitude in comparison with that of the *a*-Si:H-films. Simultaneously, the photoconductivity peak shifts to longer wavelengths (Fig. 3b). The temperature dependence of σ_{ph} for such films is similar to that for the *a*-Si:H films (Fig. 3).

(ii) The Nd, Sm, Gd, Tb, Ho, and Er impurities suppress *a*-Si:H photoconductivity (Table 1). This effect is most characteristic for the Nd and Ho impurity atoms.

3.5. Mössbauer Studies

The Mössbauer spectra of the ^{149}Sm, ^{151}Eu, and ^{161}Dy impurity atoms in the *a*-Si:H films were measured at 295 K with the $^{149}Eu_2O_3$, $^{151}Sm_2O_3$, and Gd_2O_3 (^{161}Tb) sources, respectively. The samples were prepared using metal targets enriched up to 90% with the corresponding isotopes.

The Mössbauer spectrum of ^{151}Eu for the *a*-Si:H:Eu film obtained at T_s = 380°C represents a superposition of lines corresponding to Eu^{2+} (a more intense line) and Eu^{3+} (a less intense line) (Fig. 4b). For the *a*-Si:H:Eu film obtained at T_s = 280°C, the spectrum corresponds only to the Eu^{2+} centers (Fig. 4a). The Mössbauer spectra of ^{149}Sm and ^{161}Dy for the *a*-Si:H films doped with the corresponding impurities at T_s = 380 and 280°C can be assigned to the Sm^{3+} and Dy^{3+} centers.

4. DISCUSSION

4.1. Nominally Undoped a-Si:H

The temperature dependences of conductivity $\ln\sigma = f(1/T)$ and thermoelectric power $S = f(1/T)$ are linear in the temperature range of 250–500 K, and the activation energies E_0 and E_S coincide. Consequently, in the temperature range of 250–500 K, the conduction of the *a*-Si(H) films deposited via the high-frequency sputtering of a silicon target in the gaseous mixture of argon, hydrogen, and silane is effected by carriers over the delocalized states in one of the allowed bands. The negative sign of S suggests that the conduction is effected

by electrons excited from the Fermi level to delocalized states of the conduction band, with the Fermi level lying 0.58 eV below the mobility threshold E_c of the conduction band.

4.2. Eu-Doped a-Si:H Films

The efficient Eu-doping of *a*-Si:H is attained only at a substrate temperature T_s = 380°C, whereas, at T_s = 280°C, all the europium impurity atoms prove to be electrically inactive.

For the *a*-Si:H:Eu samples prepared at T_s = 380°C, the temperature dependences $\ln\sigma = f(1/T)$ and $S = f(1/T)$ for the conductivity and the thermoelectric power, respectively, remain linear, while the activation energies E_0 and E_S coincide. Consequently, in the temperature range of 250–500 K, the conduction of *a*-Si(H):Eu films is effected by electrons over the delocalized states of the conduction band; however, the Fermi level is shifted to the threshold of mobility of the conduction band. In other words, the europium impurity atoms form a donor-type band in the *a*-Si:H mobility gap lying 0.25 eV below E_c.

The Eu^{3+} state in the Mössbauer spectrum of the *a*-Si(H):Eu sample obtained at T_s = 380°C evidently corresponds to the ionized centers of europium. It should be stressed that the Eu^{2+} state is observed also for the *a*-Si:H:Eu sample obtained at T_s = 280°C when all the europium impurity atoms are in an electrically inactive state. The presence of the Eu^{2+} state in the *a*-Si(H):Eu sample prepared at T_s = 380°C indicates that a fraction of the europium impurity atoms are in an electrically inactive state even at this temperature. The Eu^{3+} line in the Mössbauer spectrum corresponds to electrically active europium centers. From the relative intensity of these lines (Fig. 4), it is possible to determine that the fraction of electrically active europium atoms is less than 0.14.

The Eu^{2+} Mössbauer spectrum has an isomeric shift close to that in the spectrum of the EuO compound. In the structural network of *a*-Si:H, the europium impurity atoms likely form electrically inactive associates of the $[Eu^{2+}–O^{2–}]$ type.

4.3. a-Si:H Films Doped with REMs (Except for Europium)

The REM dopants in *a*-Si:H films grown at T_s = 280°C do not affect the conductivity of the material: all the impurity atoms prove to be in the electrically inactive state. Efficient doping is attained only for the *a*-Si(H) films grown at T_s = 380°C. Further, we consider only the results relevant to such films.

For the REM-doped *a*-Si:H films, it is inherent that the dependence of $\ln\sigma = f(1/T)$ conductivity is linear, but the temperature dependence of thermoelectric power behaves anomalously. We believe the obtained results can be explained if we assume that the REM

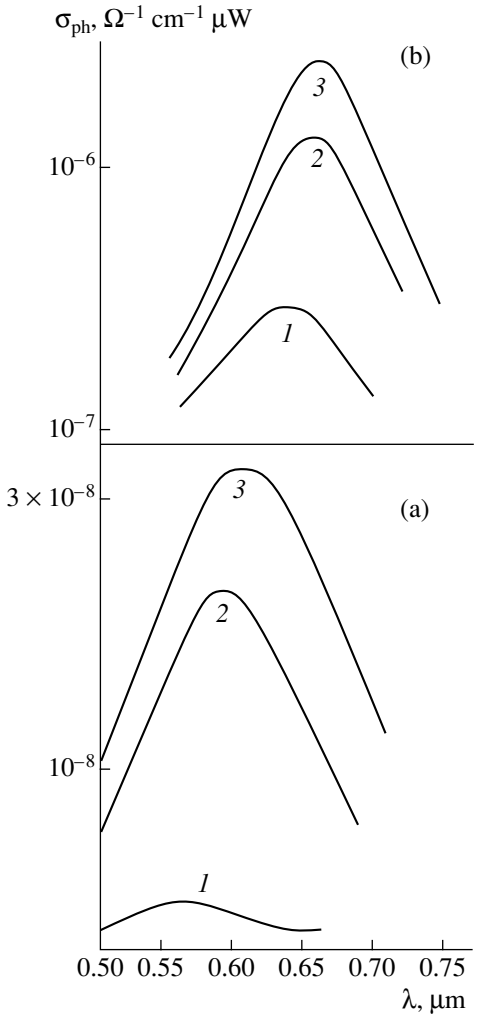

Fig. 3. Spectral dependences of photoconductivity σ_{ph} for (a) *a*-Si:H and (b) *a*-Si:H:Eu films measured at T = (*1*) 220, (*2*) 295, and (*3*) 325 K. All the films were deposited at T_s = 380°C.

impurities form an acceptor-type band in the *a*-Si:H mobility gap near its center. All the REM impurities can be divided into three groups.

(i) Tb, Dy, and Yb form the band lying 0.05–0.15 eV above the center of the mobility gap (defined as $(E_c – E_v)/2$, where E_v is the valence-band-mobility threshold). Thus, the acceptor band lies 0.7–0.8 eV below E_v. At low temperatures, the Fermi level F_0 is localized in the acceptor band and the conduction is effected in the temperature range of 250–500 K by electrons excited from the Fermi level to the delocalized states of the conduction band (we took into account the negative sign of S for these impurities) with $E_0 = E_c – F_0$ = (0.7–0.8) eV. A small magnitude of S at T < 300 K is explained by a hole-current contribution.

(ii) Nd and Ho form the band lying 0.5 eV below the mobility-gap center; at low temperatures, the Fermi level F_0 is localized in the acceptor band, and the con-

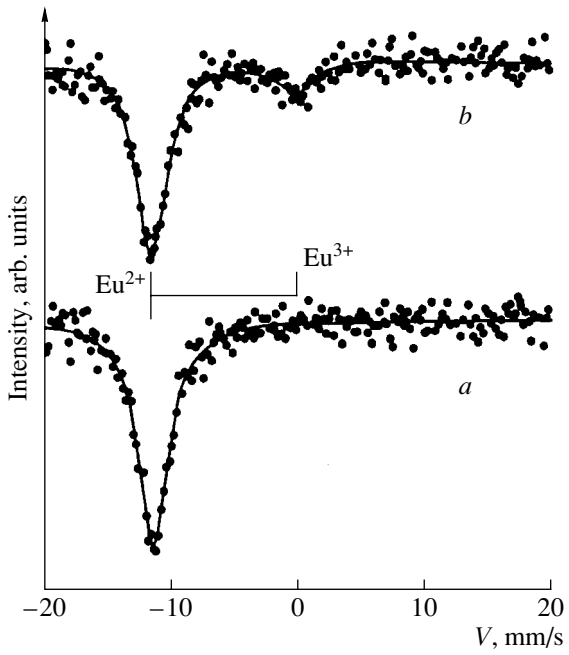

Fig. 4. Mössbauer spectra of ^{151}Eu at 295 K for the *a*-Si:H:Eu films obtained at T_s = (*a*) 280 and (*b*) 380°C. The superposition of lines corresponding to the Eu^{2+} and Eu^{3+} centers is shown.

duction is effected in the temperature range of 250–500 K predominantly by holes excited from the Fermi level to the delocalized states of the valence band (we took into account that the quantity S is positive for these impurities at $T < 300$ K) and $E_0 = F_0 - E_v = 0.7$ eV. With an increase in temperature, the Fermi level rises to E_c, and, in the temperature range of 330–370 K, the doped material behaves like an intrinsic semiconductor, with an identical contribution to conductivity from electrons and holes leading to an anomalously low magnitude of S. Finally, for a further increase in temperature, the electron conduction with the activation energy $E_0 = E_c - F_0 = 1.01$ eV begins to prevail; i.e., the anomalous situation is realized when $E_0 > (E_c - E_v)/2$. The dependence $\ln\sigma = f(1/T)$ exhibits a kink corresponding to a transition from the conduction with $E_0 = 0.7$ eV to that with $E_0 = 1.01$ eV.

Table 2. Sequence of rare-earth metals as the value of $E_c - F_0$ increases

Impurity	$E_c - F_0$, eV	σ_{ph}/σ
Yb	0.70	10
Dy	0.73	35
Tb	0.80	0.1
Gd	0.89	0.25
Er	0.91	0.25
Sm	0.97	0.20
Ho	1.01	0.03
Nd	1.01	0.02

(iii) Sm, Gd, and Er occupy an intermediate position between the first and second groups; i.e., they form an acceptor-type band in the *a*-Si:H mobility gap near its center. For them, an identical contribution to the conductivity from electrons and holes is observed in the temperature range of 330–350 K.

The Mössbauer spectra of the ^{149}Sm and ^{161}Dy impurity atoms correspond to the Sm^{3+} and Dy^{3+} charge states. These spectra are related to the electrically inactive centers of samarium and dysprosium, because the fine structure of the spectra is independent of the substrate temperature (we recall that the REM impurities affect the *a*-Si:H-conductivity parameters only at T_s = 380°C). The close proximity of isomeric shifts of the spectra of impurity atoms to those in the Sm_2O_3 and Dy_2O_3 compounds points to the formation of associations of the [Ln^{3+}–O^{2-}] type (Ln is a rare-earth atom) in the *a*-Si:H structural network. As in the case of the europium impurity atoms, the formation of such associations is responsible for the electrical inactivity of most impurity atoms.

In Table 2, we display the sequence of REMs as the difference ($E_c - F_0$) increases. In the same table, we give data on the photoconductivity of the REM-doped *a*-Si:H films. It can be seen that, for the impurities forming relatively shallow bands (Yb, Dy), an increase in photoconductivity is observed, with a distinct correlation taking place between the depth of the acceptor band and the degree of photoconductivity suppression. The latter fact has an evident explanation: deep levels are efficient recombination centers and should suppress photoconductivity. However, it should be noted that the levels formed by Yb and Dy are not shallow ($E_c - F_0 \approx 0.7$ eV) and, nevertheless, the photoconductivity is stimulated by these impurities. Therefore, there are two mechanisms of influence for REM impurities on the *a*-Si:H photoconductivity: one of them suppresses (as discussed above) and the other stimulates the photoconductivity destroying the recombination centers in the *a*-Si:H structural network. In nominally undoped *a*-Si:H, the main recombination centers are the [nitrogen–oxygen] centers. The REMs likely form associations of the [Ln^{3+}–O^{2-}] type in the *a*-Si:H structural network and, thus, destroy the [nitrogen–oxygen] associations. At least for the Eu, Sm, and Dy impurities (it is these impurities that stimulate the photoconductivity to the greatest extent), we detected such associations using Mössbauer spectroscopy.

5. PROCESSES OF SELF-ORGANIZATION AND OPTICAL ACTIVATION OF Er IONS IN *a*-Si:H FILMS

The problem of optical activation of erbium ions Er^{3+} in a silicon matrix (both in crystalline *c*-Si and amorphous *a*-Si:H:Er) is of great interest. This is

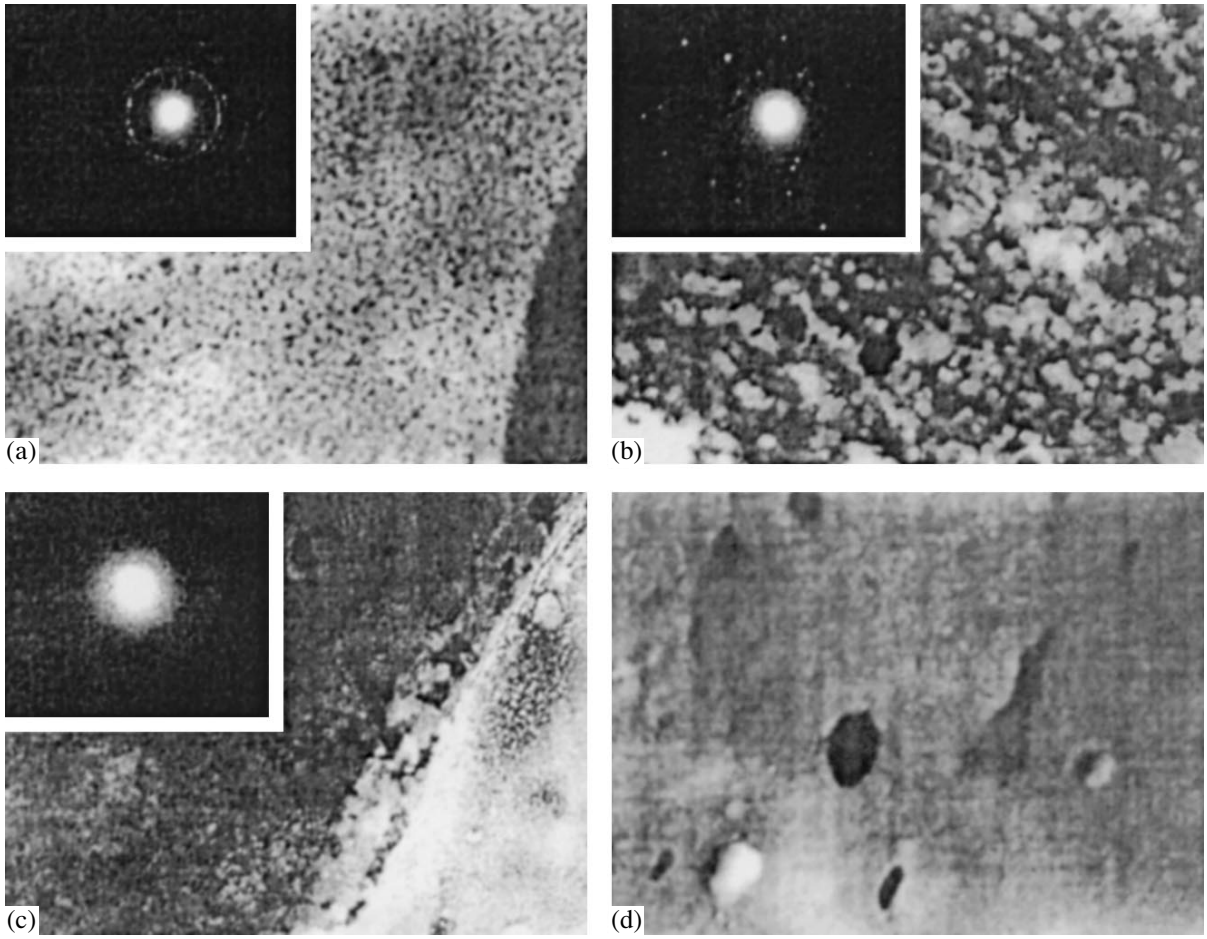

Fig. 5. Microstructure of *a*-Si:H:Er films with an erbium content C_{Er} = (a) 1.08; (b) 0.79; and (c), (d) 0.34 at. %. In the insets, the microdiffraction patterns are shown.

related to the possibility of designing 1.54-μm-wavelength emitters used in fiber links on the basis of this material and also to the possibility of the integration of these emitters into silicon technology. In addition, the investigations of REMs in semiconductors are motivated by the prospects of developing optical electron devices which combine the emission characteristics inherent to intracenter optical transitions within the 4*f* shell of REMs (as a rule, narrow temperature-stable lines) with the compactness of semiconductor devices.

Previously, we showed [3] that the optically active centers in *a*-Si:H:Er and *c*-Si:Er films are [Er–O] clusters with an Er^{3+} local symmetry similar to that in erbium oxide (Er_2O_3). At the same time, there is a certain distinction in the local symmetry of erbium atoms in the [Er–O] clusters in amorphous and crystalline silicon, which is associated with a different structure of the matrices. In the same study, we showed that the annealing of *a*-Si:H:Er films did not affect the local structure of the previously formed [Er–O] clusters. This is possible provided that only a cluster of a fairly large size is formed—on the order of the lattice constant of Er_2O_3.

The investigation of the formation of optically active centers in *a*-Si:H:Er films obtained by various methods was pursued in this study. It is shown that, using only the magnetron sputtering of a [Si + Er + O] mosaic target, the erbium-content dependence of the 1.54-μm photoluminescence (PL) line is observed. If especially pure erbium repeatedly purified by fusing in suspension was used, no such dependence was observed. It was also shown that, since the reaction of formation of [Er–O] complexes is unlikely in the gaseous phase, the advantage of the magnetron method for deposition consists in a higher rate of films grown with a reasonably high [Er–O]-complex content if a target with the oxygen impurity is used. When oxygen is introduced from the gaseous phase, no similar effect is observed.

The totality of the obtained data suggests that the intensity of the 1.54-μm PL line is influenced not only by the local surroundings of Er^{3+}, but also by the [Er–O]-cluster size. On the basis of the results of the combined investigations including the measurements of the 1.54-μm-line intensity as a function of erbium content, as well as the microdiffraction and microstruc-

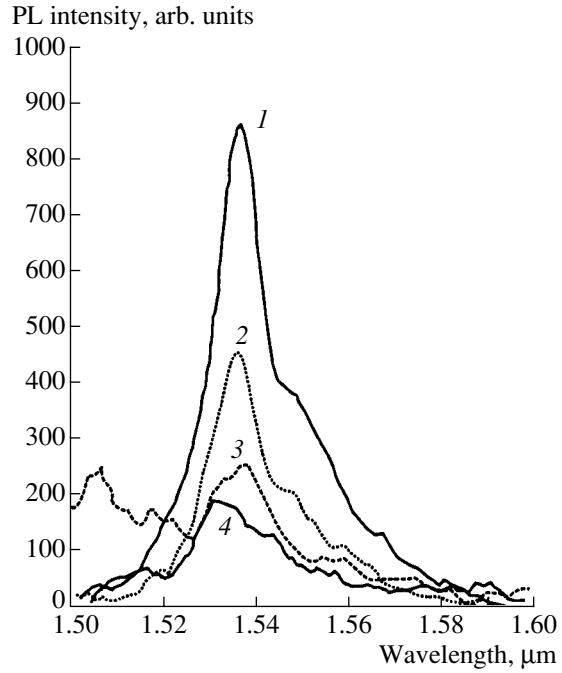

Fig. 6. Photoluminescence spectra of *a*-Si:H:Er (T = 300 K) for an erbium content C_{Er} = (*1*) 1.08, (*2*) 0.79, (*3*) 0.34, and (*4*) 1.42 at. %.

tural analyses, we show that the control parameter of the self-organization process defining the optical activation of erbium ions in *a*-Si:H:Er films is the erbium content in the target.

In Fig. 5, we show data from microdiffraction and microstructural analyses of the films under investigation. For an erbium content of 1.08 at. %, the presence of a crystalline phase can be recognized from the microdiffraction pattern (the set of diffraction rings). The analysis of this pattern showed that the interplanar spacings in the pattern correspond to Er_2O_3. From microstructural analysis, we found that the crystallite size ranged from 5 to 50 nm. The density of particles amounted to 5×10^{10} cm^{-2}.

A decrease in the Er content to 0.79 at. % results in an increase in the crystallite sizes from 50 to 250 nm and a decrease in the particle density to 5×10^9 cm^{-2}. The film has a cellular structure, with the new phase crystallized in the cells replicating the cell shape. In the microdiffraction pattern from this film, there are also reflections from the Er_2O_3 phase.

A further decrease in the Er content to 0.34 at. % gives rise to porosity of the films, with the porosity being more coarse than in the two previous cases. Against the porosity background, the poorly pronounced formation of a new phase (low-contrast crystallites with sizes close to 50–250 nm) is observed. The crystallites do not contribute to the microdiffraction pattern, in which only two diffuse rings related to the amorphous phase are observed.

In Fig. 6, we show the PL spectra in the region of 1.54 μm. A variation in crystallite sizes and in the structure of films is seen to correlate well with modifications of the spectra: a decrease in the sizes of microcrystallites, as in the case of *c*-Si n^+–p junctions, results not only in increasing the PL intensity, but also in shifting the PL peak to shorter wavelengths. In addition, two more peaks with a lower PL intensity can be distinctly seen in the PL spectrum of the film with an erbium content of 1.08 at. %. Their positions are shifted to longer wavelengths, which probably can be associated with the presence of other crystallites.

According to [4], the presence of microcrystallites is the necessary condition for transferring excitation energy to erbium ions. The excitation energy is transferred from excitons in nanocrystallites to an erbium ion with subsequent radiative recombination. As a result of this recombination, an intracenter transition proceeds to the unfilled 4*f* shell of Er and the 1.54-μm peak is observed.

We now consider the mechanism of formation of microcrystallites in the case of magnetron sputtering of a (Si + Er + O) mosaic target. The [Er–O] complexes deposited from the target to the substrate have low mobility over the surface by virtue of the relatively low (T = 300°C) substrate temperature, the large size of the complex, and the likelihood of the presence of dangling bonds. All the remaining reactions on the substrate, including the formation of erbium silicide and the conversion of oxygen to the gaseous phase due to the presence of a high content of atomic hydrogen, will proceed according to the thermodynamic parameters of this nonequilibrium process. Magnetron deposition is a thermodynamically nonequilibrium process and can produce various degrees of instability. The self-organization process accompanying the growth of multicomponent compounds is known to manifest itself via the complex of interactions between the lattice stresses, values of surface energy, and the mobility of disperse particles over the substrate surface.

In the case of magnetron deposition, the film-growth rate is high and the appearance of lattice stresses is quite probable. The appearance of the second factor, that is, the low mobility of the [Er–O] complexes on the substrate surface, is also highly probable. The surface energy, which primarily defines the critical size of the disperse-particle nucleus, is much higher for the [Si–O] and [Er–O] complexes than for the [Er–Si], [Si–Si], and [Si–H] ones. Consequently, the critical sizes of nuclei with a higher surface energy are larger than those for the low-energy complexes. Therefore, the critical nuclei with small critical radii disappear, while those with larger radii grow, which implies the growth of films according to the Stranski–Krastanov mechanism. Thus, for the optimal content of [Er–O] complexes at the target, minimum sizes and quantities of europium-silicide crystallites (optically inactive) are observed. However, it is most probably these crystallites that trig-

ger the entire process of the excitation-energy transfer by virtue of the special properties inherent to nanocrystallites. The role of the [Si–O] complexes amounts only to the competitive mechanism of formation of the [Er–O] complexes.

It should be noted that the further increase in the content of [Er–O] complexes does not enhance the intensity of the 1.54-μm-PL band. Moreover, we observed a decrease in this intensity with a further increase in the content of C_{Er} due to the appearance of a significant amount of erbium silicide. Therefore, when developing injection methods for pumping structures with *a*-Si(H):Er, it is necessary to solve the very complicated technological problem of optimizing the growth process and the concentrations of all the components.

6. CONCLUSION

We investigated the electrical and photoelectric properties of *a*-Si:H films doped with rare-earth metals. The films were obtained via the high-frequency sputtering of mosaic targets in a gaseous mixture of argon, hydrogen, and silane. The best photoelectric parameters (lowest dark mobility, highest photoconductivity) are attained at a substrate temperature T_s = 380°C. At the same temperature, we also attained efficient doping of films, whereas impurity atoms prove to be in the electrically inactive states at T_s = 280°C. These states correspond to associations of the [impurity–structure defect] type. These associations disintegrate, and the fraction of electrically active atoms increases as the substrate temperature increases.

The Nd, Sm, Gd, Tb, Dy, Ho, Er, and Yb impurity atoms form an acceptor-type band in the *a*-Si:H mobility gap, which lies near the mobility-gap center, and the Fermi level turns out to be localized in this band. Depending on the depth of the location of the acceptor band, the doped material can be *p*-type (Nd and Ho impurities), intrinsic (Sm, Er, and Ho), or *n*-type (Tb, Dy, and Yb) at $T < 300$ K. In the high-temperature region ($T > 400$ K), the conduction is effected by electrons over the delocalized states of the conduction band. Europium impurity atoms form a donor-type band in the *a*-Si:H mobility gap; this band lies 0.25 eV below the threshold of conduction-band mobility, so that the conductivity of such a material is effected by electrons over the delocalized states of the conduction band. Such a distinction of europium from all REMs is caused by the high stability of the half-filled 4*f* shell, which is characteristic of Eu atoms.

The Eu, Dy, and Yb atoms stimulate *a*-Si:H photoconductivity, which is attributed to the formation of $[Eu^{2+}–O^{2-}]$-type associations in the course of doping and the simultaneous destruction of [nitrogen–oxygen]-type recombination centers. The impurities of the remaining REMs suppress the photoconductivity, because the acceptor levels formed by REMs in the mobility gap turn out to be the main recombination centers in such materials. We observed a correlation between the degree of suppression of the photoconductivity and the depth of the position of the acceptor band for the corresponding impurity.

As a result of comprehensive physical investigations, the existence of self-organization processes was demonstrated in *a*-Si:H:Er films, specifically, the appearance of an ordered structure of [Er–O] crystallites in an unordered structural network. The control parameter of the self-organization process is the content of [Er–O] complexes in the *a*-Si:H:Er films. A decrease in crystallite sizes leads to an increase in the photoluminescence intensity at the 1.54-μm wavelength, i.e., to an increase in the optical activation of Er ions in the *a*-Si(H):Er films.

ACKNOWLEDGMENTS

This study was supported in part by the Russian Foundation for Basic Research, project no. 01-02-17825.

REFERENCES

1. *The Physics of Hydrogenated Amorphous Silicon*, Ed. by J. D. Joannopoulos and G. Lucovsky (Springer-Verlag, New York, 1984; Mir, Moscow, 1988).
2. M. M. Mezdrogina, F. S. Nasredinov, U. S. Tursunov, *et al.*, Neorg. Mater. **27**, 1123 (1991).
3. V. F. Masterov, F. S. Nasredinov, P. P. Seregin, *et al.*, Fiz. Tekh. Poluprovodn. (St. Petersburg) **32**, 708 (1998) [Semiconductors **32**, 636 (1998)].
4. G. Franzo, V. Vinciduerro, and F. Priolo, Appl. Phys. A **69**, 3 (1999).

Translated by V. Bukhanov

Semiconductors, Vol. 36, No. 11, 2002, pp. 1260–1266. Translated from Fizika i Tekhnika Poluprovodnikov, Vol. 36, No. 11, 2002, pp. 1345–1350.

ATOMIC STRUCTURE AND NONELECTRONIC PROPERTIES OF SEMICONDUCTORS

The Influence of Sinks of Intrinsic Point Defects on Phosphorus Diffusion in Si

O. V. Aleksandrov

St. Petersburg State Electrotechnical University, St. Petersburg, 197376 Russia

e-mail: aleks_ov@mailbox.alkor.ru

Submitted September 11, 2001; accepted for publication April 25, 2002

Abstract—The influence of sinks associated with structural defects is analyzed qualitatively based on the model of P diffusion in Si by the dual pair mechanism. It is demonstrated that the allowance made for sinks of self-interstitials leads to the retardation of the enhanced P diffusion for the low-content region in the tail of the concentration profile. The influence of sinks is most pronounced if the position of their peak concentration is in the region of the peak of generation of self-interstitials inside the diffusion layer. From a comparison of the result of calculations with the experimental data, the parameters of the capture of self-interstitials by structural defects, which are introduced by the P diffusion and implantation of electrically inactive Ge and N impurities, are determined. © *2002 MAIK "Nauka/Interperiodica".*

1. INTRODUCTION

For P diffusion with a high surface concentration, a number of specific features are observed that differentiate P from other dopants in Si. These are the profile plateau in the high-concentration region, the inflection and tail in the low-concentration region, and low-temperature diffusion. The redistribution of other jointly diffusing substitutional impurities in the base of transistors (dip-effect) and in deep buried layers [1–3] is yet another of these features. To explain these specific features, a number of models, which are based on different diffusion mechanisms, were suggested (see review in [4]). One more specific feature is the retardation of P diffusion in Si by structural defects. These defects are introduced by the diffusion or implantation of the P impurity itself [5–8], as well as by the implantation of electrically inactive impurities Si [9], Ge [10], and N and O [11]. The retardation manifests itself most pronouncedly in the low-concentration region of the tail of the concentration profile. In [6–8], attention was focused on the circumstance where structural defects lead to the retardation of enhanced diffusion, which is characteristic of high surface P concentrations. In order to explain the effect, a great number of reasons were put forward. Thus, for high surface P concentrations, the retardation of P diffusion was explained by both P precipitation [1, 2] and by the capture of the impurity by structural defects [12]. Such an explanation is confirmed by the irregularities found in the P concentration profiles, whose depth correlates with the secondary defects formed in the course of annealing of the implanted layers (dislocations, dislocation loops, rodlike defects) [9, 13]. The retardation of P diffusion with the introduction of Ge via diffusion was explained by the compensation of the diffusion-introduced stresses, which were assumed to be the reason for the enhanced P diffusion [5]. The retardation effect was also associated with the capture of excess intrinsic point defects, specifically, vacancies formed in the heavily P-doped layer, by dislocations [6–8]. At the present time, it is found that for the P diffusion with a high surface concentration, as well as for the thermal oxidation of Si, excess self-interstitials are generated [3]. According to the model of P diffusion by the dual pair mechanism via vacancy *PV* and interstitial *PI* pairs, the excess self-interstitials are formed due to the diffusion and subsequent decomposition of neutral *PI* pairs from the region with a high P concentration [4]. In this case, the presence of structural defects, which are the sinks for intrinsic point defects, should retard P diffusion.

The purpose of this study is to analyze qualitatively the influence of sinks, which are associated with the structural defects, on the P diffusion in Si; the model of P diffusion by the dual pair mechanism is used.

2. CONSIDERATION OF THE INFLUENCE OF SINKS

According to the model [4], the P diffusion in Si by the dual pair mechanism can be described by two equations for P itself and for the total concentration of neutral *PI* pairs and self-interstitials with the diffusivities which depend on the component concentrations; i.e.,

$$\frac{\partial C_\mathrm{P}}{\partial t} = \frac{\partial}{\partial x}\left(D_\mathrm{P}\frac{\partial C_\mathrm{P}}{\partial x}\right) - R_\mathrm{P}, \quad (1)$$

$$\frac{\partial F_I}{\partial t} = \frac{\partial}{\partial x}\left(D_{FI}\frac{\partial F_I}{\partial x}\right) - R_{FI}. \quad (2)$$

1063-7826/02/3611-1260$22.00

Here, x is the coordinate; t is time; C_P is the total P concentration; D_P is the P diffusivity, which depends on the local charge-carrier density and supersaturation by intrinsic point defects; F_I is the total concentration of neutral *PI* pairs and self-interstitials ($F_I = F + I^0$); D_{FI} is their diffusivity, $D_{FI} = (D_F F + D_I I^0)/F_I$; and D_F and D_I are the diffusivities of neutral *PI* pairs and self-interstitials, respectively. The existence of sinks for the P impurity is taken into account by introducing an additional term R_P on the right side of Eq. (1). The existence of sinks for the *PI* pairs and self-interstitials was also taken into account. To do this, an additional term R_{FI}, which describes the rate of drain to the sinks of P atoms, *PI* pairs, and self-interstitials, respectively, was introduced on the right side of Eq. (2). We assume that the capture of P atoms by sinks is either reversible or irreversible. In the first case, $R_P = k_{1P}C_{R0}C_P - k_{2P}C_{RR}$. Here, k_{1P} is the rate constant for the capture of P atoms by unoccupied sinks, k_{2P} is the rate constant for recovery of P atoms from occupied sinks, C_{R0} is the concentration of free (unoccupied) sinks (traps), and C_{RR} is the concentration of occupied sinks. In the state of local equilibrium, the diffusion with the reversible capture by traps is similar to the diffusion with the formation of immobile complexes. This process is described by the effective diffusivity, $D_{ef} = \Omega D_P$, where Ω is the coefficient of the diffusion retardation [14],

$$\Omega = \frac{1}{2}\left[1 + \frac{C_P - C_R + 1/k_P}{\sqrt{(C_P - C_R + 1/k_P)^2 + 4C_R/k_P}}\right]. \quad (3)$$

Here, C_R is the total trap concentration ($C_R = C_{R0} + C_{RR}$), and k_P is the equilibrium constant of the reaction of reversible P capture ($k_P = k_{1P}/k_{2P}$). In the case of irreversible capture, $R_P = k_{1P}C_{R0}C_P$. For diffusion-limited P capture, $k_{1P} = 4\pi r_P D_P$, where r_P is the radius of interaction of P atoms with sinks.

We assume that the capture of excess self-interstitials and *PI* pairs by sinks is irreversible. In the case of capture of neutral self-interstitials by sinks, we have $R_{FI} = k_{1I}C_{R0}(I - I_{eq})$, where k_{1I} is the rate constant for the capture of excess self-interstitials by sinks, and I^0_{eq} is the thermodynamically equilibrium concentration of neutral self-interstitials. For diffusion-limited capture, $k_{1I} = 4\pi r_I D_I$, where r_I is the radius of interaction of self-interstitials with sinks. The relation between the concentration of neutral self-interstitials and the F_I concentration takes the form $F_I = (1 + k_{FI}nC^+_P)I^0$. Here, $k_{FI} = k_F k_I$; k_F is the equilibrium constant of the formation–decomposition reaction for neutral *PI* pairs; k_I is the equilibrium constant of the recharge reaction for self-interstitials; and C^+_P and n are the concentrations of ionized P and electrons, respectively. In the case of capture of neutral *PI* pairs by sinks, we have $R_{FI} = k_{1F}C_{R0}(F - F_{eq})$, where k_{1F} is the rate constant for the capture of excess *PI* pairs by sinks, and F_{eq} is the concentration of *PI* pairs, which corresponds to the thermodynamically equilibrium concentration of self interstitials ($F_{eq} = k_{FI}nC^+_P I^0_{eq}$). For diffusion-limited capture, $k_{1F} = 4\pi r_F D_F$, where r_F is the radius of interaction of *PI* pairs with sinks. The relation between the concentration of neutral *PI* pairs and the F_I concentration takes the form $F_I = [1 + 1/(k_{FI}nC^+_P)]F$. In addition, when considering the capture of *PI* pairs by sinks, it is necessary to take into account the subsequent P release from sinks: $R_P = -R_{FI}$.

The diffusion equations (1) and (2) for P, neutral *PI* pairs, and self-interstitials with additional terms R_P or R_{FI} were solved numerically by the finite difference method using the implicit difference scheme. The initial and boundary conditions were formulated according to the experimental conditions [8–11]. In these experiments, the sinks were structural defects introduced by the P diffusion [8], as well as by the implantation of electrically inactive impurities: Ge [10] and N and O [11].

3. RESULTS OF SIMULATION

A comparison of different variants of capture of P atoms, excess self-interstitials, and *PI* pairs by sinks formed by Ge implantation was carried out for the experimental conditions reported in [10]. In this experiment, P was introduced in Si via ion implantation (45 keV, 5×10^{15} cm^{-2}) separately or jointly with the Ge implantation (125 keV, 5×10^{15} cm^{-2}). After that, thermal treatment (900°C, 10 min in N_2) was carried out. In the course of thermal treatment of the implanted layer, the primary radiation defects transform to secondary ones. The densities of structural defects in the experiment [10] were not determined. For this reason, let us assume that the sink concentration profile is associated with the concentration profile of the implanted Ge impurity, which forms numerous radiation defects per incident ion, $C_R(x, t) = kC_{Ge}(x, 0)$, where k is the proportionality coefficient. We assume that the initial concentration profiles of both P and Ge impurities are governed by the normal law:

$$C(x, 0) = \frac{Q}{\sqrt{2\pi}\Delta R_P}\exp\left[-\frac{(x - R_P)^2}{2\Delta R_P^2}\right]. \quad (4)$$

Here, Q is the amount (dose) of the dopant incorporated; R_P and ΔR_P are the mean projected range and its standard deviation, which were taken from the tables [15]. The boundary condition for thermal treatment at

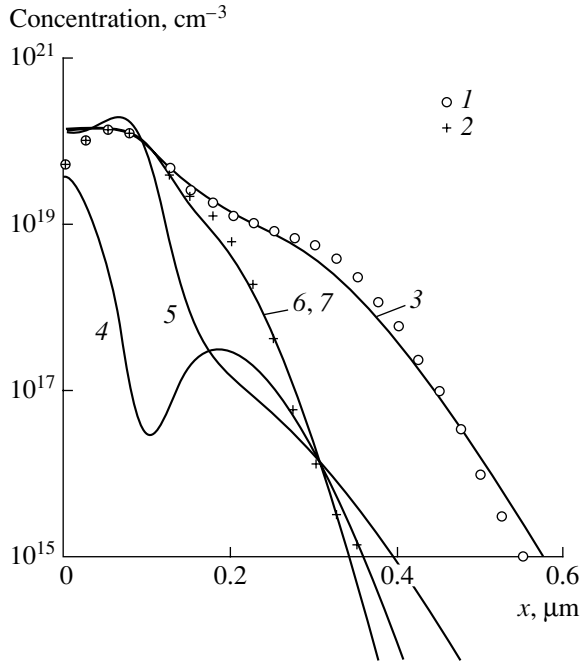

Fig. 1. Charge-carrier concentration profiles after thermal treatment (900°C, 10 min in N_2) of a Si layer implanted with P (45 keV, 5×10^{15} cm^{-2}) (curves *1*, *3*) and with Ge (125 keV, 5×10^{15} cm^{-2}) (curves *2*, *4–7*). Points (*1*, *2*) correspond to experimental data [10]; curves (*3–7*) represent the results of calculations for (*3*) $C_R = 0$; (*4–7*) $C_R = kC_{\mathrm{Ge}}$; (*4*) $k = 1$, $k_{\mathrm{P}} = 3 \times 10^{-19}$ cm^3; (*5*) $kr_{\mathrm{P}} = 1.5 \times 10^{-10}$ cm; (*6*) $kr_I = 3.4 \times 10^{-12}$ cm; and (*7*) $kr_F = 1.7 \times 10^{-10}$ cm.

the surface (for $x = 0$) and at the end of the solution region (for $x = L$) for Eqs. (1) and (2) are given by

$$\frac{\partial C_{\mathrm{P}}(0,t)}{\partial x} = \frac{\partial C_{\mathrm{P}}(L,t)}{\partial x} = 0,$$
$$F_I(0,t) = F_{IS}(t), \quad \frac{\partial F_I(L,t)}{\partial x} = 0, \tag{5}$$

where $F_{IS}(t) = [1 + k_{FI} n_S(t) C^+_{\mathrm{PS}}(t)] I^0_S$, and C^+_{PS} and n_S are the surface concentration of ionized P and electron density. Note that, in the latter expression, the surface carrier density and surface concentration of ionized P depend on the duration of thermal treatment, and the surface concentration of neutral self-interstitials I^0_S exceeds the thermodynamically equilibrium concentration I^0_{eq} by a factor of $\langle a \rangle_t$. Here, $\langle a \rangle_t$ is the supersaturation with respect to intrinsic point defects averaged by time. This supersaturation is formed in the course of annealing of the radiation defects introduced by implantation. Satisfactory agreement of the carrier-density profile calculated over the depth in the absence of sinks with the experimental profile without Ge implantation (Fig. 1, points *1*) is attained for $\langle a \rangle_t = 4.2$ (Fig. 1, curve *3*). With Ge implantation, the tail in the P profile is suppressed (Fig. 1, points *2*) below the inflection concentration ($C_k \cong 2 \times 10^{19}$ cm^{-3} at 900°C). The parameters of interaction with the sinks (k_{P}, kr_{P}, kr_I, and kr_F) were chosen in the calculation so that the P profiles passed though the point $x_j \cong 0.31$ μm with the concentration 1×10^{16} cm^{-3}. As can be seen from Fig. 1, the calculated P profiles significantly differ from the experimental one (points *2*) for both reversible (curve *4*) and irreversible (curve *5*) P capture by sinks. On the other hand, with the capture of excess self-interstitials and *PI* pairs, the calculated profiles (curves *6*, *7)* describe the experimental profile adequately and actually coincide with each other. In the case of capture of self-interstitials, the coincidence with the experiment is attained for the capture parameter $kr_I = 3.4 \times 10^{-12}$ cm. This value is significantly smaller than that for the capture of *PI* pairs, where $kr_F = 1.7 \times 10^{-10}$ cm. This means that the capture of self-interstitials by sinks is more efficient compared with the capture of *PI* pairs. According to this result, we will further calculate the capture by sinks of self-interstitials only.

Under the experimental conditions [8], the preliminary implantation of Ar^+ ions at different doses (100 and 1000 μC/cm^2) and annealing at different temperatures (1000 and 1100°C) were carried out prior to P diffusion. The subsequent P diffusion (1000°C, 5 min) led to the transformation of preliminarily introduced dislocation loops. Depending on the conditions of implantation and thermal treatment, these loops were transformed into bent dislocations, irregular dislocation networks, and dislocation clusters with dislocation densities N_d from 1×10^9 to 5×10^9 cm^{-2}. The type of defects and their densities were determined by transmission electron microscopy. We assume that the dislocations in the diffusion layer are distributed according to the normal law. In this case, the volume concentration of sinks is defined as

$$C_R(x,t) = \frac{\sqrt{N_d}}{\sqrt{2\pi}\sigma a} \exp\left[-\frac{(x - x_m)^2}{2\sigma^2}\right]. \tag{6}$$

Here, x_m and σ are the depth corresponding to the peak of the dislocation density profile and the width of this profile, respectively; and a is the interatomic distance ($a = 2.35 \times 10^{-8}$ cm in the Si lattice). As was demonstrated previously [16], the dislocations formed in the course of diffusion follow the diffusion front; they are located at the depth $(0.3–0.5)x_j$, where x_j is the p–n junction depth. For this reason, we set $x_m = 0.4x_j$ and $\sigma = 0.1x_m$ in the calculations. For the junction depth x_j, we took the coordinate corresponding to the P concen-

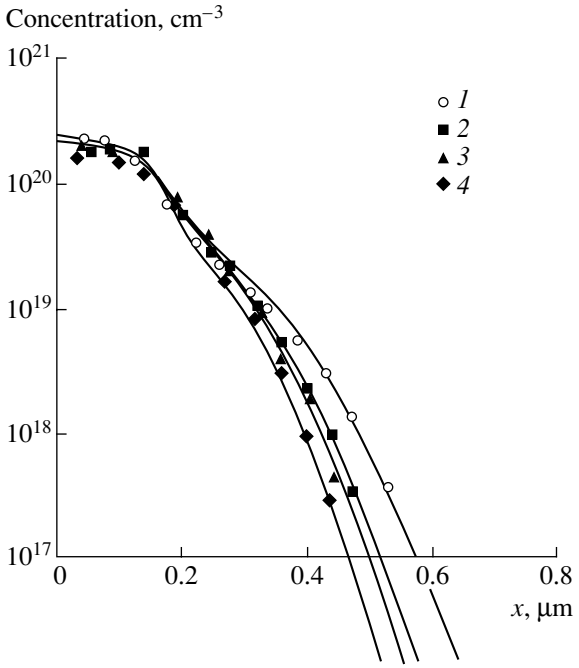

Fig. 2. Charge-carrier concentration profiles after the P diffusion (1000°C, 5 min) for the dislocation density N_d = (*1*) 0, (*2*) 1×10^9, (*3*) 3×10^9, and (*4*) 5×10^9 cm^{-2}. Points correspond to experimental data [8]: solid lines represent the results of calculations for $kr_I = 2.3 \times 10^{-10}$ cm.

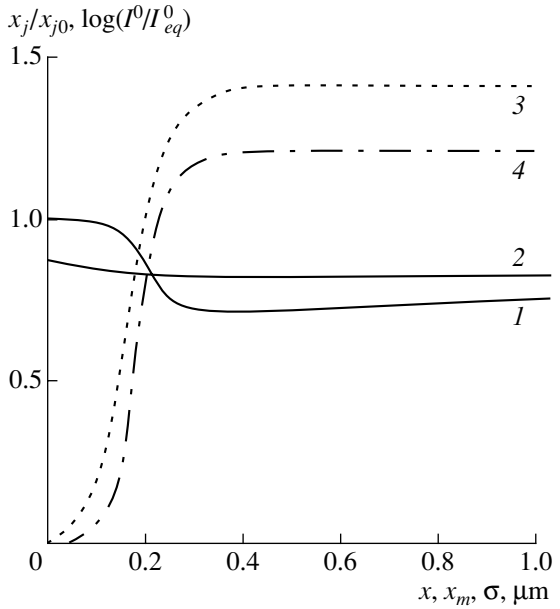

Fig. 3. Relative junction depth x_j/x_{j0} in relation to (*1*) the peak position x_m and (*2*) the width σ of the dislocation density profile. The profile of the relative supersaturation of self-interstitials I^0/I^0_{eq} over the depth is shown (*3*) by the dotted line for $N_d = 0$ and (*4*) by the dash-and-dot line for $N_d = 3 \times 10^9$ cm^{-2}.

tration of 1×10^{17} cm^{-3}. The boundary conditions for Eqs. (1) and (2) are given by

$$C_P(0, t) = C_{PS}, \quad \frac{\partial C_P(L, t)}{\partial x} = 0,$$
$$F_I(0, t) = F_{IS}, \quad \frac{\partial F_I(L, t)}{\partial x} = 0. \tag{7}$$

Here, C_{PS} is the surface P concentration, $C_{PS} \cong 8 \times 10^{20}$ cm^{-3} ($n_S \cong 2.9 \times 10^{20}$ cm^{-3}), and $F_{IS} = I^0_{eq} + F_{eq}$. The results of calculating charge-carrier profiles for the sink of excess self-interstitials for various dislocation densities and $kr_I = 2.3 \times 10^{-10}$ cm in comparison with the experimental profiles from [8] (points *1–4*) are shown in Fig. 2 (solid lines). It can be seen from Fig. 2 that, as the dislocation density increases from 1×10^9 to 5×10^9 cm^{-2}, the calculated curves exhibit a more and more pronounced suppression of the tail in the P profile at the concentrations lower than that of inflection ($C_k \cong 5 \times 10^{19}$ cm^{-2} at 1000°C), which agrees well with the experiment. Note that almost identical values of the capture parameter for self-interstitials $kr_I = (2.3–7) \times 10^{-10}$ are also obtained for misfit dislocations, which are introduced by P diffusion at 1100°C, according to the analysis of the experimental profiles given in [5]. Note (i) the strong influence of the peak position x_m (Fig. 3, curve *1*) and (ii) the weak influence of the width σ (Fig. 3, curve *2*) of the dislocation profile on the relative junction depth x_j/x_{j0}. Here, x_{j0} is the junction depth in the absence of dislocations. Result (i) is caused by the nonuniform distribution of excess self-interstitials over the diffusion layer depth both in the absence (Fig. 3, curve *3*) and in the presence (Fig. 3, curve *4*) of dislocations. The influence of x_m is most pronounced in the region of the maximum generation of self-interstitials for $x_m \cong 0.4x_{j0}$. Result (ii) is caused by the fact that the integrated sink concentration is retained as the dislocation profile depth varies in expression (6).

In experiment [11], the influence of implantation of N and O impurities on the low-temperature (500–600°C) P diffusion from the layer formed by the preliminary high-temperature (950–1000°C, 5–35 min) P diffusion was investigated. As above, we assume that the sink concentration is determined by the concentration profile of the implanted impurity $C_R(x, t) = kC_N(x, 0)$ of form (4). The boundary conditions of Eqs. (1) and (2) take the form (5), where $F_{IS}(t) = [1 + k_{FI}n_S(t)C^+_{PS}(t)]I^0_{eq}$. In this case, the initial conditions according to the model [4] are the profiles $C_P(x)$ and $F_I(x)$, which corresponds to the completion of the high-temperature stage ($C_{PS}(0) \cong 6 \times 10^{20}$ cm^{-3}, $n_S(0) \cong 2.6 \times 10^{20}$ cm^{-3}). The charge-carrier profiles calculated for the sink of excess self-interstitials in comparison with the experimental data prior to (curve *1*) and after (curves *2*, *3*) the low-temperature P diffusion (600°C, 4 h) in the absence

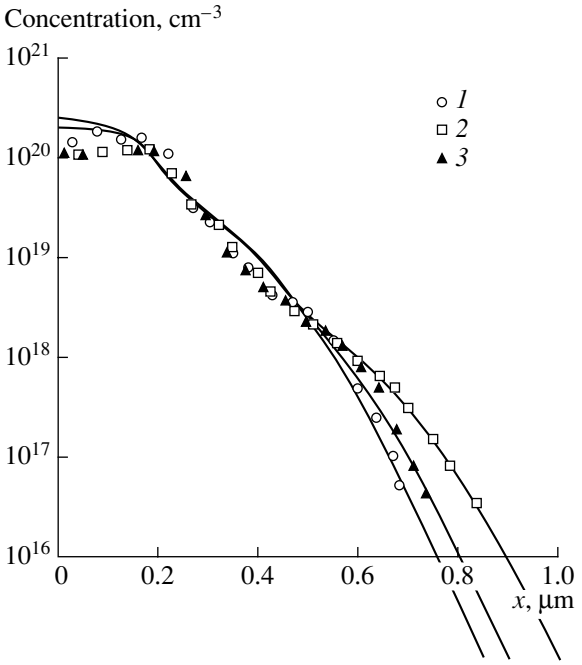

Fig. 4. Charge-carrier concentration profiles after (*1*) the high-temperature (1000°C, 5 min) and (*2*, *3*) low-temperature (600°C, 4 h) P diffusion (*1*, *2*) in the absence and (*3*) in the presence of implanted N^+ ions (100 keV, 6×10^{14} cm^{-2}). Points are experimental [11], solid lines were calculated for $kr_I = 8 \times 10^{-14}$ cm.

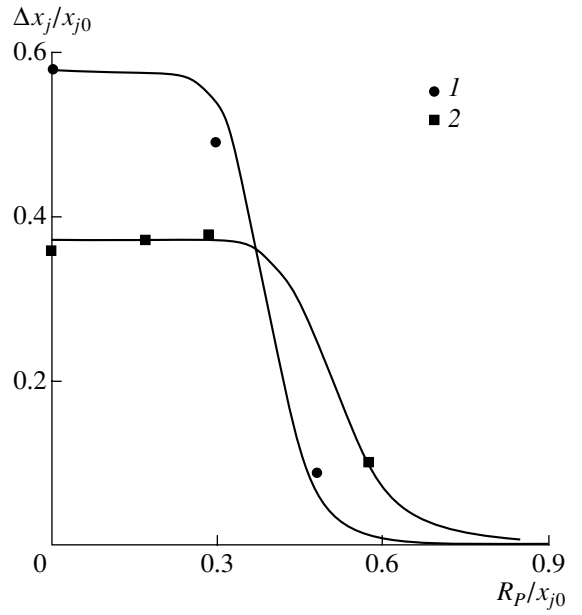

Fig. 5. Relative displacement $\Delta x_j/x_{j0}$ of *p–n* junction for the low-temperature P diffusion (500°C, 16 h) as a function of the relative range of N^+ ions for the initial junction depth x_{j0} = (*1*) 0.3 and (*2*) 0.5 μm. Circles and squares correspond to experimental data [11], solid lines represent the results of calculations for kr_I = (*1*) 6×10^{-14} and (*2*) 4×10^{-15} cm.

(curve *2*) and in the presence (curve *3*) of implanted N^+ ions are shown in Fig. 4. As can be seen from Fig. 4, the implantation of N^+ ions leads to the suppression of low-temperature P diffusion in the region of the profile tail for concentrations below the inflection concentration ($C_k \cong 1 \times 10^{18}$ cm^{-3} at 600°C). The relative displacement of the junction depth $\Delta x_j/x_{j0}$ ($\Delta x_j = x_{j0} - x_j$, where x_{j0} and x_j are the junction depths for the concentration of 1×10^{16} cm^{-3} after the high-temperature and low-temperature stages, respectively) depends strongly on the projected range R_P (Fig. 5). The latter, along with the standard deviation ΔR_P, is determined by the implantation energy. The effect of implantation of N^+ ions is most pronounced for $R_p \cong (0.4–0.5)x_{j0}$, which corresponds to the region of the most intense generation of excess self-interstitials in the diffusion layer. Note that, according to the data [11], the implantation of O ions at identical doses leads to approximately the same retardation of the low-temperature P diffusion as the implantation of N ions.

4. DISCUSSION

From a comparison of profiles calculated for various variants of capture by structural defects which are introduced by Ge implantation (Fig. 1, curves *3–6*) it can be seen that the allowance made for both the reversible and irreversible sinks of P atoms (curves *3*, *4*) does not permit one to describe the variation of the shape of the P profile adequately. Only the allowance made for the sink of excess self-interstitials and *PI* pairs (curves *5*, *6*) brings about the retardation of P diffusion in the region of the profile tail and allows one to describe it quantitatively. Note the identical shape of calculated P profiles, which were obtained with allowance made for the capture by sinks of excess self-interstitials and *PI* pairs (Fig. 1, curves *5*, *6*). This result is associated with the fact that the absorption of excess self-interstitials also occurs in the course of the drain of *PI* pairs: $R_{FI} = k_{1F}C_R(F - F_{eq}) = k_{1F}C_RF_{eq}(I - I_{eq})/I_{eq}$. The amount of P that is released in the course of this process is small compared with the amount of diffusing P. Because of this, the contribution of released P is actually imperceptible. The difference in capture parameters for self-interstitials and *PI* pairs is associated with the higher concentration of *PI* pairs in the region of the most intense generation of self-interstitials as well as with the difference in their diffusivities. Since it was found that $kr_I \ll kr_F$, one may conclude that the capture of self-interstitials by sinks is more efficient compared with the capture of *PI* pairs. The allowance made for the drain of excess self-interstitials permits one to describe the retardation of P diffusion by dislocations which are introduced in the course of P diffusion (Fig. 2, curves *2–4*). The retardation of the low-temperature P diffusion by structural defects, which are introduced via the implantation of N^+ ions, can also be described (Fig. 4, curve *3*).

The exact determination of the radius of interaction of the sink with the self-interstitial is apparently hampered in connection with the ambiguity concerning the proportionality coefficient k in the capture parameter. In the case of the ion implantation of electrically inactive impurities, the k^{-1} quantity has the physical meaning of the amount of residual (remaining after annealing) point defects m involved in the formation of a single sink. Since the radius of interaction is on the order of interatomic distances, we have $m \sim 10^4$ for the implantation of Ge ions (for example, resulting dislocation loops) and $m \approx 10^6$ for the implantation of N ions (for example, resulting micropores). If the dislocation density is known, the physical meaning of the k^{-1} quantity is the average distance (in units of the interatomic distance) between the jogs in dislocations. These jogs are sites of absorption (or escape) of intrinsic point defects. In our case, we have $k^{-1} \approx 10^2$ for misfit dislocations.

In the Panteleev model [17, 18], the specific features of P diffusion are associated with the possibility of the partial existence of P atoms at interstitial sites (P_i). Undoubtedly, a similarity between the *PI* pairs and interstitial P exists. Such a similarity is caused by the possibility of the substitution reaction of an interstitial P atom for a lattice-site Si atom, $P_i + S_S \longleftrightarrow P_S + S_i$. Here, S_S and S_i are the Si atom at the site and in the interstice of the Si crystal lattice, respectively; and P_S is the P atom at the site. However, distinctions in the behavior relative to the sinks between *PI* pairs and P_i atoms may be expected. In the model [17], the concentration of interstitial P atoms was assumed to be fairly high, since the inflection formation in P profiles for $C_k \approx 10^{19}$ cm^{-3} was associated with their equilibrium solubility. Because of this, a distinction exists between the capture of *PI* pairs and interstitial P atoms by sinks. In the latter case, one might expect a noticeable accumulation of impurities at sinks. Hence, the irregularities should emerge in P concentration profiles. Actually, irregularities in P profiles were found in several studies [9, 12]. However, these irregularities were observed for the implantation of rather high impurity doses and for the high-concentration region only. This corresponds to the situation where supersaturation of the solid solution of lattice-site P atoms in Si exists, and structural defects may become the centers of precipitation.

The retardation of P diffusion by the Ge impurity atoms in the course of the joint P–Ge diffusion was associated with the effect of compensation of introduced mismatch stresses [5, 19]. These stresses were assumed to be the cause of enhanced diffusion either directly [5] or via the dislocations formed [19]. However, note that the mismatch stresses are localized in the heavily doped part of the diffusion layer, whereas the enhancement of diffusion is observed in the lightly doped part of the layer and is extended for considerable distances into the sample bulk [1–3], where the mismatch stresses are actually absent. In the model suggested previously [4], the presence of excess self-interstitials is considered as the cause of the enhancement of both P diffusion in the tail of the concentration profile and diffusion of other substitutional impurities outside the diffusion layer. The diffusion length of self-interstitials may be as large as tens and even hundreds of micrometers in defect-free Si and significantly decreases in the presence of structural defects or other sinks.

5. CONCLUSION

Thus, the influence of sinks associated with structural defects on high-temperature and low-temperature P diffusion is analyzed quantitatively in the context of the model of diffusion by the dual pair mechanism. It is demonstrated that the allowance made for sinks of excess self-interstitials or *PI* pairs, in contrast with the sink of P atoms, permits one to describe the retardation of diffusion for the low-concentration region in the tail of the P concentration profile. In this case, the capture of self-interstitials by sinks is more efficient than the capture of *PI* pairs. The influence of sinks is most pronounced if their highest concentration is located in the region of the most intense generation of self-interstitials inside the diffusion layer, $x_m \cong (0.4–0.5)x_{j0}$. The parameters of capture of self-interstitials by structural defects introduced by P diffusion, as well as by the ion implantation of electrically inactive Ge and N impurities, are evaluated.

REFERENCES

1. S. M. Hu, in *Atomic Diffusion in Semiconductors*, Ed. by D. Shaw (Plenum, London, 1973; Mir, Moscow, 1975), Chap. 5.
2. S. M. Hu, P. Fahey, and R. W. Dutton, J. Appl. Phys. **54**, 6912 (1983).
3. P. M. Fahey, P. B. Griffin, and J. D. Plummer, Rev. Mod. Phys. **61**, 289 (1989).
4. O. V. Aleksandrov, Fiz. Tekh. Poluprovodn. (St. Petersburg) **35**, 1289 (2001) [Semiconductors **35**, 1231 (2001)].
5. S. Matsumoto, Y. Akao, K. Kohiama, and T. Niimi, J. Electrochem. Soc. **125**, 1840 (1978).
6. O. V. Aleksandrov, Élektron. Tekh., Ser. 6, No. 6 (143), 58 (1980).
7. O. V. Aleksandrov, G. A. Gavrikov, and V. I. Prokhorov, Élektron. Tekh., Ser. 2, No. 2 (145), 69 (1981).
8. O. V. Aleksandrov, G. A. Gavrikov, I. P. Matkhanova, and V. I. Prokhorov, Vopr. At. Nauki Tekh., Ser. Fiz. Radiats. Povrezhdeniĭ Radiats. Materialoved., No. 2 (16), 78 (1981).
9. M. Servidori and S. Solmi, J. Appl. Phys. **65**, 98 (1989).
10. J. R. Pfiester and P. B. Griffin, Appl. Phys. Lett. **52**, 471 (1988).
11. O. V. Aleksandrov, R. Z. Tumarov, and N. A. Kondrat'ev, in *Proceedings of the VI All-Union Conference "Interactions of Atomic Particles with a Solid", Minsk, 1981*, Part 2, p. 51.

12. V. T. Karmanov, A. F. Khokhlov, P. V. Pavlov, and E. I. Zorin, Fiz. Tekh. Poluprovodn. (Leningrad) **11**, 1871 (1977) [Sov. Phys. Semicond. **11**, 1096 (1977)].
13. D. K. Sadana, M. Strathman, J. Washburn, *et al.*, Appl. Phys. Lett. **37**, 615 (1980).
14. R. Sh. Malkovich, *Mathematical Treatment of Diffusion in Semiconductors* (Nauka, St. Petersburg, 1999), p. 160.
15. H. Ryssel and I. Ruge, *Ionenimplantation* (Teubner, Stuttgart, 1978; Nauka, Moscow, 1983).
16. S. Prussin, J. Appl. Phys. **32**, 1776 (1961).
17. V. A. Panteleev, Fiz. Tverd. Tela (Leningrad) **21**, 3388 (1979) [Sov. Phys. Solid State **21**, 1956 (1979)].
18. V. A. Panteleev, M. I. Vasilevskiĭ, G. M. Golemshtok, and V. I. Okulich, Fiz. Tverd. Tela (Leningrad) **28**, 3226 (1986) [Sov. Phys. Solid State **28**, 1820 (1986)].
19. L. A. Koledov and L. N. Sergeev, in *Proceedings of Doped Semiconductors* (Nauka, Moscow, 1977), p. 143.

Translated by N. Korovin

Semiconductors, Vol. 36, No. 11, 2002, pp. 1267–1269. Translated from Fizika i Tekhnika Poluprovodnikov, Vol. 36, No. 11, 2002, pp. 1351–1353.

ELECTRONIC AND OPTICAL PROPERTIES OF SEMICONDUCTORS

Possibility of Observing Bose–Einstein Condensation in Semiconductors via Mössbauer Spectroscopy using the ^{67}Zn Isotope

S. A. Nemov*, N. P. Seregin*, and S. M. Irkaev**

** St. Petersburg State Technical University, St. Petersburg, 195251 Russia*

*** Institute for Analytical Instrumentation, Russian Academy of Sciences, St. Petersburg, 198103 Russia*

Submitted April 1, 2002; accepted for publication April 4, 2002

Abstract—It has been determined using emission Mössbauer spectroscopy on ^{67}Cu(^{67}Zn) and ^{67}Ga(^{67}Zn) isotopes that a transition to the superconducting state leads to a change of the electron density on the metal sites of the crystal lattices of the copper–metal oxides $Nd_{1.85}Ce_{0.15}CuO_4$, $La_{0.18}Sr_{0.15}CuO_4$, $YBa_2Cu_3O_{6.6}$, $YBa_2Cu_3O_{6.9}$, $YBa_2Cu_4O_8$, $Bi_2Sr_2CaCu_2O_8$, $Tl_2Ba_2CaCu_2O_8$, $HgBa_2CuO_4$, and $HgBa_2CaCu_2O_4$. A correlation between the change in electron density and the temperature of the crystal transition to the superconducting state is found. The expected change of the electron density on ^{67}Zn nuclei for materials with a phase transition temperature below 10 K turns out to be negligible. That is why the reliable observation of a change of the electron density for the superconducting transition in semiconductors with the use of spectroscopy on the ^{67}Zn isotope appears to be unlikely. © *2002 MAIK "Nauka/Interperiodica".*

The superconducting properties of semiconductors have been studied sufficiently; the highest critical temperature T_c reaches a few tenths of a Kelvin [1]. The IV–VI semiconductors doped with Group-III impurities, In and Tl, generate resonance levels on the background of the valence band of crystals [2]. Solid solutions of $Pb_{1-x}Sn_xTe$ ($x \approx 0.5$) doped with In have the maximum critical temperature for a semiconductor, reaching 4.2 K [3]. Additional interest in them is due to similarities in their properties with the high temperature superconductors based on YBaCuO.

The study of the properties of the Bose–Einstein condensate, using the Mössbauer effect technique [4], is a new direction in the study of superconducting materials. The phenomenon of superconductivity is related to the formation of the Bose–Einstein condensate of Cooper pairs, which is described by a single coherent wave function, so that the electron density distributions on crystal lattice sites of a superconductor are different at temperatures above and below the temperature of transition to the superconducting state, T_c [5]. Mössbauer spectroscopy provides, in principle, the possibility of detecting the Bose–Einstein condensation of Cooper pairs by measuring the temperature dependence of the Mössbauer spectrum centroid (S) for superconductors at a fixed pressure P [6]:

$$\left(\frac{\delta S}{\delta T}\right)_P = \left(\frac{\delta I}{\delta \ln V}\right)_T \left(\frac{\delta \ln V}{\delta T}\right)_P + \left(\frac{\delta D}{\delta T}\right)_P + \left(\frac{\delta I}{\delta T}\right)_V. \quad (1)$$

Let us consider the right-hand side of this equality. The first term is the dependence of the isomer shift I on the volume V. The second term describes the effect of the second-order Doppler shift D. It has the following form within the Debye approximation [6]:

$$\left(\frac{\delta D}{\delta T}\right)_P = -\frac{3kE_0 \mathrm{F}(T/\Theta)}{2Mc^2}, \quad (2)$$

where k is the Boltzmann constant, E_0 is the isomeric transition energy, M is the mass of a probe nucleus, c is the speed of light in free space, Θ is the Debye temperature, and $\mathrm{F}(T/\Theta)$ is the Debye function. Finally, the third term describes the temperature dependence of the isomer shift I. It characterizes the electron density change on the Mössbauer nuclei:

$$I = \alpha \Delta |\Psi(0)|^2. \quad (3)$$

Here, $\Delta|\Psi(0)|^2$ is the difference of the relativistic electron densities at the nuclei under study in two samples, and α is the constant determined by the nuclear parameters of the isotope. It is this change in the electron density that is expected to occur at the transition of the host crystal to the superconducting state. The proper choice of the probe nucleus is necessary in order to solve this problem.

However, attempts to detect Bose–Einstein condensation in the classical superconductor Nb_3Sn, using Mössbauer spectroscopy for the ^{119}Sn isotope, failed [7]: the experimental dependence was satisfactorily described by the second-order Doppler shift, and no features in $S(T)$ behavior, which could be traced back to the change in the isomer shift, were detected. An anom-

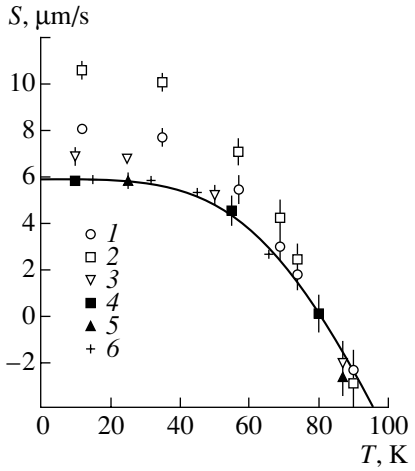

Fig. 1. Temperature dependences of the Mössbauer spectrum centroid for $^{67}Zn^{2+}$ at sites (*1*, *4*) Cu(1), (*2*, *5*) Cu(2), and (*3*, *6*) Y measured relative to its magnitudes at 90 K for (*1–3*) $YBa_2Cu_4O_8$ and (*4–6*) $YBa_2Cu_4O_x$. The solid line shows the theoretical temperature dependence of *S* for the second-order Doppler shift at $\Theta = 400$ K.

alous change of *S* in the Mössbauer spectra of ^{57}Fe impurity atoms was also not detected in high temperature superconductors [8]. These facts are accounted for by the small magnitude of Δ/G (here, Δ is the maximum achievable difference of the Mössbauer spectra isomer shifts in the normal and superconducting phases, and *G* is the experimental width of the nuclear level), which does not exceed 6 for the case of Mössbauer spectroscopy on ^{57}Fe and ^{119}Sn isotopes.

Obviously, a probe with $\Delta/2G \gg 10$ must be used in order to detect Bose–Einstein condensation using Mössbauer spectroscopy. The choice of the objects of investigation must take into consideration the necessity of introducing a Mössbauer probe into the lattice. These conditions can be fulfilled for the Mössbauer probe ^{67}Zn ($\Delta/2G \approx 200$) in lattices of copper–metal oxides and lead chalcogenides. Indeed, the daughter isotope ^{67}Zn is found at the copper site of the lattice of copper–metal oxides [4] when an emission variant of Mössbauer $^{67}Cu(^{67}Zn)$ spectroscopy is employed. At the same time, in the case of $^{67}Ga(^{67}Zn)$ emission Mössbauer spectroscopy, the daughter isotope ^{67}Zn is found at rare-earth sites in copper–metal oxides [4] or in the metal sublattice in lead chalcogenides [9].

Taking into account the aforementioned similarity in the properties of YBaCuO and IV–VI compounds with resonance levels, the experimental verification of the expounded notions on the Mössbauer spectroscopy potentiality for the study of Bose–Einstein condensation was carried out on YBaCuO samples.

The Mössbauer sources were prepared via the diffusion of radioactive carrier-free ^{67}Cu and ^{67}Ga into polycrystalline samples in evacuated quartz ampules at 450°C for 2 h. Materials obtained by annealing the initial superconducting samples in air at 600°C for 2 h, in which a transition to the superconducting state was not observed, were used as a reference. The Mössbauer spectra were measured with a modified MS-2201 commercial spectrometer with a ^{67}ZnS absorber. The temperature of the absorber was equal to 10 ± 1 K, while the source temperature could be varied within the range from 10 ± 2 to 90 ± 2 K. Typical $S(T)$ dependences are presented in Fig. 1.

It turned out that for all reference samples, within the range of 10–90 K, the temperature dependence of the spectrum centroid *S*, measured relative to its position at T_c, is well described by (2) if the Debye temperature values obtained from the thermal capacitance measurements [10–13] are used. The dependence $S(T)$ for superconducting samples at $T > T_c$ is also described by the second-order Doppler shift (2), and the Debye temperatures do not change in comparison with the reference samples. *S* depends more sharply on the temperature at $T < T_c$ than follows from (2), and, in (1), one must take into account the temperature dependence of the isomer shift.

In order to describe the observed phenomena, we introduce the maximum value of the isomer shift I_0 at $T \longrightarrow 0$ K, which is determined as the difference $I_0 = S_0 - D_0$. Here, S_0 and D_0 are, respectively, the spectrum centroid and the Doppler shift of the spectrum at $T \longrightarrow 0$ K. The isomer shift of the Mössbauer spectra is directly related via (3) to a change of the electron density on ^{67}Zn nuclei. The quantity I_0 characterizes the electron density created by the Bose–Einstein condensate when all conduction electrons have formed Cooper pairs. We used the value of α from [14] for the calculation of $\Delta|\psi(0)|^2$ from I_0.

I_0 depends on the nature of the site at which the Mössbauer probe is located: the maximum I_0 is observed for the Cu(2) sites (6.9 μm/s), a significantly lesser value, for Cu(1) sites (2.9 μm/s), and a minimum value of I_0, for Y sites (1.9 μm/s).

The dependence of $\Delta|\Psi(0)|^2$ on T_c^{-1} is depicted in Fig. 2. The quantity $\Delta|\Psi(0)|^2 = |\Psi_c(0)|^2 - |\Psi_0(0)|^2$ increases with increasing T_c, which reflects the electron density increase on ^{67}Zn nuclei at the transition from the normal phase ($|\Psi_0(0)|^2$) to the superconducting one ($|\Psi_c(0)|^2$). The dependence of $\Delta|\Psi(0)|^2$ on T_c can be understood if we recall that the standard correlation length ξ_0 (the Cooper pair size at $T \longrightarrow 0$ K) is proportional to $\xi_0 \propto T_c^{-1}$ for anisotropic superconductors, and, thus, Fig. 2 reflects the dependence of I_0 and $\Delta|\Psi(0)|^2$ on the standard correlation length ξ_0. The dependence $\Delta|\Psi(0)|^2 = f(1/T_c)$ is exponential:

$$\Delta|\Psi(0)|^2 = 0.2\exp[-31.4/T_c],$$

where $|\Psi(0)|^2$ is measured in atomic units (au).

It can be seen that the maximum possible electron density change at ^{67}Zn nuclei at the superconducting

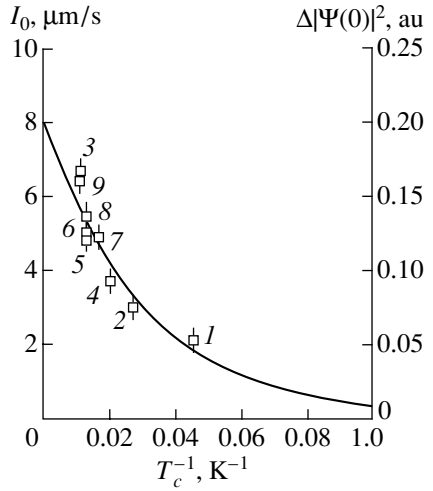

Fig. 2. Dependence of I_0 and $\Delta|\Psi(0)|^2$ on T_c^{-1}. Points with numerals represent data for (*1*) Cu(1) in $Nd_{1.85}Ce_{0.15}CuO_4$, (*2*) Cu(1) in $La_{0.18}Sr_{0.15}CuO_4$, (*3*) Cu(2) in $YBa_2Cu_3O_{6.9}$, (*4*) Cu(2) in $YBa_2Cu_3O_{6.6}$, (*5*) Cu(2) in $YBa_2Cu_4O_8$, (*6*) Cu(1) in $Bi_2Sr_2CaCu_2O_8$, (*7*) Cu(1) in $Tl_2Ba_2CaCu_2O_8$, (*8*) Cu(1) in $HgBa_2CuO_4$, and (*9*) Cu(1) in $HgBa_2CaCu_2O_6$. The data for $Nd_{1.85}Ce_{0.15}CuO_4$, $La_{0.18}Sr_{0.15}CuO_4$, and $Tl_2Ba_2CaCu_2O_8$ are taken from [2].

transition is $\Delta|\Psi(0)|^2 = 0.2$ a.u., which corresponds to the minimum possible "size" of the Cooper pair, $\xi_0^{\min}$. The existence of such a minimum size is probably related to the physical impossibility for pairs to exist when the distance between their components is less than a certain length. We can estimate $\xi_0^{\min}$ taking into consideration that the full "localization" of the Cooper pair at the Mössbauer probe ^{67}Zn (the process $3d^{10} \longrightarrow 3d^{10}4s^2$ and the Cooper pair size are determined by the atomic radius of the Zn^{2+} ion, $R \approx 0.83$ Å) must lead to an increase of the isomer shift by ~180 μm/s (transition from ZnF_2 to Zn) [14], i.e., to an electron density increase by 4.5 au. Therefore, assuming the dependence $\Delta|\Psi(0)|^2 \propto \xi_0^{-3}$ at small ξ_0, we obtain $\xi_0^{\min} \approx 2.5$ Å, which is in agreement with the conventional values $\xi_0^{\min} \approx 0.5$–30 Å [15].

It is important that, if the Cooper pair size is large (significantly larger than the atomic scale), the electron density change on the ^{67}Zn nuclei be negligible, and it is unlikely that a change in the electron density for materials with a phase transition temperature $T_c < 10$ K, using the spectroscopy on the ^{67}Zn isotope, will be reliably observed.

Thus, it is established that a transition to the superconducting state leads to a change of the electron density at the metal sites of the lattices of copper–metal oxides, with an experimentally measurable relation existing between the electron density change and the temperature of the crystal transition to the superconducting state. The expected change of the electron density at the ^{67}Zn nuclei for materials with $T_c < 10$ K is negligible, and it is unlikely that changes in the electron density can be reliably detected with the use of spectroscopy on the ^{67}Zn isotope for the superconducting transition in semiconductors based on $Pb_{1-x}Sn_xTe$:In.

ACKNOWLEDGMENTS

This study was supported by the Ministry of Education of the Russian Federation (project no. E-00-34-42) and the Russian Foundation for Basic Research (project no. 02-02-17306).

REFERENCES

1. M. L. Cohen, *et al.*, *Superconductivity*, Ed. by R. Parks (Marcel Dekker, New York, 1969; Mir, Moscow, 1972).
2. S. A. Nemov and Yu. I. Ravich, Usp. Fiz. Nauk **168**, 817 (1998) [Phys. Usp. **41**, 735 (1998)].
3. R. V. Parfeniev, D. V. Shamshur, and M. F. Shakhov, J. Alloys Compd. **219**, 313 (1995).
4. N. P. Seregin and P. P. Seregin, Zh. Éksp. Teor. Fiz. **118**, 1421 (2000) [JETP **91**, 1230 (2000)].
5. J. R. Schrieffer, *Theory of Superconductivity* (Benjamin, New York, 1964; Nauka, Moscow, 1970).
6. D. L. Nagy, in *Mössbauer Spectroscopy of Frozen Solutions*, Ed. by A. Vértes and D. L. Nagy (Akadémiai Kiadó, Budapest, 1990; Mir, Moscow, 1998).
7. J. S. Shier and R. D. Taylor, Phys. Rev. **174**, 346 (1968).
8. Yun-Bo Wang, Guo-Hui Cao, Yang Li, *et al.*, Physica C (Amsterdam) **282–287**, 1087 (1997).
9. S. A. Nemov and N. P. Seregin, Fiz. Tekh. Poluprovodn. (St. Petersburg) **36** (8), 914 (2002) [Semiconductors **36**, 852 (2002)].
10. T. Sasaki, N. Kobayashi, O. Nakatsu, *et al.*, Physica C (Amsterdam) **153–155**, 1012 (1988).
11. H. M. Ledbetter, S. A. Kim, and R. B. Goldfarb, Phys. Rev. B **39**, 9689 (1989).
12. A. Junod, T. Craf, D. Sanchez, *et al.*, Physica C (Amsterdam) **165/166**, 1335 (1990).
13. S. J. Collocott, R. Driver, C. Audrikidis, and F. Pavese, Physica C (Amsterdam) **156**, 292 (1989).
14. A. Svane and E. Antoncik, Phys. Rev. B **34**, 1944 (1986).
15. *Physical Properties of High Temperature Superconductors*, Ed. by D. M. Ginsberg (World Scientific, Singapore, 1989; Mir, Moscow, 1990).

Translated by S. Ktitorov

Semiconductors, Vol. 36, No. 11, 2002, pp. 1270–1275. Translated from Fizika i Tekhnika Poluprovodnikov, Vol. 36, No. 11, 2002, pp. 1354–1359.

ELECTRONIC AND OPTICAL PROPERTIES OF SEMICONDUCTORS

Radiation Hardness of Wide-Gap Semiconductors (using the Example of Silicon Carbide)

A. A. Lebedev*, V. V. Kozlovski, N. B. Strokan*, D. V. Davydov*, A. M. Ivanov*, A. M. Strel'chuk*, and R. Yakimova*****

** Ioffe Physicotechnical Institute, Russian Academy of Sciences, St. Petersburg, 194021 Russia*

*** St. Petersburg State Technical University, St. Petersburg, 195251 Russia*

**** Linköping University, S-581 83 Linköping, Sweden*

Submitted April 18, 2002; accepted for publication April 25, 2002

Abstract—Results obtained in studying the effect of ionizing radiation on epitaxial layers and devices based on silicon carbide (SiC) are considered. It is shown that, in investigations of wide-gap semiconductors (WGS), account should be taken of how the rate of removal of mobile charge carriers—the standard parameter in determining the radiation hardness of a material—depends on temperature. The use of data obtained only at room temperature may lead to an incorrect assessment of the radiation hardness of WGS. A conclusion is made that the WGS properties combine, on the one hand, high radiation hardness of high-temperature devices based on these semiconductors and, on the other, the possibility of effective radiation-induced doping (e.g., for obtaining semi-insulating local regions in a material at room temperature). *© 2002 MAIK "Nauka/Interperiodica".*

1. INTRODUCTION

The investigation of wide-gap semiconductors (WGS) has been one of the most rapidly developing branches of semiconductor physics in recent years. By convention, wide band-gap materials include semiconductors with a band gap $E_g > 2.3$–2.4 eV (SiC polytypes, diamond, GaN, AlN, BN, etc.). The rapid development of growth technologies for a number of WGS (SiC, GaN) yielded *n*- and *p*-type materials in a wide range of doping impurity concentrations and made it possible to create, on the basis of these materials, analogues for most of the existing devices. WGS-based devices are characterized by a number of specific features directly related to the fact that the E_g of WGS is 3–4 times greater than that in other materials.

From the standpoint of radiation hardness, two of the most important features can be distinguished:

(1) Quite a number of potential barriers in the material (ionization energy of deep centers, contact potential, Schottky barrier, etc.) are higher;

(2) The working temperature range of the devices is severalfold wider.

The second circumstance should be taken into account when comparing the radiation hardnesses of narrow band-gap (NBS) and WGS materials. Indeed, if the properties of different materials are compared at a single temperature *T*, the result may not always be correct: at this temperature, the NBS may be close to the intrinsic conduction range, whereas the WGS is only at the beginning of its working temperature range and not all of the main doping impurities have been ionized. Therefore, an "isothermal" comparison may prove incorrect in assessing the radiation hardness of a material.

The aim of the present study is to analyze how specific features of WGS may affect the radiation hardness of these semiconductors and the possibility of their radiation-induced doping (with a semi-insulating material obtained upon irradiation). We chose SiC as an example, as it is a material with the best-developed growth technology and best-understood radiation defects among WGS.

2. RATE OF CARRIER REMOVAL

2.1. Preliminary Remarks

Radiation hardness is commonly understood as the stability of parameters of a semiconductor or a semiconductor device under nuclear irradiation. The higher the irradiation dose necessary for the parameters to start changing, the better the radiation hardness of a semiconductor.

It is known that irradiation of semiconductors leads to the formation in them of deep centers—radiation defects of an acceptor or donor nature. Henceforth, we consider the irradiation of an *n*-type material for the sake of definiteness. In this case, electrons transfer under irradiation from the conduction band to deep radiation defects with acceptor nature. As a result, the conductivity of the material decreases and the semiconductor may become an insulator at large irradiation doses. This process is commonly described for various

Table 1. Contribution of radiation defects to carrier density in relation to their type and energy position in the band gap

Groups of levels	Radiation defect level at $T_M > T_{irr}$	Type of radiation defect	Δn at $T_M = T_{irr}$	Change Δn at $T_M > T_{irr}$, $\Delta n = f(T)$ (with degeneracy factor disregarded)
1	$E_F < E_{RD} < 0$	A	0	No
	$E_F < E_{RD} < 0$	D	$+N_{D1}$	No
2	$E_F < E_{RD} > 0$; $E_{RD} \geq (1/2)E_g$	A	$-N_{A2}$	$-N_{A2}/\{1 + \lambda_{A2}\exp[(E_{A2} - E_F)/kT]\}$
	$E_F < E_{RD} > 0$; $E_{RD} \geq (1/2)E_g$	D	0	$+N_{D2}/\{1 + \lambda_{D2}^{-1}\exp[(E_F - E_{D2})/kT]\}$
3	$E_{RD} < (1/2)E_g$	A	$-N_{A3}$	No
	$E_{RD} < (1/2)E_g$	D	0	No

Note: T_M is measurement temperature; T_{irr}, irradiation temperature; and Δn, contribution to carrier density.

materials using such a parameter as carrier removal rate V_d [1],

$$V_d = \Delta n/D = (n_0 - n)/D, \quad (1)$$

where n_0 and n are the carrier densities in the conduction band before and after irradiation, and D is the irradiation dose.

Let us assume that the Fermi level in the band gap lies several kT (T, temperature; k, Boltzmann constant) lower than the main donor levels and that the total concentration of the radiation defects introduced is much lower than the net concentration of donors and acceptors, $N_D - N_A$. This means that, at low irradiation doses (and this is commonly the case in determining the carrier removal rate), we believe that irradiation does significantly change the Fermi level position (E_F). Let us now consider the contribution to V_d from the radiation defects formed in relation to their type (donor D or acceptor A) and position in the band gap. All of the resulting radiation defects can be conventionally divided, depending on their energy position (E_{RD}), into three groups.

(1) Radiation defects lying higher than the main donor levels. In the case where these radiation defects are donors (D_1), they contribute to a rise in the carrier density in the conduction band by an amount equal to their concentration N_{D1}. If these radiation defects are acceptors (A_1), their formation has no effect on the carrier density in the conduction band. As the measurement temperature increases, the contributions from both types of radiation defects to the measured V_d value remain unchanged.

(2) Radiation defects lying in the upper half of the band gap below the main donor levels and the Fermi level. In the case where these radiation defects are acceptors (A_2), their introduction reduces the electron density in the conduction band by an amount equal to their concentration N_{A2}. If these radiation defects are donors (D_2), they make no contribution to the free electron density. With increasing temperature (or with the Fermi level decreasing as a result of irradiation), these radiation defects find themselves several kT away from the Fermi level and the degree of their ionization grows. As a result, the contribution from acceptor levels to the V_d value decreases and that from donor levels increases.

(3) Radiation defects lying in the lower half of the band gap. In the case where these radiation defects are acceptors (A_3), they contribute to a decrease in the carrier density in the conduction band by an amount equal to their concentration N_{A3}. If these radiation defects are donors (D_3), their formation has no effect on the carrier density in the conduction band. With increasing measurement temperature, the contributions from both types of radiation defects to the measured V_d value remain constant.

Table 1 presents the contribution of radiation defects and its temperature dependences for each type of the radiation defects mentioned (henceforth, the Fermi level position is reckoned from the valence band top). Correspondingly, we can write a formula for V_d taking into account the temperature dependence of the occupancy of levels related to radiation defects:

$$n = n_0 + D\left\{K_{D1} - K_{A3} + K_{D2}\frac{1}{1 + \lambda_{D2}^{-1}\exp[(E_F - E_{D2})/kT]} - K_{A2}\frac{1}{1 + \lambda_{A2}\exp[(E_{A2} - E_F)/kT]}\right\}, \quad (2)$$

where K_j is the total rate of introduction of jth type defects, $N_j = K_jD$ is the concentration of jth type defects, and λ_j is the degeneracy factor of the levels related to the corresponding radiation defects.

Formula (2) can be written in simplified form as

$$n = n_0 - [\Delta n_1 + \Delta n(T_M)], \quad (3)$$

where Δn_1 is the temperature-independent change in carrier density; and $\Delta n(T_M)$ is the change in carrier density, which is dependent on the measurement temperature T_M.

Table 2. Calculated threshold energies of defect formation for some semiconductors

Parameter	GaAs	Si	3*C*-SiC	Diamond	6*H*-SiC, 4*H*-SiC
Lattice constant a_0, Å	5.65	5.431	4.36	3.57	3.08
Threshold energy E_d, eV	9	12.8	37	80	153

Correspondingly, for the carrier removal rate we can write

$$V_d = V_{d_1} + V_d(T_M), \quad (4)$$

where V_{d_1} is a temperature-independent term.

An important conclusion follows from formulas (1)–(4): if two temperatures, $T_{M1} < T_{M2}$, are taken, then $V_d(T_{M1}) \geq V_d(T_{M2})$; i.e., the V_d value can only decrease as the measurement temperature increases. Therefore, we have, at limiting working temperatures (with the Fermi level close to the midgap of a given semiconductor), $(E_F \approx (1/2)E_g)$ $V_d(T_M) \approx 0$ if only acceptor radiation defects were formed under irradiation, and $V_d(T_M) < 0$ if donor radiation defects were also generated. If the total concentration of donors formed upon irradiation exceeds that of the resulting acceptors, the total V_d may be negative at high temperature, $V_{d_1} + V_d(T_M) < 0$. If this were the case, it would be more appropriate to speak about the introduction rate of carriers into the semiconductor (rather than their removal) under irradiation.

It should also be noted that the experimental value of V_d may depend on the measurement technique employed. For example, the presence of deep centers in the semiconductor before irradiation leads to an additional rise in n with increasing temperature, i.e., $n_0 = f(T)$. A situation where $n_0 = \gamma(N_D - N_A))$, with $\gamma < 1$ and γ approaching unity with increasing T, is typical of WGS, in general, and of SiC, in particular. To eliminate the influence of the temperature dependence of n_0 on the results of V_d measurements, it is necessary to measure this dependence in a sample under study before its irradiation.

These difficulties necessitate the search for other ways to compare radiation effects. For example, there is no need to heat a sample to the limiting working temperatures and measure the carrier density n_0 in order to determine V_d in the entire range of irradiation doses. The net concentration of ionized donors and acceptors $|N_D^+ - N_A^-|$ in the space charge region can serve as a measure of n_0. In this case, it suffices to measure the capacitance–voltage (C–V) characteristics at a lower temperature. Whether or not a particular level contributes to the $|N_D^+ - N_A^-|$ value measured at a given temperature depends on the relationship between the time constant of its ionization (τ) and the time (t) during which a C–V characteristic is measured, $t/\tau > 1$, i.e., $t\eta = \tau$ ($\eta < 1$). Any semiconductor is characterized by its own temperature T_{CV} at which the limiting value of V_d can be evaluated by the capacitive method. It is known that

$$\tau^{-1} = V_T \sigma_N N_c \exp(-E_i/kT),$$

where V_T is the thermal velocity of carriers, σ_N is the cross section of electron capture by a level, N_c is the density of states in the conduction band, and E_i is the ionization energy of a center.

Hence, we obtain

$$T_{CV} = E_i/k\ln(V_T \sigma_N N_c \eta t). \quad (5)$$

Assuming that $E_i = (1/2)E_g$, $\sigma_N = 10^{-16}$ cm^{-3}, $t = 600$ s, and $\eta = 0.2$, we can estimate T_{CV} for Si and 4*H*-SiC to be, respectively, ~230 and ~630 K. This estimate shows that the C–V technique can be applied at room temperature to obtain the limiting V_d value for silicon. This temperature is insufficient for determining V_d for WGS.

2.2. Experimental Data on V_d

To begin with, it can be noted that the V_{d_1} value must depend on the parameter E_d, the threshold energy of defect formation. The higher E_d, the lower, as a rule, V_d. As far as we know, the literature contains no evidence about the experimental value of E_d for SiC. In [2], mention was made of the relationship between E_d and the lattice constant (a_0) of a given semiconductor, which satisfies the phenomenological equation

$$1.117E_d = (10/a_0)^{4.363}. \quad (6)$$

Table 2 presents the results of calculation of E_d, which was carried out for a number of semiconductors using formula (6). This formula is presumably not strict enough, especially for semiconductors with a small lattice constant; however, it leads to the conclusion that the E_d value for 4*H*- and 6*H*-SiC is approximately an order of magnitude higher than that for Si and two times that for diamond (Table 2). Thus, it would also be expected that V_{d_1} for SiC is smaller than that for Si.

Let us now consider experimental studies in which the V_d value was determined for SiC polytypes irradiated with various kinds of ions. Their results, along with published values of V_d for silicon subjected to irradiation under the same conditions, are presented in Table 3.

According to the majority of the reports [3–9], $V_d(\text{Si}) \geq V_d(\text{SiC})$ at $T = 300$ K. However, the values

Table 3. V_d values for SiC and Si according to data of different authors

SiC										
Particles	α	H^+	α	Neutrons	Neutrons	Electrons	Protons			
Particle energies	1.7 MeV	350 keV	5.5 MeV	1 MeV		1 MeV	8 MeV			
D, cm^{-2}	2×10^9	1×10^{14}	2×10^{11}	10^{14}			6×10^{14}			
SiC polytype	4*H*	4*H*	6*H*	3*C*	6*H*	3*C*	6*H*		4*H*	
$N_D - N_A$, cm^{-3}	1×10^{15}	2×10^{18}		10^{16}			4×10^{16}			
T_M, K	300	300	300	300	300	300	300	650	300	650
V_d, cm^{-1}	4×10^5	2×10^4	7.8×10^4	7.2	4.5	0.014	17	−45	130	67
Reference	[3, 4]	[5]	[6]	[7]	[8]	[9]	[10]			
Si										
Particles	α			Neutrons		Electrons	Protons			
V_d, cm^{-1}	5×10^4			7.8		0.01–0.1	200–350			
Reference	[3, 4]			[7]		[1]	[12, 12]			

obtained in [3, 4], for which the reverse is true, with $V_d(\mathrm{SiC})/V_d(\mathrm{Si}) \approx 10$, drop out from this body of data. In these studies, irradiation was done with 1.7 MeV alpha particles at a dose of 2×10^9 cm^{-2}. The particle ranges were 3.8 μm for SiC and 5.9 μm for Si. It should be noted that the authors of these studies only monitored the effects occurring at the end of the particle range and, consequently, the effects they observed may be due to helium forming at this depth, rather than to radiation defects.

Moreover, the data in [3–9] were obtained at room temperature, at which the $V_d(T_M)$ value is still high for SiC. High-temperature measurements confirmed that, in the case of SiC, we have either $V_{d_1} \approx V_d(T_M)$ (4*H*-SiC) or $V_{d_1} \ll V_d(T_M)$ (6*H*-SiC) [10]. Apparently, irradiation of *n*-6*H*-SiC leads to the formation of radiation effects of both donor and acceptor nature, with donors predominant. Presumably, the same mechanism is operative in the case of *p*-6*H*-SiC, for which a change in the type of conduction, $p \longrightarrow n$, upon irradiation has been observed [13].

An approach to the analysis of how radiation defects are formed in WGS was developed [14] which is similar to the mechanism of conduction self-compensation. According to [14], a change in the type of conduction under irradiation is only characteristic of narrow band-gap semiconductors. At the same time, the conductivity of WGS subjected to irradiation tends to become intrinsic. Indeed, this assumption is in agreement with experiment if the temperatures at which V_d is measured in WGS are close to room temperature. If, however, we take into account the temperature dependence of V_d, then the approach mentioned above is only valid for 4*H*-SiC. For 6*H*-SiC and, presumably, 3*C*-SiC [15] the $N_D - N_A$ value grows under irradiation.

Thus, measuring V_d for WGS only at room temperature may prove insufficient. In view of the fact that WGS-based devices are mainly intended for high-temperature operation, investigations of the kind mentioned above may be considered incomplete.

3. RADIATION DOPING (COMPENSATION) OF WIDE-GAP SEMICONDUCTORS

Another important aspect of investigations into the interaction of ionizing radiation with a substance is radiation doping. Radiation doping of a semiconductor may lead to the formation of local regions with high resistivity, which are necessary for creating a device. It is commonly believed that the radiation hardness and the possibility of radiation doping are contradicting characteristics of a material, with a radiation-hard semiconductor considered to be unpromising for compensation by radiation doping.

We show below that such an assessment is not quite correct in the case of WGS. It is known that WGS are promising not only for high-temperature electronics, but also for a number of devices not intended for operation at a high temperature. First and foremost, these are high-frequency devices (Schottky diodes, some kinds of FETs) with a metal–semiconductor contact. Such a contact, as a rule, rapidly degrades with increasing temperature, irrespective of the maximum possible working temperatures of the semiconductor itself. If the working temperatures of a device do not greatly exceed 300 K, then we can use the V_d values obtained at this temperature for determining the efficiency of radiation doping. Another important parameter characterizing the efficiency of radiation doping is the maximum resistivity (ρ), which may be obtained for various semiconductors. This parameter can be evaluated using the known formula

$$\rho = (en\mu)^{-1}, \quad (7)$$

Table 4. Calculated ratio of highest WGS resistivity to Si resistivity, at 300 K

Semiconductor	ρ/ρ(Si)
GaAs	2.4×10^4
6*H*-SiC	6.6×10^{15}
4*H*-SiC	3.5×10^{18}

where e is the elementary charge, n is the electron density in the conduction band, and μ is the mobility.

Let us assume, when performing calculations, that, as a result of the irradiation of an *n*-type material, an acceptor level related to a radiation defect was formed at the midgap, with its ionization energy $E_i = (1/2)E_g$ and the concentration of the corresponding centers (N_{RD}) exceeding the total concentration of shallow donors, N_D. Then, n can be evaluated using the formula [16]

$$n = \frac{N_D N_c}{N_{RD} - N_D} \exp\left(-\frac{E_i}{kT}\right). \quad (8)$$

The results obtained in calculating the ratio of the resistivities of some semiconductors to the resistivity of silicon at $T = 300$ K are presented in Table 4. It can be seen that WGS markedly surpass NBS as materials for obtaining high-resistivity layers, which is in agreement with the conclusions of [14]. The semi-insulating properties of the layers are also preserved at higher temperatures. As shown by [10], the resistivity of 4*H*-SiC at $T = 450$ K is equal to the maximum value obtained for GaAs at room temperature ($\rho \sim 10^9$ Ω cm).

4. RADIATION HARDNESS OF REAL DEVICES

In the 1960s–1970s, extensive investigations that confirmed the high radiation hardness of SiC-based LEDs were carried out [17]. Today, these data have lost, to a certain extent, their topicality, since high-quality *p–n* structures have been fabricated on the basis of direct-gap WGS in recent years.

The growth of pure SiC layers made it possible to pass to the fabrication of a new group of high-voltage devices, including charge particle detectors [18, 19]. To date, a sufficient body of data on radiation hardness has been obtained for this type of devices, including data for high irradiation doses (Table 5).

It is noteworthy that nuclear particle detectors allow for the strictest and most direct comparison of the radiation hardnesses of the semiconducting materials used in their fabrication. These detectors are very sensitive to quite a number of properties: degradation of carrier transport parameters and the appearance of their nonuniformity, temporal stability of the amount (and sign) of the impurity-related space charge, presence of deep centers, and rate of carrier generation involving these centers.

As seen from Table 5, SiC detectors are at least as good as silicon devices. This follows from the fact that the carrier lifetimes in irradiated semiconductors are approximately the same. The low rate of thermal ionization of *R* centers in SiC, compared with that of the *E* center in Si, should ensure better characteristics with respect to the generation noise in SiC detectors. If we pass to a consideration of other types of devices, the advantage of SiC becomes indubitable. The order of magnitude higher critical field of electric breakdown, E_d, means that, given two devices with the same working voltage, the one based on SiC can have a doping level of the base region which is two orders of magnitude higher when compared with the Si-based device. Consequently, even when the rates of introducing compensating defects are close, compensation of SiC requires a dose that is two orders of magnitude higher than that for Si.

Moreover, the carrier removal rate can be further lowered in view of the fact that SiC is a material for high-temperature electronics and will be irradiated at high temperatures. At a low irradiation temperature ($T < 400$–500 K for SiC), the mobility of the forming primary radiation defects is low and they do not recombine, but form complexes, i.e., secondary radiation defects [20]. The aforesaid is confirmed by the fact that

Table 5. Comparison of radiation hardnesses of detectors based on Si and 6*H*-SiC (1 GeV protons)

Parameter	Si	6*H*-SiC
Highest rate of deep-center introduction, cm^{-1}	0.20	0.16
Lifetimes of electrons, τ_n, and holes, τ_p, ns	$\tau_n = 0.8$	$\tau_p = 2.4$
($D = 10^{15}$ cm^{-2})	$\tau_p = 3.7$	
Time constant of generation from the deepest radiation defect	*E* center	*R* center
	($E_c - 0.44$) eV	($E_c - 1.22$ eV)
	$\tau \approx 1.2 \times 10^{-6}$ s	$\tau \approx 1.2 \times 10^6$ s
E_{cr}, V/cm	3×10^5	$(2–3) \times 10^6$
T_{max}	~150°C	~1000°C

Note: T_{max}, the highest temperature of operation.

irradiation of SiC does not give rise to new deep centers, but only raises the concentration of the defects already present in the material [10]. As was shown for other semiconductors [21], partial recombination of the formed primary defects occurs at elevated temperatures and V_d decreases.

5. CONCLUSION

The analysis of the radiation hardness of wide band-gap semiconductors, compared with narrow band-gap materials, was based on two factors.

The first of these is associated with the structural features of a material which lead to differences in the bonding energy and threshold energy of defect formation, E_d. For example, a comparison with silicon demonstrated that SiC-based devices must have a higher radiation hardness. This follows from high E_d values and the high critical field strength of avalanche breakdown.

The second factor is the different temperature range of device operation. As a consequence, the assessment of the radiation hardness of WGS cannot rely solely upon room-temperature measurements because of the strong temperature dependence of the carrier removal rate in WGS.

It may be concluded that SiC (and, possibly, other WGS too) is a rather promising material for high-temperature radiation-hard electronics.

ACKNOWLEDGMENTS

This study was supported in part by the Royal Swedish Academy of Sciences (KVA).

REFERENCES

1. *Physical Processes in Irradiated Semiconductors*, Ed. by L. S. Smirnov (Nauka, Novosibirsk, 1972).
2. J. W. Corbett and J. C. Bourgein, in *Point Defect in Solids* (Plenum, New York, 1975), Vol. 2, p. 1.
3. B. G. Svensson, A. Hallen, M. K. Linnarsson, *et al.*, Mater. Sci. Forum **353–356**, 549 (2001).
4. A. Hallen, A. Henry, P. Pellegrino, *et al.*, Mater. Sci. Eng. **61–62**, 378 (1999).
5. R. K. Nadella and M. A. Capano, Appl. Phys. Lett. **70**, 886 (1997).
6. G. C. Rybicki, J. Appl. Phys. **78**, 2996 (1995).
7. V. Nagesh, J. W. Farmer, R. F. Davis, and H. S. Kong, Appl. Phys. Lett. **50**, 1138 (1987).
8. J. McGarrity, F. McLean, M. Dealancey, *et al.*, IEEE Trans. Nucl. Sci. **39**, 1974 (1992).
9. H. Itoh, M. Yashikawa, I. Nashiyama, *et al.*, Springer Proc. Phys. **56**, 143 (1992).
10. A. A. Lebedev, A. I. Veinger, D. V. Davydov, *et al.*, J. Appl. Phys. **88**, 6265 (2000).
11. V. S. Vavilov, N. U. Isaev, B. N. Mukashev, and A. V. Spitsyn, Fiz. Tekh. Poluprovodn. (Leningrad) **6**, 1041 (1972) [Sov. Phys. Semicond. **6**, 907 (1972)].
12. Yu. V. Bulgakov and T. I. Kolomenskaya, Fiz. Tekh. Poluprovodn. (Leningrad) **1**, 422 (1967) [Sov. Phys. Semicond. **1**, 346 (1967)].
13. V. V. Makarov, Fiz. Tverd. Tela (Leningrad) **13**, 2357 (1971) [Sov. Phys. Solid State **13**, 1974 (1972)].
14. V. L. Vinetskiĭ and L. S. Smirnov, Fiz. Tekh. Poluprovodn. (Leningrad) **5**, 176 (1971) [Sov. Phys. Semicond. **5**, 153 (1971)].
15. D. V. Davydov, A. A. Lebedev, A. S. Tregubova, *et al.*, Mater. Sci. Forum **338–342**, 221 (2000).
16. *Compensated Silicon*, Ed. by B. I. Boltaks (Nauka, Leningrad, 1972).
17. W. J. Choyke, Inst. Phys. Conf. Ser. **31**, 58 (1977).
18. F. H. Ruddy, A. R. Dullo, J. G. Seidel, *et al.*, IEEE Trans. Nucl. Sci. **45**, 536 (1998).
19. A. A. Lebedev, N. S. Savkina, A. M. Ivanov, *et al.*, Fiz. Tekh. Poluprovodn. (St. Petersburg) **34**, 249 (2000) [Semiconductors **34**, 243 (2000)].
20. H. Itoh and N. Haykawa, J. Appl. Phys. **66**, 4529 (1989).
21. V. V. Kozlovski, L. F. Zakharenkov, T. I. Kolchenko, and V. M. Lomako, Radiat. Eff. Defects Solids **138**, 63 (1996).

Translated by M. Tagirdzhanov

Semiconductors, Vol. 36, No. 11, 2002, pp. 1276–1282. Translated from Fizika i Tekhnika Poluprovodnikov, Vol. 36, No. 11, 2002, pp. 1360–1366.

ELECTRONIC AND OPTICAL PROPERTIES OF SEMICONDUCTORS

Kinetic Theory of Negative Magnetoresistance as an Alternative to Weak Localization in Semiconductors

V. É. Kaminskiĭ

Institute of Radio Engineering and Electronics, Russian Academy of Sciences, Moscow, 101999 Russia
e-mail: kamin@mail.cplire.ru

Submitted May 14, 2001; accepted for publication March 28, 2002

Abstract—A time-independent solution to the kinetic equation for the one-electron density matrix at an arbitrary magnetic field and linear in the electric field has been obtained within the nonequilibrium electron gas approximation. The case of scattering on deformation potential is considered. Expressions for the conductivity tensor are obtained in the form of sums over the magnetic quantization states. They are shown to coincide with classical ones in the absence of a magnetic field. Under weak magnetic fields, the magnetoresistance is positive when electron mobility is high and negative when it is low. It changes sign as the field increases when the mobility is intermediate. The magnetoresistance of the degenerate electron gas is nonzero. The conductivity tensor describes its oscillations in the quantizing magnetic field. Their amplitude and the magnetoresistance mean values increase with increasing magnetic field and mobility. © *2002 MAIK "Nauka/Interperiodica".*

1. INTRODUCTION

The kinetic equation for the electron distribution function is traditionally applied to describe galvanomagnetic effects in semiconductors. Such an approach is valid in most cases for a weak magnetic field. However, a whole series of specific effects reveal themselves at strong fields, and these cannot be described within the framework of such an approach. This becomes most apparent for the magnetoresistance oscillations (Shubnikov–de-Haas effect). The problem of transverse galvanomagnetic effects was solved for strong magnetic fields by Adams and Holstein [1]. The authors calculated the conductivity tensor elements as functions of the magnetic field B and the temperature for various electron scattering mechanisms. However, the logarithmic divergence under zero electron energy in the nondegenerate case necessitated the introduction of a cutoff so that averaging over the states could be carried out. This shows the limitations of the approach introduced in [1]. Similar expressions for the 2D electrons were derived in [2].

There is now a considerable amount of experimental data that cannot be explained either by using the classical approach or the one developed in [1] (see, e.g., the review [3]). The longitudinal and transverse negative magnetoresistance (NMR) is a typical example. This phenomenon is observed in various semiconducting objects both under strong and weak magnetic fields. NMR was observed in, e.g., lightly [4] and heavily [5] doped germanium. In the latter case, this phenomenon was observed on both sides of the metal–insulator transition point, with the magnetoresistance (MR) becoming positive under strong fields in the metallic state. In the dielectric state, however, NMR was observed within all ranges of the fields (0–10 T). At the same time, a change in the sign of MR was observed in the dielectric state [4]. MR of various kinds was observed in *n*-AlGaAs/GaAs heterostructures [6] at a temperature of 4.2 K. MR was positive in structures with a high mobility and high surface density of carriers. The MR of low-mobility structures was negative within the field range of 0 to ~0.5 T. It changed sign with a further increase in the field. MR remained negative up to the onset of quantum oscillations in structures with a low carrier mobility and low surface density. In the center of a quantum well (QW) in *n*-GaAs/$In_{0.07}Ga_{0.93}As$/*n*-GaAs heterostructures δ-doped with silicon, NMR was observed up to fields of about 6 T within the temperature range of 0.4–40 K [7]. At the same time, positive MR (antilocalization) was observed under very weak fields in InP/$In_{0.53}Ga_{0.47}As$ heterostructures [8] with a higher mobility and a larger surface density of electrons. In the low-density case, NMR was observed within the entire range of the fields. Quantum quasi-1D threads were obtained in [9] through δ-doping of the GaAs vicinal face with tin. NMR was observed up to fields of about 6 T along the threads and up to 30 T across them. The carbon nanotubes were 1D-conducting crystals. The band gap and the type of conduction (metallic or semiconducting) of the nanotube are determined by its crystal structure (see, e.g., the review [10]). A rise of nanotube conductance with the magnetic field is observed in most of the experiments. NMR is observed both in single nanotubes [11] and in films

composed of them [12, 13] at fields up to 14 T within the temperature range of 0.1–180 K. This is observed in films where the magnetic field is directed both along and across the nanotube axes. The discussed experimental data show that NMR is a characteristic feature of many conducting objects with different structures and dimensionality. This phenomenon cannot be explained either by classical transport theory or within the framework of the approach described in [1]. The explanation of NMR in [4, 5, 7–9, 11–13] is based on weak localization theory and interference corrections to conductivity [14–16]. The time of electron wave phase decoherence due to inelastic scattering is introduced in this theory. In actual fact, this is an adjustable parameter [7] and must be determined from experimental data. In addition, when analyzing experimental data within the framework of weak localization theory, some difficulties are encountered [3, 4, 7], e.g., a difference in the sign of MR in samples with close parameters (compare [4, 5], [6], and [7–8]). The MR of 2D holes in AlGaAs/GaAs/AlGaAs heterostructures was studied within the density and temperature ranges of $(3.8–17.0)\times 10^9$ cm^{-2} and 4–320 mK, respectively. The NMR values obtained amounted to only a few percent of those predicted by the weak localization theory. In addition, high NMR onset temperatures (about 200 K) are observed in nanotubes. Therefore, we can suppose that weak localization is not the only mechanism of NMR. At certain conditions, NMR can be observed without it. A general quantum description of the transport that is valid both for weak and strong fields is necessary in this case to analyze the experimental data on magnetotransport.

Describing the electron transport using the one-electron density matrix is one possibility. Scattering on the acoustic deformation potential (along with the impurity scattering) is the leading momentum relaxation mechanism in nonpolar semiconductors (silicon, germanium, carbon). In polar ones (like GaAs), it dominates at rather low temperatures ($T < 77$ K). In this work, the kinetic equation for a one-electron density matrix is solved assuming a small deviation from the equilibrium state in terms of the deformation potential scattering mechanism; expressions for the conductivity tensor are derived. It follows from these expressions that when there is a certain relation between semiconductor parameters without weak localization the NMR effect can take place.

2. THEORY

The diagonal matrix elements of the electron momentum operator components that are transverse to the magnetic field are known to vanish at the magnetic field. As a result, the electron transport in the quantizing magnetic field cannot be described using the Boltzmann equation: the density matrix must be used. In this work, we restrict our consideration to the study of electron transport in an isotropic semiconductor with the parabolic dispersion law. We assume the magnetic field with the induction B to be directed along the z axis, and we assume that the electric field E_x is applied in the x direction. In the general case, the electric current density can be calculated from the relation

$$\mathbf{j} = \mathrm{Tr}(R\mathbf{J}), \tag{1}$$

where Tr stands for the trace of the operator, R is the statistical operator (density matrix), and $\mathbf{J}$ is the current density operator at the magnetic field.

Properties of the system under consideration are described within the one-electron approximation by the Hamiltonian

$$H = H_0 + W + U = H_e + H_p + W + U, \tag{2}$$

where H_e is the electron Hamiltonian at the magnetic field, H_p is the phonon Hamiltonian in the secondary-quantization representation, W is the electron–phonon interaction operator, and $U = -qE_x x$ is the potential energy operator. The statistical operator must be determined in order to calculate the current. This operator in the Schrödinger representation satisfies the quantum Liouville equation

$$i\hbar\frac{\partial R}{\partial t} = [HR]. \tag{3}$$

In solving this equation, we consider the sum $W + U$ as a perturbation. With the vector potential chosen in the gauge $\mathbf{A} = (0, Bx, 0)$, the wave functions of the operator H_0 are

$$\psi = \exp[i(k_y y + k_z z)]\, f(\eta)\chi_s|N\rangle, \tag{4}$$

where

$$\eta = \frac{x + k_y\lambda^2}{\lambda}, \quad \lambda^2 = \frac{\hbar}{qB},$$

$\mathbf{k}$ is the electron wave vector, χ_s is the spin wave function, and $|N\rangle$ is the phonon wave function in the occupation number representation. The x-dependent part $f(\eta)$ of factorized wave functions (4) are always normalized to unity and can be written as [18]

$$f_n(\eta) = \left(\frac{1}{\sqrt{\pi}\lambda 2^n n!}\right)^{1/2}\exp\left(-\frac{\eta^2}{2}\right)H_n(\eta). \tag{5}$$

The electron energy in this case is

$$E = \frac{\hbar^2 k_z^2}{2m} + \hbar\omega\left(n + \frac{1}{2}\right) + \mu_B g s B, \tag{6}$$

where $\omega = \dfrac{qB}{m}$, μ_B is the Bohr magneton, g is the Lande factor, and $s = \pm\dfrac{1}{2}$. Thus, the electron state $|i\rangle$ in the chosen representation is defined by a set of quantum numbers (n, k_y, k_z, s).

Since the current and perturbation operators do not contain spin operators, their matrix elements are diago-

nal in spin variables. The phonon system is assumed to be in equilibrium. In this case, all matrix elements are also diagonal in phonon variables. For concision, we shall omit them and take them into account only when making summation over the states.

We solve Eq. (3) by iterations. The validation of this method and the procedure for deriving an approximate equation are given in detail in [19]. Using the basis of wave functions (4), from (3) we obtain

$$(E_1 - E_2)R_{12} + U_{13}R_{32} - R_{13}U_{32} + i\pi S_{12} = 0 \quad (7)$$

for the stationary state, where

$$\begin{aligned} S_{12} &= \sum w(\mathbf{q})\{\delta(E_2 - E_3 - \hbar\Omega) \\ &\times [(N+1)M^+_{14}(\delta_{43} - R_{43})M_{35}R_{52} - N(\delta_{14} - R_{14}) \\ &\times M^+_{43}R_{35}M_{52}] + \delta(E_2 - E_3 + \hbar\Omega)[NM_{14}(\delta_{43} - R_{43}) \\ &\times M^+_{35}R_{52} - (N+1)(\delta_{14} - R_{14})M_{43}R_{35}M^+_{52}] \\ &+ \delta(E_1 - E_3 - \hbar\Omega)[(N+1)R_{14}M^+_{45}(\delta_{53} - R_{53})M_{32} \\ &- NM^+_{13}R_{34}M_{45}(\delta_{52} - R_{52})] + \delta(E_1 - E_3 + \hbar\Omega) \\ &\times [NR_{14}M_{45}(\delta_{53} - R_{53})M^+_{32} \\ &- (N+1)M_{13}R_{34}M^+_{45}(\delta_{52} - R_{52})]\}. \end{aligned} \quad (8)$$

Here, $\hbar\Omega(\mathbf{q})$ is the energy of phonons, N is their distribution function, $w(\mathbf{q})$ is a function describing the electron–phonon interaction, M_{ij} is the matrix element of the plane phonon waves on the basis of wave functions (4), and the "+" sign denotes Hermitian conjugation. In (8), it is necessary to sum over all states except $|1\rangle$ and $|2\rangle$ and over the phonon wave vector values. It is well known that, strictly speaking, (3) does not describe an irreversible behavior of the electron system. Additional considerations must be used to obtain such a behavior [1]. One can modify the Hamiltonian or use some sort of artificial mathematical approach to reflect the interaction of the system with the environment. A hypothesis of the initial approximation for the density matrix diagonal part, i.e., the distribution function, is the most widely used of such approaches. Let us represent the density matrix as

$$R_{12} = F_1\delta_{12} + G_{12}\delta(k_{y1} - k_{y2}), \quad (9)$$

where $G_{12} \equiv G_{n_1n_2}(k_{z_1}, k_{z_2})$. If the electric field does not disturb the translation invariance of the electronic system, the Fermi–Dirac distribution depending on the energy (6) and on the quasi–Fermi level E_F is usually chosen as $F_1 = F(E_1)$. Such a choice is, in fact, based on the local equilibrium principle, which is widely used in semiconductor theory. This approximation is quite satisfactory at high temperatures. However, corrections to the distribution function due to the simultaneous action of the electric field and the electron scattering must be taken into consideration at low temperatures. Such a correction was obtained in [1] in the first nonvanishing order in scattering. However, it is valid only under strong fields. The general procedure for obtaining corrections is presented in [19]. Its essence is in the expansion of the Gibbs statistical operator in terms of interaction considered as perturbation. The distribution function approximation that is linear in the electric field can be represented as

$$F_1 + \frac{\partial F_1}{\partial E}U_{12}F_2Z,$$

where summing over the subscript "2" is implied; U_{12} is the potential energy matrix element; and Z is a function, which is a result of summing over all orders of scattering. This function depends on the magnetic field, relaxation parameters, and the distribution function. We do not analyze the form of this function in this study. We only note that it vanishes as the magnetic field approaches zero. Then, from (9) we obtain

$$R_{12} = \left(F_1 + \frac{\partial F_1}{\partial E}U_{12}F_2Z\right)\delta_{12} + G_{12}\delta(k_{y1} - k_{y2}). \quad (10)$$

It is noteworthy that, including U in the basic Hamiltonian, one can easily obtain a solution similar to those in (4–6). Just such a solution was used in [1]. However, the wave functions of such a Hamiltonian do not satisfy the conditions for Hermitian conjugation and completeness. This became explicit for solutions (5) in the limit $B \longrightarrow 0$.

Let us seek a solution linear in G for Eq. (7). For scattering on the deformation potential of acoustic phonons (DA-phonons), we obtain

$$w(\mathbf{q}) = w_0 q, \quad (11)$$

where $w_0 = \hbar E_A^2/2\rho s^2$. At moderately low temperatures,

$$N \approx \frac{kT}{\hbar sq} \gg 1. \quad (12)$$

As is known from semiconductor theory, the acoustic phonon energy can be neglected in the energy conservation law when $T > 11$ K. Then, substituting (8)–(12) into (7), after simple integration, we obtain

$$\begin{aligned} &(E_1 - E_2)G_{12} + U_{12}(F_2 - F_1) - iqE_x\eta_{12}Q_{12} \\ &+ i\frac{kTw_0}{2\pi\lambda^2\hbar}\sum_3\int dk_{z3}\{[\delta(E_2 - E_3) + \delta(E_1 - E_3)] \\ &\times [G_{12} - \delta_{12}G_{33}(K_{z12} - k_{z2} + k_{z3})]\} = 0, \end{aligned}$$

where $\eta_{12} = \int f_1\eta f_2 d\eta$,

$$\begin{aligned} Q_{12} = \frac{kTw_0}{2\pi\lambda\hbar}\sum_3\int dk_{z3}\Big[&\frac{\partial F_2}{\partial E_2}(1 + F_2 - F_1)\delta(E_2 - E_3) \\ &+ \frac{\partial F_1}{\partial E_1}(1 + F_1 - F_2)\delta(E_1 - E_3)\Big]Z. \end{aligned}$$

It is noteworthy here that integration in (8) can be easily done only for DA-phonons, since the product $Nw(\mathbf{q})$ does not depend on q. This is not the case for other scattering mechanisms; consequently, we have not succeeded in obtaining simple expressions. It is easy to verify the solution to this equation:

$$G_{12} = \frac{U_{12}(F_1 - F_2) + iq\eta_{12}Q_{12}}{E_1 - E_2 + i\hbar\nu_{12}}, \tag{13}$$

where

$$\nu_{12} = \frac{kTw_0}{2\pi\lambda^2\hbar}\sum_3\int dk_{z3}[\delta(E_2 - E_3) + \delta(E_1 - E_3)].$$

Matrix elements of the current density and the potential energy are readily calculated and have the form

$$j_{x12} = i\frac{x_{12}}{\lambda^2}D_{12}, \quad j_{y12} = \left(\frac{x_{12}}{\lambda^2} - k_{y1}\right)D_{12},$$

$$j_{z12} = -k_{z1}D_{12}, \quad U_{12} = -qE_x x_{12},$$

where

$$D_{12} = \frac{q\hbar}{m}\delta(k_{y1} - k_{y_2})\delta(k_{z1} - k_{z2}).$$

Substituting them and (13) into (1), we finally obtain for the conductivity tensor

$$\sigma_{xx} = \frac{q^2\omega}{(2\pi)^2\hbar}\sum_{s,n}(n+1)dk_z\left[\frac{\nu_{n,n+1}(F_n - F_{n+1}) - \omega Q_{n,n+1}}{\omega^2 + \nu^2_{n,n+1}}\right],$$
$$\sigma_{xy} = \frac{q^2\omega}{(2\pi)^2\hbar}\sum_{s,n}(n+1)dk_z\left[\frac{\omega(F_n - F_{n+1}) + \nu_{n,n+1}Q_{n,n+1}}{\omega^2 + \nu^2_{n,n+1}}\right], \tag{14}$$

where

$$F_n \equiv F(E_n), \quad E_n = \frac{\hbar^2k_z^2}{2m} + \hbar\omega\left(n + \frac{1}{2}\right) + \mu_B gsB,$$

$$\nu_{nm} = \frac{\hbar\omega}{4\sqrt{kT}\tau_{DA}}\sum_l\left[\frac{\theta(z_{nl})}{\sqrt{z_{nl}}} + \frac{\theta(z_{ml})}{\sqrt{z_{ml}}}\right],$$

$$Q_{nm} = \left[\frac{\hbar\nu_{nm}}{2}\frac{\partial F_n}{\partial E_n}(1 + F_n - F_m) + \frac{\hbar\nu_{mm}}{2}\frac{\partial F_m}{\partial E_m}(1 + F_m - F_m)\right]Z,$$

$$z_{nl} = \hbar\omega(n - l) + \frac{\hbar^2k_z^2}{2m}, \quad \tau_{DA} = \frac{\pi\hbar^4\rho s^2}{\sqrt{2}(mkT)^{3/2}E_A^2}.$$

Using the obtained results, it is easy to show that with the conditions under consideration,

$$\sigma_{zz} = \frac{q^2\omega}{(2\pi)^2\hbar}\sum_{s,n}\int dl_z\frac{k_z}{\nu_{n,n}}\left(-\frac{\partial F_n}{\partial k_z}\right). \tag{15}$$

Under strong magnetic fields, when $\omega \gg \nu$, the relations (14) reduce to the ones obtained in [1]. If we use the Poisson formula for summation in this case for the degenerate electron gas, we obtain expressions similar to the ones derived in [1, 2].

For scattering on the deformation potential of optical phonons, we obtain

$$w(\mathbf{q}) = w_0 = \frac{\hbar D^2}{2\rho\Omega_0},$$

where Ω_0 is the optical phonon frequency. The calculation is carried out similarly to the preceding case, and the conductivity tensor is described by the same expressions. The momentum relaxation frequency has the form

$$\nu_{12} = \frac{w_0}{4\pi\lambda^2\hbar}\sum_3\int dk_z[\delta(E_2 - E_3 - \hbar\Omega_0)(N + 1 - F_{2-}) + \delta(E_2 - E_3 + \hbar\Omega_0)(N + F_{2+}) + \delta(E_1 - E_3 - \hbar\Omega_0) \times (N + 1 - F_{1-}) + \delta(E_1 - E_3 + \hbar\Omega_0)(N + F_{1+})],$$

where $F_{i\pm} = F(E_i \pm \hbar\Omega_0)$.

3. DISCUSSION OF RESULTS AND COMPARISON WITH EXPERIMENT

The obtained expressions are finite at any magnetic field. However, they are not easy to analyze directly. That is why we will consider some limiting cases. In the weak-field limit, when $\alpha = \hbar\omega/kT \ll 1$, we can take the spin energy at the magnetic field to be zero and replace summation over n by integration. From (14), after simple algebra and angular integration, we obtain

$$\sigma_{xx} = \sigma_{Bxx} + \frac{2q^2}{\sqrt{\pi}m}N_c\alpha\int\sqrt{x}dx\frac{\nu}{\omega^2 + \nu^2}\left(-\frac{\partial F}{\partial x}\right),$$
$$\sigma_{xy} = \sigma_{Bxy} + \frac{2q^2}{\sqrt{\pi}m}N_c\alpha\int\sqrt{x}dx\frac{\omega}{\omega^2 + \nu^2}\left(-\frac{\partial F}{\partial x}\right), \tag{16}$$

where σ_{Bxx}, σ_{Bxy} are values calculated from the Boltzmann equation (see, e.g., [20]), N_c is the density of states in the conduction band, $x = E/kT$, and

$$\nu = \frac{1}{2\tau_{DA}}(\sqrt{x} + \sqrt{x + \alpha}).$$

Z was assumed to be zero when deriving (16). It is noteworthy here that, within this approximation, σ_{zz} (15) coincides with the classical expression. It is seen that there are additional terms in (16) in comparison with

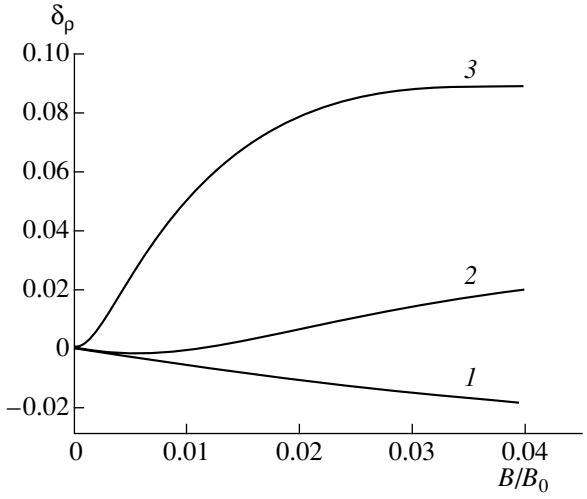

Fig. 1. Magnetic field dependence of the magnetoresistance at various values of the electron scattering parameters γ: (*1*) 5, (*2*) 20, and (*3*) 100.

the classical expressions. They are due to special features of the electron dynamics in a magnetic field. Motion in the direction transverse to a magnetic field is known as diffusion. Using the relation

$$\lambda^2(n+1) \equiv x^2_{n,n+1} = (k_y)^2_{n,n+1}\lambda^2,$$

we obtain from (14) for the diffusion coefficient at the magnetic field

$$D_H = \omega^2\left\langle \frac{\nu_{n,n+1}x^2_{n,n+1}}{\nu^2_{n,n+1}+\omega^2}\right\rangle.$$

In the case of $\omega\tau \ll 1$, we obtain

$$D_H = \frac{1}{m}\left\langle \frac{E_n + \frac{\hbar\omega}{2}}{\nu_n}\right\rangle = D + \frac{\hbar}{2m}\omega\tau,$$

where D is the diffusion coefficient in the absence of a magnetic field; the angular brackets indicate averaging. Thus, the diffusion coefficient and, therefore, the electron mobility is higher under a weak magnetic field than in the absence of a field. NMR is a result of it.

The expressions (16) are formally obtained for the deformation potential scattering. However, they coincide with σ_{Bxx} and σ_{Bxy} at $B = 0$. Therefore, they must be valid at least under weak fields and for other scattering mechanisms as well. In actual fact, the resistivity

$$\rho = \frac{\sigma_{xx}}{\sigma^2_{xx}+\sigma^2_{xy}}$$

is measured in experiments. It is known that $\rho(B) > \rho(0)$ in the classical mode [20]. In (16), σ_{xx} has an additional term that is linear in the field. As a result of it, the function $\rho(B)$ has a minimum with $\rho_m < \rho(0)$ within the range $0 < B < B_1$ and $\rho(B_1) = \rho(0)$ at the boundaries of this interval. The values ρ_m and B_1 depend on the electronic system parameters and temperature. As follows from (16), if the electrons are nondegenerate ($E_F < 0$), $\delta_\rho = \delta\rho/\rho(0)$ does not depend on the electron density. In this case, ρ_m and B_1 are determined by two parameters,

$$B_0 = \frac{mkT}{\hbar q} \quad \text{and} \quad \gamma = \frac{kT\tau}{\hbar},$$

where τ is the mean electron momentum relaxation time. It is noteworthy that the kinetic approach presented above is valid for nondegenerate electronic systems when $\gamma \gg 1$ [20].

The $\delta_\rho(B)$ dependences are presented in Fig. 1 for various magnitudes of γ. The calculation is carried out for a wide-band semiconductor with *n*-type conduction at $E_F/kT = -5$. At the given temperature, the calculated dependences are related to materials with different electron mobility values. At room temperature and when the effective mass is equal to the free electron mass, the mobilities are 200, 800, and 4000 $cm^2\ V^{-1}\ s^{-1}$, respectively. Under these conditions, the magnetic field varies in the range from 0 to 10 T. As is seen from Fig. 1, MR is always negative and the parameter B_1 is infinite at low electron mobility. At high mobility, the MR is always positive and $B_1 = 0$. At intermediate values of the mobility, B_1 is finite and MR changes its sign. These conclusions are, of course, valid only for $\alpha \ll 1$; at small values of electron mobility, B_1 will be finite under strong fields. It is noteworthy that dependences similar to the curve for $\gamma = 5$ were observed in 3D [4], 2D [7], and 1D [9] semiconductors.

The scattering frequency is known to increase with the doping impurity concentration. Correspondingly, γ decreases and the magnitude of NMR increases. This accounts qualitatively for the difference between the results obtained in [4] and [5] for samples with different concentrations of doping impurities. It should be noted that such a simple relation between the concentration of impurities and NMR takes place in a nondegenerate semiconductor at $E_F/kT < -2$. If the concentration of impurities is high and $E_F > 0$, the dependence becomes complicated. In the case of scattering on charged impurities, $\nu \propto T^{3/2}$. In reality, the dependence is weaker for impurity scattering, due to the temperature dependence of the activated doping impurity concentration and screening effects. In spite of this, however, γ rises with temperature for this scattering mechanism. As follows from Fig. 1, the NMR magnitude decreases as γ increases under a fixed value of the magnetic field. This accounts qualitatively for the temperature dependence of NMR obtained in [4, 7, 9]. The dependences shown in Fig. 1 are calculated for scattering on the DA-phonons. The dependence of MR on γ for other scattering mechanisms is qualitatively the same. The quantitative characteristics are determined by the type of the function $\nu(E)$.

The magnetic field dependence of the Hall coefficient (R_H) for various values of γ are presented in Fig. 2.

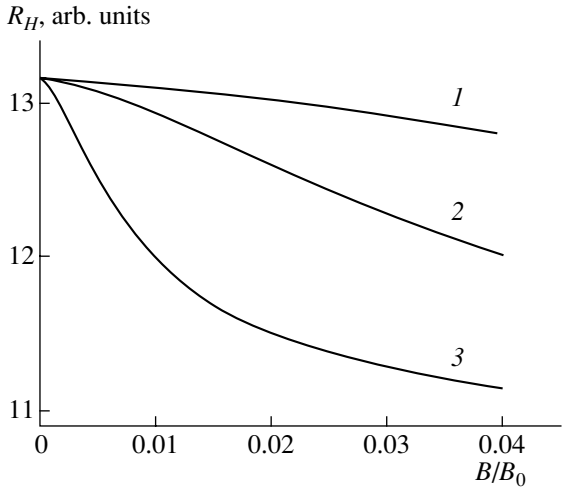

Fig. 2. Magnetic field dependence of the Hall coefficient at the same values of the electron scattering parameter that were used for Fig. 1.

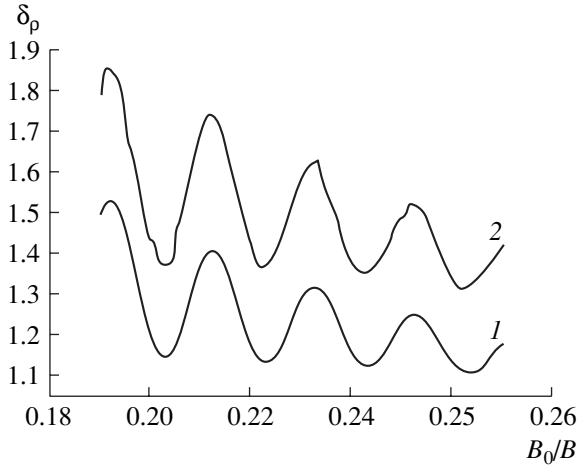

Fig. 3. Magnetic field dependence of the magnetoresistance of the degenerate electronic system at $\gamma = 43$ (*1*) and $\gamma = 866$ (*2*).

The same parameter values as in the case of Fig. 1 were used for calculation. R_H is seen to weakly decrease with increasing field for all values of γ. Since the electron density is assumed to be constant in calculations, these dependences reflect a change of the Hall constant as the field increases.

Classical MR in degenerate electron gas is known to be zero [20]. If we replace the derivative of the distribution function in (16) with the delta function, we obtain

$$\delta_\rho = -\frac{\hbar\omega}{E_F + \hbar\omega} < 0. \quad (17)$$

Exact calculation shows that the dependence $\delta_\rho(B)$ in the region of very weak fields can be an alternating function when there is simultaneous action of different relaxation mechanisms and the proper form of the $\nu(E)$ function is present. Expressions (14) and (16) are formally obtained for a bulk semiconductor. However, the qualitative difference between characteristics of 3D and 2D electron gases under a magnetic field is rather small. That is why these expressions can be used for a qualitative explanation of the difference between the characteristics of the degenerate 2D electron gas, which was obtained in [7–9]. In particular, (17) adequately describes the experimental dependence [7] for fields at which $\alpha < 1$.

The magnetoresistance δ_ρ is an oscillating function of B^{-1} under strong fields and low temperatures. The $\delta_\rho(B)$ dependence is depicted in Fig. 3 for two magnitudes of γ, to which correspond γ equal to 5 and 100 at room temperature. The calculation has been carried out using (14) for scattering on DA-phonons at $T = 4$ K and $E_F/kT = 50$. Z is assumed to equal unity, which corresponds to the approximation used in [1]. If we neglect in (14) the first small term in the expression for σ_{xx} and the second term in the expression for σ_{xy}, the expressions (14) are reduced to the results of [1]. As is seen from Fig. 3, the MR does oscillate with a period proportional to B^{-1} (at $E_F > \hbar\omega$). The amplitude of the oscillations and the mean value increase with increasing field and decreasing scattering frequency. The calculation shows that the Hall coefficient does not depend on the magnetic field. It is dependences of this kind that are usually observed in experiments. It follows from calculations that the oscillation amplitude strongly depends on the value of Z and on the type of its field dependence. If $Z \ll 1$ (a Boltzmann electron gas), oscillations are absent and δ_ρ steadily grows as the field increases. It should be noted here that σ_{xx} (16) also depends on the field value under strong fields.

4. CONCLUSION

Modern conceptions relate NMR to weak localization, with the necessary condition for its occurrence being the disordered distribution of scattering centers in the semiconductor. Here, we have solved the kinetic equation for the density matrix at the quantizing magnetic field, taking into account the scattering of the deformation potential. The results obtained show that transverse NMR can be observed in an electron gas without a random potential. This is a result of consistently taking the magnetic quantization into account.

The solutions obtained, in contrast to [1], have no limitation on the magnetic field magnitude. The term similar to the one obtained in [1] dominates in σ_{xx} at strong fields. However, the parameter Z is shown in this paper to differ from unity and to depend on the magnetic field, in contrast to the value implicitly taken in [1]. Moreover, the expressions for the conductivity tensor contain terms similar to the ones obtained by Lifschitz [21], which appeared earlier than [1]. The results obtained combine and generalize both approaches.

Calculations shows that the kind of NMR considered should actually be observed at weak fields and low electron mobility. The analysis indicates that a qualitatively similar dependence of MR should be observed in low-dimensional electronic systems as well. A quantitative analysis for such systems will be carried out in the next paper.

Low mobility occurs in conventional semiconductors (Si, Ge, GaAs) under heavy doping. Weak localization can take place under such conditions, and the interpretation of NMR becomes ambiguous. However, there exist a number of semiconductors (like GaN) that have low mobility in the undoped state. Graphite and nanotubes prepared from it can be assumed to belong to this family as well. NMR should be observed in such semiconductors even when there is high crystal perfection of the samples.

ACKNOWLEDGMENTS

This study was supported in part by the Russian interdisciplinary scientific program "Physics of Solid-State Nanostructures" (project no. 97-1093/4).

REFERENCES

1. E. Adams and T. Holstein, J. Phys. Chem. **10**, 254 (1959).
2. A. Isihara and L. Smirčka, J. Phys. C **19**, 6777 (1986).
3. S. S. Murzin, Usp. Fiz. Nauk **180**, 387 (2000).
4. N. G. Zhdanova, M. S. Kagan, and E. G. Landsberg, Zh. Éksp. Teor. Fiz. **117**, 761 (2000) [JETP **90**, 662 (2000)].
5. A. I. Veĭnger, A. G. Zabrodskiĭ, and T. V. Tisnek, Fiz. Tekh. Poluprovodn. (St. Petersburg) **34**, 774 (2000) [Semiconductors **34**, 746 (2000)].
6. V. I. Kadushkin and E. V. Klyshevich, Izv. Vyssh. Uchebn. Zaved., Fiz. **42**, 67 (1999).
7. G. M. Minkov, S. A. Negashev, O. E. Rut, *et al.*, Phys. Rev. B **61**, 13 172 (2000).
8. A. M. Kreshchuk, S. V. Novikov, T. A. Polyanskaya, and I. G. Savel'ev, Fiz. Tekh. Poluprovodn. (St. Petersburg) **31**, 459 (1997) [Semiconductors **31**, 391 (1997)].
9. A. D. Visser, V. I. Kadushkin, V. A. Kul'bachinskiĭ, *et al.*, Pis'ma Zh. Éksp. Teor. Fiz. **59**, 340 (1994) [JETP Lett. **59**, 363 (1994)].
10. A. V. Eletskiĭ, Usp. Fiz. Nauk **167**, 945 (1997) [Phys. Usp. **40**, 899 (1997)].
11. L. Langer, R. Bayot, E. Grivei, *et al.*, Phys. Rev. Lett. **76**, 479 (1996).
12. S. N. Song, X. K. Wang, R. P. H. Chang, and J. B. Ketterson, Phys. Rev. Lett. **72**, 697 (1994).
13. G. Baumgartner, M. Carrerd, L. Zuppiroli, *et al.*, Phys. Rev. B **55**, 6704 (1997).
14. S. Hikami, A. Larkin, and Y. Nagaoka, Prog. Theor. Phys. **63**, 707 (1980).
15. B. Altshuler, D. Khmel'nitskii, A. Larkin, and P. Lee, Phys. Rev. B **22**, 5142 (1980).
16. B. L. Al'tshuler, A. G. Aronov, D. E. Khmel'nitskiĭ, and A. I. Larkin, Zh. Éksp. Teor. Fiz. **81**, 768 (1981) [Sov. Phys. JETP **54**, 411 (1981)].
17. A. P. Mills, A. P. Ramírez, X. P. A. Gao, *et al.*, cond-mat/0101020 (2001).
18. L. D. Landau and E. M. Lifshitz, *Course of Theoretical Physics*, Vol. 3: *Quantum Mechanics: Non-Relativistic Theory* (Nauka, Moscow, 1989, 4th ed.; Pergamon, New York, 1977, 3rd ed.), Chap. 15.
19. A. I. Akhiezer and S. V. Peletminskii, *Methods of Statistical Physics* (Nauka, Moscow, 1977; Pergamon, Oxford, 1981), Chaps. 3–5.
20. A. I. Anselm, *Introduction to Semiconductor Theory* (Nauka, Moscow, 1978; Prentice-Hall, Englewood Cliffs, 1981), Chap. 9.
21. I. M. Lifshits, Zh. Éksp. Teor. Fiz. **3**, 774 (1956).

Translated by S. Ktitorov

Semiconductors, Vol. 36, No. 11, 2002, pp. 1283–1287. Translated from Fizika i Tekhnika Poluprovodnikov, Vol. 36, No. 11, 2002, pp. 1367–1371.

SEMICONDUCTOR STRUCTURES, INTERFACES, AND SURFACES

The Influence of Adsorbate on the Work Function and Penetrability of the Surface Potential Barrier of GaAs(110) Single Crystal

Yu. I. Asalkhanov*^ and V. N. Abarykov**

** East-Siberian State Technological University, Ulan-Ude, 670013 Russia*

*** Buryat Research Center, Siberian Division, Russian Academy of Sciences, Ulan-Ude, 670048 Russia*

^e-mail: fizika@esstu.ru

Submitted December 18, 2001; accepted for publication March 25, 2002

Abstract—The characteristic features of variations in the current–voltage characteristics of the current of slow monoenergetic electrons, which are introduced into single-crystal GaAs(110) from vacuum, were established with the removal of the native oxide layer from the surface. It is demonstrated that the work function decreases and the penetrability of the potential barrier increases with the temperature of thermal treatment of the crystal in high vacuum. The oxide removal was monitored simultaneously by ellipsometry. According to calculations from the Drude equations, the thickness of the removed layer is no larger than 20 Å. © *2002 MAIK "Nauka/Interperiodica".*

1. INTRODUCTION

One of the fundamental characteristics of a solid is its work function, which is equal to the sum of the surface potential barrier and electron affinity [1]. The temperature dependence of the work function, the difference in electron reflectances from the surface potential barrier of solids, the existence of a space-charge layer, and the device configuration introduce their *a priori* unknown contributions to experimental results. In these conditions, the exact determination of the variation of the work function of real surfaces in different emission processes becomes problematic. This variation is treated as the Schottky effect.

At the same time, a method for detecting a variation in the work function exists; this method (the Anderson method of retarding potential [2]) eliminates most, if not all, of the difficulties associated with the subsequent interpretation of the results obtained. Since this method, similarly to the Shelton method [3], permits measuring the variation of the work function for various solids, its application is of considerable theoretical and practical interest.

The essence of the method is as follows. A collimated beam of slow monoenergetic electrons with an energy E_p = 0–10 eV is directed at a right angle to the surface of the sample under investigation. In this case, electrons partially penetrate into the sample, are partially reflected from the surface, and are collected by a Faraday cup. The sum of currents of the sample and the Faraday cup should be constant. The current–voltage (*I–V*) characteristic is plotted. This characteristic reflects the dependence of the sample (collector) current on the bias voltage, or, to be more precise, on the electron energy. Further, the sample (collector) is replaced by another one, and the *I–V* characteristic is plotted again. The variation in the work function of the sample under investigation relative to the starting sample, which is usually called the reference sample, is determined from the shift of the *I–V* characteristic along the axis of electron energies.

The successful use of the retarding potential method is based on a theoretically and experimentally proven concept—to bring about a collector current, the bias voltage V_c, which is reckoned from the Fermi level of the emitter $E_{F(e)}$, should shift the Fermi level of the collector $E_{F(c)}$ in the energy diagram by a magnitude $eV_c \geq (\varphi_e - \varphi_c)$. Here, e is the elementary charge; and φ_e and φ_c are the work functions of the emitter and collector, respectively. For the emitter temperature T = 0 K, the collector potential should be equal to the Fermi level of the emitter, whereas with increasing temperature, allowance should be made for the Boltzmann distribution $\exp[(E_{F(e)} - E)/kT]$, where T is the emitter temperature, k is the Boltzmann constant, and E is the highest energy of the emitted electron.

The purpose of this study is to demonstrate the efficiency of using the retarding potential method to detect variations in the work function and penetrability of the surface potential barrier of solids having a submonolayer surface coverage with an adsorbate using the example of single-crystal GaAs(110) with the step-by-step freeing of the surface from native oxide.

1063-7826/02/3611-1283$22.00

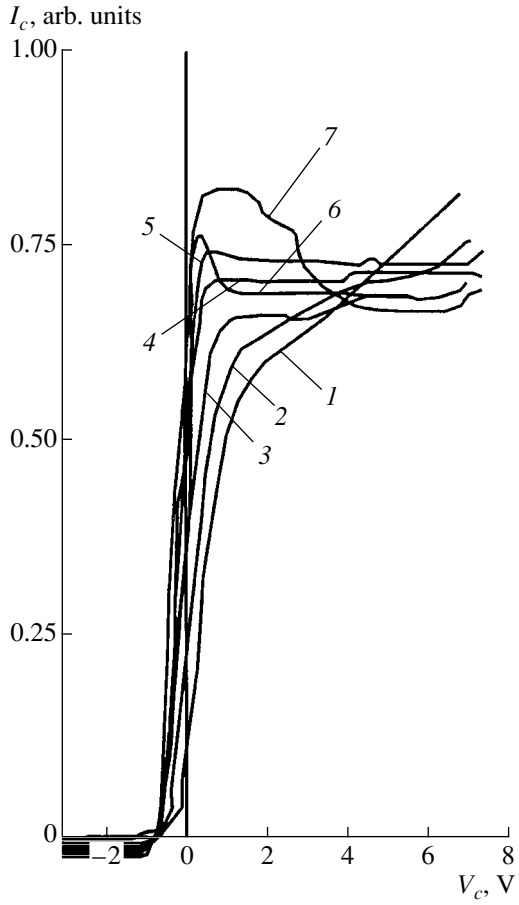

Fig. 1. Variation in current–voltage characteristics on heating the GaAs(110) samples to temperatures T = (*1*) 300, (*2*) 450, (*3*) 470, (*4*) 500, (*5*) 520, (*6*) 550, and (*7*) 590 K.

2. THEORY

Free electrons of a solid have an energy distribution given by the Fermi–Dirac function and form a current when passing across a potential barrier with a height $eV = \varphi_e + eV_c$. The magnitude of this current, according to the Richardson equation, equals [4]

$$I_c = I_s \exp(eV/kT), \quad (1)$$

where

$$I_s = AT^2 \exp(-e\varphi_e/kT), \quad (2)$$

$A = 120$ A/(cm^2 K^2).

It follows from Eqs. (1) and (2) that, at a constant emitter temperature, the dependence of the collector current on the bias voltage V_c on the semilog scale should have the form of two intersecting straight lines, one of which is parallel to the axis of electron energies. The position of the crossing point along the axis of electron energies E_p determines the work function of the collector φ_c relative to the emitter, whereas the slope dI_c/dV_c determines the penetrability of the potential barrier of the collector $D(E, d)$, where $E = E_p = (\varphi_e + eV_c)$ is the electron energy, and d is the potential-barrier width.

A variation in the energy structure of the surface layer of the collector in the course of adsorption–desorption processes at the collector surface leads to a variation in the electron-density distribution in the region mentioned. This should be detected as an increase or a decrease in one or both parameters of the *I–V* characteristic.

3. EXPERIMENTAL

The measurements were carried out in an all-metal vacuum system. This system made it possible to investigate the adsorption–desorption processes at the solid surface with the simultaneous use of ellipsometry and the Anderson retarding potential. The mass spectrum of thermal desorption from the surfaces of the samples under investigation was recorded under a limiting pressure of residual gases no higher than $(2–3) \times 10^{-7}$ Pa [5]. The optically polished samples were mounted on a Mo disk of diameter 30 mm and thickness ~1 mm, which was pressed hard through a ceramic plate to the surface of a Ta cylinder, which contains a W coil. Heating the sample from room temperature to 1800 K was accomplished by passing a certain current through the coil and, if necessary, by the electron bombardment of the cylinder. The temperature was measured by Pt–Pt/Rh and Chromel–Copel thermocouples welded to the Mo disk. The thermocouple readings were monitored by an LOP-72 optical pyrometer. The samples of the material under investigation with the given heating system were mounted on a special holder [6], which provided for their motion and angular adjustment. The electron gun used for obtaining a beam of slow monoenergetic electrons and the procedure of recording the *I–V* characteristic are described in detail elsewhere [7, 8]. The *I–V* characteristics given below were recorded using a PDP-002 two-coordinate recorder after establishing their steady states at a given sample temperature.

4. RESULTS AND DISCUSSION

The series of sequential measurements of *I–V* characteristics during the cleaning of the surface of the GaAs(100) single-crystal in the course of thermal treatment in the temperature range mentioned is shown in Fig. 1. According to the mass-spectrometry measurements, the adsorbate removed in this temperature range is composed predominantly of CO and CO_2 molecules. The exception is the outburst temperature of about 870 K, at which numerous peaks beyond the mass of 58, caused by As and Ga oxides, emerge in the mass-spectrum. It can be seen that the work function φ_c generally decreases as the thermal treatment temperature increases. This is shown by the shift of the inflection

region of the *I–V* characteristic to the left along the axis of electron energies. The distribution of electron energy in the beam remains unchanged. The penetrability of the surface potential barrier $D(E, d)$ increases as the adsorbate is removed. This is confirmed by an increase in the current of low-energy electrons (E_p = 0–2 eV) which are present in the beam.

The multiple repetition of the cycles ⟨heating the crystal from room temperature to the given temperature T_i⟩–⟨cooling to room temperature⟩ causes the variations of *I–V* characteristics that are reversible with temperature. The total period of reversibility is no less than 2–3 days. Each specific *I–V* characteristic, which corresponds to a certain temperature in the range from 300 K to T_i, is reproduced within 5–10 min after establishing the given temperature. The special features of the characteristic do not vary for at least 3–4 h at 300 K. On the other hand, the process of varying the *I–V* characteristic is irreversible. Initial heating of the crystal to another temperature T_k ($T_k > T_i$) gives rise to a *I–V* characteristic which differs considerably from that obtained at T_i. This is especially true for the φ_c and $D(E, d)$ quantities. The first of these quantities steadily decreases, whereas the second one analogously increases with increasing temperature.

Multiple repetitive heating of the single crystals in the range from room temperature to T_k also points to the total reversibility of variations in the *I–V* characteristics with temperature in a given range. In this case, the *I–V* characteristics are different at the same temperature if the initial thermal treatment was carried out at T_i and T_k.

The shape of the curves after heating the samples to $T > 470$ K approaches the theoretical one according to Eqs. (1) and (2). After heating the GaAs(110) single crystal to temperatures exceeding 750 K, a peak emerges in the initial part of the *I–V* characteristic. This peak, which is predicted by quantum mechanics, is determined by the Bragg reflection of electrons from the surface. As follows from the dependence presented, the adsorbate, which is removed from the surface in the temperature range mentioned, increases the work function of the GaAs(110) single crystal by a magnitude close to 0.4 eV.

The character of variation in the *I–V* characteristic of the samples upon cooling the GaAs(110) single crystal to room temperature from the temperature of the first heating is illustrated in Fig. 2. The solid lines in Fig. 2 represent the *I–V* characteristics for various temperatures of initial sample heating; the dashed lines paired with them represent the *I–V* characteristics recorded after cooling the samples from the temperatures mentioned to room temperature.

We compared the variations in the *I–V* characteristics of the semiconductor single crystal (GaAs, the (100) surface) and metal (W single crystal, the (100) surface) in the course of the step-by-step removal of the

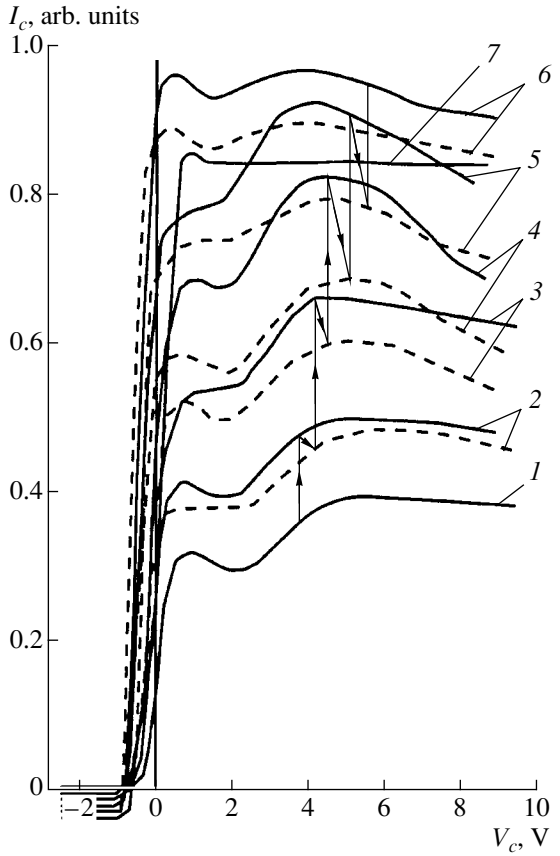

Fig. 2. Variation in current–voltage characteristics for the GaAs(110) single crystal with temperature *T* of first heating (solid lines) and after cooling to room temperature (dashed lines). *T* = (*1*) 300, (*2*) 330, (*3*) 380, (*4*) 440, (*5*) 490, (*6*) 620, and (*7*) 770 K.

native oxide layer from the surface. This comparison permits us to suggest that the variations in the *I–V* characteristics of these solids, along with other common features, have substantial distinctions. In both cases, the theoretically predicted shape of the *I–V* characteristics is established only at a definite stage of cleaning of the surface of the adsorbate. In both cases, the irreversible decrease in the work function is associated with an increase in the thermal heating temperature for the samples mentioned, i.e., with a decrease in the coverage of their surfaces by the adsorbate. The work function of the metal single crystal decreases steadily with the removal of residual oxides, whereas $D(E, d)$ increases steadily. In contrast with this, for the semiconductor, a similar decrease in the work function, when the heating temperature approaches the onset of sublimation of the single crystal, gives way to an increase in the work function. In this case, the barrier penetrability $D(E, d)$ somewhat decreases, as can be seen from the *I–V* characteristic (*7*) in Fig. 2. It should be noted that the *I–V* characteristic (*7*), in contrast to other characteristics

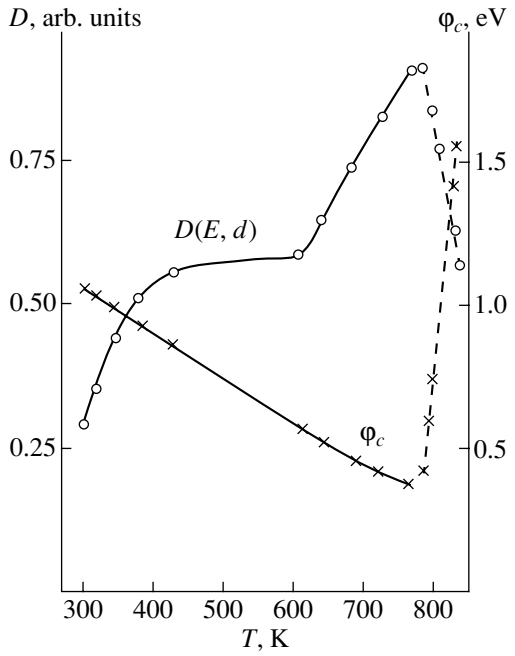

Fig. 3. Variations in φ_c and $D(E, d)$ for the GaAs single-crystal samples after heating to temperatures indicated. The zone of unstable values of φ_c and $D(E, d)$ is represented by the dashed line.

shown in Fig. 2, is unstable with respect to temperature variations.

The feature of variations in the work function φ_c and penetrability of the surface potential barrier $D(E, d)$ of GaAs(110) single crystals on the removal of the native oxide layer from the surface are shown in Fig. 3. The parameters were recorded immediately on cooling the sample from the temperatures shown in Fig. 3 to room temperature. It should be noted that although the samples under investigation comprised a single wafer, both their ellipsometry parameters and initial *I–V* characteristics were always different. The spread was no less than one degree of arc for the variation in the amplitude ellipsometric parameter Ψ and several degrees for the variation in the phase shift Δ. The difference between the initial currents of the *I–V* characteristics is about 10^{-7} A. The slope of the initial portion of the *I–V* characteristic of the rapid current increase with electron energy differs by a factor of no less than 2. However, the general features of variations in the *I–V* characteristics with the thermal treatment temperature are identical. For the metal, the initial currents of the *I–V* characteristics are independent of the sample temperature and the degree of surface coverage by the adsorbate. For the semiconductor, these currents decrease synchronously with the sample temperature, and the magnitude of reduction increases as the surface is cleansed of residual oxide.

A decrease in the work function with the removal of adsorbate both for the metal and for the semiconductor points to a reduction of the surface potential φ_s and, consequently, to the acceptor nature of the energy levels of the adsorbate–solid system.

With the constant coverage of sample surfaces with the adsorbate, their heating leads to a decrease in the adsorbate layer thickness and to a decrease in the thickness of the double layer, which is formed by the surface states of the crystal and adsorbate molecules (atoms). In this case, adsorbate removal leads to a decrease in the φ_s quantity. The heating of semiconductors causes an exponential increase in the electron density in the double layer, which is more extended compared with that in metal. This leads not only to a sharper decrease in the layer thickness but also to an increase in the total negative charge of surface states. This apparently causes a decrease in the initial currents of the *I–V* characteristics with temperature. At the measurement temperatures mentioned, the determining type of semiconductor conduction is intrinsic conduction, whereas the work function equals $\varphi_c = \chi + E_g/2 + \varphi_s$, where χ is the electron affinity and E_g is the band gap.

According to ellipsometry measurements, which were carried out according to the procedure described in detail elsewhere [8] simultaneously with the detection of variations mentioned in the *I–V* characteristics, the total thickness of the adsorbate layer removed was 20 Å.

5. CONCLUSION

(1) Synchronous variations in the *I–V* characteristics and ellipsometry parameters, whose sensitivity to variations in the surface coverage of the solid body with an adsorbate of the submonolayer range amounts to about 0.02 monolayers, are observed. These variations suggest that the retarding potential method is an efficient method for monitoring variations both in the amount of gases adsorbed and in residual oxides on the solid surface. The method allows for the direct monitoring of the adsorption–desorption processes as these are taking place.

(2) The surface potential of the solid φ_c depends on the temperature and the amount of adsorbate at the surface as indicated by the existence of reversible and irreversible variations in the *I–V* characteristics upon heating of the sample.

(3) The synchronous decrease in the initial current of the *I–V* characteristics of GaAs(110) single crystals and the actual absence of this phenomenon for the W(100) single crystal is apparently caused by the substantial difference in the Debye screening length of these materials. This suggests that the retarding potential method allows for the detection of variations in the charge-carrier density with temperature in the surface region of semiconductors.

REFERENCES

1. T. Bechshtedt and R. Enderlein, *Semiconductor Surfaces and Interfaces. Their Atomic and Electronic Structures* (Academie-Verlag, Berlin, 1988; Mir, Moscow, 1990).
2. P. A. Anderson, Phys. Rev. **75** (8), 1205 (1949).
3. H. Shelton, Phys. Rev. **107** (6), 1553 (1957).
4. E. H. Rhoderick, *Metal-Semiconductor Contacts* (Claredon, Oxford, 1978; Radio i Svyaz', Moscow, 1982).
5. Yu. I. Asalkhanov, K. N. Ivanov, and D. Ts. Shirapova, Prib. Tekh. Éksp., No. 1, 167 (1991).
6. Yu. I. Asalkhanov, D. D. Dondokov, and I. T. Pron'kinov, USSR Inventor's Certificate 1406661, Byull. Izobret., No. 24 (1988).
7. Yu. I. Asalkhanov, I. I. Dombrovskiĭ, and S. A. Alekseev, Prib. Tekh. Éksp., No. 1, 135 (1992).
8. Yu. I. Asalkhanov, Author's Abstracts of Candidate's Dissertation (Leningr. Gos. Univ., Leningrad, 1975).

Translated by N. Korovin

Semiconductors, Vol. 36, No. 11, 2002, pp. 1288–1293. Translated from Fizika i Tekhnika Poluprovodnikov, Vol. 36, No. 11, 2002, pp. 1372–1378.

LOW-DIMENSIONAL SYSTEMS

ZnMnSe/ZnSSe Type-II Semimagnetic Superlattices: Growth and Magnetoluminescence Properties

A. A. Toropov*^, A.V. Lebedev*, S. V. Sorokin*, D. D. Solnyshkov*, S. V. Ivanov*, P. S. Kop'ev*, I. A. Buyanova, W. M. Chen**, and B. Monemar****

** Ioffe Physicotechnical Institute, Russian Academy of Sciences, Politekhnicheskaya ul. 26, St. Petersburg, 194021 Russia*

^ e-mail:toropov@beam.ioffe.rssi.ru

*** University of Linkoping, S-581 83 Linkoping, Sweden*

Submitted April 1, 2002; accepted for publication April 4, 2002

Abstract—A ZnSSe/ZnMnSe type-II semimagnetic superlattice was pseudomorphically grown via molecular beam epitaxy on a GaAs substrate. The superlattice-layer thicknesses and compositions were chosen so that compressive strains in the ZnMnSe layer compensated tensile strains in the ZnSSe layer. The photoluminescence spectra in an external magnetic field demonstrate the effect of "giant Zeeman splitting of an exciton". Simulation of the luminescence-line shift in a magnetic field allowed us to determine more accurately the band offsets at the ZnSSe/ZnMnSe interface. © *2002 MAIK "Nauka/Interperiodica".*

1. INTRODUCTION

Interest in II–VI semimagnetic semiconductor compounds, and especially in nanostructures based on these compounds, has significantly increased recently. The reason for this is a number of recent publications concerning possible applications of such materials in the rapidly developing field of "spintronics" [1], in particular, the effective injection of spin-polarized electrons from bulk layers [2–4] or a superlattice [5] of II–VI semimagnetic semiconductors into the nonmagnetic region of a semiconductor structure. Creation of new spintronic devices requires the development of techniques for growing high-quality heterostructures which contain defect-free layers of semimagnetic (diluted magnetic) semiconductors (DMSs).

A wide range of DMSs grown successfully via molecular-beam epitaxy (MBE) on GaAs substrates is represented by ZnSe and CdSe, as well as by solid solutions that are based on these semiconductors, and contain fairly low concentrations of magnetic Mn^{2+} ions. However, equilibrium lattice constants of all relevant binary compounds (5.668, 6.077, and 5.904 Å for ZnSe, CdSe, and MnSe, respectively) exceed the lattice constant of GaAs (5.6532 Å). The mismatch magnitude defines the maximum (critical) thickness of a layer that can be pseudomorphically grown, i.e., without stress relaxation. The latter is accompanied by the generation of extended defects, particularly, misfit dislocations that cause degradation of the optical and transport properties of the structure. Among the aforementioned binary materials, the maximum critical thickness (600–1000 Å) is observed in pure ZnSe. An increase in the Mn-ion concentration in $Zn_{1-x}Mn_xSe$ solid solutions increases the mismatch and decreases the critical thickness of a defect-free layer. As a result, strict restrictions are imposed on the thicknesses of epilayers and superlattices (SLs) or on the number of quantum wells (QWs) in the sample.

A considerable increase in the total thickness of SLs and multiple quantum wells (MQWs), which consist of highly stressed pseudomorphic layers, can be obtained using the method of stress compensation [6, 7]. The essence of this method consists in compensation of stresses (caused by the mismatch of the layer and substrate lattice constants) by introducing another layer of appropriate thickness with the opposite sign of the lattice parameter mismatch. For the pseudomorphic growth of such a heterostructure with alternating oppositely strained layers, it is necessary to fulfill two conditions: the thickness of each layer, as well as that of the whole structure, should not exceed the relevant critical value. When applied to II–VI compounds, such an approach made it possible to realize the pseudomorphic growth of ZnSSe/ZnCdSe MQWs with a total thickness of 6600 Å, whereas the critical thicknesses of separate layers were in the range of 100–200 Å [7].

In this paper, we report data on the MBE growth and results of studies of the magnetooptical properties of a semimagnetic superlattice with oppositely strained layers: ZnMnSe (compressive strain) and ZnSSe (tensile strain). The thicknesses and compositions of layers were chosen so that the average lattice constant of the whole structure virtually coincided with the lattice constant of the GaAs substrate.

The structure of this paper is as follows. In Section 2, the sample design and MBE-growth conditions are

1063-7826/02/3611-1288$22.00

described and the results of X-ray diffraction studies of the structure are reported. Section 3 is concerned with low-temperature photoluminescence (PL) in a magnetic field. In Section 4, a theoretical analysis based on the results of X-ray and magnetooptical measurements is carried out. This analysis allowed us to infer the type-II band structure of the superlattice and estimate the values of the band offsets at the ZnMnSe/ZnSSe interface. Section 5 summarizes the experimental results.

2. DESIGN, EPITAXIAL-GROWTH CONDITIONS, AND STRUCTURAL CHARACTERISTICS OF THE SAMPLE

The conditions for stress balance in a multilayer sample grown on a substrate with a lattice constant a_0 are fulfilled when the average lattice constant in the plane of layers ($a_\parallel$) is equal to a_0. The quantity $a_\parallel$ can be expressed as

$$a_\parallel = \frac{\sum_i a_i G_i h_i}{\sum_i G_i h_i}, \quad (1)$$

where summation is performed over all layers of the structure; and a_i, h_i, and G_i are the equilibrium lattice constant, the thickness, and the shear modulus for the ith layer, respectively. In order to compensate the compressive strain in a ZnMnSe layer grown on GaAs substrate, we have to introduce a layer whose lattice constant is smaller than $a_0 = 5.6532$ Å. To this end, the ZnSSe ternary solid solution was chosen. With the use of formula (1) and the parameters of binary compounds listed in the table, we chose the following parameters of the period of a superlattice that satisfy the conditions of the stress balance: $Zn_{0.96}Mn_{0.04}Se$ (5 nm)/$ZnS_{0.15}Se_{0.85}$ (5 nm). The lattice constants and elastic constants of the ternary solid solutions were determined via linear interpolation between the relevant values for binary materials. Since there are no data concerning the elastic constants of cubic MnSe, the elastic constants of ZnSe were used for the $Zn_{0.96}Mn_{0.04}Se$ solid solution with a low Mn content.

The sample grown by MBE on a GaAs (001) substrate consisted of alternating layers: buffer layers (20-nm ZnSe and 20-nm $ZnS_{0.06}Se_{0.94}$), a ZnMgSSe quaternary solid solution (0.2 μm) matched with GaAs in the lattice parameter, a 15-period $Zn_{0.96}Mn_{0.04}Se$ (5 nm)/$ZnS_{0.15}Se_{0.85}$ (5 nm) superlattice, ZnMgSSe (0.1 μm), and ZnSe (5 nm). We used Zn, Mg, Mn, Se, and ZnS as sources of molecular beams. The growth temperature was chosen to be 270°C, with the aim of obtaining the desirable S content in the ZnMgSSe layers grown by MBE in optimal conditions (the ratio of elements VI/II ≈ 1) using the strong temperature dependence of the incorporation coefficient of S [14]. Correspondingly, ZnMnSe layers were grown on the surface stabilized by Se atoms.

Parameters of binary compounds

Parameter	ZnSe	ZnS	MnSe
a_0, Å	5.668 [8]	5.4093 [9]	5.904 [10]
c_{11}, Mbar	0.826 [11]	1.067 [11]	
c_{12}, Mbar	0.498 [11]	0.666 [11]	
a_c, eV	−4.17 [11]	−4.09 [11]	
a_v, eV	1.65 [11]	2.31 [11]	
b, eV	−1.2 [11]	−0.8 [11]	
Δ_{SO}, eV	0.43 [11]	0.07 [11]	
E_{vav}, eV	−8.37 [11]	−9.15 [11]	
m_e/m_0	0.16 [8]	0.34 [12]	
m_{hh}/m_0	0.6 [8]	1.76 [13]	
m_{lh}/m_0	0.145 [8]	0.23 [13]	
E_g, eV (at 0 K)	2.821 [8]	3.84 [11]	

Note: a_0 is the equilibrium lattice constant; c_{11} and c_{12} are elastic constants; a_c, a_v, and b are the deformation potentials; Δ_{SO} is the energy of spin–orbit splitting; m_e, m_{hh}, and m_{lh} are the effective masses of electrons, heavy holes and light holes, respectively; and m_0 is the free electron mass.

The rocking curve of X-ray diffraction measured with a double-crystal X-ray diffraction spectrometer for the (004) reflection is shown in Fig. 1. The curve includes the main diffraction peak from the superlattice (0) and equally spaced satellites (+1 and –1). The main peak virtually coincides with the narrow diffraction peak from the GaAs substrate. This indicates that the stress balance conditions are fulfilled in the superlattice. The superlattice period (9.8 ± 0.5) nm, estimated

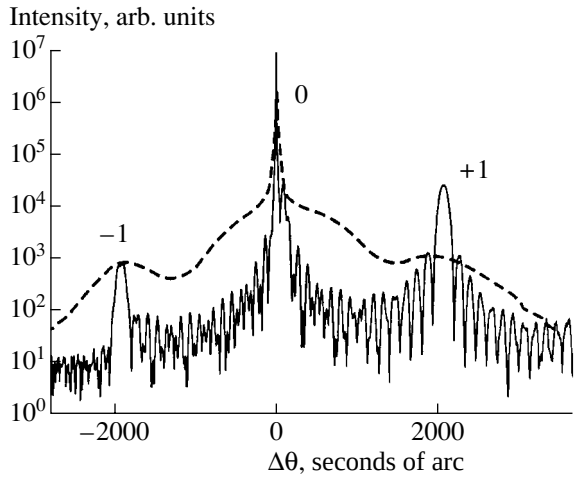

Fig. 1. (θ – 2θ) rocking curve of X-ray diffraction for the (004) reflection, measured (dashed line) and calculated (solid line) with parameters corresponding to the best fit with magnetooptical experimental data.

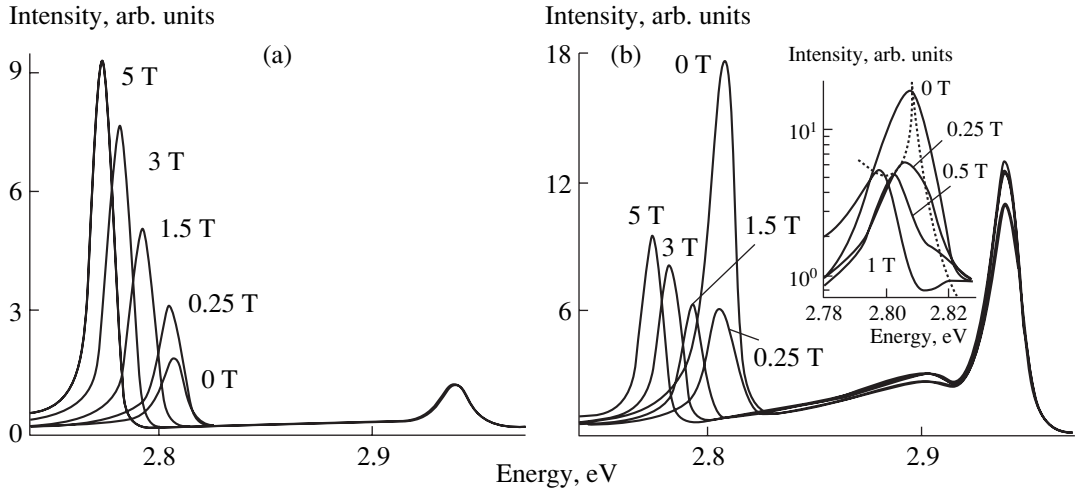

Fig. 2. Magnetophotoluminescence spectra measured in cases of (a) σ^+ polarization and (b) σ^--polarization. (Inset (b) shows spectra on semilog scale).

from the distance between satellites, is in good agreement with the design parameters.

3. MAGNETOPHOTOLUMINESCENCE MEASUREMENTS

In order to measure magnetophotoluminescence spectra, the sample was placed in a helium cryostat with a superconducting magnet supplying magnetic fields as high as 5 T. Liquid helium vapor was pumped out from the cell to maintain the sample temperature $T = 1.8$ K. All spectra discussed in this paper were measured in the Faraday geometric layout (the direction of the magnetic field coincided with the direction in which photoluminescence was detected (z axis) and with the crystal growth axis). Luminescence was excited with an Ar^+-laser operating at ultraviolet wavelengths (352–372 nm). The excitation light was linearly polarized. A quarter-wave plate and linear polarizer were placed sequentially to analyze the circular polarization of PL.

PL spectra measured in fixed magnetic fields for circular polarizations σ^+ (a) and σ^- (b) are shown in Fig. 2. There are three peaks in the spectrum detected in zero magnetic field. Two peaks (in the vicinity of 2.94 and 2.90 eV) are related to PL from "confining" ZnMgSSe layers. One of these peaks (~2.94 eV) is caused by the luminescence of localized or bound excitons with energies close to the absorption edge of ZnMgSSe. The other peak (~2.90 eV) was tentatively attributed to recombination of donor–acceptor pairs in the same layer. The peak at ~2.81 eV is related to the exciton PL from the semimagnetic ZnMnSe/ZnSSe superlattice.

Such an interpretation of the spectrum is in good agreement with the observed effect of the magnetic field. Indeed, both short-wavelength peaks (2.90 and 2.94 eV) behave similarly: the peak location virtually does not depend on the magnetic field. The only effect we have observed is the occurrence of weak σ^- polarization of peaks with an increase in the magnetic field. The degree of circular polarization does not exceed 10% in the magnetic field $B = 5$ T. Such behavior is typical of wide-gap nonmagnetic compounds based on ZnSe (see, for example, [15]), because the Zeeman splitting of exciton levels in the magnetic fields we used is much less than the widths of the peaks observed in our experiments.

The third peak located at longer wavelengths behaves quite differently. An increase in the magnetic field results in a noticeable shift (~40 meV at $B = 5$ T) and σ^+ polarization of this peak. The degree of σ^+ polarization in the peak maximum is about 90% in magnetic fields $B < 1$ T, and it levels off in higher magnetic fields. In addition, the peak is split into two components in σ^--polarized spectra in magnetic fields $B < 2$ T, as can be seen from Fig. 2b (inset). The dependences of the positions of these peaks in σ^+ and σ^- polarizations on the magnetic field are shown in Fig. 3.

Such behavior is typical of the giant Zeeman exciton-splitting effect [16], which is usually observed in DMSs due to the *s–d* (*p–d*) exchange interaction between Mn^{2+} ions and electrons (holes). According to the well-known selection rules for optical transitions [17], σ^+ polarization corresponds to recombination of an exciton with the total component of the angular momentum of +1. We should note that, in a thin strained ZnMnSe layer, a compressive strain causes the splitting of a fourfold degenerate hole level into two doubly degenerate levels of light and heavy holes with the components of angular momentum $|\pm 1/2\rangle$ and $|\pm 3/2\rangle$, respectively (see scheme in Fig. 4). The ground hole state is the heavy-hole level, the twofold degeneracy of which is removed by a magnetic field directed along the z axis. As a result, the exciton $|-1/2, +3/2\rangle$ is a basic, optically active state where the symbol $s(m)$ in the designation $|s, m\rangle$ indicates the z component of the electron spin (the hole angular momentum). The total

component of angular momentum of such an exciton is equal to +1, which is in agreement with the observed σ^+ polarization of the PL peak with a lower energy. In accordance with the selection rules, the upper component of the heavy-hole exciton doublet, $|+1/2, -3/2\rangle$, should manifest itself in the σ^- polarization. This allows us to identify the upper component with the weak feature we observed on the short-wavelength side of the main peak in the σ^--polarized PL spectra.

4. BAND OFFSETS AT THE ZnMnSe/ZnSSe INTERFACE

4.1. Band Offsets under Zero Magnetic Field

In order to estimate the values of the band offsets at the $Zn_{1-x}Mn_xSe/ZnS_ySe_{1-y}$ interface, we used previously published data on the band offsets at the interfaces in $Zn_{1-x}Mn_xSe/ZnSe$ and $ZnSe/ZnS_ySe_{1-y}$ unstrained layers and the "transitivity rule". The Van de Walle theory [11] was used to take into account the effect of strains caused by the mismatch of the layer and substrate lattice parameters on band offsets.

It is well known that the difference between the band gaps (E_g) of $Zn_{1-x}Mn_xSe$ and ZnSe is primarily caused by the conduction-band offset. In accordance with the data reported in [18, 19], the contribution of the valence-band offset to the total offset ranges from 5 to 20%. This value depends on x. Taking into account the weak dependence of E_g on x in the region of low Mn concentrations allows us to ignore the valence-band offset at the $Zn_{1-x}Mn_xSe/ZnSe$ interface in the sample with $x \sim 0.04$.[1] Compressive strain in a pseudomorphic $Zn_{1-x}Mn_xSe$ layer causes an increase in the band gap mainly due to an increase in the conduction-band energy. As for the valence band, the effect of plane strains in the pseudomorphic layer on the band structure can be considered as a sum of two components, uniform compression and uniaxial compressive strain [11]. The first component reduces the energy of the valence-band centroid. Uniaxial compressive strain removes the degeneracy of the heavy- and light-hole bands and increases the energy of the heavy-hole band. The second effect is dominant in $Zn_{1-x}Mn_xSe$. It results in a shift-up of the energy of the heavy-hole band in $Zn_{1-x}Mn_xSe$ in comparison with ZnSe and leads to the formation of a type-II band structure at the interface when the $Zn_{1-x}Mn_xSe$ layer serves as a barrier for electrons and as a well for holes.

At the interface of unstrained $ZnSe/ZnS_ySe_{1-y}$ layers, the contribution of the valence band to the total band offset is dominant [11, 21]. Moreover, a large value of bowing in the $E_g(y)$ dependence (according to the estimation made in [22], the bowing parameter for the ZnS_ySe_{1-y} solid solution is 0.43 eV) leads to the formation of type-II bands at the interface in a wide range of solid-solution compositions. In this case, the ZnS_ySe_{1-y} layer serves as a barrier for holes and as a well for electrons. Tensile strains in the pseudomorphic ZnS_ySe_{1-y} layer cause an additional increase in the band offsets at the interface both for electrons and heavy holes.

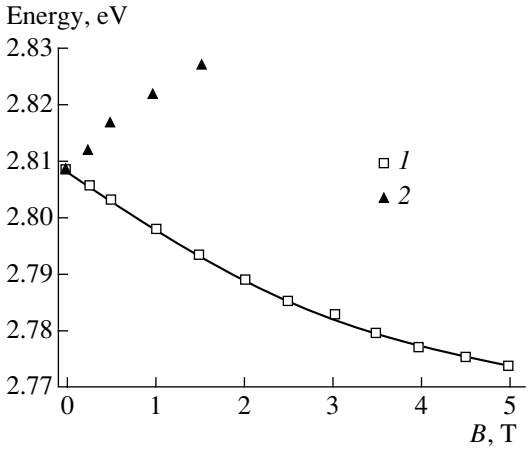

Fig. 3. The magnetic-field dependences of locations of (*1*) the main PL peak observed in the cases of both σ^+ and σ^- polarizations, and (*2*) the poorly pronounced spectral feature observed only in the case of σ^- polarization. The solid line corresponds to the best theoretical fit.

All considered data on the band arrangement at the $Zn_{1-x}Mn_xSe/ZnSe$ and $ZnSe/ZnS_ySe_{1-y}$ interfaces allow us to infer a type-II $Zn_{1-x}Mn_xSe/ZnS_ySe_{1-y}$ quantum well: electrons and holes are localized in ZnS_ySe_{1-y} and $Zn_{1-x}Mn_xSe$ layers, respectively (the scheme in Fig. 4 shows the relative band position in unstrained $Zn_{1-x}Mn_xSe$ and ZnS_ySe_{1-y} and the effect of elastic strains and magnetic field on these bands). The largest error in calculating the band offsets at the interface is introduced due to the lack of reliable data concerning band offsets at the interface of unstrained ZnSe and ZnS_ySe_{1-y} layers. The use of approximate values for "absolute" band energies for unstrained ZnSe and ZnS, given by Van de Walle in [11] (the energies of the conduction-band bottom and the centroid of the three valence bands at the Γ point are denoted in [11] as E_c and E_{vav}, respectively), as well as other parameters listed in the table, yield the following values of offsets for the valence band (heavy holes) and the conduction band at the $Zn_{0.96}Mn_{0.04}Se/ZnS_{0.15}Se_{0.85}$ interface: $\Delta V_{hh} = 134$ meV and $\Delta V_c = 54$ meV. As will be shown further on, fitting of the structure parameters based on the experimental data of X-ray diffraction and the exciton Zeeman splitting makes it possible to determine these values more accurately.

[1] The dependence $E_g(x)$ was calculated using empirical formulas $E_g(x) = 2.821 - 0.145x + 4.073x^2$ ($x < 0.13$), and $E_g(x) = 0.4906x^2 - 0.3727x + 2.8143$ ($x > 0.13$) which satisfactorily describe the experimental dependences reported in [20].

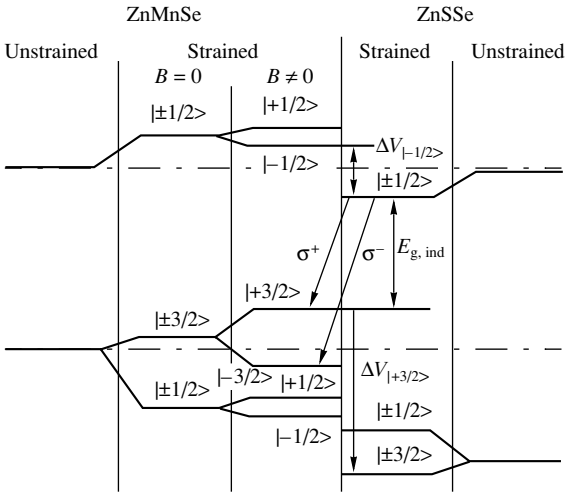

Fig. 4. Effects of strains and a magnetic field on the band structure of the ZnMnSe and ZnSe solid solutions. Strains arise under pseudomorphic growth on GaAs. Arrows correspond to layer-to-layer ("oblique") interband transitions with the lowest energy allowed in σ^+ and σ^- polarizations. Dot-and-dash lines show the location of bands for unstrained ZnSe.

4.2. Effect of Magnetic Field on Band Offsets

The main effect of the magnetic field in the range of $B < 5$ T on the band structure of DMS is the giant Zeeman splitting [10, 16]. The shifts of the conduction band ($\Delta E_{c,\pm1/2}$) and the split-off heavy-hole band ($\Delta E_{hh,\pm3/2}$) can be written as

$$\Delta E_{c,\pm1/2} = \pm\frac{1}{2}xN_0\alpha\langle S_z\rangle, \quad (2a)$$

$$\Delta E_{hh,\pm3/2} = \pm\frac{1}{2}xN_0\beta\langle S_z\rangle. \quad (2b)$$

Here, x is the concentration of Mn^{2+} ions, $N_0\alpha$ and $N_0\beta$ are exchange constants, and $\langle S_z\rangle$ is the average value of the z spin component of Mn^{2+} ions,

$$\langle S_z\rangle = S_0 B_{5/2}\left(\frac{(5/2)g\mu B}{kT_{\text{eff}}}\right), \quad (3a)$$

$$T_{\text{eff}} = T + T_0, \quad (3b)$$

where $g = 2$, μ is the Bohr magneton, $B_{5/2}$ is the modified Brillouin function for spin 5/2, and S_0 and T_0 are phenomenological parameters that describe the antiferromagnetic interaction between spins of Mn^{2+} ions. In calculations, we used values of $N_0\alpha = 0.26$ eV and $N_0\beta = -1.31$ eV, which were measured in bulk ZnMnSe [23]. The dependence of S_0 on the concentration of Mn^{2+} ions was determined by interpolating the experimental data obtained in [24].

For well-known values of band offsets at $B = 0$ (ΔV_{hh} and ΔV_c) and parameters of layers (x and y), expressions (2) and (3) make it possible to determine the potentials of electrons with spin $s = -1/2$ and holes with the component of angular momentum $m = +3/2$ for an arbitrary magnetic field. These parameters are used in calculations of ground confined energy levels of the MQW structure (E_e and E_{hh}) in the effective-mass approximation in terms of the simple model of spherically isotropic bands. Negligible band shifts for the nonmagnetic material ZnS_ySe_{1-y}, which are caused by a magnetic field, are disregarded in this calculation. In this case, the energy of an exciton $|-1/2, +3/2\rangle$ in σ^+ polarization can be written as

$$E_{|-1/2,+3.2\rangle} = E_{g,\text{ind}} + \Delta E_{hh,3/2} + E_e + E_{hh} - E_b, \quad (4)$$

where E_b is the exciton binding energy, and $E_{g,\text{ind}}$ is the band gap, which corresponds to indirect optical transitions in type-II quantum wells under zero magnetic field (Fig. 4). The value of $E_b \sim 14$ meV was obtained using the variational method previously developed for coupled quantum wells [25]. Such an exciton is a type-II exciton, whose electron and hole are separated in space in the entire range of magnetic fields. Since the estimated band offsets at $B = 0$ essentially exceed the change in the potential, caused by the magnetic field, the dependence of E_b on the magnetic field can be ignored.

The exciton energy was derived from the measured magnetophotoluminescence spectra by estimating the Stokes shift $\Delta E_{\text{st}} = 0.6\Gamma$, where Γ is the full width at half-height of the PL peak related to localized excitons [26]. In the sample with a low concentration of Mn^{2+} ions [27], the magnetopolaron effect was considered as rather weak and thus disregarded. The theoretical curve obtained from the numerical solution of the system of equations (5a)–(5d) was fitted to the experimental dependence of the PL-peak energy on the magnetic field $E_{\text{PL}}(B)$ taking into account the X-ray diffraction data:

$$E_{\text{PL}}(B, x, T_{\text{eff}}) = E_{g,\text{ind}} + \Delta E_{hh,3/2}(x, T_{\text{eff}}, B) + E_e(\Delta V_c, x, T_{\text{eff}}, B) + E_{hh}(\Delta V_{hh}, x, T_{\text{eff}}, B) - E_b - \Delta E_{\text{st}}, \quad (5a)$$

$$\Delta V_c(x) = E_g^{\text{ZnMnSe}}(x) - E_{g,\text{ind}}, \quad (5b)$$

$$\Delta V_{hh}(y) = E_g^{\text{ZnSSe}}(y) - E_{g,\text{ind}}, \quad (5c)$$

$$x = f(\theta_0, y). \quad (5d)$$

Here, E_g^{ZnMnSe} and E_g^{ZnSSe} are the band gaps of pseudomorphic layers of solid solutions in zero magnetic field, calculated with the use of parameters listed in the table. T_{eff}, $E_{g,\text{ind}}$, and y were used as adjustable parameters. Equation (5d) establishes a functional link between x and y, which follows from the Bragg law for the measured location of "zero" reflection of X-ray diffraction ($\theta_{0'}$) from the periodical $Zn_{1-x}Mn_xSe/ZnS_ySe_{1-y}$ structure with fixed values of layer thicknesses. The best fit,

shown in Fig. 3a by the solid line, corresponds to the following values of the parameters: $y = 0.159$, $x = 0.033$, $T_{\text{eff}} = 6.7$ K, $E_{g,\text{ ind}} = 2.806$ eV, $\Delta V_{hh} = 110$ meV, and $\Delta V_c = 23$ meV. The solid line in Fig. 1 is the result of simulation of the diffraction curve in the semikinematic approximation for the structure with refined values of x and y parameters. The widths of the minibands of heavy holes (0.1 meV) and electrons (17 meV) were obtained by calculating the spectrum of the electron and hole states of the superlattice in terms of the Kronig–Penney model. In accordance with these values, quantum wells for a heavy hole are isolated, while the electron potential can be considered as a system of coupled quantum wells. We should note that coupling between electron quantum wells was explicitly considered in the calculation of E_e and E_b. The values of x and y, obtained through fitting, are in good agreement with the design parameters. Nevertheless, the band offsets are much smaller than the values obtained in subsection 4.1 using the parameters E_c and E_{vav} for ZnSe and ZnS from [11]. The difference is most probably caused by the ambiguity of the published data on the relative position of ZnSe and ZnS bands as well as by errors in the determination of important parameters of the ZnS_ySe_{1-y} ternary solid solution.

5. CONCLUSION

A semimagnetic pseudomorphic multilayer $Zn_{1-x}Mn_xSe/ZnS_ySe_{1-y}$ structure was grown via MBE on a GaAs substrate. In this structure, stress balance was achieved: compressive stresses in $Zn_{1-x}Mn_xSe$ layers were compensated by tensile stresses in ZnS_ySe_{1-y} layers. Estimations based on the transitivity rule and known data on the band offsets at the ZnMnSe/ZnSe and ZnSe/ZnSSe interfaces allowed us to conclude that the band structure belongs to type II: ZnMnSe and ZnSSe layers serve as QWs for holes and electrons, respectively. An appreciable shift of the PL exciton line is observed in an external magnetic field. This shift is primarily governed by the (p–d)-exchange interaction between holes, localized in ZnMnSe layers, and Mn^{2+} ions. The simultaneous fitting of the location of the PL line recorded in a magnetic field and X-ray diffraction rocking curves made it possible to determine more accurately the compositions of ternary solid solutions in the sample and band offsets at the ZnMnSe/ZnSSe interface.

ACKNOWLEDGMENTS

This study was supported by the Russian Foundation for Basic Research (project nos. 00-02-16997 and 02-02-17643), INTAS (grant no. 01-2375), Ministry of Science and Technology of the Russian Federation program “Physics of Solid-State Nonostructures”, the Volkswagen Foundation, and the Swedish Royal Academy of Sciences.

REFERENCES

1. G. A. Prinz, Science **282**, 1660 (1998).
2. M. Oestreich, J. Hübner, D. Hägele, *et al.*, Appl. Phys. Lett. **74**, 1251 (1999).
3. R. Fiederling, M. Keim, G. Reuscher, *et al.*, Nature **402**, 787 (1999).
4. B. T. Jonker, Y. D. Park, B. R. Bennett, *et al.*, Phys. Rev. B **62**, 8180 (2000).
5. Ya. V. Terent’ev, A. A. Toropov, S. V. Sorokin, *et al.*, Phys. Status Solidi B **229**, 765 (2002).
6. D. C. Houghton, M. Davies, and M. Dion, Appl. Phys. Lett. **64**, 505 (1994).
7. T. V. Shubina, S. V. Ivanov, A. A. Toropov, *et al.*, J. Cryst. Growth **184/185**, 596 (1998).
8. H. J. Lozykowsky and V. K. Shastri, J. Appl. Phys. **69**, 3235 (1991).
9. *Landolt-Börnstein: Numerical Data and Functional Relationships in Science and Technology, New Series* (Springer-Verlag, Berlin, 1982).
10. J. K. Furdina and J. Kossut, *Semiconductors and Semimetals*, Vol. 25: *Diluted Magnetic Semiconductors* (Academic, New York, 1988).
11. C. Van de Walle, Phys. Rev. B **39**, 1871 (1989).
12. H. Kukimoto and S. Shionoya, J. Phys. Chem. Solids **29**, 935 (1968).
13. P. Lawaetz, Phys. Rev. B **4**, 3460 (1971).
14. S. V. Ivanov, S. V. Sorokin, P. S. Kop’ev, *et al.*, J. Cryst. Growth **159**, 16 (1996).
15. G. V. Astakhov, D. R. Yakovlev, V. P. Kochereshko, *et al.*, Phys. Rev. B **60**, 8485 (1999).
16. J. A. Gaj, R. Planel, and G. Fishman, Solid State Commun. **29**, 435 (1979).
17. *Optical Orientation*, Ed. by F. Meier and B. P. Zakharchenya (North-Holland, Amsterdam, 1984; Nauka, Leningrad, 1989).
18. E. Deleporte, T. Lebihen, B. Ohnesorge, *et al.*, Phys. Rev. B **50**, 4514 (1994).
19. P. J. Klar, D. Wolverson, J. J. Davies, *et al.*, Phys. Rev. B **57**, 7103 (1998).
20. R. B. Bylsma, W. M. Becker, J. Kossut, *et al.*, Phys. Rev. B **33**, 8207 (1986).
21. C. Priester, D. Bertho, and C. Jouanin, Physica B (Amsterdam) **191**, 1 (1993).
22. R. Mach, P. Flogel, L. G. Sunlina, *et al.*, Phys. Status Solidi B **109**, 607 (1982).
23. A. Twardowski, M. von Ortenberg, M. Demianiuk, and R. Pauthenet, Solid State Commun. **51**, 849 (1984).
24. W. Y. Yu, A. Twardowski, L. P. Fu, *et al.*, Phys. Rev. B **51**, 9722 (1995).
25. S. M. Cao, M. Willander, E. L. Ivchenko, *et al.*, Superlattices Microstruct. **17**, 97 (1995).
26. K. P. O’Donnel, P. J. Parbrook, F. Yang, *et al.*, Physica B (Amsterdam) **191**, 45 (1993).
27. C. D. Poweleit, L. M. Smith, and B. T. Jonker, Phys. Rev. B **50**, 18 662 (1994).

Translated by I. Kucherenko

Semiconductors, Vol. 36, No. 11, 2002, pp. 1294–1298. Translated from Fizika i Tekhnika Poluprovodnikov, Vol. 36, No. 11, 2002, pp. 1379–1383.

LOW-DIMENSIONAL SYSTEMS

Ordering of Nanostructures in a Si/$Ge_{0.3}Si_{0.7}$/Ge System during Molecular Beam Epitaxy

G. E. Cirlin[1, 2, 3]*, V. A. Egorov[1, 2, 3], L. V. Sokolov[3, 4], and P. Werner[4]

[1] *Institute for Analytical Instrumentation, Russian Academy of Sciences, St. Petersburg, 198063 Russia*

[2] *Ioffe Physicotechnical Institute, Russian Academy of Sciences, St. Petersburg, 194021 Russia*

[3] *Max-Planck Institut für Mikrostrukturphysik, D-06120 Halle/Saale, Germany*

[4] *Institute of Semiconductor Physics, Siberian Division, Russian Academy of Sciences, Novosibirsk, 630090 Russia*

** e-mail: cirlin@beam.ioffe.rssi.ru*

Submitted April 24, 2002; accepted for publication April 24, 2002

Abstract—The structural properties of nanoobjects in a heteroepitaxial Si/$Ge_{0.3}Si_{0.7}$/Ge system have been studied using atomic-force microscopy. The formation of nanometer islands occurs at a lower Ge thickness than in the case of Si/Ge heteroepitaxy. The effects of the spatial ordering of the nanostructures are found: the formation of groups of *hut*-clusters around craters at the initial stage of the formation of 3D objects, and the alignment of *dome*-clusters in rows as the amount of deposited Ge rises. © *2002 MAIK "Nauka/Interperiodica".*

1. INTRODUCTION

The study of self-ordering on the surface of semiconductors of various compositions is attracting considerable attention. One of the main lines of inquiry is the study of the spontaneous formation of nanosize clusters in strained heteroepitaxial systems; upon the subsequent overgrowth with the material of a substrate they can form quantum dots (QD), where 3D-quantization and, consequently, the formation of an atomic-like energy spectrum can be observed [1, 2]. Spatial ordering of such nanostructures can occur at specific growing parameters. These ordered structures are required for the fabrication of various devices, such as distributed feedback lasers and memory devices. The spontaneous ordering of QDs into rows on vicinal (100) GaAs surfaces [3], spatial ordering and a reduced variation in QD size in 3D multilayer structures [4], etc., were observed in the InGaAs/GaAs system. Similar effects were found in multilayer structures with germanium QDs in a silicon matrix [5].

To fabricate ordered structures, it is necessary, among other things, to produce a spatially nonuniform stress field in the layer underlying the one which contains nanostructures. Then, it is energetically favorable for quantum-size clusters to be formed in the local maxima or minima (depending on the distance from strained layers and the chosen specific material). To produce such fields, profiled substrates, or those prepared by lithography, are used [6], dislocation grids are formed in underlying layers [7], and so on. However, these methods are not always efficient for device production due to the high density of structural defects in such structures.

As the sublayer, we propose to use a strained quantum well (QW) whose composition and thickness are definitely below the critical thickness of dislocation and 3D-island formation (e.g., via the Stranski–Krastanow mechanism). This QW must, on the one hand, produce stress fields and, on the other hand, contain a low density of structural defects. As a model, we have chosen a heteroepitaxial Si/Ge system with a lattice mismatch of ≈4%.

2. EXPERIMENT

Growth was performed using a Riber SIVA 45 (France) MBE system, with (100) *p*-Si boron-doped substrates having 5–20 Ω cm conductivity. Commercial substrates, 5 in. in diameter, from OKMETIC (Sweden) were used. The chemical treatment of substrates was described in [8]. The prepared substrates were dried using argon with a purity of 6.0 and immediately loaded into the MBE-machine lock chamber. This method allowed for the removal of the oxide layer from the Si surface through radiation heating to 840°C in the growth chamber. The sample heater was rotated during growth; the nonuniformity of the temperature field over the substrate surface was ≈5%. The stability of the deposition rate was ensured by two feedback mass-spectrometers tuned to masses of 28 (Si) and 74 (Ge). The residual atmospheric vapor pressure during the growth was not worse than 5×10^{-10} Torr. The state of the surface was monitored *in situ* by means of reflection high-energy electron diffraction (RHEED).

The structures under study were comprised of a 500-Å-thick Si buffer layer and a 50-Å $Ge_{0.3}Si_{0.7}$ sublayer covered with a thin (5 Å) layer of pure Si, onto which 6–12 Å of Ge were deposited. During the deposition of the QD sheet, after each monolayer (ML) grown, there were two-minute breaks (starting from the

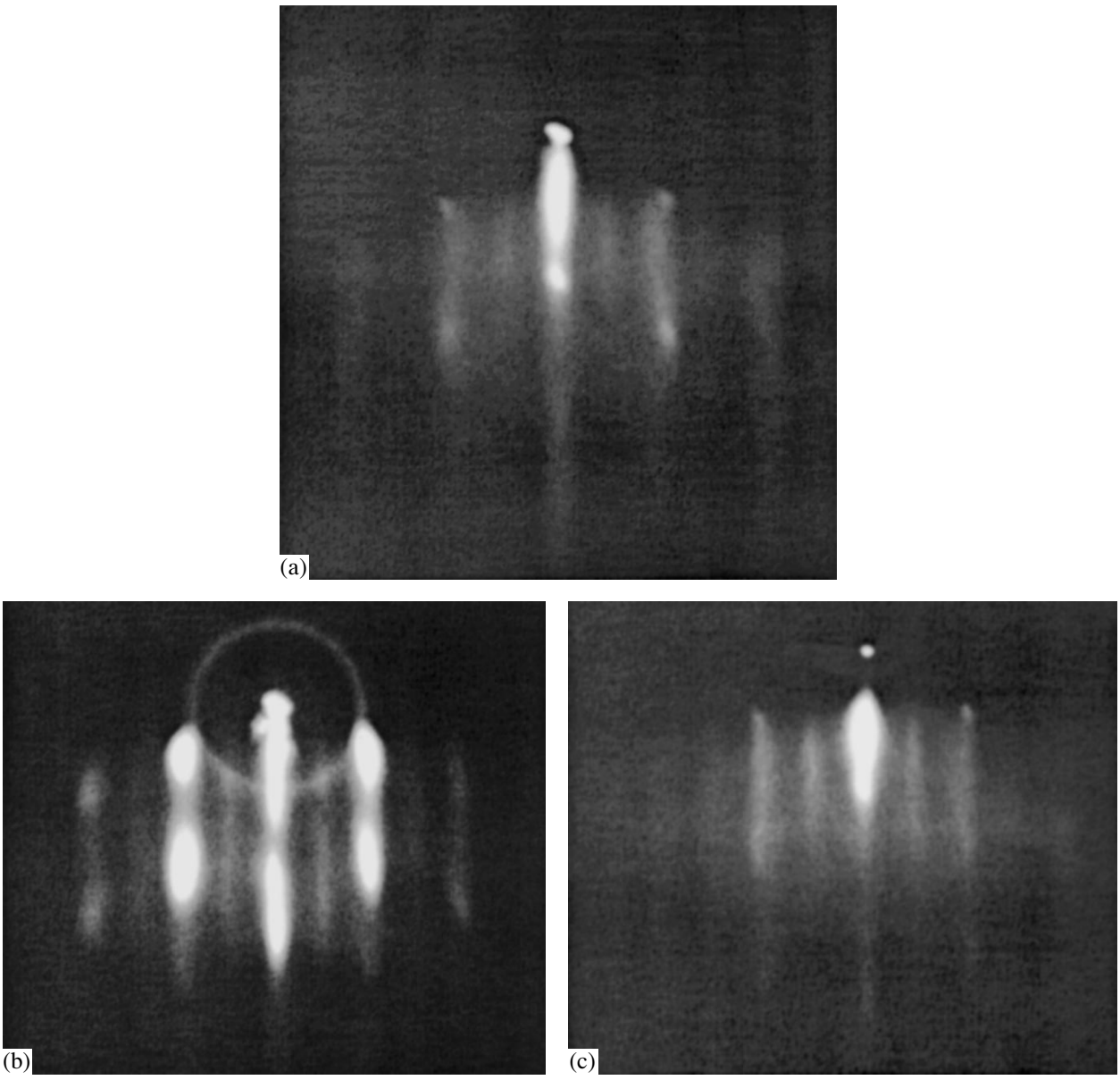

Fig. 1. RHEED patterns after the deposition onto the surface of (a) 4 Å of Ge with a GeSi sublayer, (b) 6 Å of Ge with a GeSi sublayer, and (c) 6 Å of Ge without a sublayer.

fourth) with the rotation stopped in order to record the RHEED pattern. The substrate temperature was T_{sub} = 450°C for the buffer layer and T_{sub} = 500°C for the rest of the structure. The growth rates were 0.5 Å/s for the buffer, 0.11 Å/s for the active region, and 0.05 Å/s for Ge. The surface was characterized *ex situ* using an atomic force microscope (AFM) manufactured by Digital Instruments Inc. (USA).

3. RESULTS AND DISCUSSION

The RHEED patterns observed during the growth confirm the planarity of the sublayer and the thin Si cap layer. Further, after the deposition of approximately. 4 Å of Ge, the RHEED patterns indicate the formation of a corrugated surface (Fig. 1a), and 3D-islands are formed when the Ge thickness amounts to 6 Å (Fig. 1b). It is worth noting that no substantial deviation from the initial (2 × 2) surface reconstruction was observed even when 6 Å of Ge was deposited onto a Si surface without a sublayer (Fig. 1c). The results obtained suggest that the $Ge_{0.3}Si_{0.7}$ sublayer induces stresses in the top portion of the structure, thus resulting in an earlier transition from 2D to 3D growth. Figure 2 presents an AFM surface image of a sample containing 6 Å of Ge as the top layer. As seen in the figure, nanoislands (so-called *hut*-clusters) appear on the surface in spite of the yet subcritical thickness of the Ge layer (after which the transition from planar to 3D growth occurs). It is neces-

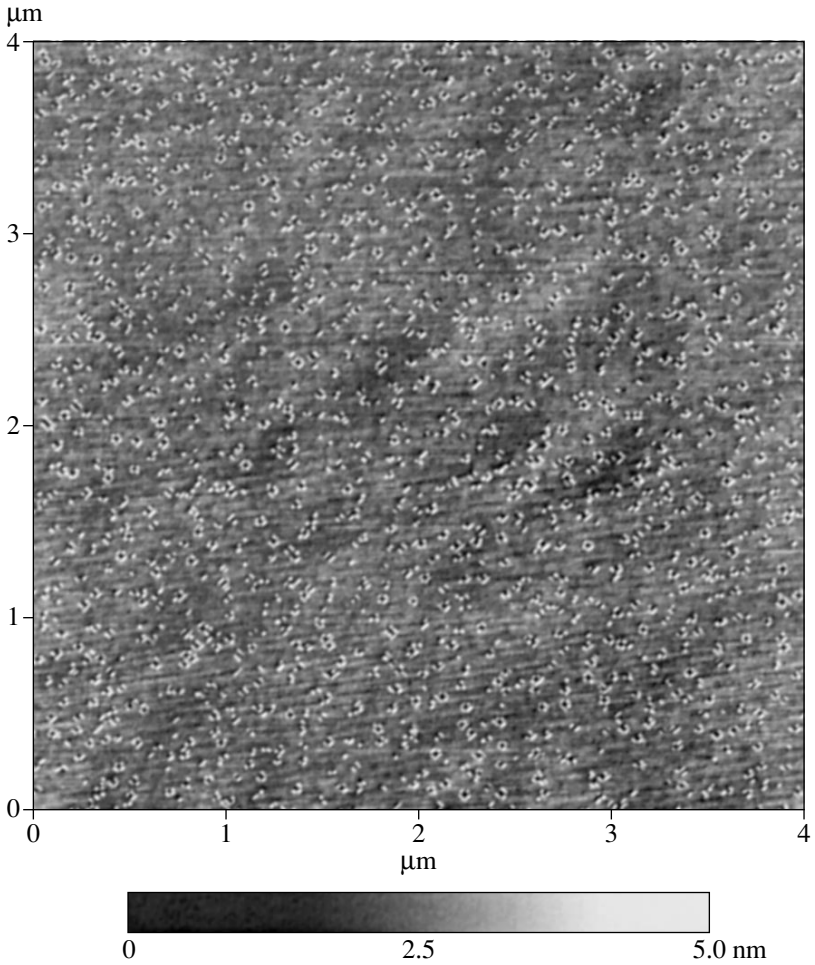

Fig. 2. Surface AFM image of a structure with a GeSi sublayer after the deposition of 6 Å of Ge.

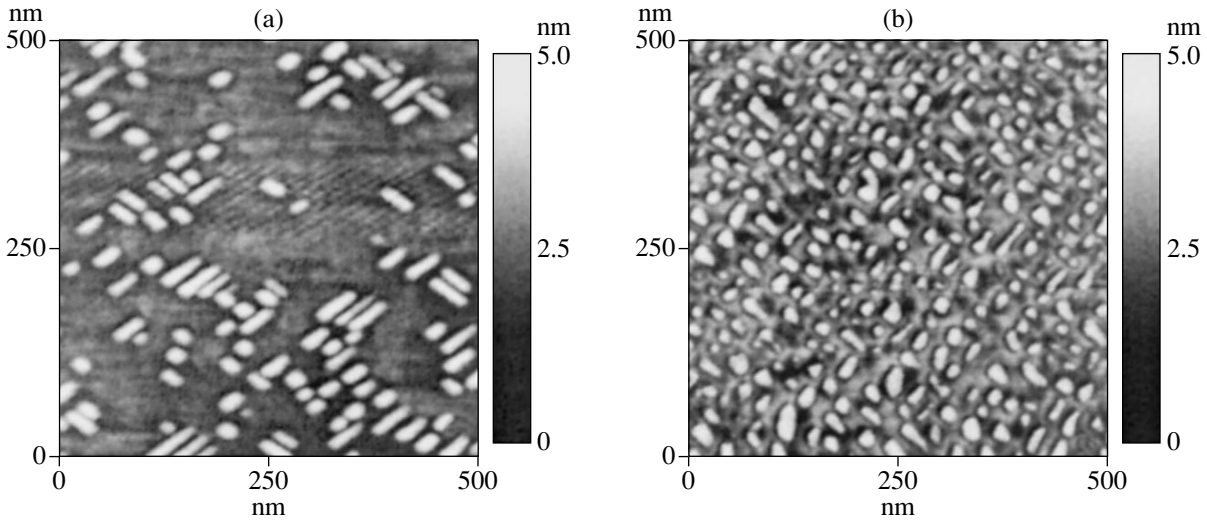

Fig. 3. Surface AFM image of a structure with a GeSi sublayer after the deposition of (a) 7 Å of Ge and (b) 9 Å of Ge.

sary to note that when deposition onto Si free of a strained sublayer was carried out, the critical thickness determined from the behavior of the surface RHEED patterns was d_{crit} = 7 Å. The lateral dimensions of the islands are 20–50 nm in length and ≈8 nm in width. A small scatter in width is worth noting. The height of the islands is also nearly uniform; it is ≈2 nm. An interesting feature is the formation of craters, up to 3 nm in

depth, in whose neighborhood groups of islands with mutually perpendicular {011} orientations are preferentially formed.

Raising the deposited layer thickness to 7 Å results in a rise in the density of islands (Fig. 3a), with a simultaneous decrease in the density of craters when the thickness is increased to 9 Å (Fig. 3b). Nearly the entire surface is covered with hut-clusters, their density is maximal, and the craters virtually disappear. In this situation, the dimensions and shapes of islands are not strongly changed in comparison with the case of deposition of 6 Å of Ge. With the amount of the deposited Ge rising, the RHEED patterns reveal the formation of a more pronounced faceted structure, which is probably related to the increase in the density of nanoislands. When the amount of the deposited Ge increases to 12 Å, the structure surface changes drastically. Typical of this case is the formation of large Ge clusters of the *dome* and *super-dome* type [9] (Fig. 4a) with a distinctly pronounced facet structure observed in the RHEED patterns (Fig. 4b). The super-dome clusters are 50–150 nm in lateral size and ≈20 nm in height. Their density substantially decreases. As seen in the AFM images presented, in all the cases, the Ge nanoislands are regularly aligned along definite directions on the surface. In the last case, super-dome clusters form chains along the [11*n*] directions, where *n* is an integer between 2 and 4, with the short-range order preserved.

As seen in Fig. 2, though solitary islands occur, the overwhelming majority of islands are located around the craters and aligned with a high degree of ordering in definite crystallographic directions. A possible mechanism for the formation of such clusters is as follows: elastic stresses induced by the GeSi sublayer and/or random fluctuations of the QW composition can give rise to local continuity disruptions in the thin capping Si layer. These breaks are the centers of increased concentrations of Ge adatoms owing to a long-range potential of the defect–adatom type [10]. However, at the initial stage before 4 ML, the deposited amount of Ge is insufficient for the formation of 3D islands and the diffusion of Ge atoms from a GeSi QW occurs. As a result, the effective amount of Ge on the surface increases. This transport of a material is most efficient for centers of elastic stresses (craters), and it is more energetically favorable for Ge nanoislands to be formed in groups in the vicinity of local breaks in the Si layer. The interruption of growth during the initial moments of island formation additionally stimulates the migration of Ge adatoms to local centers of elastic stresses. As the thickness of the deposited Ge grows, nanoislands gradually fill the surface first and then the craters. The observed, clearly pronounced ordering of nanoislands into rows with a further increase in the amount of Ge cannot be explained by the effect of "step stacking," which is typical of, e.g., vicinal surfaces [11]. A possible explanation of this effect may be the formation of a quasi-periodic macroscopic relief on the surface due to the elastic interaction of a strained QW with an ensemble of nanoislands.

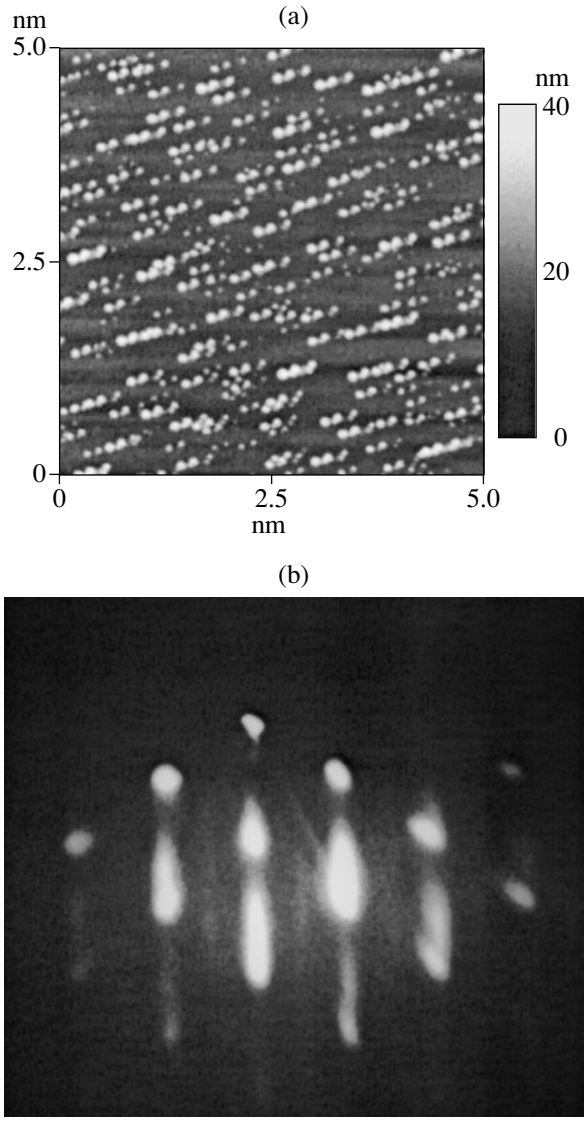

Fig. 4. (a) Surface AFM image of a structure with a GeSi sublayer after the deposition of 12 Å of Ge; (b) the corresponding RHEED pattern.

Thus, we have studied some of the ordering effects arising in a Si/$Ge_{0.3}Si_{0.7}$/Ge system during MBE growth. In this system, nanosize islands form earlier than in the case of conventional Si/Ge heteroepitaxy. The special features of our case is the ordering of nanoislands according to size, and also according to the spatial position of groups at the initial stage, and the long-range order in the rows of nanoislands formed during further deposition of Ge.

ACKNOWLEDGMENTS

This study was supported in part by the scientific program of the St. Petersburg Scientific Center and the

Ministry of Industry and Science of the Russian Federation, "Low-Dimensional Quantum Structures." One of us (G.E.C.) is grateful to the Humboldt Foundation.

REFERENCES

1. N. N. Ledentsov, V. M. Ustinov, V. A. Shchukin, *et al.*, Fiz. Tekh. Poluprovodn. (St. Petersburg) **32**, 385 (1998) [Semiconductors **32**, 343 (1998)].
2. D. Bimberg, M. Grundmann, and N. N. Ledentsov, *Quantum Dot Heterostructures* (Wiley, Chichester, 1998).
3. G. E. Cirlin, G. M. Guryanov, A. O. Golubok, *et al.*, Appl. Phys. Lett. **67**, 97 (1995).
4. G. É. Tsyrlin, V. N. Petrov, S. A. Masalov, and A. O. Golubok, Fiz. Tekh. Poluprovodn. (St. Petersburg) **33**, 733 (1999) [Semiconductors **33**, 677 (1999)].
5. J. Tersoff, C. Teichert, and M. G. Lagally, Phys. Rev. Lett. **76**, 1675 (1996).
6. O. G. Schmidt, N. Y. Jin-Phillipp, C. Lange, *et al.*, Appl. Phys. Lett. **77**, 4139 (2000).
7. D. D. Chambliss, R. J. Wilson, and S. Chiang, Phys. Rev. Lett. **66**, 1721 (1991).
8. G. É. Cirlin, P. Werner, G. Gösele, *et al.*, Pis'ma Zh. Tekh. Fiz. **27** (1), 31 (2001) [Tech. Phys. Lett. **27**, 14 (2001)].
9. O. P. Pchelyakov, Yu. B. Bolkhovityanov, A. V. Dvurechenskiĭ, *et al.*, Fiz. Tekh. Poluprovodn. (St. Petersburg) **34**, 1281 (2000) [Semiconductors **34**, 1229 (2000)].
10. A. Madhukar, Surf. Sci. **132**, 344 (1983).
11. P. Smilauer, Vacuum **50**, 115 (1998).

Translated by D. Mashovets

Semiconductors, Vol. 36, No. 11, 2002, pp. 1299–1302. Translated from Fizika i Tekhnika Poluprovodnikov, Vol. 36, No. 11, 2002, pp. 1384–1387.

AMORPHOUS, VITREOUS, AND POROUS SEMICONDUCTORS

Effect of Fullerene on the Photogeneration and Transport of Charge Carriers in Triphenylamine-Containing Polyimides

E. L. Aleksandrova

Research Institute of Optical Materials Technology, "Vavilov State Optical Institute" All-Russia Scientific Center, Birzhevaya liniya 14, St. Petersburg, 190164 Russia

Submitted March 28, 2002; accepted for publication March 28, 2002

Abstract—Based on studies of the quantum yield and drift mobility of charge carriers in thin films of fullerene-containing dye-sensitized polyimides performed in wide ranges of electric-field strengths ($(1–10) \times 10^5$ V cm^{-1}) and temperatures (77–350 K), a mechanism of the interaction of fullerene molecules with aromatic fragments of polyimides and dye anions is suggested. It was found that fullerene, being an efficient sensitizer of the photoeffect in aromatic triphenylamine-containing polyimides, reduces by more than an order of magnitude the photosensitivity and mobility of charge carriers in dye-sensitized polyimides, restoring these parameters to values typical of unsensitized polyimides. © *2002 MAIK "Nauka/Interperiodica"*.

Organic polymeric semiconductors with high thermal stability and photosensitive properties that can be varied by a change in the molecular structure of such semiconductors are of interest for the fabrication of both molecular recording media and emitting diodes based on such media. Polyimides (PIs), which are characterized by efficient photogeneration and transport of charge carriers, belong to a class of such polymers. The PIs, whose structures include donor nitrogen-containing aromatic fragments (especially triphenylamine (TPA) ones [1] with low ionization potentials and capacity conformation phototransformations), exhibit the following features. First, the photoeffect with a quantum yield close to unity can be efficiently sensitized [2]. Second, the drift mobility can be controlled by changing the sign of charge carriers; thus, the value of the drift mobility can be varied in the range from 10^{-5} to 10^{-3} cm^2 V^{-1} s$^-$ [C]. Sensitization and change in transport properties were accomplished by the introduction of various acceptor sensitizers with quite high electron affinities A_A (in particular, dyes and fullerene) into PIs.

As was shown in [2], the high efficiency of sensitization of aromatic PIs by fullerene is due to the high energies A_A of C_{60} and C_{70} molecules and the ability of interacting TPA fragments to undergo conformation phototransformations from a neutral pyramidal to an ionized planar form. The intermediate state between the above-mentioned forms ensures maximum overlapping of the π electronic systems of TPA fragments and fullerene molecules and promotes maximum efficiency of their donor–acceptor (D–A) interaction. As a result, the charge-transfer degree δ and the quantum yield of generation of electron–hole pairs η_0 are rather high. The quantum yield η_0, in accordance with the Onsager model [4, 5] applicable to polymeric systems, characterizes the efficiency of separation of charge carriers in the initial stage of photogeneration (up to a distance between carriers equal to the thermalization radius r_t) and governs the quantum yield of carrier photogeneration $\eta = \eta_0 f_d(r_t, E, \varepsilon, T)$, where f_d is the probability of field-assisted thermal dissociation of photogenerated electron–hole pairs in an external electric field of strength E, T is the temperature, and ε is the relative permittivity. The transport of electron–hole pairs through the π-conjugated system of a polymer at distances between carriers in a pair no larger than $r_c = 20$ nm (the value at which carriers become free) is an activated process with the activation energy $E_a \propto (\varepsilon r_t)^{-1}$. Hence, the determination of E_a and the comparison of this value with the found activation energy of free-charge-carrier transport would make it possible to find out whether fullerene affects the photogeneration throughout or only its initial stage, essentially increasing the probability of charge transfer in D–A complexes.

The aim of this study is to investigate the effect of fullerene (which is an efficient acceptor for electrons) on photogeneration and free-charge-carrier transport in TPA-containing PIs, including dye-sensitized ones.

The investigations were performed for PI containing triphenylamine diamine donor fragments with an ionization potential I_D = 6.9 eV [6] and diphenyloxide (DPO) diimide acceptor fragments with A_A = 1.12 eV [1]. With the aim of increasing the photosensitivity and mobility of charge carriers, PI was sensitized by a Malachite Green (MG) dye with maximum spectral sensitivity at a wavelength of 647 nm. This dye belongs to the class of triphenylmethane dyes (with the spatial structure of cations similar to that in TPA). The contents of the dye and fullerene (the latter was a mixture

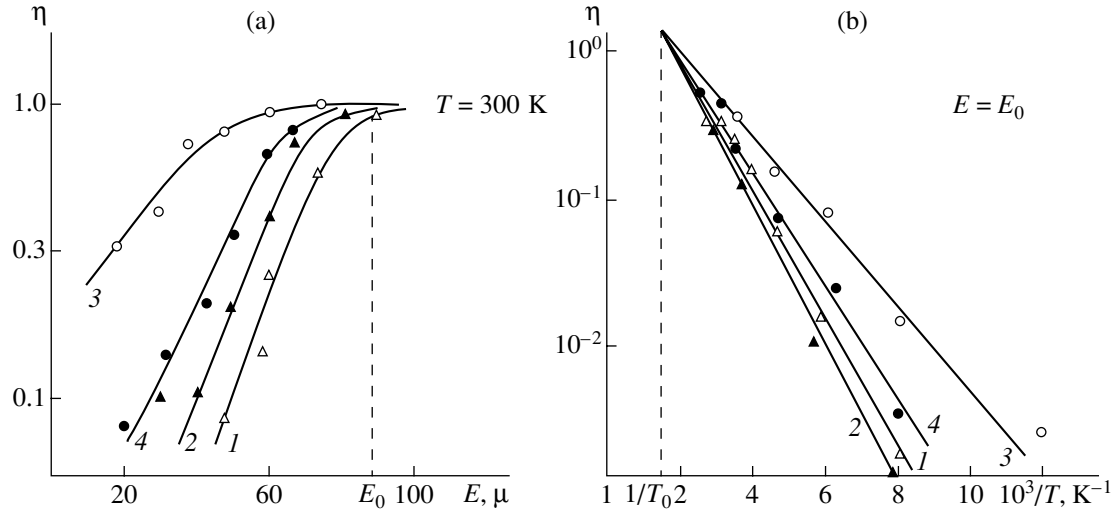

Fig. 1. (a) Field and (b) temperature dependences of the photogeneration quantum yield of (*1*) unsensitized, (*2*) fullerene-sensitized, (*3*) MG-sensitized, and (*4*) sensitized with MG and fullerene TPA-containing PI layers with $d = 2$ μm. The photon energies correspond to the regions of highest sensitivity and are equal to (*1*) 3.0, (*2*) 2.4, (*3*) 1.9, and (*4*) 2.0 eV.

of C_{60} and C_{70} in a ratio of 87 : 13) were 1 and 0.5 mol %, respectively. Layers of PI were deposited by centrifuging an 8% solution in chloroform on glass substrates coated with conducting layers of In_2O_3(Sn). The thickness of the deposited layers d was in the range of 1–12 μm.

The photogeneration quantum yield and photosensitivity $S_{0.1}$ were measured in the electrophotographic mode using the technique reported in [5] and in the spectral range of 400–750 nm at $E = (1–10) \times 10^5$ V cm^{-1} and $T = 77–350$ K. The condition for the complete collection of photogenerated charge carriers was satisfied by using the method of a "photogeneration wedge" [7] for positively and negatively charged layers of various thicknesses (d^+) and (d^-), respectively. In the ranges of field strengths $E < E_0$ and thicknesses $d < d_0$, where the measured $\eta(E)$ dependences coincided, the relative change in the electron and hole mobilities, $\mu_{e,h}$, was estimated for various samples by

$$\mu_{e,h} = (d_0/E_0)(E_0/d_0)^{-1}\mu_{e,h1}, \qquad (1)$$

where (E_0/d_0) and $\mu_{e,h1}$ are the ratios of E_0 and d_0 and mobilities for samples with $\mu_{e,h}$, measured using the technique reported in [3]. The energies E_a and radii r_t were determined by measuring the slopes of temperature dependences $\eta(1/T)$ and field dependences $\eta(E)$, respectively, in accordance with the method reported in [6, 7].

The measurements of current–voltage characteristics of the investigated samples showed that the introduction of a MG dye resulted in a decrease of the resistance ρ by two orders of magnitude (from 10^9 to 10^7 Ω [3]). The photocurrent $i \propto \eta\mu$ through sensitized PI layers increased by 2–3 orders of magnitude at $T = 300$ K, and at $E = 10^5$ V cm^{-1} it was as high as approximately 0.5 mA [3]. Notably, under these conditions, the quantum yield η changed by no more than a factor of 2 [8].

The drift mobility of charge carriers changed most drastically due to the introduction of MG. It was found in [C] that, while only holes are mobile in unsensitized PI layers, electrons become mobile too in MG-sensitized PI. At $T = 300$ K and $A = 2 \times 10^4$ V cm^{-1}, the drift hole mobility μ_h is equal to 1.5×10^{-4} cm^2 V^{-1} s^{-1} in the unsensitized PI, while, in the MG-sensitized PI, μ_h is equal to 4×10^{-4} cm^2 V^{-1} s^{-1} and the electron mobility μ_e significantly increases to as high as 1.6×10^{-3} cm^2 V^{-1} s^{-1}.

The values of drift mobility in the investigated samples were larger [3] than for anthracene-based PIs [9]. This fact points to the enhancement of transport properties of TPA-containing PIs (a TPA fragment, unlike anthracene, in addition to an aromatic π system, contains a N atom that, as is known [10], increases the hole mobility). An approximation of the $\mu_h(E)$ dependence in the range of field strengths $E > 10^5$ V cm^{-1} using the Pool–Frenkel law yields the following values of the β coefficient: 3.5×10^{-4} eV (V cm^{-1})$^{0.5}$ for unsensitized PI, which virtually coincides with the relevant value typical of anthracene-based PIs ($\beta = 4.0 \times 10^{-4}$ eV (V cm^{-1})$^{0.5}$ [9]), and 1.9×10^{-4} eV (V cm^{-1})$^{0.5}$ for MG-sensitized PI. Since $\beta = [e/\varepsilon\varepsilon_0]^{0.5}$, the determined values of β were used to derive the relative permittivity: $\varepsilon = 3.5 \pm 0.3$ and 5.3 ± 0.5 for unsensitized and MG-sensitized TPA-containing PIs, respectively. The electron and hole mobilities that were estimated using (1) from the values of $d_0^+ = 3.0$, 2.5, 5.9, and 3.0 μm and $d_0^- = 1.5$, 1.6, 12.0, and 1.0 μm for unsensitized PI (Fig. 1a, curve *1*), fullerene-sensitized PI (curve *2*), and PI sensitized by fullerene and MG (curve *4*) differ by no more than 20%. At the same time, the hole and electron mobilities

in MG-sensitized PI exceed the corresponding values for pure PI by a factor of 3 and by a factor of more than 10, respectively. Hence, it follows that the introduction of fullerene into PI causes virtually no change in μ_e and μ_h, while the photosensitivity (Fig. 2, curve *2* in relation to curve *1*) and the quantum yield increase by approximately a factor of 5 [2].

The introduction of fullerene molecules into MG-sensitized PI restores its resistance ρ to the resistance of unsensitized PI (~10^9 Ω) and virtually does not change η (at $T = 300$ K); although, for unsensitized PI, an increase in the photosensitivity $S_{0.1}$ by a factor of ~5 was reported in [2]. The photosensitivity spectrum of PI sensitized by MG and fullerene (Fig. 2, curve *4*) is the sum of spectra of MG-sensitized (curve *3*) and fullerene-sensitized (curve *2*) PIs, only with much lower photosensitivity.

The slope of the temperature dependences of η (which characterizes the activation energy E_a) decreased by a factor of nearly 2 due to the introduction of MG (Fig. 1b, curve *3* in relation to curve *1*) and by less than 5% due to the introduction of fullerene (curves *2*, *4*). The thermalization radii calculated using the values of E_a for unsensitized TPA-containing PI ($\varepsilon = 3.5$ [1]) and the same PI sensitized by MG ($\varepsilon = 5.2$ [1, 2]) and fullerene ($\varepsilon = 4.6$ [2]) are equal to 21.5, 30.5, and 17.0 nm, respectively. These values are in good agreement with the previously reported ones [1, 8]. The obtained dependences intersect at $T_0 = 570$ K, i.e., at the value of T that is close to the glass transition temperature of PIs (320–350°C). The obtained value of T_0 is smaller than the relevant value for PIs studied in [9].

It can be seen from Fig. 1b that the introduction of MG into PI results in a decrease in E_a from 0.20 ± 0.02 (for unsensitized PI) to 0.12 ± 0.01 eV (curve *3*), while the introduction of fullerene results in an increase in E_a to 0.21 ± 0.02 eV. The introduction of both MG and fullerene causes a decrease in E_a to 0.15 eV (however, this value exceeds the relevant value for MG-sensitized PI). The mobility activation energy $E_a = 0.15$ eV; i.e., it is on the same order of magnitude as the photogeneration activation energy. Hence, we may conclude that the transport of bound and free charge carriers occurs with similar activation energies and that an increase in η due to the introduction of C_{60} molecules into PI is principally related to the effect of fullerene in the initial stage of photogeneration, when fullerene causes large η_0. The activation energy E_a, as was shown in [5], depends on the values of I_D and A_A for fragments via which the transport of charge carriers occurs, i.e.,

$$E_a \approx A_A - I_D. \quad (2)$$

The introduction of fullerene into MG-sensitized PI results in a decrease in the electron mobility to $\mu_e < 10^{-6}$ cm^2 V^{-1} s^{-1}, while the hole mobility μ_h is restored to the relevant value of unsensitized PI and becomes equal to 2×10^{-4} cm^2 V^{-1} s^{-}. Thus, the introduction of fullerene into MG-sensitized PI restores its photosensitivity, quantum yield, and mobility to values typical of unsensitized PI; i.e., it neutralizes the effect of MG. The neutralizing effect of fullerene is also confirmed by measurements of luminescence spectra [8]. The introduction of fullerene into MG-containing PI extinguishes the MG luminescence band and restores the luminescence spectrum of PI sensitized by two acceptors to the initial spectrum of PI [6].

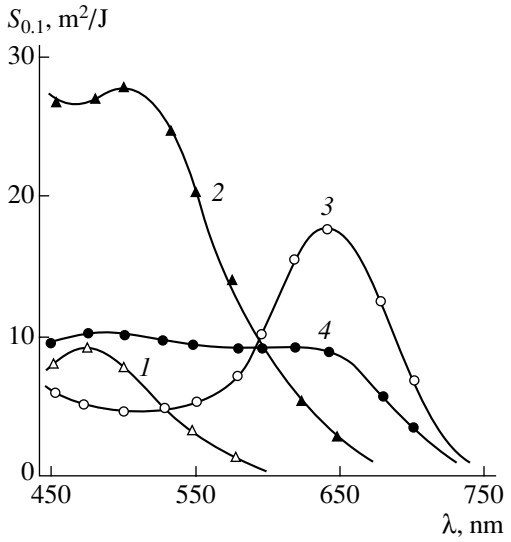

Fig. 2. Photosensitivity spectra of (*1*) unsensitized, (*2*) fullerene-sensitized, (*3*) MG-sensitized, and (*4*) sensitized with MG and fullerene TPA-containing PI layers with $d = 2$ μm.

Let us consider a plausible mechanism of charge-carrier transport caused by the introduction of fullerene into MG-sensitized TPA-containing PI. As is known [1], monomeric units of PI are D–A complexes formed by diamine donor and diimide acceptor fragments. Due to the low I_D of donor TPA fragments, the presence of a nitrogen atom in each fragment, and the rather high concentration $N > 10^{18}$ cm^{-3}, the efficient transport of holes with $\mu_h \propto R_{\mathrm{TPA}}^{-2}$ (where R_{TPA} is the distance between TPA fragments; $R_{\mathrm{TPA}} \propto N^{-1/3}$) occurs via these fragments. The probability of electron transport via O bridges of acceptor fragments is low due to small values of A_A. As a result of fullerene introduction, donor TPA-fragments begin to interact with electron-accepting fullerene molecules, screening them and thus prohibiting carrier transport via fullerene molecules. Electrons become mobile in PIs containing MG molecules, whose anions ClO_4^- have high values of A_A and thus increase the transport probability for carriers with $\mu_e \propto R_a^{-2}$, where R_a is the distance between acceptor fragments. Taking into account that the dye concentration $c = 1\%$ (for similar molecular weights of MG molecules and PI monomeric units), $R_a \approx c^{1/3} R_{\mathrm{TPA}} \approx 0.2 R_{\mathrm{TPA}}$. The introduction of fullerene molecules with high ener-

gies A_A that exceed those of diimide fragments and dye anions, as may be expected in accordance with (2), should increase the electron mobility, in spite of an increase in the distance between acceptors, since $R_f(c_f) = 2R_{ClO_4^-}(c)$. However, μ_e decreases by more than two orders of magnitude ($\mu_e < 10^{-6}$ cm^2 V^{-1} s^{-1}) rather than by a factor of 4. Apparently, TPA fragments around fullerene molecules interact with anions to form neutral structures $C_{60}^- - TPA^+ - ClO_4^-$ that have low values of A_A and are located at large distances from each other, due to which the jump probability is lowered for electrons. Holes migrate via TPA fragments that do not interact with C_{60} molecules. The number of TPA fragments is less in comparison with that in the initial PI; as a result, the hole mobility also decreases (approximately by a factor of 2 in comparison with the initial PI).

Thus, the results of the performed studies allow us to conclude the following:

(i) The activation energies of photogeneration and carrier transport are of the same order of magnitude, which indicates that both the transport of bound charge carriers in the final photogeneration stage, i.e., during the thermally assisted field dissociation of a Coulomb pair, and the carrier drift occur via similar hop mechanisms;

(ii) The introduction of fullerene into MG-sensitized PI results in the neutralization of centers via which electrons migrate (ClO_4^-), which suppresses the electron conductivity and restores the hole conductivity to the value of μ_h, which is typical of unsensitized PI; i.e., the introduction of fullerene neutralizes the dye effect;

(iii) The neutralization of centers via which electrons are transported is caused by D–A interaction of ClO_4^- anions with electron-accepting fullerene molecules surrounded by positively charged aromatic TPA fragments. As a result, A–D–A ($C_{60}^- - TPA^+ - ClO_4^-$) structures are formed which, due to their net neutrality, reduce the jump probability.

REFERENCES

1. B. M. Rumyantsev, V. I. Berendyaev, and N. A. Vasilenko, Vysokomol. Soedin. **39**, 720 (1997).
2. E. L. Aleksandrova, N. B. Kamanina, and Yu. A. Cherkasov, Opt. Zh. **65** (8), 87 (1998) [J. Opt. Technol. **65**, 676 (1998)].
3. L. P. Kazakova and E. L. Aleksandrova, Fiz. Tekh. Poluprovodn. (St. Petersburg) **35**, 695 (2001) [Semiconductors **35**, 666 (2001)].
4. L. Onsager, Phys. Rev. Lett. **34**, 559 (1934).
5. E. L. Aleksandrova and Yu. A. Cherkasov, Opt. Spektrosk. **64**, 1047 (1988) [Opt. Spectrosc. **64**, 624 (1988)].
6. L. V. Gurvich, G. V. Karachevtsev, V. N. Kondrat'ev, Yu. A. Lebedev, V. A. Medvedev, V. K. Potapov, and Yu. S. Khodeev, *Bond-Breaking Energies. Chemical Ionization Potentials and Electron Affinity* (Nauka, Moscow, 1974).
7. E. L. Aleksandrova and Yu. A. Cherkasov, Zh. Nauchn. Prikl. Fotogr. Kinematogr. **31** (1), 61 (1986).
8. E. L. Aleksandrova and Yu. A. Cherkasov, Opt. Zh. **67** (3), 34 (2000) [J. Opt. Technol. **67**, 241 (2000)].
9. A. R. Tameev, V. I. Berendyaev, and B. V. Kotov, Zh. Nauchn. Prikl. Fotogr. Kinematogr. **42** (2), 38 (1997).
10. J. Hirsh, J. Phys. C **12**, 321 (1979).

Translated by Yu. Sin'kov

Semiconductors, Vol. 36, No. 11, 2002, pp. 1303–1307. Translated from Fizika i Tekhnika Poluprovodnikov, Vol. 36, No. 11, 2002, pp. 1388–1392.

PHYSICS OF SEMICONDUCTOR DEVICES

Flattening of Dynamic Dielectric Phase Grating and Single-Mode Lasing under the Conditions of Transverse Oscillations of Luminous Flux

A. P. Astakhova, T. N. Danilova, A. N. Imenkov, N. M. Kolchanova, and Yu. P. Yakovlev

Ioffe Physicotechnical Institute, Russian Academy of Sciences, Politekhnicheskaya ul. 26, St. Petersburg, 194021 Russia

Submitted March 27, 2002; accepted for publication March 29, 2002

Abstract—Emission spectra and the intensity patterns of InAsSbP/InAsSb/InAsSbP-based diode lasers with different cavity lengths and a spectral range of 3–4 μm were studied. It is ascertained experimentally that a 200- to 300-μm-long and 18-μm-wide laser cavity ensures single-mode lasing, during which the wavelength decreases with current by about 100 Å and the top of the intensity pattern becomes bimodal, thus indicating that there are transverse spatial oscillations of laser flux in the cavity. In a 300- to 500-μm-long cavity, several tens of modes are generated mainly on the long-wavelength side of the mode that prevailed initially at the lasing threshold and spatial oscillations of laser flux are not observed. Single-mode lasing is attained due to the fact that the transverse oscillations of laser flux flatten the dynamic dielectric phase grating, which is usually produced by the interaction between lasing modes, and prevent an increase in amplification on the long-wavelength side of the dominant mode. © *2002 MAIK "Nauka/Interperiodica".*

INTRODUCTION

Frequency-tunable heterostructure lasers operating in the 2- to 4-μm range are the basic active elements of laser-diode spectroscopy systems. As a consequence, it is important to develop single-frequency laser diodes that can be tuned by current in a wide range of frequencies. Nonlinear optical phenomena, such as the dependence of permittivity on laser-radiation intensity, may be of use in meeting this challenge.

A decrease in the intensity of the emitted radiation in the direction from the cavity center to the side walls and a corresponding reduction of the refractive index results in laser beam self-focusing [1–3]. We have also observed self-focusing in InAsSb/InAsSbP-based lasers [4]. Theoretical and experimental evidence of the fact that self-focusing is accompanied by an almost instantaneous increase or decrease (depending on the value of the drive current and the parameters of the diode structure) in the lasing wavelength with current was obtained in [5]. Later on, in order to expand the wavelength tuning range, the injection at the side walls of a cavity was intensified, which caused a considerable reduction in permittivity at the cavity walls with current [6]. The resulting decrease in the mean refractive index with current led to a blue shift of the lasing frequency. The frequency tuning range was as wide as 300 GHz [7]. The spatial distribution of the radiation intensity indicates predominant generation of longitudinal cavity modes and the appearance of spatial oscillations of the laser flux across the cavity [5–8]. The transverse modes are suppressed by the spatial oscillations of laser flux [9], as follows from the conservation of its frequency and spatial shape.

In this study, we find the conditions under which not only the transverse modes but also the longitudinal modes (except for one) are suppressed.

EXPERIMENTAL

Similar to [4–12], *p*-$InAs_{0.48}Sb_{0.17}P_{0.35}$/*n*-$InAs_{0.95}Sb_{0.05}$/*n*-$InAs_{0.48}Sb_{0.17}P_{0.35}$ heterostructures were grown by liquid-phase epitaxy on *p*-InAs substrates (h = 300 μm) doped with Zn up to a hole concentration of 10^{19} cm^{-3}. An I-type heterojunction was formed between a 1- to 3-μm-thick narrow-gap active layer with a band gap of 0.4 eV at 77 K and 2-μm-thick InAsSbP confining layers with a band gap of 0.6 eV at 77 K. The electron concentration in the nominally undoped active region was $(2–4) \times 10^{16}$ cm^{-3}. The free carrier concentrations in the Sn-doped *n*-InAsSbP limiting layer and in the Sn-doped *p*-InAsSbP confining layer adjacent to the substrate were $(2–5) \times 10^{18}$ and 10^{18} cm^{-3}, respectively. After epitaxial growth, the substrate was thinned to 100 μm. Two-groove mesachips with a stripe width of 18 μm and a step of 500 μm were formed using standard photolithography technique. Diode lasers with Fabry–Perot cavities with a length of 200–500 μm were obtained by cleaving. Laser chips were mounted on the surface of a special copper holder [13, 14], which enabled the inserting of the laser into an evacuated helium cryostat for heat removal.

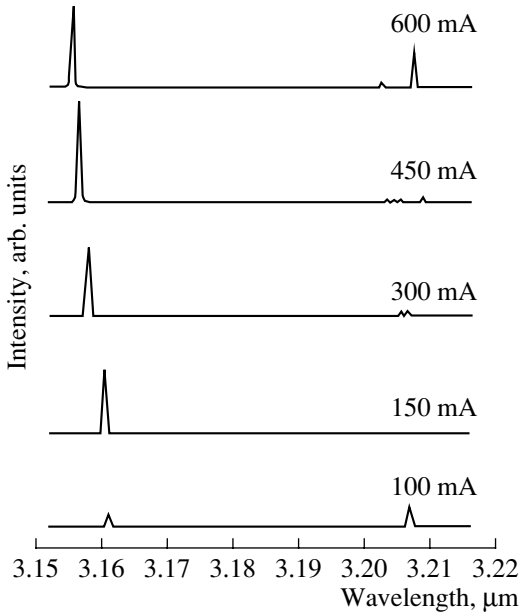

Fig. 1. Emission spectra of a *V*-11671 No. 3 frequency-tunable laser with a cavity length L = 230 μm and a threshold current I_{th} = 90 mA at different currents.

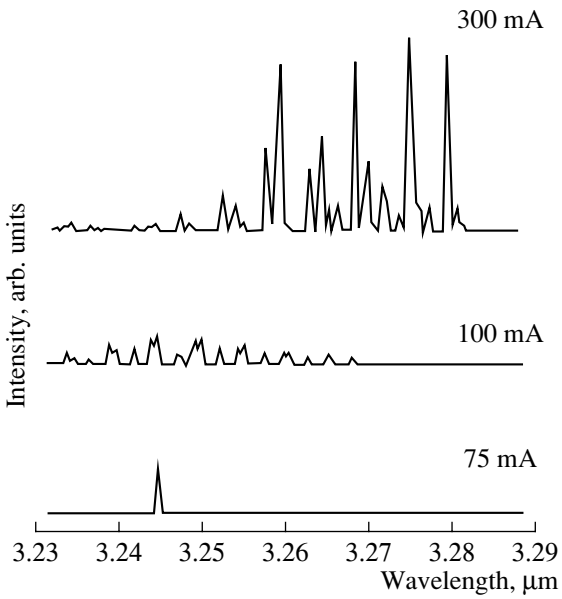

Fig. 2. Emission spectra of a *V*-1188 No. 3 weakly tunable laser with a cavity length L = 500 μm and a threshold current I_{th} = 70 mA at different currents.

In short-cavity (200 μm) laser structures, the prevalence of a longitudinal spatial mode is expected [9]. As follows from our previous study [15], the diode structures with a long cavity (500 μm) allow for both the longitudinal and transverse modes to be generated. Spectral characteristics and intensity patterns of radiation in the plane parallel to the *p*–*n* junction at different injection currents were studied. The measurements were performed at the liquid-nitrogen temperature; the laser was pumped by square pulses of current with a duration of 20 μs and an off-duty factor of 50.

The laser under study was placed in an evacuated Dewar flask on one edge of an electrically heated copper rod. The other edge of the rod was cooled by liquid nitrogen via a thermistor. The temperature of the laser was determined from the drop of voltage across the calibrated silicon diode and could be varied from 78 to 300 K. Radiation spectra were measured at the exit of the grating spectrometer using an InSb photodiode cooled by liquid nitrogen. The intensity patterns were measured in the far-field zone at a distance of 57 mm from the laser using a PbSe photoresistor that was moved in the direction perpendicular to the optical axis of the laser. A synchronous pulse detector measured the intensity of radiation. All the experiments were carried out with the same measuring system maintained in the same conditions at a laser temperature of 78 K to avoid possible systematic errors.

RESULTS

With respect to the type of spectra emitted, the diode lasers may be divided in two groups: frequency-tuned lasers, whose lines continuously vary their spectral position with pump current (Fig. 1), and weakly tuned (Fig. 2) lasers, whose spectra shift only slightly with current. A typical spectrum of a weakly tuned laser usually contains up to 10 lines corresponding to the longitudinal cavity modes and as many or more lines corresponding to the transverse spatial modes. The predominance of long-wavelength modes over short-wavelength ones grows with the pump current. Statistically, the cavity length of weakly tunable lasers is larger (300–500 μm) than that of tunable ones (200–300 μm). A typical frequency spectrum of a tunable laser consists of several lines when there is either a small (from 1 to 1.5 times) or a large (more than 5 times) excess of current over the threshold value (Fig. 1). For intermediate values, a single line is dominant (Fig. 3a). The spectral position of this line at different currents is shown in Fig. 3b. For the diode laser studied, the wavelength tuning range is nearly 70 Å at the liquid-nitrogen temperature, which is 1.5 times greater than the intermode intervals. As was previously noted [5], the threshold current of lasing I_{th} may differ from that of the tunable mode generation I_{tun}. At currents of about $I_{tun} = 1.3I_{th}$, the tunable line flared at the expense of the quenching of other lines (Figs. 1, 3).

The radiation spectrum of weakly tunable lasers under near-threshold pump currents usually displays only one mode (Fig. 2). As the current grows, additional lines appear. A further increase in the injection current gives rise to long-wavelength spectral lines; transverse modes, whose wavelengths are spaced from those of the longitudinal ones by less than an intermode interval, can also be clearly seen.

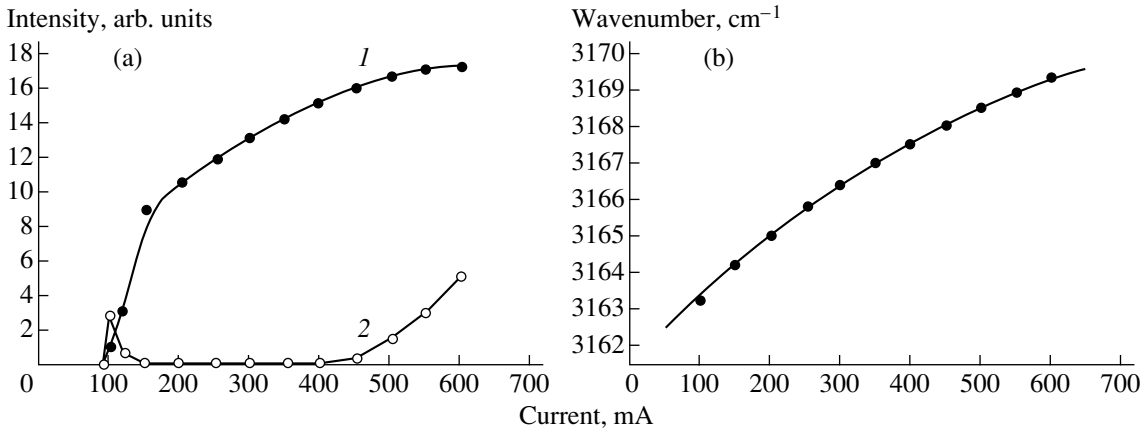

Fig. 3. (a) (*1*) Intensity of the main tuning mode and (*2*) total intensity of all the modes except for the main one and (b) spectral position of the main mode versus the pump current for a *V*-11671 No. 3 tunable laser with a cavity length $L = 230$ μm and a threshold current $I_{th} = 90$ mA.

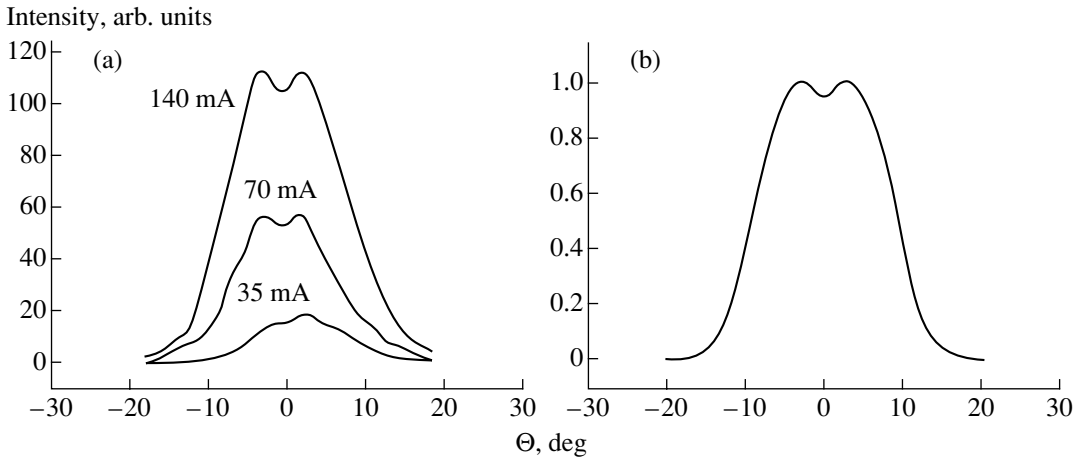

Fig. 4. Intensity patterns in the far field: (a) experimental curves obtained for a *V*-12152 No. 71 tunable laser with a cavity length $L = 300$ μm and a threshold current $I_{th} = 32$ mA, (b) calculation for the laser flux oscillating between the positions of the farthest peaks of the second transverse mode.

For tunable lasers, the intensity patterns in the plane of a *p*–*n* junction in the far zone at different injection currents are presented in Fig. 4. It can be seen that, when there are small currents near the threshold, the pattern is almost Gaussian. When the threshold current is exceeded, the pattern has two distinct peaks that are located symmetrically about zero and remain unblurred with an increase in current. The highly symmetric distribution of the intensity about the coordinate origin and only the weak dependence of the curve shape on current should be noted. The area under the intensity distribution curve varies proportionally to the current. According to the pattern, peaks are spaced by 6°–8° and the depth of the dip between them amounts to 5–6% of their amplitude.

DISCUSSION

As follows from the results obtained, when there is considerable excess of current over the threshold, both the tunable and weakly tunable lasers produce a variety of lines corresponding to longitudinal and transverse cavity modes. It was also shown that an increase in the cavity length not only enlarges the number of longitudinal modes generated but also gives rise to transverse modes.

Let us consider the conditions required for the transverse mode to appear in the absence of the spatial oscillations of light flux.

The interval between a transverse and a longitudinal mode $\Delta\lambda_j$ depends on the wavelength λ, cavity width b, and refractive index n as follows:

$$\Delta\lambda_j = j(j+2)\frac{\lambda}{2n^2}\left(\frac{\lambda}{2b}\right)^2, \qquad (1)$$

where $j = 0, 1, 2, 3, \ldots$ is the quantum number of the spatial mode. The longitudinal mode corresponds to $j = 0$.

The interval between modes with the same number $\Delta\lambda$ depends on the wavelength λ, cavity length L, and the effective refractive index $n^* = n\left(1 - \frac{\lambda}{n}\frac{dn}{d\lambda}\right)$ as

$$\Delta\lambda = \frac{\lambda^2}{2Ln^*}. \quad (2)$$

For an approximate correspondence between the longitudinal and transverse mode wavelengths, the interval $\Delta\lambda_j$ should be close to the sum of the integer $\Delta\lambda$ intervals. When equal optical losses are assumed, the appearance of longitudinal or transverse modes at a certain point of the spectrum is almost equiprobable if their wavelengths are close to each other; i. e., the difference is much less than the intermode interval.

In reality, optical losses for the transverse modes are greater than those for the longitudinal ones because of a decrease in the refractive index with the number of transverse modes for a given wavelength and the associated deterioration of optical confinement in the direction normal to the *p–n*-junction plane. Therefore, the transverse modes with small numbers deserve special attention. Coincidence between the transverse and longitudinal modes on an energy scale is most probable at the cavity length of 500 μm. Thus, if such a cavity has a stripe width of 18 μm, the first and the second transverse modes fall into the spectral positions of longitudinal modes. As a result, the transverse and the longitudinal modes have an equal wavelength and an equal probability of being generated. This leads to the overlapping of lines corresponding to the transverse and longitudinal modes, which is displayed in experiment as a grouping of lines. The transverse modes preclude the formation of a smooth waveguide, since they do not promote a reduction in the concentration of nonequilibrium carriers at the center of a cavity. This is the reason why lasers with a 500-μm-long cavity are hardly tunable. There is another important phenomenon that cannot be disregarded [3, 16]: the amplification increases on the long-wavelength and decreases on the short-wavelength side of each intense mode due to the nonlinear scattering of radiation by the electron density waves produced during the interaction of an intense mode with a mode of lower intensity. The presence of even two close modes is sufficient for the phase dynamic grating of the refractive index to appear and give rise to the scattering mentioned above. Therefore, the spectral overlapping of the longitudinal and transverse modes in 18-μm-wide and 500-μm-long cavities necessarily leads to multimode lasing. With an increase in the pump current, more and more long-wavelength modes are generated, while the short-wavelength modes are still retained. As a result, several tens of modes support each other. When the cavity length is between 200 and 300 μm, the transverse mode is spaced from the longitudinal one by half of the intermode interval, i. e., by the value that is equal to the whole intermode interval in lasers with a cavity length of 500 μm. When the spectral position of the amplification peak coincides with that of the longitudinal mode, the transverse modes cannot be generated because of insufficient amplification. The longitudinal mode reduces the concentration of carriers near the longitudinal axis of the waveguide due to the stimulated recombination and thus increases permittivity in this region. This results in the formation of a smooth waveguide, where the stimulated spatial oscillations of the radiation flux completely suppress the transverse modes.

In the conditions of a smooth concentration-based waveguide, where the optical flux oscillates, the phase dynamic dielectric grating, typically produced by two generating modes, flattens out considerably. This grating levels off by a factor of 10^3, because the frequency of spatial oscillations in the range of flattening (10^{12} Hz) is three times greater than the inverse effective lifetime of the carriers, which corresponds to the frequency width of the dielectric grating. As a consequence, only the spectral line that is closest to the peak of amplification remains. Thus, it can be seen that the intensity of the tuned mode increases at the expense of the quenching of the other modes. In order to obtain tuning in a wide range of wavelengths, the rate of the shift of the amplification peak with current should be the same as that of the lasing line when the spatial oscillations of the laser flux come into existence. Quenching of the sum and difference frequencies in the lasing spectrum increases the quantum yield. An abrupt change in the intensity of the tunable line in Fig. 3a can apparently be attributed to this transition to single-mode operation. In smooth waveguide conditions, the lasing wavelength can be tuned continuously if it is close to the amplification spectral peak. If the laser line shifts from the amplification peak by the longitudinal intermode spacing, a mode-to-mode transition can occur and the single-mode lasing at another mode will proceed [7, 17]. Figure 3 illustrates the disappearance of the weak side modes when the current ranges from I_{th} to $1.3I_{th}$ and the generation of only single-mode lasing in the range of $1.5I_{th}$–$5I_{th}$, in which case the lasing wavelength changes by 70 Å. The appearance of long-wavelength modes at high injection currents (higher than $4I_{th}$) at 7–9 intermode distances from the dominant mode (Figs. 1, 3) can possibly be related to the absence of flattening of the phase dielectric grating at these frequencies and an increase in the additional amplification with current. According to [8], the presence of spatial oscillations in the tunable lasers may be proved by the fact that the intensity pattern becomes two-humped in the far zone by only a small angle, which is smaller than that possible when the transverse modes are generated.

Thus, the formation of a smooth concentration waveguide leads to a pronounced flattening of the dynamic dielectric phase grating, which usually builds up due to the interaction between generating modes, and thus prevents the appearance of modes with longer wavelengths. The formation of a smooth concentration

waveguide and the establishment of the transverse oscillations of laser flux there are favored in the case of different spectral positions of the transverse and longitudinal modes when the dimensions of the cavity are definite. As a result of the spatial oscillations of laser flux, only the mode that is closest to the amplification peak remains. The widest range of tuning can be attained at the temperature at which the rate of the amplification peak shifting with current is equal to that of the lasing mode. The attainment of spatial oscillations of the laser flux across the cavity enabled the production of high-frequency single-mode heterojunction lasers that are tunable in a wide range (up to 300 GHz) and are capable of operating in the temperature range 10–100 K at wavelengths of 3–4 μm.

REFERENCES

1. R. Y. Chiao, E. Yarmire, and C. H. Townes, Phys. Rev. Lett. **13** (15), 479 (1964).
2. I. H. B. Thompson, Opto-Electron. (London) **4**, 257 (1972).
3. P. G. Eliseev and A. P. Bogatov, Tr. Fiz. Inst. Akad. Nauk SSSR **166**, 15 (1986).
4. T. N. Danilova, O. I. Evseenko, A. N. Imenkova, *et al.*, Pis'ma Zh. Tekh. Fiz. **22** (16), 7 (1996) [Tech. Phys. Lett. **22**, 645 (1996)].
5. T. N. Danilova, A. P. Danilova, O. G. Ershov, *et al.*, Fiz. Tekh. Poluprovodn. (St. Petersburg) **31**, 1392 (1997) [Semiconductors **31**, 1200 (1997)].
6. A. P. Danilova, T. N. Danilova, A. N. Imenkov, *et al.*, Fiz. Tekh. Poluprovodn. (St. Petersburg) **33**, 1088 (1999) [Semiconductors **33**, 991 (1999)].
7. A. P. Danilova, A. N. Imenkov, N. M. Kolchanova, *et al.*, Fiz. Tekh. Poluprovodn. (St. Petersburg) **34**, 243 (2000) [Semiconductors **34**, 237 (2000)].
8. A. P. Danilova, T. N. Danilova, A. N. Imenkov, *et al.*, Fiz. Tekh. Poluprovodn. (St. Petersburg) **33**, 1014 (1999) [Semiconductors **33**, 924 (1999)].
9. A. P. Astakhova, T. N. Danilova, A. N. Imenkov, *et al.*, Fiz. Tekh. Poluprovodn. (St. Petersburg) **34**, 1142 (2000) [Semiconductors **34**, 1100 (2000)].
10. A. N. Imenkov, N. M. Kolchanova, P. Kubat, *et al.*, Fiz. Tekh. Poluprovodn. (St. Petersburg) **34**, 1468 (2000) [Semiconductors **34**, 1406 (2000)].
11. A. N. Imenkov, N. M. Kolchanova, P. Kubat, *et al.*, Fiz. Tekh. Poluprovodn. (St. Petersburg) **35**, 375 (2001) [Semiconductors **35**, 360 (2001)].
12. A. N. Imenkov, N. M. Kolchanova, K. D. Moiseev, *et al.*, Rev. Sci. Instrum. **72**, 1988 (2001).
13. A. A. Popov, V. V. Sherstnev, Yu. P. Yakovlev, *et al.*, Pis'ma Zh. Tekh. Fiz. **23** (22), 72 (1997) [Tech. Phys. Lett. **23**, 890 (1997)].
14. A. A. Popov, V. V. Sherstnev, Yu. P. Yakovlev, *et al.*, Spectrochim. Acta A **54**, 821 (1998).
15. A. N. Baranov, T. N. Danilova, O. G. Ershov, *et al.*, Pis'ma Zh. Tekh. Fiz. **19** (17), 30 (1993) [Tech. Phys. Lett. **19**, 543 (1993)].
16. A. P. Bogatov, P. G. Eliseev, and B. N. Sverdlov, Kvantovaya Élektron. (Moscow) **1**, 2286 (1974).
17. A. P. Danilova, A. N. Imenkova, N. M. Kolchanova, *et al.*, Fiz. Tekh. Poluprovodn. (St. Petersburg) **33**, 1469 (1999) [Semiconductors **33**, 1322 (1999)].

Translated by A. Sidorova

Semiconductors, Vol. 36, No. 11, 2002, pp. 1308–1314. Translated from Fizika i Tekhnika Poluprovodnikov, Vol. 36, No. 11, 2002, pp. 1393–1399.

PHYSICS OF SEMICONDUCTOR DEVICES

High Power Single-Mode (λ = 1.3–1.6 μm) Laser Diodes Based on Quantum Well InGaAsP/InP Heterostructures

A. Yu. Leshko*, A. V. Lyutetskiĭ*, N. A. Pikhtin*, S. O. Slipchenko*, Z. N. Sokolova*, N. V. Fetisova*, E. G. Golikova, Yu. A. Ryaboshtan**, and I. S. Tarasov***

** Ioffe Physicotechnical Institute, Russian Academy of Sciences, St. Petersburg, 194021 Russia*

*** Sigm Plus Co., Moscow, 117342 Russia*

Submitted April 8, 2002; accepted for publication April 11, 2002

Abstract—The possibility of achieving maximal optical output power in the single-mode lasing for mesa-stripe laser diodes fabricated on the basis of InGaAsP/InP quantum-well heterostructures with separate confinement have been studied both experimentally and theoretically. The basic condition for the single-mode lasing of laser diodes in a wide range of driving currents is shown to be the precise choice of the effective refractive index Δn_L discontinuity in the plane parallel to the *p*–*n* junction. A InGaAsP/InP separate confinement heterostructure with a step waveguide, with a threshold current density of 180 A/cm^2 and an internal quantum efficiency of stimulated emission of 93–99%, has been manufactured via the MOCVD method. The optimization of the mesa-stripe diode design for the developed InGaAsP/InP heterostructure is carried out with the aim of achieving maximal optical output power in the case of single-mode lasing. An output power of 185 mW is attained in the laser diode with the mesa-stripe width W = 4.5 μm (λ = 1480 nm). The maximal continuous output power was as high as 300 mW. The full width at half-maximum (FWHM) of the lateral far-field pattern increased by 1° relative to the threshold value. © *2002 MAIK "Nauka/Interperiodica".*

1. INTRODUCTION

Recently, there has been a significant increase in interest in power laser diodes emitting in the spectral range of 1300–1600 nm in the zero lateral optical mode. This interest is caused, first of all, by their use in fiber-optics cables, as a pumping source for Er^{3+}-doped fiber-optical amplifiers, and for Raman fiber amplifiers operating at 1400–1500 nm [1]. A stable output power at the level of hundreds of milliwatts, high radiative efficiency of the laser diode, exact peak wavelength of the radiation, and efficiency of the input into the optical fiber are needed. All these requirements must be taken into account in the development of single-mode laser diodes.

Only a few companies in the world (Furukawa Electric, JDS-Uniphase, Princeton Lightwave) have attained maximal continuous optical output power in single-mode emission [2–4]. The main criterion of the single-mode operation was the stability of the full width at half-maximum (FWHM) and the far-zone field configuration, beginning from the lasing threshold or higher. As a result of this circumstance, the attainment of maximal output power of single-mode radiation in continuous lasing, exceeding 300 mW (at room temperature), for laser diodes emitting in the wavelength range of 1.3–1.6 μm is a topical task.

The aim of this work is to study, develop, and manufacture high-power single-mode lasers on the basis of InGaAsP/InP quantum-well (QW) heterostructures emitting at 1300–1600 nm.

Designing and manufacturing single-mode laser diodes, i.e., diodes emitting in the zero transverse mode, is a complex problem. Many requirements must be met for solving it. Firstly, precision design of the laser heterostructure, providing minimal internal optical losses (α_i), cut-off voltage (U_c), and maximal internal quantum efficiency of the stimulated emission (η_i), is necessary. As was shown in our preceding study [5, 6], the QW InGaAsP/InP separate confinement double heterostructure (QW SC DHS) is optimal for attaining maximum optical power in a laser diode with a single aperture (λ = 1.3–1.6 μm). The use of a step waveguide in the InGaAsP/InP QW SC DHS provides the possibility of attaining almost 100% internal quantum efficiency for the stimulated radiation. This is connected with a decrease in the leakage electron current above the threshold due to the transfer of the carriers from the QW region to the heterointerface between the waveguide and the *p*-type emitter [6, 7].

InGaAsP/InP QW SC DHSs have been manufactured using the MOCVD-epitaxy technique [8]; a schematic diagram is presented in Fig. 1.

The heterostructures consisted of wide-gap heavily doped *n*- and *p*-InP layers acting as emitters; a step waveguide made on the basis of In–Ga–As–P ternary solid solutions (E_{gW1} = 1.03 eV, E_{gW2} = 1.24 eV) with a total thickness of 0.65 μm; and an active zone formed

by two strained InGaAsP QWs (d_{QW} = 65 Å) with a InGaAsP barrier layer between them (E_{gb} = 1.03 eV, d_b = 200 Å). A stop-layer of InGaAsP with a thickness of 70 Å, which serves to terminate the chemical etching of the heterostructure during the preparation of the design of the mesa-stripe laser diode, is grown in the top *p*-InP emitter.

The second basic problem in achieving lasing by a laser diode of the fundamental optical mode is the choice of a design that will enable the formation of a waveguide in the plane parallel to the *p–n* junction. For obtaining the waveguide effect in the horizontal direction, the most effective are the mesa-stripe and "buried-mesa" laser diode designs [2, 3]. The mesa-stripe design of a laser diode is distinguished by reliability, simplicity of fabrication, and small internal losses introduced during the formation of the mesa-stripe [9]. One of the advantages of the buried-mesa design is the possibility of obtaining ultralow threshold currents and better frequency characteristics [2]. However, its serious shortcoming is related to technological difficulties encountered in practice [2]. This largely determined our choice in favor of the mesa-stripe design.

Forming a horizontal waveguide in the plane parallel to the laser heterostructure *p–n*-transition is accomplished by establishing an effective refractive index discontinuity Δn_L between the active and passive regions of the mesa stripe. A fairly definite value of Δn_L must be chosen in order to ensure the single-mode operation of the laser diode. Δn_L in the mesa-stripe laser diode design based on QW SC DHS depends mainly on the following parameters: the emission wavelength λ, the mesa-stripe contact width *W*, the etching depth Δh, and the thickness D_w and energy gap E_g^w of the waveguide layers. The free carrier density in the heterostructure layers and the real temperature in the active layer also influence Δn_L.

Calculation of the effective refractive index Δn_L profile in the mesa-stripe laser diode design based on the InGaAsP/InP QW SC DHS was carried out using the passive-waveguide model [10]. It is based on the description of the waveguide properties in the horizontal direction in terms of the effective refractive indices for the separate active and passive regions of the mesa-stripe laser. Calculations were carried out for various values of the heterostructure parameters λ, E_g^w, D_w, and Δh. The conditions for the stability of the optimal values of the heterostructure parameters η_i, α_i, and U_c were taken into account in the calculations. Figure 2 shows one such calculated dependence of the mesa-stripe width satisfying the single-mode cut-off condition on the effective refractive index discontinuity for the chosen design of the laser heterostructure (λ = 1480 nm) (Fig. 1).

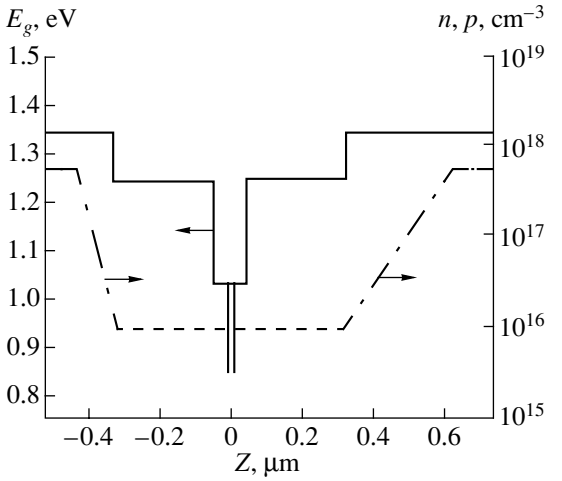

Fig. 1. Band diagram of the InGaAsP/InP quantum-well heterostructure with separate confinement (solid line) and calculated doping profiles for the silicon donor (dashed line) and zinc acceptor (dot-dashed line).

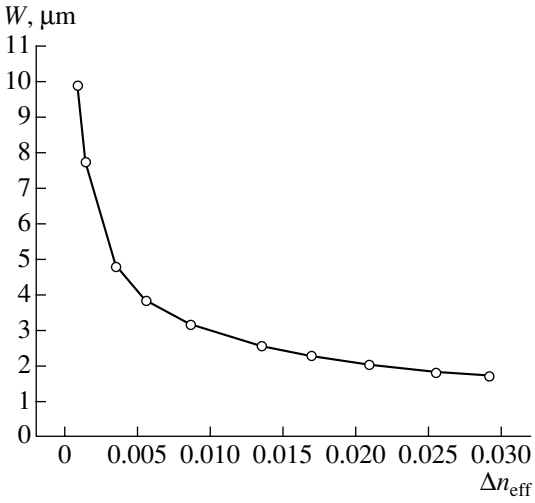

Fig. 2. Calculated dependence of the mesa-stripe width *W* on the effective refractive index discontinuity Δn_{eff} corresponding to the first mode cutoff.

The mesa-stripe heterolasers with the parameters W = 4.5 μm and $\Delta n_L = (3.8–4.5) \times 10^{-3}$ were fabricated from the grown heterostructure (batch KR1439-1) using results of the calculations. The band structure of this heterostructure is presented in Fig. 1. A masking photoresist layer was introduced in order to form the mesa stripe. Chemical etching was performed through this mask [11]. Grooves were etched on both sides of the mesa stripe; their depth was determined by the position of the stop-layer that formed during the growth process in the *p*-InP emitter.

It is necessary to try to increase the mesa-stripe width in order to attain maximum output power of the laser diode; this lowers the optical power density at the output mirror and, therefore, increases the operating

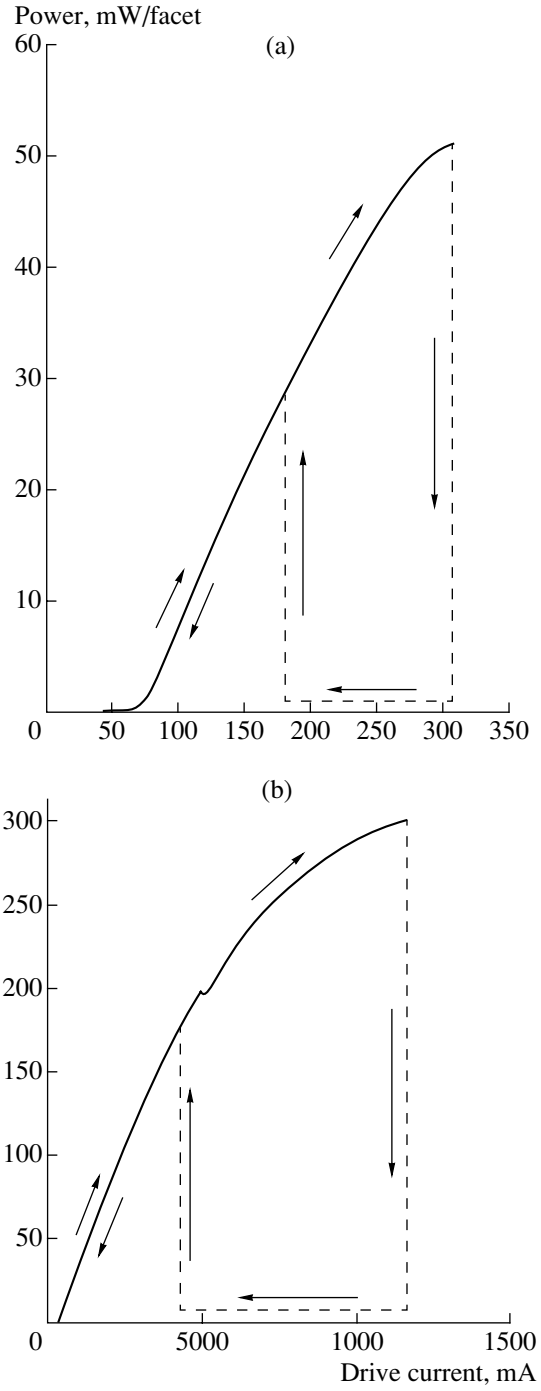

Fig. 3. *E–I* characteristic for the laser diodes in the CW lasing mode with the heat sink temperature 20°C over the entire range of driving currents: (a) KR1439-1 batch with a cavity length L = 1000 μm and natural mirrors at the cavity faces; (b) KR1439-2 batch with a cavity length L = 1500 μm, with a high (95%) and low (5%) reflectivity of coating on the cavity faces.

current. However, since the mesa-stripe maximum width W_{max} of the single-mode lasers is also determined by the efficiency of radiation input into the one-mode fiber, the upper limit is chosen to be W_{max} = 5 μm.

2. EXPERIMENTAL RESULTS

All of the manufactured mesa-stripe laser heterostructures were cleaved into separate laser chips with a cavity length L = 0.3–3 mm, which were soldered with indium to copper heat sinks with the stripe contact down.

A typical light–current (*E–I*) characteristic during the continuous pumping mode for the laser diodes manufactured on the basis of a KR1439-1 heterostructure is presented in Fig. 3a. It is seen that breakdown of the *E–I* characteristic occurs when the current density is quite small. It is significant that the suppression of lasing has a reversible hysteretic character and, therefore, this is not due to catastrophic degradation of the optical mirror. The observed effect is due to the fact that the calculation results presented in Fig. 2 do not reflect in full measure all the processes taking place in real devices. It is known, for instance, that an increase in the free charge carrier density decreases the refractive index of a material [12]. Thus, an increase of the injection current up to the threshold value I_{th} leads to a decrease in the refractive index of the active region due to the accumulation of injected carriers in the QW region up to the threshold concentrations n_{th} and p_{th}. A further increase of the driving current leads to an increase in the free carrier density in the waveguide layers owing both to the injection process and to the ejection of electrons from the QW into the barrier layers [7, 13]. The total contribution of injected carriers can lead, in the extreme case, to the collapse of the built-in waveguide or to the formation of an antiwaveguide [14]. The suppression of lasing was observed in virtually all of the laser diodes fabricated from heterostructures of the KR1439-1 batch. The dependence of the driving current densities, at which the suppression of lasing occurs, on the laser diode cavity length is sublinear. This fact can be related to the nonlinear dependence of the threshold carrier density on the total loss [15].

Since the efficiency of the laser diode is less than 100%, some of the power is dissipated into heat, which leads to an increase in the operating temperature of the active region of the laser diode. The overheating can reach 60°C or higher for high-power semiconductor laser diodes operating at maximum driving currents [5]. Such strong overheating of the active region significantly changes the refractive indices of the layers situated in the pumped region of the laser diode. Increased temperature is known to increase the refractive index of semiconductors. Therefore, the effective index of the active region increases, which leads to a rise in the effective refractive index discontinuity for the horizontal waveguide and, thus, to the enhancement of the discontinuity. Overheating of the active region relative to the heat sink is considerably less in the pulsed lasing mode than in the continuous-wave (CW) mode [5]. This may be the reason for the fact that the current density values corresponding to the suppression of lasing were less in the pulsed mode (pulse duration 1 μs) than in

CW operation. For example, for the laser diode with a cavity length L = 1 mm, lasing suppression occurs at 300 and 200 mA for the CW and pulsed lasing modes, respectively.

We manufactured mesa-stripe lasers with a higher effective refractive index discontinuity $\Delta n_L = (6.2–6.8) \times 10^{-3}$ in order to prevent the suppression of lasing. As a result, the laser diodes manufactured from such a heterostructure (KR1439-2 batch) do not exhibit hysteresis of the *E–I* characteristic over the entire region of stable lasing. Thus, the value of the effective refractive index discontinuity $\Delta n_L = (6.2–6.8) \times 10^{-3}$ is large enough to prevent collapse of the built-in waveguide, which is related to an increase in the free charge carrier density in the waveguide layers and in the active region. The single-mode lasing under the continuous pumping of such laser diodes with natural mirrors persists up to a power of 70 mW per mirror.

The deposition of reflecting ($R > 95\%$) Si/SiO_2 and antireflecting ($R < 5\%$) SiO_2 coatings at the faces of the Fabry–Perot cavity of the laser diode allowed us to double the output radiation power in the case of single-mode lasing. Such an increase is due not only to a small change in the threshold current density (and, as a result, in the threshold carrier density), but because of the influence of sputtered Si/SiO_2 layers on the mode structure of the emitted radiation [16]. A 185-mW output power was attained for single-mode lasing, and 300-mW, in the case of CW in lasers with coatings deposited at room temperature [17]. The *E–I* characteristic for the CW lasing of such laser diodes is presented in Fig. 3b. A linear dependence is observed over the entire range of single-mode lasing. A kink, smooth saturation, and the suppression of lasing are observed successively in the *E–I* characteristic after a further increase in the driving current (Fig. 3b).

Typical emission patterns in the far zone in the plane parallel to the *p–n* junction at various values of the continuous driving current for lasers manufactured from KR1439-2 heterostructures are shown in Fig. 4a. It is seen that the kink (sharp bend) in the *E–I* characteristic (Fig. 3b) corresponds to a rotational displacement of the far-field pattern relative to the normal to the output mirror by a few degrees. Such behavior of the far-field is called *beam steering*. Many works are dedicated to the analysis of this phenomenon, but a consensus on its nature has not been achieved [18–20]. We believe that this is related to the transformation of the effective refractive index profile due to the influence of the injected charge carriers on the optical properties of semiconductor materials. Such a transformation displaces the axial mode and necessitates beam propagation at some angle relative to the cavity axis. In other words, the excess value of the effective refractive index discontinuity is too small to suppress the influence of the injected carriers on the waveguide properties of the horizontal waveguide.

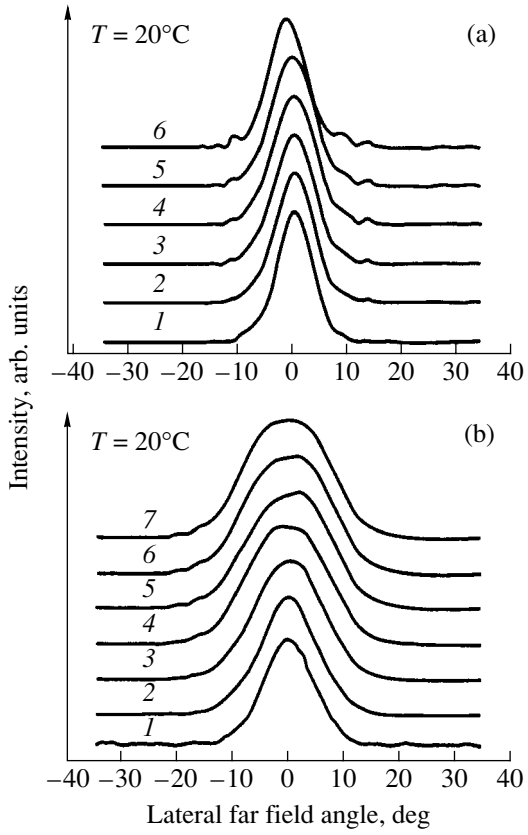

Fig. 4. Distribution of the radiation intensity in the far-field zone in the plane parallel to the *p–n* junction at various values of the output optical power: (a) laser diode from the KR1439-2 batch, pattern FWHM ($\Theta_\parallel$): (*1*) 7.9°, (*2*) 8.0°, (*3*) 8.5°, (*4*) 9.0°, (*5*) 9.1°, and (*6*) 7.9°; CW emission power: (*1*) 5, (*2*) 25, (*3*) 50, (*4*) 100, (*5*) 185, and (*6*) 200 mW; (b) laser diode of the KR1439-3 batch, pattern FWHM ($\Theta_\parallel$): (*1*) 10.1°, (*2*) 11.5°, (*3*) 14.2°, (*4*) 16.5°, (*5*) 17.3°, (*6*) 17.7°, and (*7*) 17.9°; CW emission power: (*1*) 20, (*2*) 40, (*3*) 60, (*4*) 80, (*5*) 100, (*6*) 125, and (*7*) 150 mW.

It should be noted that the far-field laser emission pattern virtually does not change with increasing driving current until the appearance of a sharp bend in the *E–I* characteristic. The polar pattern width of the radiation field at half intensity ($\Theta_\parallel$) slightly increases from 8° (near the lasing threshold) to 9° (at the output power of 185 W). Such stable behavior of the polar pattern confirms the single-mode lasing of the laser diode within the stated range of output power.

The measured pattern of the far-field radiation in the plane perpendicular to the *p–n* junction also shows lasing of the zero optical mode. The value $\Theta_\perp$ is equal to 38°–40° over the entire range of driving current values. This is in accordance with the theoretically calculated field distribution in the vertical direction for the given values of the thickness D_w and the energy gap E_g^w of the waveguide layers (see Fig. 1).

A further increase in the effective refractive index discontinuity Δn_L up to $(7–8) \times 10^{-3}$ (KR1439-3 batch)

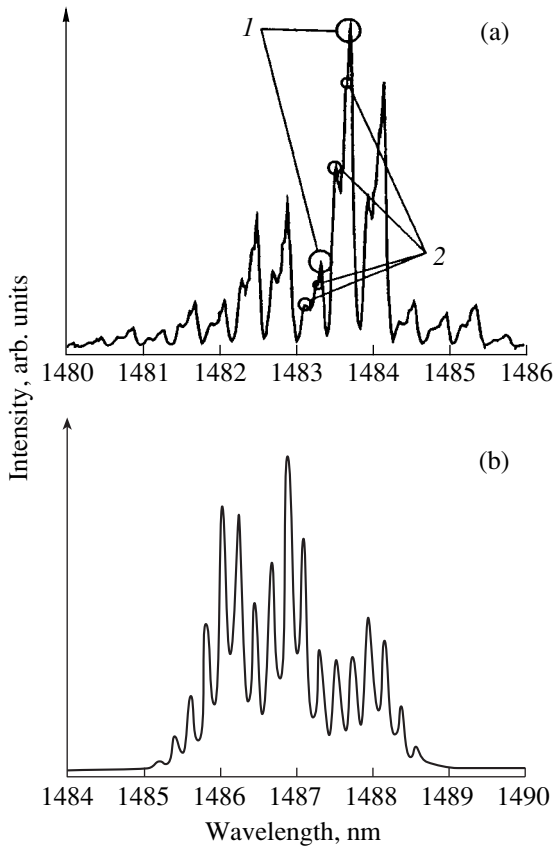

Fig. 5. Emission spectrum of the laser diode operating at the current $2I_{th}$: (a) KR1439-3 batch, the cavity length L = 770 μm, (*1*) peaks related to the axial (fundamental) mode and (*2*) those related to the higher-order modes; (b) KR1439-2 batch, L = 1500 μm.

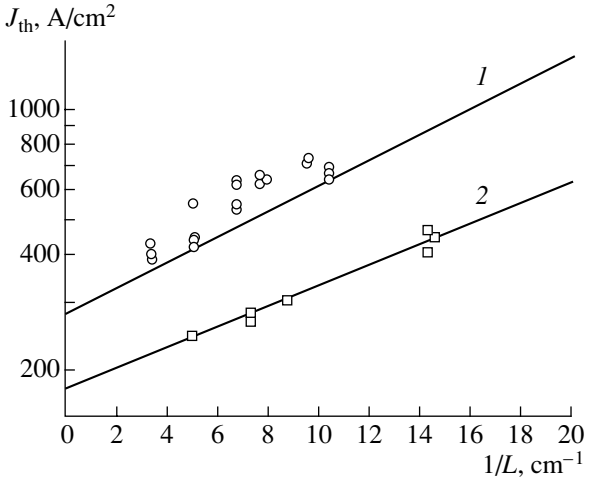

Fig. 6. Experimental dependence of the threshold current density J_{th} on the reciprocal cavity length 1/L for the laser diodes of the KR1439-2 batch: (*1*) with the stripe width W = 4.5 μm and (*2*) with W = 100 μm.

leads to the appearance of a kink (sharp bend) in the laser *E–I* characteristic at driving currents near the threshold value. A significant continuous rise in the FWHM of the radiation pattern in the horizontal plane takes place as the driving current increases. It should be noted that the far-field intensity distribution is well described by a Gaussian. Such a laser operation mode can be called single-lobe. Only when the driving current density is high enough do additional directional lobes appear in the far-field pattern, which confirms the presence of higher order modes (Fig. 4b).

Investigating the emission spectra of laser diodes (KR1439-3 batch) has shown that, just above the lasing threshold, the radiation is not single-mode. This manifests itself in the fact that additional peaks appear in the electroluminescence (EL) spectrum at the lasing threshold (Fig. 5a), in addition to the peaks related to the fundamental mode with the inter-mode distance $\Delta\lambda$ determined by the expression [10]

$$\Delta\lambda = \frac{\lambda^2}{2nL\left(1 - \frac{\lambda}{n}\frac{dn}{d\lambda}\right)}, \quad (1)$$

where λ is the lasing wavelength, L is the Fabry–Perot cavity length, and n is the refractive index of the waveguide medium.

Distances between the neighboring peaks in the spectra of diodes manufactured from KR1439-1 and KR1439-2 structures (Fig. 5b) have constant values of $\Delta\lambda$ which are in strict correspondence with the values found from (1). It is of particular importance that this agreement was valid over the entire range of driving current values for the laser diode operating under conditions of stable single-mode lasing.

Mainly laser diodes with naturally cleaved mirrors were used for the investigation and characterization of the parameters of the manufactured heterostructures. For instance, dependences of the threshold current density on the cavity length of laser diodes manufactured from the KR1439-2 batch are presented in Fig. 6. The data for lasers with a wide stripe contact, W = 100 μm, manufactured from a similar heterostructure are presented for comparison in the same figure. The threshold current density at the infinite cavity length is 190 A/cm^2 and 290 A/cm^2 for W = 100 μm and W = 4.5 μm (KR1439-2 batch), respectively. An increase in the threshold current density in the mesa-stripe lasers with a narrow contact is due to the lateral spreading of the current under the mesa-stripe contact [15].

The internal quantum efficiency of the stimulated emission, η_i, and the internal losses α_i are important parameters for attaining high power and efficiency in laser diodes. These parameters were determined from the experimental dependence of the reciprocal differen-

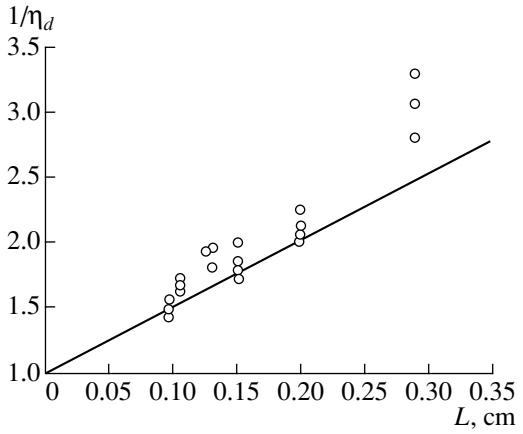

Fig. 7. Experimental dependence of the reciprocal external differential quantum efficiency $1/\eta_d$ on the cavity length L for the laser diodes of the KR1439-2 batch.

tial quantum efficiency on the laser cavity length (Fig. 7) via a known formula [21]:

$$\eta_d = \eta_i \frac{\alpha_{ex}}{\alpha_{ex} + \alpha_i}, \quad (2)$$

where $\alpha_{ex} = 1\backslash L \ln(1\backslash R)$ is the emission output loss (R is the reflectivity of the naturally cleaved laser diode mirrors). Thus, the determined values are as follows: η_i = 93–99% and α_i = 5–7 cm^{-1} for all batches of the heterostructures used. The values for external differential quantum efficiency in the laser diodes with a cavity length L = 1–1.5 mm are within the range of 0.47–0.57 W/A, which is one of the best results for laser diodes of the InGaAsP/InP system.

3. CONCLUSION

The main requirement to be satisfied in order to guarantee single-mode emission in a wide range of driving current values for laser diodes with heterostructures of optimal design is the precise choice of the effective refractive index discontinuity value Δn_L between the active and passive regions of the mesa-stripe in the plane parallel to the *p–n* junction. Any deviation from optimal Δn_L, toward both lower and higher values, leads to essential deterioration of the emission efficiency characteristics in the single-mode operation of the laser diode. For example, a decrease in Δn_L for diodes with a narrow mesa stripe ($W < 4.5$ μm) and a weak longitudinal waveguide leads to an essential increase in the threshold current density, particularly owing to the current spreading effect [15] and a sharp lowering of the minimal driving current, which is, in turn, due to the suppression of lasing. Owing to an insignificant increase in Δn_L relative its optimal value, additional peaks corresponding to the higher order modes appear in the EL spectrum of the laser diode just above the lasing threshold.

Thus, the parameters of a InGaAsP/InP quantum-well heterostructure, grown by MOCVD, with separate confinement and a step waveguide, as well as the mesa-stripe design of the laser diode, were determined theoretically and experimentally in order to attain a high output power in the single-mode operation. An output power of 185 mW was obtained for the single-mode CW laser diode operation (λ = 1480 nm) in lasers with a mesa-stripe width W = 4.5 μm and $\Delta n_L = (6.2–6.8) \times 10^{-3}$. An increase in the FWHM of the emission pattern in the horizontal plane was 1° in comparison with the threshold value. The emission spectrum consisted of a set of longitudinal modes with a fixed $\Delta\lambda$ corresponding to the spacing between modes of the Fabry–Perot cavity. The maximum CW output power of the manufactured lasers was 300 mW.

ACKNOWLEDGMENTS

We thank N.F. Kadashuk, T.N. Drokina, and N.A. Rudova for help in preparing the laser diode samples.

This study was supported in part by grants from the Russian interdisciplinary scientific and engineering program, “Physics of Solid-State Nanostructures.”

REFERENCES

1. S. Namiki, IEEE J. Sel. Top. Quantum Electron. **7** (1), 3 (2001).
2. T. Namegaya, R. Katsumi, N. Iwai, *et al.*, IEEE J. Quantum Electron. **29** (6), 1924 (1993).
3. A. Mathur, M. Fisher, M. Ziari, *et al.*, Electron. Lett. **35** (12), 983 (1999).
4. D. Garbuzov, R. Menna, A. Komissarov, *et al.*, in *Proceedings of Optical Fiber Communication Conference* (Optical Society of America, Washington, DC, 2001), Technical Digest Series, OSA Trends in Optics and Photonics, Vol. 54, PD18 1-3.
5. E. G. Golikova, V. A. Kureshov, A. Yu. Leshko, *et al.*, Fiz. Tekh. Poluprovodn. (St. Petersburg) **34** (7), 886 (2000) [Semiconductors **34**, 853 (2000)].
6. E. G. Golikova, V. A. Kureshov, A. Yu. Leshko, *et al.*, Pis’ma Zh. Tekh. Fiz. **26** (20), 40 (2000) [Tech. Phys. Lett. **26**, 913 (2000)].
7. A. Yu. Leshko, A. V. Lyutetskiĭ, N. A. Pikhtin, *et al.*, Fiz. Tekh. Poluprovodn. (St. Petersburg) **34** (12), 1457 (2000) [Semiconductors **34**, 1397 (2000)].
8. E. G. Golikova, V. A. Gorbylev, N. Yu. Davidyuk, *et al.*, Pis’ma Zh. Tekh. Fiz. **26** (6), 5 (2000) [Tech. Phys. Lett. **26**, 225 (2000)].
9. E. G. Golikova, V. A. Gorbylev, Yu. V. Il’in, *et al.*, Pis’ma Zh. Tekh. Fiz. **26** (7), 57 (2000) [Tech. Phys. Lett. **26**, 295 (2000)].
10. S. L. Chuang, *Physics of Optoelectronic Devices* (Wiley, New York, 1995).
11. M. A. Ivanov, Yu. V. Il’in, N. D. Il’inskaya, *et al.*, Pis’ma Zh. Tekh. Fiz. **21** (5), 70 (1995) [Tech. Phys. Lett. **21**, 198 (1995)].

12. J.-P. Weber, IEEE J. Quantum Electron. **30** (8), 1801 (1994).
13. D. Z. Garbuzov, A. V. Ovchinnikov, N. A. Pikhtin, *et al.*, Fiz. Tekh. Poluprovodn. (Leningrad) **25**, 928 (1991) [Sov. Phys. Semicond. **25**, 560 (1991)].
14. A. Komissarov, M. Maiorov, R. Menna, *et al.*, in *Proceedings of Conference on Laser and Electro-Optics, CLEO'2001, 2001*, CMG1.
15. N. A. Pikhtin, S. O. Slipchenko, Z. N. Sokolova, and I. S. Tarasov, Fiz. Tekh. Poluprovodn. (St. Petersburg) **36** (3), 364 (2002) [Semiconductors **36**, 344 (2002)].
16. Zh. I. Alferov, M. A. Ivanov, Yu. V. Il'in, *et al.*, Pis'ma Zh. Tekh. Fiz. **21** (5), 64 (1995) [Tech. Phys. Lett. **21**, 195 (1995)].
17. N. A. Pikhtin, N. V. Fetisova, E. G. Golikova, *et al.*, in *Proceedings of European Conference on Optical Communication, ECOC'01, 2001,* Vol. 2, p. 166.
18. W. D. Herzog, B. B. Goldberg, and M. S. Unlu, IEEE Photonics Technol. Lett. **12** (12), 1604 (2000).
19. Gen-Lin Tan, R. S. Mand, and J. M. Xu, IEEE J. Quantum Electron. **33** (8), 1384 (1997).
20. R. Gordon and J. Xu, IEEE J. Quantum Electron. **35** (12), 1904 (1999).
21. N. C. Casey, Jr. and M. B. Panish, *Heterostructure Lasers* (Academic, New York, 1978; Mir, Moscow, 1981).

Translated by S. Ktitorov

Semiconductors, Vol. 36, No. 11, 2002, pp. 1315–1321. Translated from Fizika i Tekhnika Poluprovodnikov, Vol. 36, No. 11, 2002, pp. 1400–1407.

PHYSICS OF SEMICONDUCTOR DEVICES

High Efficiency (η_D > 80%) Long Wavelength (λ > 1.25 μm) Quantum Dot Diode Lasers on GaAs Substrates

S. S. Mikhrin*^, A. E. Zhukov*, A. R. Kovsh*, N. A. Maleev*, A. P. Vasil'ev*, E. S. Semenova*, V. M. Ustinov*, M. M. Kulagina*, E. V. Nikitina*, I. P. Soshnikov*, Yu. M. Shernyakov*, D. A. Livshits*, N. V. Kryjanovskaya*, D. S. Sizov*, M. V. Maksimov*, A. F. Tsatsul'nikov*, N. N. Ledentsov*, D. Bimberg, and Zh. I. Alferov***

** Ioffe Physicotechnical Institute, Russian Academy of Sciences, St. Petersburg, 194021 Russia*

*** Technical University of Berlin, D-10623 Berlin, Germany*

^ e-mail: mikhrin@pop.ioffe.rssi.ru

Submitted April 23, 2002; accepted for publication April 25, 2002

Abstract—Diode lasers based on several layers of self-organized quantum dots (QD) on GaAs substrates were studied. The lasing wavelength lies in the range λ = 1.25–1.29 μm, depending on the number of QD layers and optical losses. A record external differential efficiency of 88% and the characteristic temperature of threshold current, 145 K, were obtained. The internal losses, and also threshold and spectral characteristics, are correlated with the optical gain and radiative recombination efficiency, which are strongly dependent on the design of the active region and growth modes. *© 2002 MAIK "Nauka/Interperiodica".*

1. INTRODUCTION

The considerable attention given recently to quantum dots (QDs) in the InAs/(Al)GaAs system is motivated mainly by the possibility of using the spontaneous transformation of the InAs layer into an array of 3D islands in order to achieve, in lasers based on GaAs substrates, an emission wavelength λ = 1.3 μm, which corresponds to minimal dispersion and the second spectral window of optical fibers. The employment of QDs embedded in an external strained InGaAs quantum well (QW) or formed by atomic-layer epitaxy made possible the reproducible fabrication of 1.3-μm lasers with an ultralow threshold current density (19 A cm^{-2} [1], 16–22 A cm^{-2} [2]). However, a relatively low surface density of QDs (~5×10^{10} cm^{-2} per QD layer), which provides for the low density of the transparency current, also results in small values of the maximal optical gain achievable in lasing via the ground state of QDs. With the emission output losses rising, the saturation of gain causes a superlinear increase in the threshold current density and further leads to the transition to the generation via the first excited state of the QD array, which is accompanied by a short-wavelength shift of the lasing wavelength [3]. The necessity to maintain the lasing wavelength in the spectral range of interest (1.3 μm) and to reduce the threshold current density stimulates the application of a laser cavity design with minimal output losses, as in lasers with four cleaved faces [4] and stripe lasers with a high-reflection coating of faces [1, 5] or long stripes [2, 6].

According to the well-known relation between the emission output efficiency and the cavity losses, these designs are mainly characterized by low *external* differential efficiency η_D [7]:

$$\eta_D = \eta_i \frac{\alpha_m}{\alpha_m + \alpha_{in}}, \tag{1a}$$

$$\alpha_m = \frac{1}{2L} \ln\left(\frac{1}{R_1 R_2}\right), \tag{1b}$$

where η_i is the internal quantum efficiency of the stimulated radiation, known also as the internal differential efficiency; α_m and α_{in} are the radiation output losses and internal losses of the laser cavity, respectively; L is the cavity length; and R is the reflectivity of faces. For example, the external differential efficiency reported in [1] was only 2%.

The lasers based on self-assembled QDs have already demonstrated the possibility, in principle, of obtaining high external differential efficiency. In particular, maximal η_D values, above 80%, have been reported for short-wavelength ($\lambda \approx$ 0.94–0.98 μm) lasers [8, 9]. However, for longer wavelength (λ > 1.22 μ) QD lasers, which are of interest for fiber-optical communication systems, the highest reported η_D are only 55–57% [10–12] for systems with two [10] or three [11, 12] QD layers.

The optical gain of a QD laser can be improved by increasing the number of deposited QD layers in the active region. However, the amount of deposited InAs necessary to form a QD array emitting near 1.3 μm is

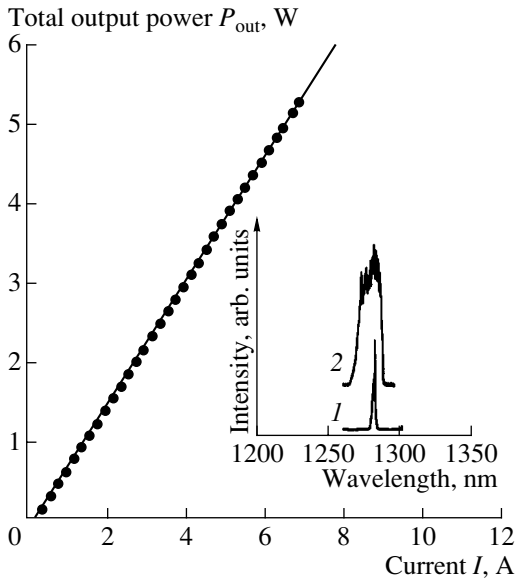

Fig. 1. The total optical power vs. current for a 1.5-mm-long laser with an active region with 10 QD layers (points), and approximation by Eq. (2). Inset: the emission spectra at a current of 1.1 and $15I_{th}$.

considerably larger than for short-wavelength QDs, typically 5–6 monolayers (ML) instead of ≈2 ML. A further increase in the number of QD layers usually leads to the build-up of mismatch stresses in the active region of a long-wavelength laser, thus impairing the threshold current density and the internal efficiency, which is presumably due to the formation of point defects. It is necessary to note also that, in spite of the theoretically predicted possibility of achieving a high temperature stability of laser characteristics, the T_0 values currently being obtained are lower than those for QW lasers.

In the present study, we demonstrate that the optimization of the laser design and the growth conditions of QDs, as well as of the whole laser structure, provides the possibility of raising the number of QD layers in the laser active region to at least ten without sacrificing the threshold characteristics. In these structures, the rise of the threshold current density with the number of layers increasing is associated first of all with increasing transparency current, which is estimated to be 6 A cm^{-2} per QD layer. The rise of the saturated gain results in a considerable broadening of the range of output losses at which long-wavelength lasing via the QD ground state is observed. Combined with a nearly 100% internal differential efficiency and low internal losses (1.2 cm^{-1}), this provided a record external differential efficiency of 88% in a structure with ten QD layers. The characteristic temperature of the threshold current also increased to 145 K. This combination of device characteristics seems very attractive for the applications of QD arrays of this kind in the active regions of the transmission modules of vertical-cavity surface-emitting lasers (VCSELs) and single-mode stripe lasers, in which an extremely high threshold gain is required.

2. EXPERIMENT

The laser structures with separate confinement of charge carriers and the light wave were grown via MBE. The active region of the structures consisted of two, five, or ten InAs QD layers embedded in an external strained InGaAs QW and separated with 33-nm-thick GaAs spacers. QDs were obtained by depositing an InAs layer with an effective thickness of 3 ML, with subsequent overgrowing with a 5-nm-thick $In_{0.15}Ga_{0.85}As$ layer. The width of the AlGaAs/GaAs waveguide was about 0.4 μm. $Al_xGa_{1-x}As$ emitter layers 1.5-μm-thick with an effective content of Al x of 70% were doped with Si and Be to obtain an electron and hole density of 5×10^{17} cm^{-3}, respectively.

It is necessary to note that this set of laser structures was grown under optimal conditions for the deposition of emitter layers with a high Al content in order to achieve their high optical and structural performance; these conditions were also optimized for the active region itself, with special attention given to the reproducibility of such characteristics of its deposition as temperature and arsenic flux. Comparison with the lasers grown under standard MBE conditions (see, e.g., [12]), presented below, shows that this optimization strongly modifies device characteristics.

The structures produced were used to fabricate stripe lasers with a shallow-mesa configuration, with 100-μm-wide and 0.5- to 2-mm-long stripes. No coating was deposited onto the cleaved cavity faces. Several laser structures with four cleaved faces were also studied. The device characteristics were recorded in the temperature range of 20–65°C under excitation with current pulses 1 μm wide and with a 2-kHz repetition frequency.

3. RESULTS AND DISCUSSION

3.1. Differential Efficiency and Internal Losses

The external differential efficiency and the threshold current were estimated from the measured light–current characteristics of stripe lasers at 20°C. Figure 1 presents, as an example, the total optical power P_{out} vs. the driving current I for a laser with ten QD layers, with a stripe length of about 1.5 mm. The inset shows the emission spectra above the generation threshold. The lasing wavelength of 1.28 μm is maintained up to very high values of output power (above 5 W). Fitting the known light–current relation above the generation threshold [7] (line) to the experimental data (points),

$$P_{out} = \frac{\varepsilon \eta_D}{q}(I - I_{th}), \qquad (2)$$

where ε is the emitted photon energy and q is the elementary charge, we find that the threshold current I_{th}

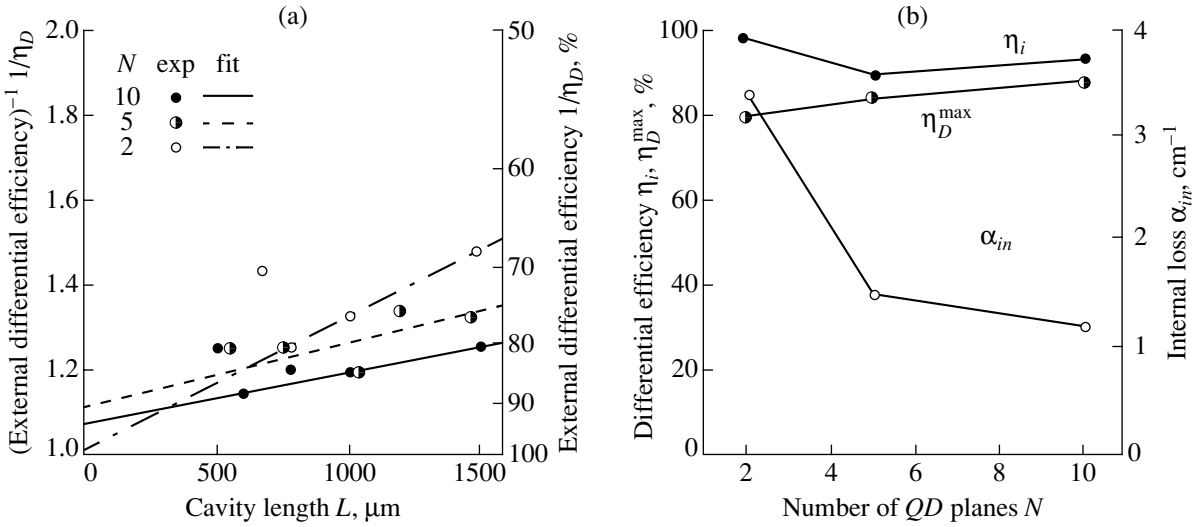

Fig. 2. (a) External differential efficiency η_D vs. the length of a stripe laser for structures with a different number of QD layers (symbols) and fitting by relation (1) (lines). (b) Maximal external differential efficiency η_D^{max}, internal quantum efficiency η_i, and internal losses α_{in} vs. the number of QD layers.

and the external differential efficiency η_D for this device is 220 mA (147 A cm^{-2}) and 80% (0.78 W A^{-1}), respectively.

The dependence of the external differential efficiency on the cavity length is summarized in Fig. 2a for laser structures with a different number of QD layers in the active region. Only the data for cavity lengths at which the lasing occurs via the QD ground state (the wavelength in the range 1.25–1.29 μm) are presented. All the lasers under study exhibit an external differential efficiency above 60%. The maximal measured η_D are 80, 84, and 88% for two, five, and ten QD layers, respectively. To the authors' knowledge, these are the highest reported values not only for long-wavelength QD lasers, but for all 1.3-μm diode lasers of any type grown on GaAs substrates [13]; these values are also among the best for QD lasers of any spectral range [8, 9].

The experimental data are fairly well approximated by the dependence (1a) (line in Fig. 2a), which allows evaluation of the internal differential efficiency and the internal losses as 98.5, 90, and 93%, and 3.4, 1.5, and 1.2 cm^{-1} for two, five, and ten QD layers, respectively. Figure 2b presents the dependence of these parameters, and also of the maximal measured differential efficiency, on the number of QD layers in the active region. In all cases, η_i remains in the limit of 90–100%. Thus, in contrast to [2], no regular dependence of the internal differential efficiency on the design of the active region of the laser (in our case, the number of QD layers) is observed. This can be associated with the higher achieved level of the internal differential efficiency in our structures, since, in the above-mentioned study, the lasers with η_i in the range of 30–55% were under correlation. It is necessary to remark in this context that the approximation of the external differential efficiency using the relation (1a) is somewhat conditional, since this fitting implies that the internal differential efficiency and the internal losses are invariable for all cavity lengths. By contrast, the dependence of η_i and α_{in} on the losses, mentioned in [14], results from the interconnection of all these parameters with the position of the quasi-Fermi levels in the laser active region. Further, the inevitable scatter of data is due to the possible heterogeneity of an epitaxial structure and imperfections in stripe fabrication (e.g., imperfection of cleavages).

Therefore, only average values can be discussed for the parameters η_i and α_{in} obtained by the above-mentioned approximation. Nevertheless, their variation with the modification of the design of the active region allows us to reveal definite tendencies. In particular, we observe a steady decrease of internal losses as the number of QD layers increases, which is especially prominent at the transition from two to five QD layers. The internal losses of a diode laser combine the contributions of several mechanisms [15]. Among them, the most important are the losses due to scattering on the imperfections of the waveguide, absorption by free carriers in the waveguide, and absorption by free carriers in the emitter layers. The contribution of the waveguide scattering to internal losses is defined mainly by the perfection of the epitaxial growth technology, including the planarity of the emitter–waveguide interfaces, possible inclusions with a different structure, and so on. During the early stages of QD laser studies, it was conjectured that a quasi-periodical structure modulation in the middle of the laser waveguide, induced by 3D QD islands, could result in a drastic increase in internal losses. The considerable internal losses (30–50 cm^{-1}) observed in the first QD lasers seemingly confirmed

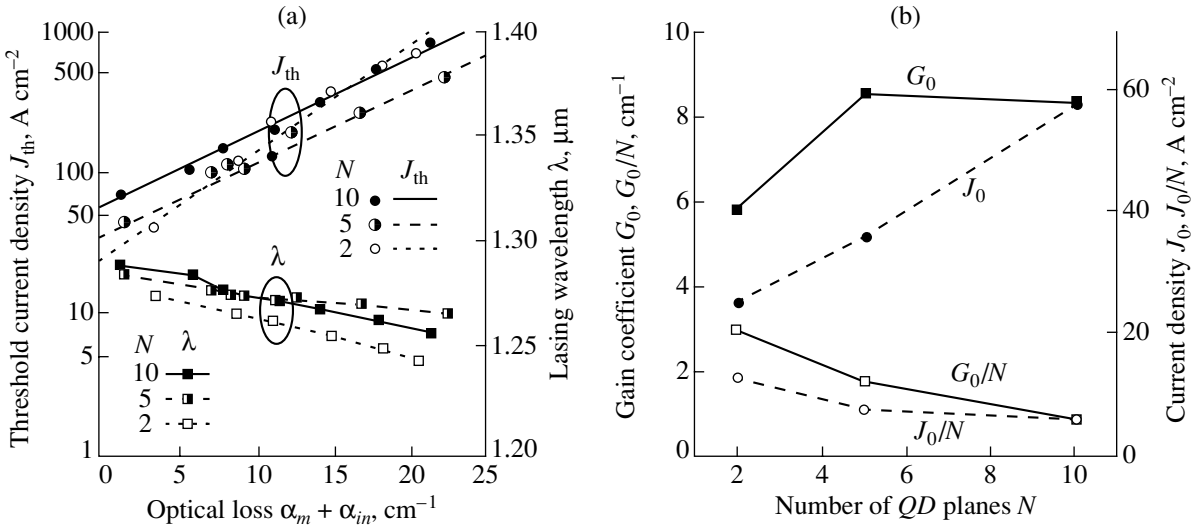

Fig. 3. (a) Threshold current density J_{th} and the lasing wavelength λ vs. the total optical losses for structures with a different number of QD layers (symbols) and fitting by relation (3) (lines). (b) The gain parameter G_0 and the transparency current density J_0, and their values reduced to the number of QD layers (G_0/N, $J_0/$) vs. the number of QD layers.

this hypothesis. However, further studies of multilayer QD lasers failed to confirm this assumption. In fact, a rise in the QD density, that is, in the scattering center density in the laser waveguide, results in a decrease, not an increase, of internal losses (Fig. 2b). Therefore, the self-organized islands do not exert any pronounced effect on internal losses in a laser. Thus, the main contribution is due to the absorption by free carriers.

The contributions to the internal losses from absorption by free carriers in the emitter layers and in the waveguide are proportional to the free carrier density in the respective regions. In emitter layers, the free carrier density is defined by the doping level, and QDs do not affect this type of losses. In contrast, the carrier density in the waveguide and the relevant internal losses can strongly depend on the QD design in the active region. When the surface density of the QD array increases, thus raising the value of the saturated gain, the necessary threshold gain is reached at a lower energy of the quasi-Fermi level, which results in a lower population of states in the matrix (waveguide) and, therefore, reduces the internal losses; this is in agreement with the experimentally observed dependence (Fig. 2b). The reasons for the close similarity of internal losses estimated for five- and ten-layer lasers will be clarified after the investigation of the gain characteristics of these structures.

3.2. Optical Gain

A considerable increase of the external differential efficiency in the lasers based on several QD layers is defined, along with the above-discussed decrease of internal losses, by the extended range of the emission output losses at which lasing via the QD ground state is accessible. In this context, it is necessary to discuss the gain characteristics of the multilayer lasers under study. An experimental correlation between the cavity length and the threshold current density and the estimated values of internal losses allows us to reconstruct the dependence of the threshold current density on total losses ($\alpha_m + \alpha_{in}$), as shown by symbols in Fig. 3a, for laser structures with a different number of QD layers. As seen, increasing the number of QD layers in the active region of the laser leads to a rise in the current corresponding to zero losses (transparency current), due to the higher amount of QD states in the active region. At the same time, in lasers with five and ten QD layers, the threshold current density increases more slowly as the losses rise than in a laser with two QD layers, which is indicative of a higher optical gain. For these lasers, the threshold current density values J_{th} are in the range of 100–200 A cm^{-2} for stripes with a length over 1 mm and increase to 500 A cm^{-2} at L = 0.5 mm. The maximum optical gain is about 23 cm^{-1}.

Experimental relations between the modal gain and the threshold current density were approximated by a logarithmic function (lines) commonly used to describe QD laser characteristics:

$$g = G_0 \ln(J_{th}/J_0), \qquad (3)$$

where G_0 is the gain parameter, and J_0 is the transparency current of an active region. Figure 3b presents these gain parameters, along with their values normalized to the number of layers (G_0/N, J_0/N), as functions of the number of QD layers. The estimated J_0 values steadily increase as N rises; they are 25, 38, and 58 A cm^{-2} for two, five, and ten QD layers, respectively.

The density of the transparency current (i.e., the current necessary for population inversion in the active region) can be estimated from the lifetime τ and the

total surface density of the array (the product of the QD density in a QD layer, n_{QD}, by the number of QD layers in the laser active region, N):

$$J_0 = N\frac{qn_{QD}}{\tau}. \quad (4a)$$

Here, q is the elementary charge, and the lifetime is defined by the relation between the rates of radiative and nonradiative recombination, denoted by subscripts r and nr, respectively:

$$\frac{1}{\tau} = \frac{1}{\tau_r} + \frac{1}{\tau_{nr}}. \quad (4b)$$

Simple estimates assuming 100% efficiency of the radiative recombination ($\tau_r \ll \tau_{nr}$), along with typical values of the surface density of the self-organized QD array and the radiative recombination rate ($4–5 \times 10^{10}$ cm^{-2} and 1–2 nm, respectively [3]), yield a transparency current density of about 5 A cm^{-2} per QD layer. The transparency current densities per QD layer obtained for five- and ten-layer lasers are within 6–7 A cm^{-2}; this correlates perfectly with the given estimations, which leads to the assertion that no other recombination channels except for radiative recombination via the QD ground state exist in these multilayer lasers. At the same time, the reduced value of the transparency current in a two-layer laser is somewhat higher; it is 12.5 A cm^{-2}. We believe that this results from an additional contribution of the recombination via the states in a matrix (waveguide) due to a higher occupancy of the upper-lying states in this structure, which also correlates with higher internal losses in a two-layer laser.

With the number of QD layers rising, the total gain parameter G_0 must increase linearly if the contributions from each of the QD layers to the optical gain are equal. Evidently, in reality the gain of each of the QD planes must be multiplied by some weighting coefficient depending, in particular, on the optical mode intensity at a given plane. The experimentally observed G_0 values are 5.8, 8.5, and 8.3 cm^{-1} for two, five, and ten QD layers, respectively, which yields 2.9, 1.7, and 0.83 cm^{-1} in terms of a single QD layer (Fig. 3b). Thus, the magnitude G_0/N, which characterizes the averaged contribution of a single QD layer to total gain, decreases as the number of QD layers in the active region increases. In this connection, it is worth noting that, when several QD layers are repeatedly deposited in the active region, the flanking QD planes are located apart from the peak of the optical mode in the laser cavity. This fact reduces the contribution of the additional QD planes to the total optical gain. We have calculated the distribution of the optical mode intensity for the given configuration of laser cavities with different numbers of QD layers and found that the average factor of optical confinement in five- and ten-layer lasers decreases to 91 and 71%, respectively, relative to the corresponding value for a two-layer laser. Another factor depressing the gain parameter G_0/N in multilayer structures may be the nonuniform distribution of carrier density over QDs in different layers separated by relatively thick (33 nm) spacers. G_0 can be further enhanced by reducing the spacer thickness, which will lead to the concentration of active layers in the central part of the waveguide and improve the uniformity of their filling with carriers. However, the reduction of the spacer thickness demands further optimization of the growth modes in order to suppress the possible relaxation of elastic stresses in multilayer structures.

Figure 3a also depicts the dependence of the lasing wavelength on total losses. In the entire range of losses presented, lasing occurs via the ground state of QDs. Depending on the level of losses and the number of QD layers in the active region, the lasing wavelength is 1.245–1.29 μm. As seen, an increase in losses results in a certain short-wavelength shift of the wavelength; when losses are equal, the emission of a two-layer laser is distinctly shorter wavelength than that of five- and ten-layer lasers. In fact, the lasing wavelength follows the position of quasi-Fermi levels at the generation threshold. Increasing the carrier density necessary to reach the generation threshold and the related separation of quasi-Fermi levels induce the observed short-wavelength shift with the augmentation of losses. In this case, the rise of the Fermi energy results in the carrier density rising not only in the active region, but also in the laser waveguide. The higher the gain of an active medium, the smaller the separation of quasi-Fermi levels necessary to compensate the growing losses. This implies not only a smaller short-wavelength shift of the emission of high-gain lasers (five or ten lasers), but also a smaller population in the laser waveguide, which correlates well with the discussed decrease of internal losses as the number of QD layers increases. The proximity of the gain parameters of five- and ten-layer lasers results in the close similarity of their spectral characteristics, as well as in the above-mentioned similarity of internal losses.

3.3. Optimization of Growth Conditions

As stated above, the lasers under study were grown in optimized conditions, which suppress the formation of point defects and dislocations in the active region of multilayer structures. Figure 4a presents the threshold current density J_{th} vs. the number of QD layers for structures grown in standard (unshaded circles) and optimized (shaded circles) conditions. To make the comparison of structures with different numbers of layers less ambiguous, we present the data for lasers with four cleaved faces. This configuration of laser structures allows minimization of emission output losses, owing to the formation of a circular laser mode. In this situation, a minimal threshold current density is achieved, which is defined only by internal losses of the laser cavity, thus allowing for the estimation of the upper limit of the transparency current for a given active region. It is worth noting that J_{th} values for lasers

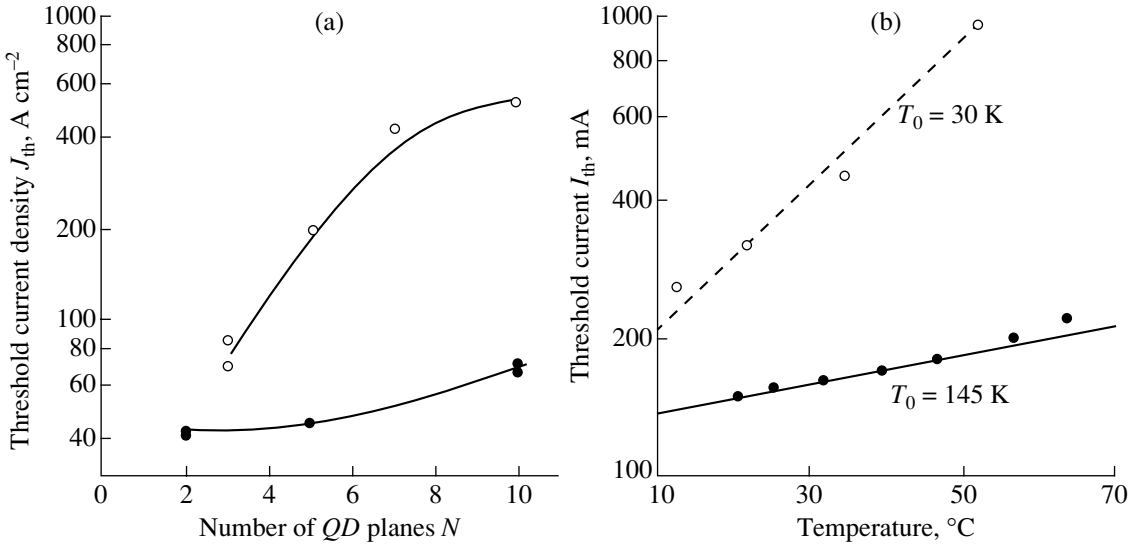

Fig. 4. (a) Threshold current density J_{th} of lasers with four cleaved faces vs. the number of QD layers for standard (open circles) and optimized (solid circles) laser structures. (b) Temperature dependences of the threshold current for stripe lasers based on standard (open circles, N = 3, L = 2 mm) and optimized (solid circles, N = 5, L = 1.5 mm) laser structures and fitting by relation (5) (lines).

with four cleaved faces, grown in optimized conditions, correlate well with the transparency current value estimated from the gain characteristics.

As seen from the figure, the variation of the threshold current density with the number of layers in the active region is noticeably weaker for lasers grown under optimized conditions. In this case, the increasing of the threshold current density as the number of layers increases is related mainly to the increase of the transparency current as the number of QD layers rises. However, in the case when an increase in the number of layers is followed by the formation of nonradiative recombination centers, J_0 can increase more steeply with N, in accordance with Eq. (4). We believe that it is this situation that occurs under standard growing conditions. Therefore, optimizing the growth conditions allows for the fabrication of a QD array with higher structural perfection.

The nonradiative recombination in the active region and waveguide can result not only in the augmentation of the threshold current, but also in its steeper dependence on temperature. In its turn, the suppression of nonradiative recombination through the optimization of growth conditions provided a considerable improvement in the temperature stability of QD laser characteristics. Symbols in Fig. 4b present the threshold current J_{th} vs. temperature for stripe lasers fabricated from epitaxial structures grown in standard or optimized conditions. Lines represent fitting to the experimental data by the relation

$$I_{th}(T) = I_{th}\big|_{20^\circ\mathrm{C}} \exp\left(\frac{T - 20^\circ\mathrm{C}}{T_0}\right), \qquad (5)$$

where T_0 is the characteristic temperature of the threshold current.

In the case of standard conditions, J_{th} sharply increases with temperature and T_0 is only 30 K, while in all the studied lasers grown under optimized conditions T_0 exceeds 100 K when the stripe length is similar. As shown in Fig. 4b, the characteristic temperature of a 1.5-mm-long laser based on an optimized five-layer structure is 145 K. As far as we know, this value is currently the highest one obtained for QD lasers operating in the 1.3-μm wavelength range; it exceeds the best previously reported value [11] by 15%.

4. CONCLUSION

The optimization of the design and growth conditions of 1.25- to 1.3-μm lasers based on a large number of self-organized QD layers allowed us to suppress the formation of nonradiative recombination centers associated with the relaxation of stresses in multilayer QD structures. As a result, a lower threshold current density with a weaker temperature dependence is achieved. The characteristic temperature T_0 is 145 K, which is the best value for long-wavelength QD lasers grown on GaAs substrates. The estimated density of the transparency current per QD layer is 6–7 A cm^{-2}, which correlates quite well with the prediction for the ideal case. It is shown that the internal losses in the lasers based on self-organized QDs are related mainly to the light absorption by free carriers filling the laser waveguide. The augmentation of the number of QD layers allows improvement of the gain characteristics; it reduces the internal losses and the threshold current density and also improves the stability of the wavelength as the

emission output losses rise. The combined effect of the reduction in internal losses to 1.2 cm^{-1}, the possibility of operating in the mode of high emission output losses, and nearly 100% internal differential efficiency in the lasers under study allowed us to achieve a record value of 88% for the external differential efficiency. Further optimization of multilayer QD structures should open the way for the usage of narrower spacer layers separating the QD layers, which will lead to even higher gain, owing to the enhancement of the optical confinement factor and more uniform filling of the active region.

ACKNOWLEDGMENTS

This study was supported by the Russian Foundation for Basic Research (project no. 00-02-17039), the program "Physics of Solid-State Nanostructures," INTAS, and NanOp.

A.E. Zhukov and V.M. Ustinov are grateful to the Foundation for the Support of Russian Science.

REFERENCES

1. G. Park, O. B. Shchekin, D. L. Huffaker, and D. G. Deppe, IEEE Photonics Technol. Lett. **13**, 230 (2000).
2. G. T. Liu, A. Stinz, H. Li, *et al.*, IEEE J. Quantum Electron. **36**, 1272 (2000).
3. A. E. Zhukov, V. M. Ustinov, and Zh. I. Alferov, in *Selected Topics in Electronics and Systems*, Vol. 16: *Advances in Semiconductor Lasers and Applications to Optoelectronics*, Ed. by M. Dutta and M. A. Stroscio (World Scientific, Singapore, 2000), p. 263.
4. Yu. M. Shernyakov, D. A. Bedarev, E. Yu. Kondrat'eva, *et al.*, Electron. Lett. **35**, 898 (1999).
5. G. Park, O. B. Shchekin, S. Csutak, *et al.*, Appl. Phys. Lett. **75**, 3267 (1999).
6. G. T. Liu, A. Stinz, H. Li, *et al.*, Electron. Lett. **35**, 1163 (1999).
7. N. C. Casey, Jr. and M. B. Panish, *Heterostructure Lasers* (Academic, New York, 1978; Mir, Moscow, 1981), Vol. 1.
8. F. Klopf, J. P. Reithmaier, and A. Forchel, Appl. Phys. Lett. **77**, 1419 (2000).
9. A. E. Zhukov, A. R. Kovsh, S. S. Mikhrin, *et al.*, Electron. Lett. **35**, 1845 (1999).
10. X. Huang, A. Stinz, C. P. Hains, *et al.*, Electron. Lett. **36**, 41 (2000).
11. H. Chen, Z. Zou, O. B. Shchekin, and D. G. Deppe, Electron. Lett. **36**, 1703 (2000).
12. A. E. Zhukov, A. R. Kovsh, N. A. Maleev, *et al.*, Appl. Phys. Lett. **75**, 1926 (1999).
13. V. M. Ustinov and A. E. Zhukov, Semicond. Sci. Technol. **15**, R41 (2000).
14. P. M. Smowton and P. Blood, IEEE J. Quantum Electron. **3**, 491 (1997).
15. P. Blood, in *Physics and Technology of Heterojunction Devices*, Ed. by D. V. Morgan and R. H. Williams (P. Peregrinus, London, 1991), Chap. 7, p. 231.

Translated by D. Mashovets